Thermo-Hydraulic-Mechanical-Air Coupling Finite Element Analysis and Its Application to Geotechnical Engineering Problems

熱・土・水・空気連成有限要素解析手法の開発およびその地盤工学問題への応用

December 2013

Yonglin Xiong

Department of Scientific and Engineering Simulation
Nagoya Institute of Technology, Japan

Thermo-Hydraulic-Mechanical-Air Coupling Finite Element Analysis and Its Application to Geotechnical Engineering Problems

熱・土・水・空気連成有限要素解析手法の開発およびその地盤工学問題への応用

A dissertation submitted in partial fulfillment of the requirements for the doctoral degree of engineering

Submitted by

Yonglin Xiong

Supervised by

Professor **Feng Zhang**

Department of Scientific and Engineering Simulation

Nagoya Institute of Technology, Japan

December 2013

Preface

In this dissertation, as another effective method to study and investigate the mechanism of the geotechnical disasters relating with the multi-phase problem, a unified thermo-hydraulic-mechanical-air (THMA) coupling finite element method (FEM) has been proposed and its application to boundary value problems has also been introduced to verify the availability. The main contents of this dissertation are listed as following:

1) As we all known, the accuracy of a numerical simulation mainly depends on whether the constitutive model can adequately describes the various features of soils, which are affected by its property (density, bonding, degree of saturation, temperature) and several loading condition (e.g., cyclic loading, stress history, strain rate and creep). In this dissertation, therefore, two rational constitutive models for soft rock and saturated/unsaturated soil are introduced, whose verifications are confirmed in detail by the drained triaxial compression tests and the creep tests under different temperatures and triaxial plane-strain tests, the drying-wetting tests, 1D consolidation tests.

2) The theory of a thermo-hydraulic-mechanical-air coupling finite element method is explained and derived in detail. In the field equations, the excessive pore water pressure, the excessive pore air pressure, the displacement of solid phase and the temperature are used as unknown variables. In the THMA FE-FD scheme, FEM is used for spatial discretization of the equilibrium and the energy conservation equations, while the backward finite difference scheme is used for the spatial discretization of the continuity equation.

3) In order to verified the availability of the proposed numerical method, the model tests on slope failure due to water injection or rainfall are firstly simulated by the proposed numerical method at room temperature based on the proposed unsaturated model. Because the analysis is based on the soil-water-air fully coupling scheme, not only the seepage of water due to rainfall or water injection, the change of the degree of saturation, the migration of the air pressure, but also

the mechanical behaviors of the unsaturated soil such as the deformation of the ground, the change of pore water pressure, the formation of the shear band occurred in the slope failure, can be simulated on the whole in an unified way, judging from the comparisons between the measured and calculated results. It is particularly worth mentioning that due to the incorporation of a proper constitutive model for unsaturated soil, the calculation can well simulate the different failure behavior of the model Shirasu ground observed in the tests that, in Case 1 (bottom water injection) and Case 3 (top water injection), the slope collapses entirely while in Case 2 (back water injection), only the toe of the slope failed. In the analyses, all the material parameters of the Shirasu in different test cases are the same, which makes the sense for the application of the proposed numerical method.

4) A field heating test, carried out within a saturated soft rock called as Opalinus clay by Mont Terri underground laboratory, is simulated with the proposed analysis based on the modified thermo-elasto-viscoplastic model. It is found that the proposed numerical method can well describe the THM behavior observed in the test, such as the changes of temperature, the excessive pore water pressure (EPWP) and the heat-induced strain.

5) Finally, a heating experiment is simulated, using the same proposed numerical method, in order to investigate the THMA behavior of bentonite-host rock composite structure under unsaturated condition. In the simulation, the mechanical behaviors of host rock and bentonite are described by the proposed models for soft rock and unsaturated soil in this dissertation respectively. Based on the simulated results, it is known that the present simulation can properly describe the THMA behaviors observed in the heating experiment such as the hydration of water, the evolution of temperature, the evolution of excessive pore water pressure to some extent.

According to the above discussions, it is, therefore, reasonable to conclude that the proposed unified THMA numerical method can be applied into the multi-phase geotechnical problems.

Acknowledgements

The work for this dissertation is completed at the Department of Scientific and Engineering Simulation, Nagoya Institute of Technology during the period from April 2011 to March 2014. The completion of this dissertation could not have been finished without the support and encouragement from professors and colleagues, to whom I would like to express my whole hearted thanks and appreciation.

First and foremost, I would like to express my heartiest gratitude and deepest indebtedness to my research supervisor Professor Feng Zhang, Department of Scientific and Engineering Simulation, Nagoya Institute of Technology, for his valuable guidance, continuous inspiration and selfless supports throughout this research work. In the past five years, he was not only a good supervisor, but also like a kind father. Professor's rigorous spirits and creative sights in the research will continue to be beneficial to the author's work in the future. Besides Prof. F. Zhang provided much help in my research, I couldn't forget his help for me when I met a traffic accident in October, 2013. I feel like to express my thanks again to Prof. F. Zhang and his wife – Mrs. Yin Mao for their kindness and supports.

Specially, I want to express my sincere thanks to Professor Atsushi Yashima, Gifu University, who gives me a lot of good ideas and advices as my reviewer of doctoral dissertation. And thanks for coming all the way from Gifu University to attend my defense for doctoral dissertation.

I want to express my great appreciations to Honorary Professor Teruo Nakai, Nagoya Institute of Technology, who is one of my respected professors. His passion about the research impressed me deeply.

I would like to express my thanks to Professor Maeda Kenichi, Nagoya Institute of Technology, who gives me many valuable suggestions on this research work.

I would like to express my much gratitude to Associate Professor Md. Shahin Hossain,

THERMO-HYDRAULIC-MECHANICAL-AIR COUPLING FINITE ELEMENT ANALYSIS AND ITS APPLICATION TO GEOTECHNICAL ENGINEERING PROBLEMS

Contents

CHAPTER 1 GENERAL INTRODUCTION

1.1 Background of the Study

Multi-phase problem has drown more attention recently because of its wide involvement in geotechnical engineering problems as shown in Fig.1.1, not only in instant failure problem like slope failure, debris flow, liquefaction, but also in long-term stability problem like deep geological repository of high-level radioactive waste. Numerous researches, both in laboratory/field tests and numerical simulation/prediction, have been conducted in this field ceaselessly. Yet it is still far away from the state with which we can satisfy. The key problem is that, in most cases, people have to simplify a real geotechnical problem with some assumptions and to pick up one or several factors he thinks the most important and takes them as his concern while other factors are neglected. For instant, constitutive model is always divided into two parts, one for saturated material and another is for unsaturated. Thermal and viscoplastic effects are the other questions needed to be improved. What we want to emphasize here is that, the physical states, such as the saturation (S_r) or the temperature (T) are only the states of a geomaterial, you cannot say that the geomaterial is a different material when the states are different. Unfortunately, in most cases, a constitutive model usually only considers the geomaterial in a specific state, in other words, it can describe the mechanical behavior of the geomaterial in the specific state but cannot fit anymore at other states.

In order to investigate the mechanisms and phenomena of these disasters, the field tests, of course, may be the best choice, but it is rarely done because of high cost. Even sometime it is impossible to reproduce the whole process in the field tests such as the geological disposal of the high-level nuclear waste, because the heating period caused by the high-level nuclear waste will last for tens of thousands of years or even longer for some radioactive substances. Numerical simulation, therefore, will be another effective method to describe and predict the mechanisms and behaviors on the condition that the numerical method is able to fit the results of field experiments or model tests, at least in a limited period.
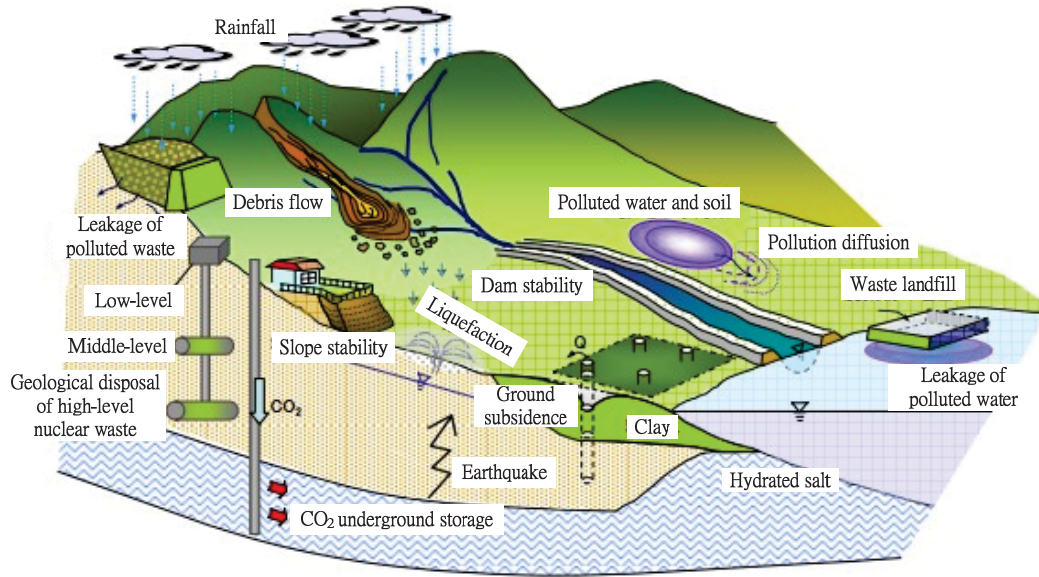
Fig.1.1 Geotechnical disasters related with multiphase problems (data from Nishigaki)

 In this dissertation, two parts can be divided:

(1) The first part is the basic theory of numerical analysis. As we all known, the accuracy of a numerical simulation mainly depends on whether the constitutive model can adequately describes the various features of soils, which are affected by its property (density, bonding, degree of saturation, temperature) and several loading condition (e.g., cyclic loading, stress history, strain rate and creep). At the same time, a reasonable and good numerical method is also needed to ensure the accuracy and reliability of numerical simulation.

In this study, two constitutive models are firstly introduced, one is the thermo-elasto-viscoplastic model for soft sedimentary rock, and the other one is the thermo-elastoplastic model for unsaturated soil. The validations of two models have been clarified in detail in this study.

Then field equations of thermo-hydraulic-mechanical-air coupling finite element method has been derived in detail based on the FE-FD scheme in soil-water two-phase field proposed by Oka et al. (1994).

(2) The second part is the application of the proposed numerical analysis. In this study, Simulations for an isotropic element heating test (Baldi et al., 1991) and a

real-scale field heating test (Gens et al., 2007) have been first conducted to verify the applicability of the proposed numerical method. Then the triaxial tests on unsaturated silty clay (Oka et al., 2010a) and the model tests on slope failure in a compacted unsaturated Shirasu (Kitamura et al, 2007) have been also simulated in order to check the validation of the proposed numerical analysis.

1.2 Review of Previous Work

1.2.1 Related to constitutive models of geomaterials

No one doubts the fact that a rational and applicable constitutive model is crucial important to the accuracy of the numerical simulations for boundary value problem (BVP). A good constitutive model must have the following features: first of all, it can describe the main characteristics of the geo-material, such as the strain softening, strain hardening, the time-dependency, the thermal dependency and the intermediate-stress dependency. Meanwhile, it should employ as few parameters as possible, with definite physical meaning, to simply the calibration of the model for each geo-material. Finally it should be able to describe the main characteristics under different loading and drained conditions.

It is well known that Cam-clay model with few parameters is regarded as the first elastoplastic model to describe the behavior of saturated clay (Schofied and Wroth, 1968) and applied into boundary value problems successfully. Henkel's (1960) finding that the volume change of a saturated clay exhibited stress independency also provided experimental support of the theoretical basis of the Cam-clay model. Cam-clay model, however, can only describe well the behaviors of remolded soil or lightly overconsolidated soil.

Hashiguchi (1978) introduced the concept of subloading yield surface into Cam-clay model to describe the behaviors of heavily overconsolidated soil such as positive dilatancy during strain hardening. It is worth noting that the Cam-clay model with subloading yield surface was based not on the classical but on the unconventional plasticity (Drucker, 1988). In the classical plasticity, the behavior of soil is considered as pure elasticity when reloading occurs after unloading, but it is regarded as elastoplastic response in the unconventional plasticity as shown in Fig.1.2. In addition, a

normal consolidated soil is unloaded from A to B and then reloaded from B to C, the soil will change into overconsolidated state. In other words, the plasticity will be also generated in overconsolidated state.

(a) Classical plasticity   (b) Unconventional plasticity
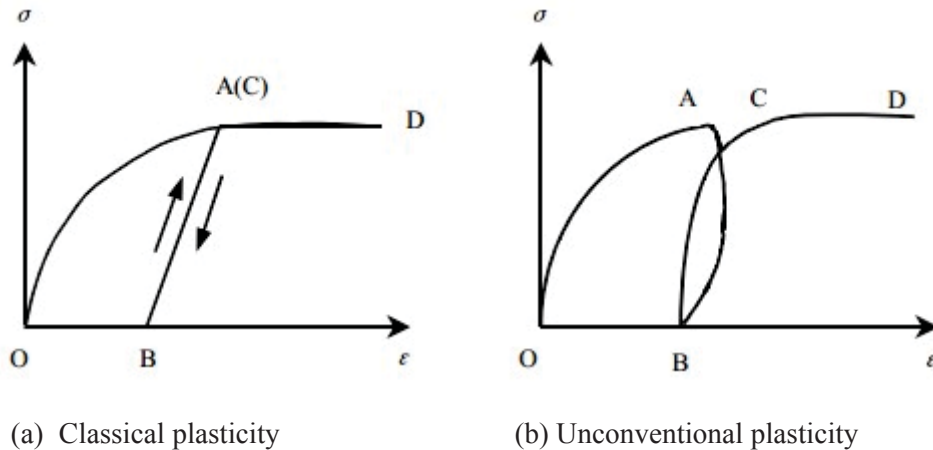
Fig.1.2 Stress-strain relationship of classical and unconventional plasticity

The superloading yield surface concept proposed by Asaoka et al. (1998) was newly introduced to the Cam-clay model in order to describe the mechanical behaviors of highly structured soils, in which de-structured soils were assumed to follow the Cam-clay model. The structured state of a soil is simply defined as the size ratio of the Cam-clay yield surface and subloading yield surface, and the superloading yield surface lies above the Cam-clay yield surface. On the basis of unconventional plasticity theory, the superloading yield surface concept, together with subloading yield surface concept, describes the degradation processes from both an overconsolidated state to a normally consolidated state and a structured state to a de-structured state. These degradation processes continue gradually with ongoing plastic deformation.

Nakai and Hinokio (2004) proposed a simple elastoplastic model for normally and overconsolidated soil with unified material parameters based on the SMP (Spatial Mobilized Plane) concept (Mastuoka and Nakai,1974) and t_{ij} concept. This model can take into consideration the influence of density and/or confining pressure on the deformation and strength characteristics of soils, but also can take into account the influence of intermediate principal stress on the deformation and strength of soils and the stress path dependency on the plastic flow.

Regarding soft rock as a heavily overconsolidated soil, Zhang et al. (2005) proposed a simple elasto-viscoplastic model of soft rocks based on Cam-Clay model, using the concept of subloading yield surface (Hashiguchi and Ueno, 1977) and the t_{ij} concept (Nakai and Mihara, 1984). This model can not only describe the time dependent behaviors of soft rocks, but also can take into consideration the influence of intermediate stress properly.

Zhang and Zhang (2009) proposed a simple thermo-elasto-viscoplastic model for soft sedimentary rock, which can not only describe properly the thermodynamic behavior, but also overconsolidated and time-dependent behavior of soft sedimentary rocks in the ordinary stress space based on the model proposed by Zhang et al. (2005).

With regard to unsaturated soil, since the pioneering work by Alonso et al. (1990), in which Barcelona Basic Model (BBM) was proposed using the concept of loading-collapse (LC) yield surface and suction increase (SI) yield surface and regarded as one of the fundamental models for unsaturated soil, a number of elasto-plastic constitutive models have been developed for modeling the behavior of unsaturated soil. Some of these models are proposed in the space of net stress and suction such as Cui and Delage (1996), Chiu and Ng. (2003) and Sheng et al. (2008), whereas others are in the space of Bishop's effective stress and suction such as Kohgo et al.(1993), Loret and Khalili, (2002) and Sun et al. (2007a). More recently, some constitutive models used the effective stress and degree of saturation as independent state variables have been also established such as Ohno et al. (2007), Zhang and Ikariya (2011) and Zhou et al.(2012a, 2012b). As pointed out by Zhang and Ikariya (2011), using effective stress and degree of saturation in modelling unsaturated soil is much easier and smoother to describe the behavior of soil from unsaturated state to saturated state than using net stress or effective stress and suction as independent state variables.

1.2.2 Related to field theory of numerical analysis

Soil-water coupled two-phase field theories were developed and established in the process of intensive research on the phenomenon of soil consolidation and liquefaction. Many coupling schemes are based on Biot's two-phase mixture theory. Biot (1941) proposed his famous three-dimensional consolidation theory that can take into account

the flow of pore water in soils. Based on Biot's theory, Oka *et al.* (1991, 1994) proposed a soil-water coupled two-phase field theory with u-p formulation. The solid's displacement and pore water pressure are taken as the basic variables in governing equations. An FEM-FDM coupled scheme is used for the spatial discretization of the governing equations to reduce the total degrees of freedom. The finite difference method is used for the spatial discretization of the continuity equations, while the finite element method is used for the spatial discretization of the equilibrium equation, and Newmark's β-methods is used for the time discretization of both equations.

In the original work by Oka *et al.* (1991, 1994), the governing equations of two-phase field theory were derived based on the assumption of infinitesimal strain. But considering that during liquefaction large deformation will probably occur, the assumption of infinitesimal strain is not suitable and sufficient for liquefaction analysis. Using the finite deformation algorithm, Ye (2006) re-derived the governing equations of Oka's two-phase theory.

Oka et al. (2010b), a multiphase deformation analysis of a river embankment was carried out using a soil-water-air fully coupling finite element method, in which a complex elasto-viscoplastic constitutive model for unsaturated soil proposed by Oka et al. (2008) was used. Iwai et al. (2013) also conducted a numerical simulation for the deformation of sea bed due to the pressure reduction of methane hydrate, which is called as depressurization method in the excavation process of the methane hydrate. In Iwai's calculation, a multi-phase-mixture theory, in which not only the soil-water-air coupling problem but also the energy conservation was considered, was employed in the finite deformation analysis for the deformation problem caused by the depressurization of the methane hydrate beneath sea bed.

1.2 Organization of the Dissertation

This dissertation consists of eight chapters and is organized as follows:

In Chapter 2, a thermo-elasto-viscoplastic model in ordinary stress space (Zhang and Zhang, 2009) is modified using the t_{ij} concept, which can not only describe the influence of temperature on the deformation and the strength of geomaterials but also can take into account the influence of intermediate principal stress. It needs to be

emphasized here that compared with the model proposed by Zhang et al. (2005), only one physical property, the thermal expansion coefficient, is added to the modified model in the framework of the critical state soil mechanics. Then the performance of the modified model is confirmed with the drained triaxial compression tests and the creep tests under different temperatures and triaxial plane-strain tests.

In Chapter 3, a new thermo-elastoplastic constitutive model for saturated /unsaturated soil based on the model proposed by Zhang and Ikariya (2011) is conducted to consider the influence of temperature. At the same time, a new moisture characteristic curve (MCC) conducted by Zhang and Ikariya (2011) is also modified by using a simple way proposed by Sheng and Zhou (2011) to describe the influence of the deformation under undrained condition. The newly proposed model can describe well the hydro-mechanical coupling behavior often observed in the test for unsaturated soil, that is, the effect of deformation on the MCC is possible to be described, and vice versa. At the same time, the effect of temperature on the deformation and strength of unsaturated soil in the proposed model can be reasonable to be considered. The validations of the proposed model have been confirmed by the drying-wetting tests, 1D consolidation tests, and triaxial compression shear tests under different conditions.

In Chapter 4, the field equations of a thermo-hydraulic-mechanical-air fully (THMA) coupling finite element method is derived in detail. In the field equations, the excessive pore water pressure, the displacement of solid phase and the temperature are used as unknown variables. In the THMA FE-FD scheme, FEM is used for spatial discretization of the equilibrium and the energy conservation equations, while the backward finite difference scheme proposed by Akai and Tamura (1978) is used for the spatial discretization of the continuity equation.

In Chapter 5, first of all, the triaxial compression tests under undrained and unvented condition are simulated by the proposed THMA numerical method in order to verify the validity of the proposed numerical method. In the simulation, the elementary behavior of the triaxial tests is calculated with 3D FE-FD analysis using one-element mesh. From the comparisons between the test and simulation, it is found that the proposed numerical method can well describe the test behaviors such as the skeleton stress path, the stress-strain relation, and the developments of PWP and PAP under

different suctions.

The model tests on slope failure due to water injection or rainfall have then been simulated by the same proposed numerical method. Because the method is based on the soil-water-air fully coupling scheme, not only the seepage of water due to rainfall or water injection, the change of the degree of saturation, the migration of the air pressure, but also the mechanical behaviors of the unsaturated soil such as the deformation of the ground, the change of pore water pressure, the formation of the shear band occurred in the slope failure, can be simulated on the whole in an unified way, judging from the comparisons between the measured and calculated results. It is particularly worth mentioning that due to the incorporation of a proper constitutive model for unsaturated soil, the calculation can well simulate the different failure behavior of the model Shirasu ground observed in the tests that, in Case 1 and Case 3, the slope collapses entirely while in Case 2, only the toe of the slope failed. In the analyses, all the material parameters of the Shirasu in different test cases are the same, which makes the sense for the application of the proposed numerical method. It is worth noting that the temperature, one the state variable, is assigned as constant throughout the simulation in the THMA analysis.

In Chapter 6, an isotropic element heating test is firstly simulated by the proposed THMA analysis based on the modified thermo-elasto-viscoplastic model presented in Chapter 2. The calculation can explain well the phenomenon observed in the test that the heat-induced volumetric strain measured by the water discharge changes from shrinking to expansion as OCR increases during the isotropic heating process. From the THMA analysis, it is found that soil skeleton always expands with the increase of temperature regardless of what kind of OCR may be. The discharge of the water is just caused by different thermal expansion properties of the soil particles and the pore water. In a word, this phenomenon is merely a boundary value problem with soil-water interaction, not an inherent property of the rock itself that was regarded by some researchers.

Then a field test of heating process (Gens et al., 2007) is also simulated with the proposed THMA analysis based on the modified thermo-elasto-viscoplastic model. It is found that the proposed numerical method can well describe the THM behavior observed in the test, such as the changes of temperature, the EPWP and the heat-induced

strain. In the THMA analysis of this chapter, the degree of saturation is always 1.0 because the test is under saturated ground.

In Chapter 7, finally, a heating experiment (Munoz, 2006) is simulated, using the same proposed numerical method, in order to investigate the THMA behavior of bentonite-host rock composite structure under unsaturated condition. The program is based on a FE-FD scheme in fully coupled soil-water-air three-phase field theory under non-isothermal condition. In the simulation, a rational constitutive model using the Bishop-type skeleton stress and the degree of saturation as the state variables is adopted, which can describe the behavior of saturated and unsaturated soil in unified way. Based on the simulated results, it is known that the present simulation can properly describe the THMA behaviors observed in the heating experiment such as the hydration of water, the evolution of temperature, the evolution of excessive pore water pressure to some extent. It is, therefore, possible to apply this numerical method to investigate the real field problem in the geologic disposal of high-level radioactive waste (HLW). It is worth noting that the air pressure is assumed as constant throughout the simulation in the THMA analysis.

References

1) Akai, K. and Tamura, T. (1978): Numerical analysis of multi-dimensional consolidation accompanied with elasto-plastic constitutive equation, Journal of Japanese Civil Engineering Society, No. 269, 95-104 (in Japanese).

2) Alonso, E. E., Gens, A., and Josa, A. (1990): A constitutive model for partially saturated soils. Geotechnique, 40(3): 405-430.

3) Asaoka, A., Nakano, M. and Noda. T. (1998): Super loading yield surface concept for the saturated structured soils, Proc. of the Fourth European Conference on Numerical Methods in Geotechnical Engineering-NUMGE98, 232-242.

4) Baldi G, Hueckel T, Peano A, Pellegrini R. (1991): Developments in modeling of thermo-hydro-geomechanical behavior of Boom clay and clay-based buffer materials, Report EUR 13365, Commission of the European Communities, Nuclear science and technology.

5) Biot, M. A. (1941): "General theory of three-dimensional consolidation", Journal of *Applied Physics*, Vol. 12, 155-164

6) Cui, Y. J. and Delage, P. (1996): Yielding and plastic behavior of an unsaturated compacted silt, Geotechnique, 46(2), 291-311.

7) Chiu, C. F., and Ng, C. W. W. (2003). A state-dependent elasto-plastic model for saturated and unsaturated soils. Geotechnique, 53(9): 809-829.

8) Drucker, D.C. (1988): Conventional and unconventional plastic response and representation, Applied Mechanics Review, Vol.41, No.4, 151-167.

9) Gens A., Vaunat J., Garitte B. and Wileveau Y. (2007): In situ behavior of a stiff layered clay subject to thermal loading: observations and interpretation, *Geotechnique*, Vol.57, No. 2, 207-228.

10) Henkel, D.J. (1960): The shear strength of saturated remoulded clay, *Proceedings of Research Conference on Shear Strength of Cohesive Soils at Boulder, Colorada*, 533-540.

11) Hashiguchi, K. and Ueno, M. (1977): Elastoplastic constitutive laws of granular

material, Constitutive Equations of Soils, *Pro. 9th Int. Conf. Soil Mech. Found. Engrg., Spec. Ses. 9, Murayama, S. and Schofield, A. N. (eds.), Tokyo, JSSMFE*, 73-82.

12) Iwai, H., Oka, F., Kimoto, S., Kitano, T. and Akai, T. (2013): A numerical simulation of decomposition behavior and ground deformation of methane hydrate bearing sediments induced by depressurization method, *Proc. of 13th Japan Symposium on Rock Mechanics & 6th Japan-Korea Joint Symposium on Rock Engineering*, 401-405.

13) Kitamura, R., Sako, K., Kato, S., Mizushima, T. and Imanishi, H. (2007): Soil tank test on seepage and failure behaviors of Shirasu slope during rainfall, *Japanese Geotechnical Journal*, Vol. 2, No. 3, 149-168 (in Japanese).

14) Kohgo, Y., Nakano, M., and Miyazaki, T. (1993): Theoretical aspects of constitutive modelling for unsaturated soils. Soils and Foundations, 33(4): 49-63.

15) Loret, B., and Khalili, N. (2002): An effective stress elastic-plastic model for unsaturated porous media. *Mechanics of Materials*, 34(2): 97-116.

16) Mastuoka, H. and Nakai, T. (1986): Stress-deformation and strength characteristics of soil under three different principal stresses, *Soils and Foundations*, Vol.29, No.1, 119-137.

17) Munoz, J. (2006): Thermo-hydro-mechanical analysis of soft rock, application to a large scale heating test and large scale ventilation test, PhD thesis.

18) Nakai, T. and Mihara, Y. (1984): A new mechanical quantity for soils and its application to elastoplastic constitutive models. *Soils and Foundations*, Vol.24, No.2, 82-94.

19) Nakai T. and Hinokio M. (2004): A simple elastoplastic model for normally and over consolidated soils with unified material parameters, *Soils and Foundations*, Vol.44, No.2, 53-70.

20) Oka, F., Yashima, A., Shibata, T., and Kato, M. (1991): A finite element analysis of liquefaction of seabed due to wave action, *GEO-COAST*, 91, 621-626

21) Oka, F., Yashima, A., Shibata, T., Kato M. and Uzuoka, R. (1994b): FEM-FDM coupled liquefaction analysis of a porous soil using an elasto-plastic model", *Applied Scientific Research*, Vol.52, 209-245

22) Oka, F., Feng, H. and Kimoto, S. (2008): A numerical simulation of triaxial tests of unsaturated soil at constant water and constant air content by using an elasto-viscoplastic model, *Proceeding of 1st European conference on unsaturated soils*, 735-741

23) Oka, F., Kodaka, T., Suzuki, H., Kim, Y., Nishimatsu, N. and Kimoto, S. (2010a): Experimental study on the behavior of unsaturated compacted silt under triaxial compression, *Soil and Foundations*, Vol. 50, No. 1, 27-44.

24) Oka, F., Kimoto, S., Takada, N., Gotoh, H. and Higo, Y. (2010b): A seepage-deformation coupled analysis of an unsaturated river embankment using a multiphase elasto-viscoplastic theory, *Soil and Foundations*, Vol. 50, No. 4, 483-494.

25) Ohno, S., Kawai, K. and Tachibana, S. (2007): Elasto-plastic constitutive model for unsaturated soil applied effective degree of saturation as parameter expressing stiffness. *JSCE*, 63(4), 1132-1141. (in Japanese)

26) Schofied, A.N. and Wroth, C.P. (1968): Critical state soil mechanics, McGraw-Hill.

27) Sheng, D., Fredlund, D. G., and Gens, A. (2008): A new modelling approach for unsaturated soils using independent stress variables. *Canadian Geotechnical Journal*, 45(4): 511-534.

28) Sheng, D. and Zhou, A.N. (2011): Coupling hydraulic with mechanical models for unsaturated soils, *Canadian Geotechnical Journal*, 48(5): 826-840.

29) Sun, D. A., Cui, H. B., Matsuoka, H., and Sheng, D. (2007a). A three-dimensional elastoplastic model for unsaturated compacted soils with hydraulic hysteresis. *Soils and Foundations*, 47(2): 253-264.

30) Zhou, A. N., Sheng, D. C., Sloan, S. W. and Gens, A. (2012a): Interpretation of unsaturated soil behaviour in the stress-saturation space, I: Volumetric change and

water retention behaviour, *Computers and Geotechnics*, 43, 178-187.

31) Zhou, A. N., Sheng, D. C., Sloan, S. W. and Gens, A. (2012b): Interpretation of unsaturated soil behaviour in the stress-saturation space, II: Constitutive relationships and validations, *Computers and Geotechnics*, 43, 111-123.

32) Zhang F., Yashima A., Nakai T., Ye G. L. and Aung H. (2005): An elasto-viscoplastic model for soft sedimentary rock based on tij concept and subloading yield surface, *Soils and Foundations*, Vol. 45, No. 1, 65-73.

33) Zhang S. and Zhang F. (2009): A thermo-elasto-viscoplastic model for soft sedimentary rock, *Soils and Foundations*, Vol. 49, No. 4, 583-595.

34) Zhang, F. and Ikariya, T. (2011): A new model for unsaturated soil using skeleton stress and degree of saturation as state variables. Soils and Foundations, 51(1), 67-81.

CHAPTER 2 MODIFIED THERMO-ELASTO-VISCOPLASTIC CONSTITUTIVE MODEL FOR SOFT SEDIMENTARY ROCK

2.1 General

As a candidate engineering material of geological repository of high-level nuclear waste, generally speaking, mechanical behavior of soft sedimentary rock is thermo-elasto-plastic, strain hardening-strain softening and time dependent. Physically, soft sedimentary rock has an unconfined compressive strength of 1~20 MPa and its mechanical behavior is between the behavior of soil and rock.

In terms of the mechanical behavior of soft sedimentary at room temperature, much research had been done within the framework of continuum mechanics. Oka and Adachi (1985) proposed an elastoplastic model with strain softening for soft rock, based on which a finite element analysis can lead to a unique solution (Adachi and Oka, 1995) for initial value and boundary value problems. An elasto-viscoplastic model, which can describe not only the strain softening behavior but also the time-dependency property of soft rock, was proposed by Adachi et al. (1990). Zhang et al. (2005) assumed that the soft rock can be regarded as a heavily overconsolidated soil and proposed an elasto-viscoplastic model for soft rock, using the concept of subloading yield surface (Hashiguchi and Ueno, 1977) and the t_{ij} concept (Nakai and Mihara, 1984). This model can not only describe the time dependent behaviors of soft rocks, but also can take into consideration the influence of intermediate stress properly.

As for the thermal behavior of the geomaterials, some thermo-elasto- viscoplastic models have been proposed, most of which are deduced using the thermodynamic theorems to establish a series of restricted relations for the variables involved in the models, e.g. stress tensor, strain tensor, hardening parameters and entropy at first, and then deduced the models using common concepts such as flow rule, yielding function, plastic potential, normality rule and etc. Detailed discussion on this issue can be found in the review by Kitagawa (1972), the work by Rojas et al. (2000) and the book by Lebon et al. (2008). In proposing a thermodynamic model, the most important but very

difficult step is to formulize the thermodynamic functions, which satisfies above-mentioned restricted relations for the variables, which always makes the model too complicated and difficult to understand.

A simple thermo-elasto-viscoplastic model for soft sedimentary rock under ordinary *p-q* stress space has been proposed by Zhang & Zhang (2009), which can not only describe properly the thermodynamic behavior, but also overconsolidated and time-dependent behavior of soft sedimentary rocks. And it is proved that the proposed model satisfies the 1st and 2nd thermodynamic theorems in the framework of non-equilibrium thermodynamics. However, the influence of the intermediate principal stress, which plays an important role in describing the mechanical behavior of geomaterials in a generalized stress state, cannot be described properly in the original model.

In this chapter, a thermo-elasto-viscoplastic model (hereafter it will be called as original model) proposed by Zhang and Zhang (2009) is firstly introduced simply, and then modified model is derivate in order to take into consideration the influence of the intermediate principal stress in the t_{ij} stress space. The validity of the modified model was confirmed by laboratory tests on soft sedimentary rock (Nishimura, 2013) and manmade soft rock (Sekine, 2009).

2.2 Modified Thermo-Elasto-Viscoplastic Constitutive Model for Soft Sedimentary Rock

2.2.1 Brief description of original thermo-elasto-viscoplastic model

It is well known that change of temperature may generate elastic strain, under some circumstances, may even generate plastic strain. Zhang and Zhang (2009) proposed a constitutive model (later it will be called as original model) in which an equivalent stress induced by temperature change is adopted in order to consider the influence of temperature on the deformation and strength of soft rock as shown in Fig.2.1.

Similar to the elastic volumetric strain, it is reasonable to assume that the plastic volumetric strain of geomaterials is made up from two independent parts, that is, thermodynamic ε_v^{pT} and stress-induced $\varepsilon_v^{p\sigma}$, and can be expressed as:

$$\varepsilon_v^p = \varepsilon_v^{p\sigma} + \varepsilon_v^{pT} \qquad \text{or} \qquad d\varepsilon_v^p = d\varepsilon_v^{p\sigma} + d\varepsilon_v^{pT} \tag{2.2.1}$$
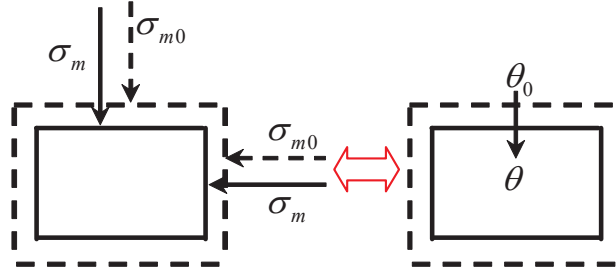
Fig.2.1. Similarity of volumetric strains caused by real mean stress σ_m and equivalent stress $\tilde{\sigma}_m$ due to change of temperature (Zhang and Zhang, 2009)

The elastic volumetric strain is calculated in the following due to the change of temperature ΔT :

$$\varepsilon_v^{eT} = 3\alpha_T^s \Delta T = 3\alpha_T^s(T - T_0) \Rightarrow \dot{\varepsilon}_v^{eT} = 3\alpha_T^s \dot{T} \Rightarrow \dot{\varepsilon}_{ij}^{eT} = \alpha_T^s \dot{T}\delta_{ij} \tag{2.2.2}$$

where, T is present temperature, T_0, a reference temperature, is an arbitrary value and is taken as the global average temperature, that is, 15°C. α_T^s is the linear thermal expansion coefficient of solid phase of geomaterial whose value should be negative because compression is usually taken as positive in geomechanics.

Based on the concept of equivalent stress and Hook's theory, the equivalent stress is expressed as:

$$\tilde{\sigma}_m = \sigma_{m0} + 3K^s\alpha_T^s(T - T_0) \tag{2.2.3}$$

where, σ_{m0}, usually is taken as 98kPa, is a reference mean stress, K^s is the bulk modulus of solid phase.

On the other hand, the thermodynamic plastic volumetric strain ε^{pT} is also evaluated by e-ln$p$ relation based on the equivalent stress as shown in Fig.2.2 and given as

$$\varepsilon_v^{pT} = C_p \ln\frac{\tilde{\sigma}_m}{\tilde{\sigma}_{m0}} = C_p \ln\frac{\tilde{\sigma}_m}{\sigma_{m0} + 3K\alpha_T^s(T_0 - T_0)} = C_p \ln\frac{\sigma_{m0} + 3K^s\alpha_T^s(T - T_0)}{\sigma_{m0}} \tag{2.2.4}$$

where, $C_p = (\lambda - \kappa)/(1 + e_0) = E_p/(1 + e_0)$, e_0 is reference void ratio at σ_{m0} , λ is

compression index and κ is swelling index.
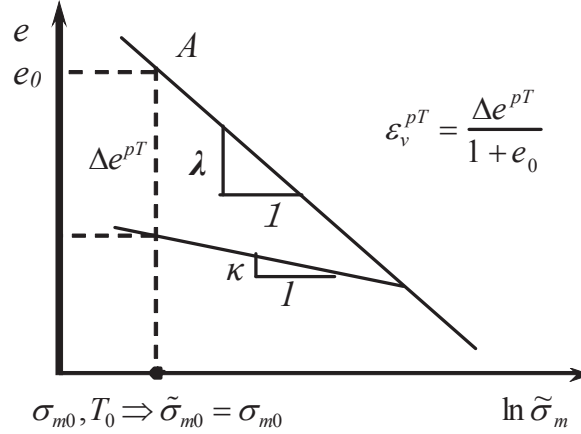
Fig.2.2. Illustration of the relation between equivalent stress and void ratio difference (Zhang and Zhang, 2009)

The original model was proposed within the framework of critical state soil mechanics and based on subloading concept proposed by Hashiguchi and Ueno (1977), a brief description of the yield surface passing through present stress and temperature state is presented as Fig.2.3 and be given as:

$$f(\sigma,T,\varepsilon_v^p) = \ln\frac{\sigma_m}{\sigma_{m0}} + \frac{\sqrt{3}\sqrt{J_2}}{\mathrm{M}\sigma_m} + \ln\frac{\sigma_{m0} + 3K^s\alpha_T^s(T-T_0)}{\sigma_{m0}} - \frac{1}{C_p}\left(\varepsilon_v^p - \frac{\rho}{1+e_0}\right) = 0 \qquad (2.2.5)$$

where, ρ is called as the extended void ratio difference that includes the stress-induced void ratio difference ρ^σ and the equivalent stress-induced void ratio difference ρ^T, whose expressions can be referred to the paper by Zhang and Zhang (2009). $\sqrt{J_2}$ is the second invariant of the deviatoric stress tensor.

An associate flow rule is employed in the model, namely:

$$d\varepsilon_{ij}^{p\sigma} = \Lambda\frac{\partial f}{\partial \sigma_{ij}} \qquad (2.2.6)$$

In the constitutive model, the consistency equation must be obeyed:

$$df = 0 \Rightarrow df = \frac{\partial f}{\partial \sigma_{ij}}d\sigma_{ij} + \frac{\partial f}{\partial T}dT - \frac{1}{C_p}\left(d\varepsilon_v^p - \frac{d\rho}{1+e_0}\right) = 0 \qquad (2.2.7)$$
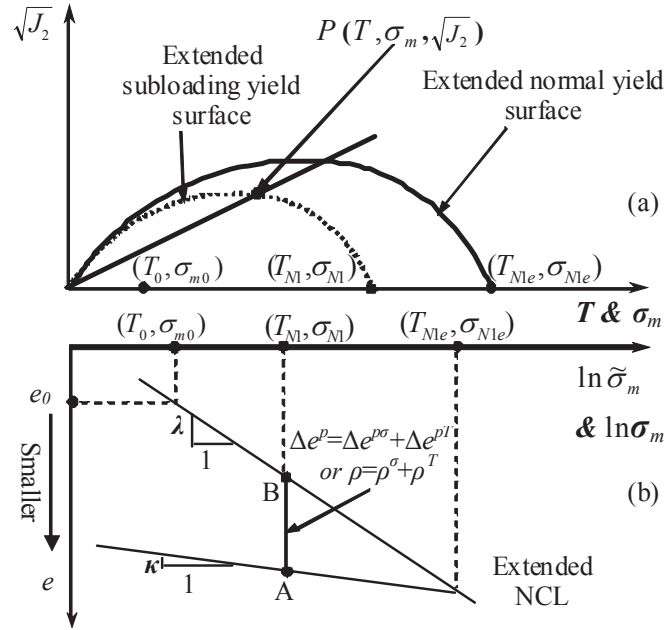
Fig.2.3. Extended normal yield surface and extended subloading yield surface (Zhang and Zhang, 2009)

Similar to the evolution equation proposed by Zhang et al. (2005), the evolution equation for extended void ratio difference is expressed by the sum of actual stress σ_m and equivalent stress increment $(\tilde{\sigma}_m - \sigma_{m0})$ in order to consider both the influence of stress and temperature in the following way:

$$\frac{d\rho}{1+e_0} = -\Lambda \frac{G(\rho,t)}{\sigma_m + (\tilde{\sigma}_m - \sigma_{m0})} + h(t) = -\Lambda \frac{G(\rho,t)}{\sigma_m + 3K^s \alpha_T^s (T - T_0)} + h(t) \qquad (2.2.8)$$

where,

$$\begin{cases} h(t) = \dot{\varepsilon}_v^0 \left[1 + t/t_1 \right]^{-\tilde{\alpha}} \\ G(\rho,t) = a\rho^{1+C_n \ln(1+t/t_1)} = a(\rho^T + \rho^\sigma)^{1+C_n \ln(1+t/t_1)} \end{cases} \qquad (2.2.9)$$

$\dot{\varepsilon}_v^0$ is an initial volumetric strain rate at time $t=0$ which represents the time when shearing begins. t_1 is a unit time and used to standardized the time and always take the value of 1.0. $\tilde{\alpha}$ is a time dependent parameter that controls the gradient of strain rate vs. time in logarithmic axes during a creep test. C_n controls the strain rate dependency of soft rocks. It should be pointed out that the values of the time dependent parameters C_n and $\tilde{\alpha}$ are not objective and are dependent on the unit of time. In its application to

boundary value problem, however, if the unit of time used in numerical analysis is the same as the one used in determining the parameters based on laboratory tests, then there is no problem in using the model.

Substituting Eqs.(2.2.1), (2.2.4), (2.2.6) and (2.2.8) into Eq.(2.2.7), the positive variable Λ can be written as

$$\Lambda = (\dot{f}_\sigma + \frac{h(t)}{C_p}) / \frac{h^p_{sub}}{C_p} \tag{2.2.10}$$

where $\dot{f}_\sigma = \dfrac{\partial f}{\partial \sigma_{ij}} \dot{\sigma}_{ij}, \quad h^p_{sub} = \dfrac{\partial f}{\partial \sigma_{kk}} + \dfrac{G(\rho,t)}{\sigma_m + 3K^s \alpha^s_T (T - T_0)} \tag{2.2.11}$

The stress rate is calculated by Hooke's law as:

$$\dot{\sigma}_{ij} = E_{ijkl} \dot{\varepsilon}^{e\sigma}_{kl} = E_{ijkl} (\dot{\varepsilon}_{kl} - \dot{\varepsilon}^p_{kl} - \dot{\varepsilon}^{eT}_{kl}) \tag{2.2.12}$$

Substituting Eqs.(2.2.1), (2.2.2), (2.2.4), (2.2.6), (2.2.8) and (2.2.12) into Eq.(2.2.7), the positive variable Λ can also be written as

$$\Lambda = \frac{\dfrac{\partial f}{\partial \sigma_{ij}} E_{ijkl} \dot{\varepsilon}_{kl} + \dfrac{h(t)}{C_p}}{\dfrac{\partial f}{\partial \sigma_{ij}} E_{ijkl} \dfrac{\partial f}{\partial \sigma_{kl}} + \dfrac{h^p_{sub}}{C_p}} - \frac{\dfrac{\partial f}{\partial \sigma_{ij}} K^s \delta_{ij} \left(C_p \dfrac{3K^s \alpha^s_T}{\sigma_{m0} + 3K^s \alpha^s_T (T - T_0)} + 3\alpha^s_T \right) \dot{T}}{\dfrac{\partial f}{\partial \sigma_{ij}} E_{ijkl} \dfrac{\partial f}{\partial \sigma_{kl}} + \dfrac{h^p_{sub}}{C_p}} \tag{2.2.13}$$

The loading criteria is given as:

$$\left\| d\varepsilon^{p\sigma}_{ij} \right\| > 0 \text{ if } \Lambda > 0 \text{ and } \begin{cases} \dot{f}_\sigma > 0 & hardening \\ \dot{f}_\sigma < 0 & softening \\ \dot{f}_\sigma = 0 & pure\,creep \end{cases} \tag{2.2.14}$$

$$\left\| d\varepsilon^{p\sigma}_{ij} \right\| = 0 \text{ if } \Lambda \le 0 \text{ elastic}$$

It is known that the only linear thermal expansion coefficient, which has very clear physical meaning and can be easily determined with thermodynamic test, is added into the new model compared with the model proposed by Zhang et al. (2005). Moreover, it had been verified that the first and second thermodynamic theorems are satisfied. The detailed description can be referred to the work by Zhang and Zhang (2009).

2.2.2 Derivation of Modification thermo-elasto-viscoplastic model

Unfortunately, the influence of the intermediate principal stress, which plays an important role in describing the mechanical behavior of geomaterials in a generalized stress state, cannot be described properly in the original model. It is commonly accepted that the shear strength of a soil under the condition of Lode-angle θ not equal zero will be overestimated by a Cam-clay type model whose yielding surface is a circle in the π-plane (Mises type), if the radius of the circle is coincident with the strength of other failure criteria at conventional triaxial compression (Nakai and Mihara, 1984). Fig.2.4 shows the stress-dilatancy relations obtained from the tests on Ohya stone (Ye et al., 2004), a green tuff that distributes wildly in Northeast Japan, in normal stress space and t_{ij} stress space (Nakai and Mihara, 1984) respectively. It can be seen that the stress-dilatancy relations in normal stress space scatters in a wide range while those in the t_{ij} stress space shows a relative clear correlation, which makes it easier to establish a proper plastic potential. In this paper, the t_{ij} concept is introduced into to the original model.

Zhang et al. (2005) proposed an elasto-viscoplastic model for soft sedimentary rock that can take into consideration the influence of intermediate stress on the deformation and strength of geomaterials by adopting the t_{ij} concept and the concept of subloading (Hashiguchi and Ueno, 1977). Meanwhile a reformed subloading concept adopted in the work by Nakai and Hinokio (2004) was also used. Based on the works by Zhang et al. (2005), the original model is modified to describe the influence of the intermediate principal stress. It is assumed that the plastic potential takes the same form as the work by Zhang et al. (2005), and is expressed as (see Fig.2.5),

$$f(t_{ij}, \varepsilon_v^p, T) = f_\sigma(t_{ij}) - \frac{1}{C_p}[\varepsilon_v^p - \frac{\rho}{1+e_0}] = 0 \qquad (2.2.15)$$

where,

$$f_\sigma(t_{ij}) = \ln(t_N / t_{N0}) + \xi(X) \qquad (2.2.16)$$

$$\varsigma(X) = \frac{1}{\beta}(\frac{X}{M^*})^\beta, \quad M^* = \left(X_{CS}^\beta + X_{CS}^{\beta-1} Y_{CS} \right)^{1/\beta} \qquad (2.2.17)$$

$$X_{CS} = \frac{\sqrt{2}}{3}\left(\sqrt{R_{CS}} - \frac{1}{\sqrt{R_{CS}}}\right), \quad Y_{CS} = \frac{1-\sqrt{R_{CS}}}{\sqrt{2}(\sqrt{R_{CS}}+0.5)} \tag{2.2.18}$$

$$\varepsilon_v^p = C_p \ln\frac{t_{N1e}}{t_{N0}}, \quad C_p = \frac{E_p}{1+e_0} = \frac{\lambda-\kappa}{1+e_0} \tag{2.2.19}$$

$$\rho = E_p \cdot \ln\frac{t_{N1e}}{t_{N1}} = (1+e_0)\cdot C_p \cdot \ln OCR \tag{2.2.20}$$

t_N and t_S are the modified mean effective stress and the shear stress in t_{ij} stress space. $X = t_S/t_N$ represents the shear stress ratio. t_{N0} is a reference mean stress and takes the value as 98kPa. M^* is the intercept of stress-dilatancy curve with X axis, as shown in Fig.2.5(b). X_{CS} and Y_{CS} are the stress ratio and the plastic strain increment ratio at the critical state and can be expressed by $R_{CS} = \sigma_1/\sigma_3$, the principal stress ratio at critical state under triaxial loading. t_N is the present stress state and t_{N1} is the cross point of the axis of $t_S = 0$ with the subloading yield surface that passes through the present stress state. t_{N1} and t_{N1e} are the cross points of the subloading and normal yield surfaces with the mean stress axis t_N, as shown in Fig.2.5(a). e_0 is the initial void ratio at $t_N = t_{N0} = 98$kPa under isotropic normal consolidated condition.
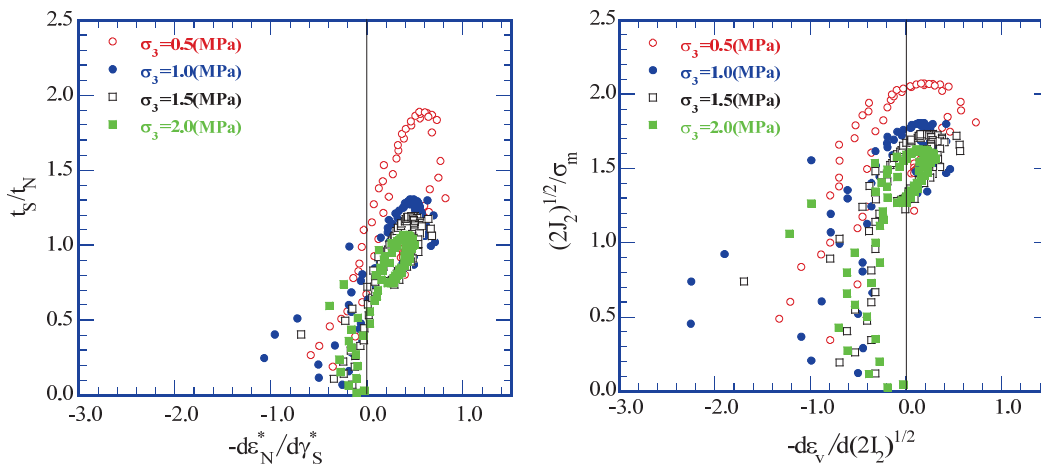
(a) Plane-strain compression
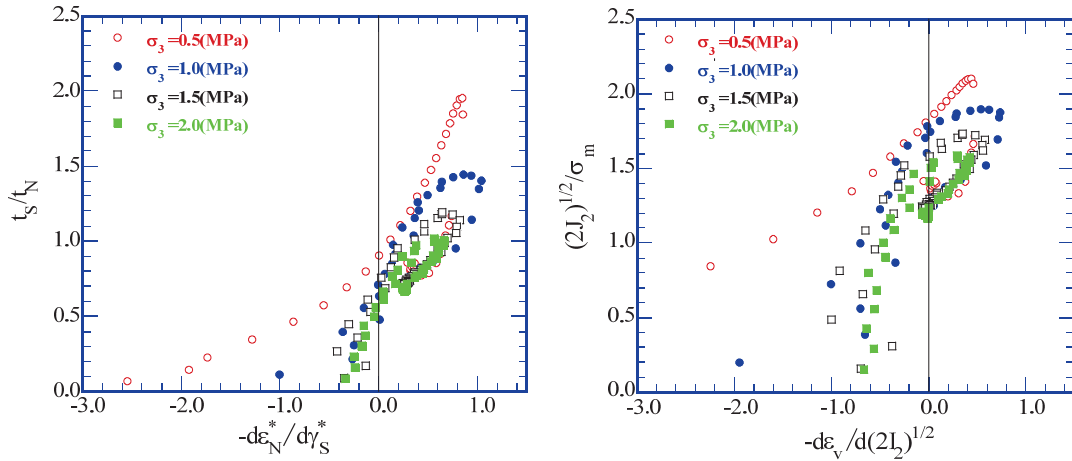
(b) Triaxial compression

Fig.2.4 Stress-dilatancy relations of Ohya stone in different stress space (Ye et al, 2004)

(a) Yield surfaces and definition of ρ (b) Stress-dilatancy relation
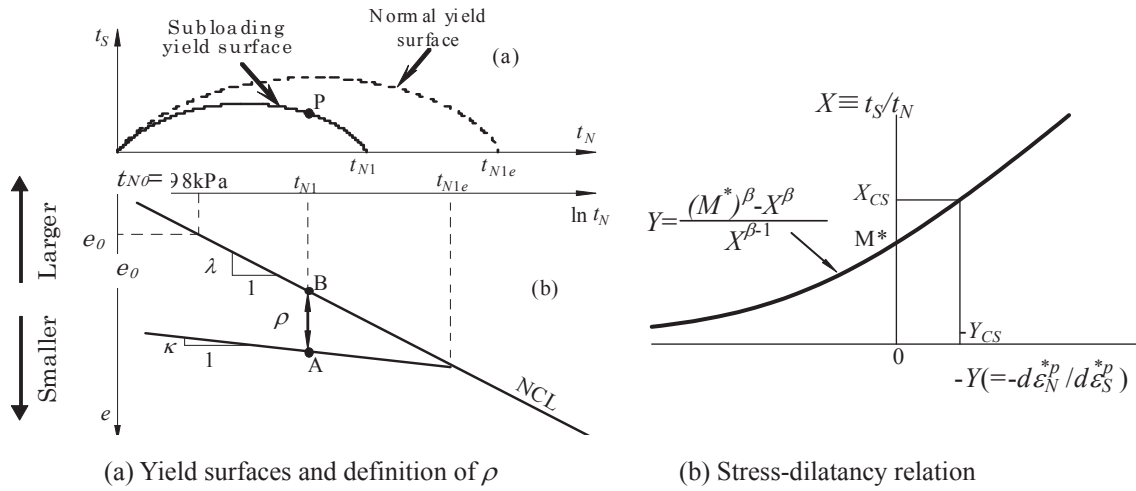
Fig.2.5 Subloading yield surface, normal yield surface, definition of ρ and
stress-dilatancy relation (Nakai and Hinokio, 2004)

Eq.(2.2.15) is differentiated as:

$$\dot{f} = 0 \Rightarrow \frac{\partial f}{\partial \sigma_{ij}} \dot{\sigma}_{ij} - \frac{1}{C_p}[\dot{\varepsilon}_v^p - \frac{\dot{\rho}}{1+e_0}] = 0 \tag{2.2.21}$$

The evolution of the void ratio difference ρ, is given in the same form as the
original model, only by substituting the normal stress with the modified mean stress t_N,
which can both consider the influence of the stress and the temperature and is written as

in the following equation:

$$\dot{\rho}/(1+e_0) = -\Lambda \frac{G(\rho,t)}{t_N + 3K^s \alpha_T^s (T-T_0)} + h(t) \tag{2.2.22}$$

where, $G(\rho,t)$ and $h(t)$ are the same as those expressed in Eq.(2.2.9). Associated flow rule is also adopted in the model:

$$\dot{\varepsilon}_{ij}^p = \Lambda \frac{\partial f}{\partial t_{ij}}, \quad \dot{\varepsilon}_v^p = \Lambda \frac{\partial f}{\partial t_{kk}} \tag{2.2.23}$$

Substituting Eqs.(2.2.22) and (2.2.23) into Eq.(2.2.21), Λ can be obtained:

$$\Lambda = \frac{\dot{f}_\sigma + h(t)/C_p}{h_T^p/C_p} \tag{2.2.24}$$

$$h_T^p = \frac{\partial f}{\partial t_{kk}} + \frac{G(\rho,t)}{t_N + 3K\alpha_T^s(T-T_0)}, \quad \dot{f}_\sigma = \frac{\partial f}{\partial \sigma_{ij}}\dot{\sigma}_{ij} \tag{2.2.25}$$

Under the creep state ($\dot{f} = (\partial f/\partial \sigma_{ij})\dot{\sigma}_{ij} = 0$), the following relation can be obtained:

$$\dot{f}_\sigma = 0 \Rightarrow \Lambda = h(t)/h_T^p \tag{2.2.26}$$

On the other hand, the rate of stress tensor is calculated by corresponding Hooke's theory:

$$\dot{\sigma}_{ij} = E_{ijkl}\dot{\varepsilon}_{kl}^{e\sigma} = E_{ijkl}[\dot{\varepsilon}_{kl} - \dot{\varepsilon}_{kl}^p - \dot{\varepsilon}_v^{eT}\frac{\delta_{kl}}{3}] \tag{2.2.27}$$

Substituting Eqs.(2.2.22), (2.2.23) and (2.2.27) into Eq.(2.2.21), Λ can also be expressed in the following way:

$$\Lambda = (\frac{\partial f}{\partial \sigma_{ij}}E_{ijkl}\dot{\varepsilon}_{kl} + \frac{H(t,T)}{C_p})/D_T \tag{2.2.28}$$

where,

$$H(t,T) = h(t) - C_p\frac{\partial f}{\partial \sigma_{kk}}B_T\dot{T}, \quad D_T = \frac{\partial f}{\partial \sigma_{ij}}E_{ijkl}\frac{\partial f}{\partial t_{kl}} + \frac{h_T^p}{C_p}, \quad B_T = 3\alpha_T^s \tag{2.2.29}$$

The Eq.(2.2.27) can be changed as:

$$\dot{\sigma}_{ij} = (E_{ijkl} - E_{ijkl}^p)\dot{\varepsilon}_{kl} - A_T E_{ijqr}(\partial f/\partial t_{qr}) - K^s B_T \dot{T}\delta_{ij} \tag{2.2.30}$$

where,

$$E_{ijkl}^{p} = E_{ijqr}E_{mnkl} \frac{\partial f}{\partial \sigma_{mn}} \frac{\partial f}{\partial t_{qr}} / D_{T}, \quad A_{T} = \frac{H(t,T)}{D_{T} \cdot C_{p}} \tag{2.2.31}$$

The loading criteria are given in the same way as the model proposed by Zhang et al. (2005):

$$\left\| \dot{\varepsilon}_{ij}^{p} \right\| > 0 \quad \text{if} \ \Lambda > 0 \quad \text{and} \ \begin{cases} \dot{f}_{\sigma} > 0 & \text{hardening} \\ \dot{f}_{\sigma} < 0 & \text{softening} \\ \dot{f}_{\sigma} = 0 & \text{pure creep} \end{cases} \tag{2.2.32}$$

$$\left\| \dot{\varepsilon}_{ij}^{p} \right\| = 0 \quad \text{if} \ \Lambda \le 0 \quad \text{elastic}$$

Nine parameters are involved in the modified model, which is totally the same as the model proposed by Zhang et al. (2005), with the only difference that in order to describe the thermodynamic behavior of geomaterials, the thermal expansion coefficient, a physical property whose value is fixed for a given geomaterial, is added to the model. Parameters, M, e_0, and v are the same as those in Cam-clay model. The other parameters are listed below,

E: Young's modulus

E_p (=$\lambda-\kappa$): Plastic modulus that equals to the difference between compression index $\lambda$and swelling index κ.

a: Controls the losing rate of overconsolidation

$\tilde{\alpha}$: The gradient of strain rate - time relation in logarithmic axes.

β: Controls the shape of the yield function

C_n: Controls the strain rate dependency

α_T^s : Linear coefficient of thermal expansion

These parameters have clear physical meanings and can be determined by triaxial compression tests and creep tests. The detailed description about the calibration method for these nine parameters can be referred to the work (Zhang et al., 2005).

2.2.3 Performance and verification of the modified model

In order to verify the performance of the modified model, some typical mechanical and thermodynamic behaviors of Tage stone in drained triaxial compression and creep tests (Nishimura, 2013) are simulated. Tage stone is a special type of Ohya stone, a volcanic tuff that widely distributes in northeast Japan and usually called as green tuff.

Some basic physical properties of Tage stone and its description can be referred to the work by (Nishimura, 2013).

In the Nishimura's work, thermal triaxial compression tests and creep tests were conducted under 20ºC, 40ºC, 60ºC and 80ºC, respectively. The detailed testing condition of the compression tests are listed in Table 2.1. In the thermal triaxial creep tests, instead of being applied abruptly, the axial loads are applied with a constant axial load rate until the specified creep stresses are reached. The detailed testing conditions of the creep tests are listed in Table 2.2. In addition, back pressures of 0.49MPa are applied in all the tests to increase the saturation of the specimen.

Table 2.1 Testing condition of thermal drained triaxial compression tests on Tage stone (Nishimura, 2013)

Temperature [ºC]	20, 40, 60, 80
Confining stress [MPa]	0.49, 0.98
Axial strain rate [%/min.]	0.002

Table 2.2 Testing condition of thermal drained triaxial creep tests on Tage stone (Nishimura, 2013)

Temperature [ºC]	20, 40, 60, 80	
Creep stress [MPa]	7.4 (σ_3=0.49 MPa)	9.1 (σ_3=0.98 MPa)
Confining stress [MPa]	0.49, 0.98	
Axial loading rate [kN/min.]	0.05	

Table 2.3 Physical properties and material parameters of Tage stone

E (MPa)	E_p	a	$\tilde{\alpha}$	β	C_n	v	R_{CS}		e_0
1000.	0.04	3000.	0.50	1.1	0.025	0.12	6.9 (σ_3=0.49 MPa)	6.0 (σ_3=0.98 MPa)	0.50

Specific gravity G_s=2.54; σ_c =19.6 MPa; α_T^s =2.5×10⁻⁵

(a) Constant comfining stress σ_3=0.49MPa

(b) Constant comfining stress σ_3=0.98MPa

Fig.2.6 Theoretical and test results of drained triaxial compression tests for Tage stone under different constant temperatures

The physical properties and the material parameters of Tage stone are listed in Table 2.3. It should be emphasized that all the parameters used in the model are taken the same for a given geomaterials under different confining pressures, with the only exception, that is, the value of the stress ratio at critical state R_{CS}. The reason why using this parameter calibration can be referred to the works by Adachi and Ogawa (1980) and Adachi and Takase (1981).

Fig.2.6 show the comparison between the theoretical and test results of Tage stone in drained thermal triaxial compression tests under different constant temperature during shearing process. Fig.2.7 shows the comparison between the theoretical and the test results of the strain rate of Tage stone in drained thermal triaxial creep tests under different constant temperature during shearing and creep process. It is known from these comparisons that the theoretical stress-strain-dilatancy relation considering the thermodynamic effect under the conventional triaxial compression tests are basically coincident with those obtained from the element tests. There is, however, a big difference between the theoretical simulation and experiment of triaxial creep tests, especially under high confining pressure, in which the theoretical creep failure times are about one-order longer than the test results. It should be stated clearly that the creep stress was not loaded abruptly on the sample. The sample was firstly loaded to the prescribed creep stress in a constant loading rate that is the same as those of the conventional triaxial compression test. Therefore, the time axis in Fig.4 is started at the beginning of the compression process and only the creep process is depicted in the figure. The parameters used in the simulation of the creep tests are the same as those in the compression tests.
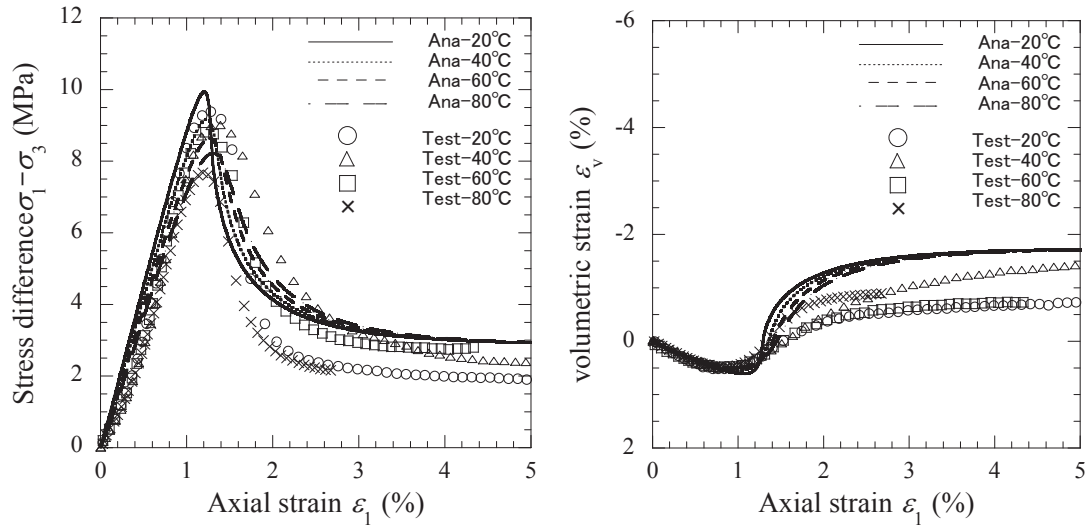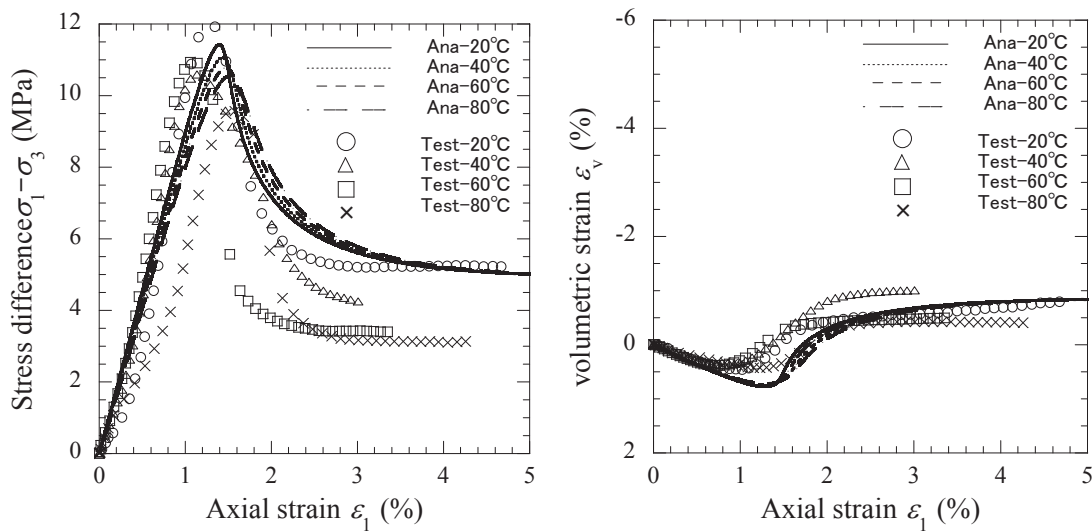

(a) Constant comfining stress σ_3=0.49MPa (b) Constant comfining stress σ_3=0.98MPa
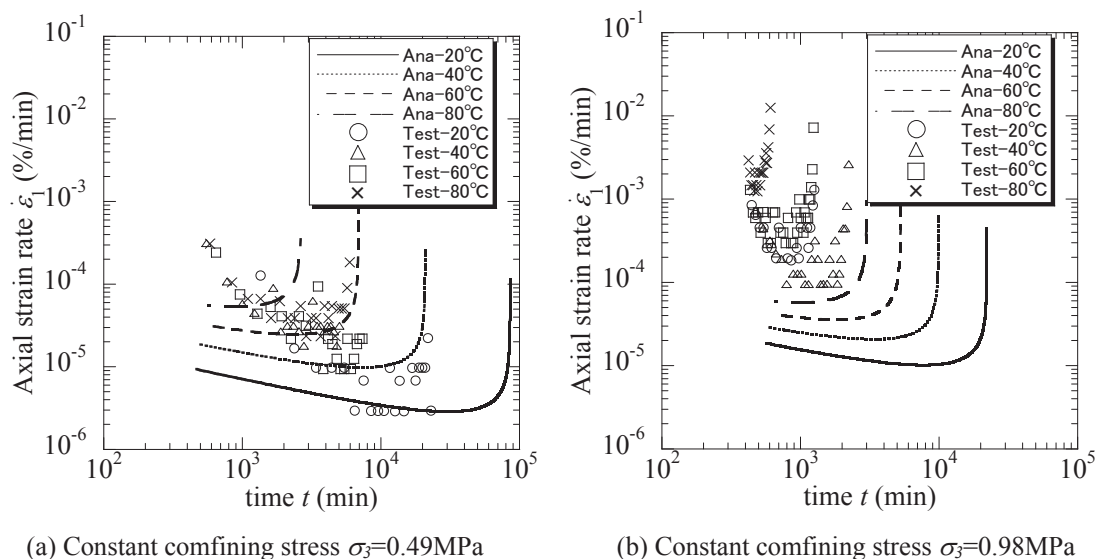
Fig.2.7 Theoretical and test results of drained triaxial creep tests for Tage stone under different constant temperatures

The validity of the modification of the model was also checked by conventional

triaxial compression and creep tests at room temperature (Sekine et al., 2009) on a manmade soft rock under drained condition. The manmade soft rock is made from gypsum and diatom and its composition and material properties are listed in Tables 2.4 and 2.5. Conventional triaxial compression tests were conducted under different confining stresses and shear strain rates with constant strain rate loading condition. The confining stresses used in the tests are $\sigma_3 = 0.1$, 0.3 and 1.0MPa and the loading rate are 1.0, .1 and 0.01%/min respectively. The creep stresses used in the creep tests are 80% of the peak stresses of the specimen at the same confining stress in triaxial compression test. It is confirmed that the strength and dilatancy behavior of the specimens under drained and undrained condition are almost the same and that there is no water observed along the shear band after the loading reached residual state, which means pore water has little influence on the mechanical behavior of the manmade soft rock. The physical properties and material parameters of the manmade soft rock are listed in Table 2.6. The calibration method for the determionation of these parameters are the same as that in the work by Zhang et al. (2005). Figs.2.8, 2.9 and 2.10 show the comparison between the theoretical and the test results, which indicate that the theoretical prediction of the modified model can not only decribe the triaxial compression tests but also the triaxial creep tests in their overall behavior with a set of unified parameters.

Fig.2.8 Theoretical and test results of drained triaxial compression tests for manmade soft rock under different loading rate (Room temperature)

Table 2.4   Material weight ratio of manmade soft rock

Gypsum	Diatom	Water	Retardation
1.0	0.3	1.0	0.4 %

Table 2.5   Physical properties of manmade soft rock

Wet unit weight (g/cm^3)	Water content (%)	Uniaxial strength (MPa)
1.45～1.51	67.9～73.5	1.68～1.83

Fig.2.9 Theoretical and test results of drained triaxial compression tests for manmade rock under different confining stresses (Room temperature)

As to the validation of the transformed stress t_{ij} to consider the influence of intermediate principal stress, many researches have been reported in literature, e.g., the work by Zhang et al., (2003), Nakai and Hinokio (2004). In order to check the influence of intermediate principal stress, the test results of artificial soft rock under the plane-strain condition at room temperature (Nishigami and Horii, 1993) are used to verify the validity of the modified model. The plane-strain condition of the samples was realized by clasping the sample with two vertical steel plates that were very stiff and supported by several fixed rollers in the test. The detailed information about the test and sample can be referred to the work by Nishigami and Horii, (1993).
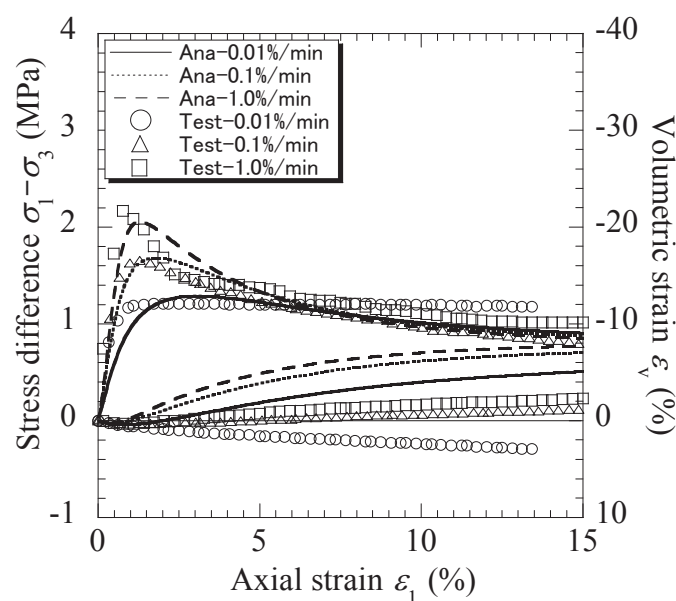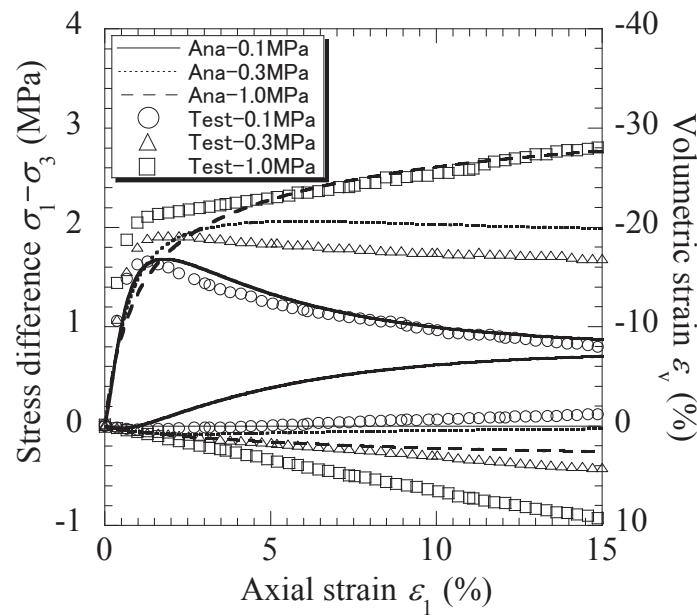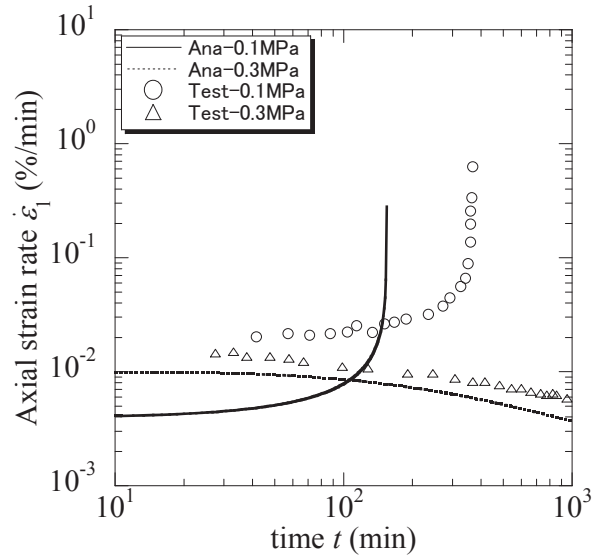
Fig.2.10 Theoretical and test results of drained triaxial creep tests for manmade rock under different confining stress (Room temperature)

Table 2.6 Physical properties and material parameters of manmade soft rock

E (MPa)	E_p	a	$\tilde{\alpha}$	β	C_n	v	R_{CS}			e_0
900.	0.14	300.	0.65	1.1	0.27	0.15	9.0 (σ_3=0.1MPa)	7.5 (σ_3=0.3MPa)	4.0 (σ_3=1.0MPa)	1.05

σ_c =5.0 MPa; α_T^s =8.0×10⁻⁶

σ_c =5.0 MPa; $\alpha_T^s =8.0\times10^{-6}$

Three test results are employed in the comparison between the theoretical simulation and the experiment. The confining pressures (σ_3) of the samples were 0.196MPa, 0.294MPa and 0.392MPa, respectively. It should be pointed out that the material parameters used in the modified model are the same as that used in the original model, except for the parameter, β, which controls the shape of the yield function. Table 2.7 lists the material parameters of the artificial soft rock.

Fig.2.11 shows the comparison of stress-strain-dilatancy relation of artificial soft rock under plane-strain condition by original model and modified model. It is known from the figures that the theoretical simulations with modified model describe the experimental results much better than those with original model, and that the influence of intermediate principal stress (σ_2) can be described properly with a set of unified material parameters. The reason is quite clear because the extended Von-Mises failure criteria used in Cam-Clay model overestimates the shear strength of geomaterials.
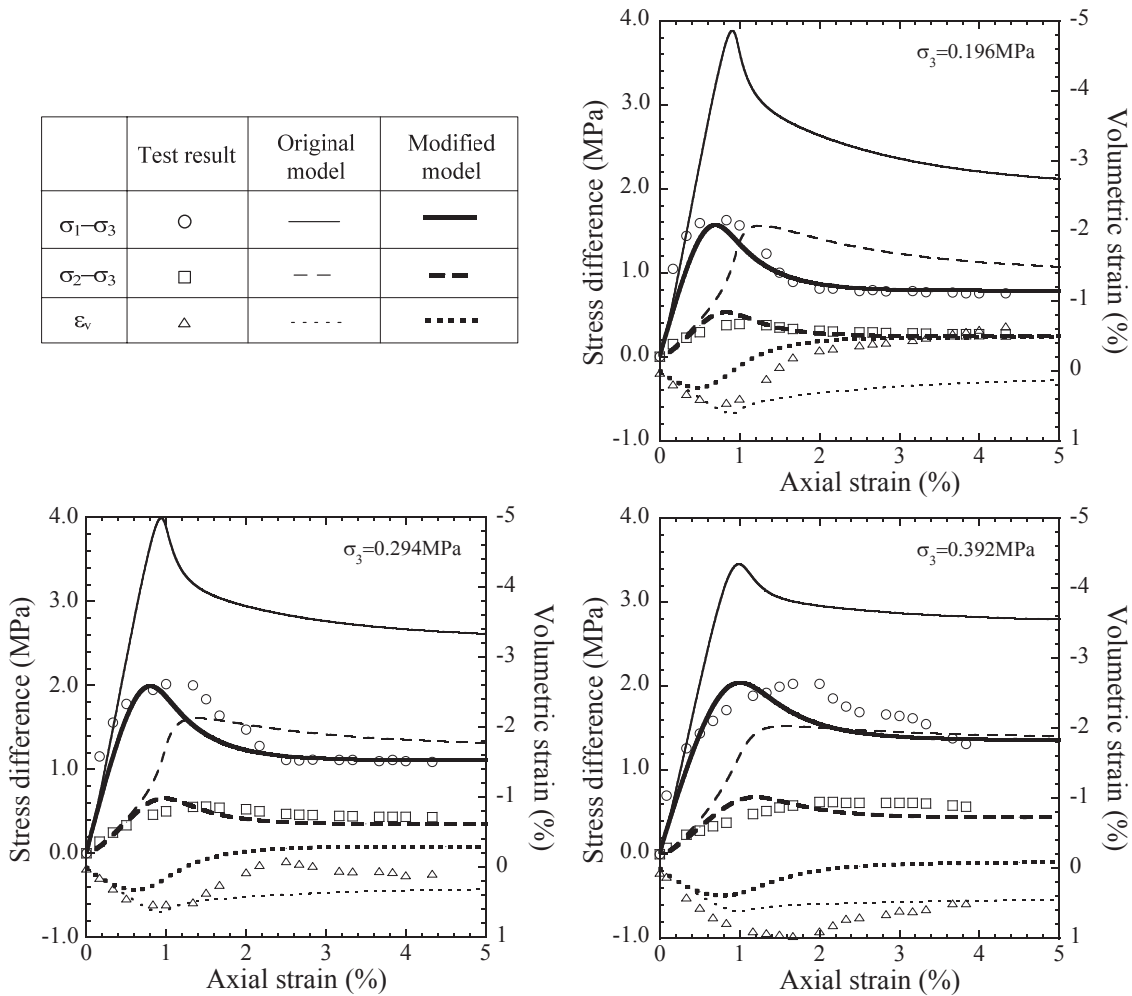
Fig.2.11 Comparison of stress-strain-dilatancy relation of artificial soft rock under plane-strain condition by original model and modified model

Table 2.7 Physical properties and material parameters of artificial soft rock (Nishigami and Horii, 1993)

The same parameters in the modified model and the original model (Zhang and Zhang, 2009)										Parameter only for the modified model
E (MPa)	E_p	a	$\tilde{\alpha}$	e_0	C_n	v	R_{CS}			β
600.	0.005	500.	0.85	0.70	0.0	0.08	3.8 (σ_3=0.196MPa)	3.65 (σ_3=0.294MPa)	3.45 (σ_3=0.392MPa)	1.5

σ_c =10.0 MPa; α_T^s =8.0×10^{-6}

From above verification with element tests, it is reasonable to conclude that the

modified model can properly describe the thermodynamic behavior of soft rock under the thermal triaxial compression and the creep tests, along with the other basic characteristics of the soft sedimentary rock, such as the strain rate dependency, influence of intermediate principal stress.

2.3 Conclusions

In this chapter, a thermo-elasto-viscoplastic model in normal stress space (Zhang and Zhang, 2009) is modified using the t_{ij} concept, which can not only describe the influence of temperature on the deformation and the strength of geomaterials but also can take into account the influence of intermediate principal stress. It needs to be emphasized here that compared with the model proposed by Zhang et al. (2005), only one physical property, the thermal expansion coefficient, is added to the modified model in the framework of the critical state soil mechanics. Then the performance of the modified model is confirmed with the drained triaxial compression tests and the creep tests under different temperatures.

References

1) Adachi, T. and Oka, F., 1995. An elasto-plastic constitutive model for soft rock with strain softening, Int. Jour. for Numerical and analytical Method in Geomechanics, Vol. 19, 233-247.

2) Adachi, T., Oka, F., and Poorooshasb, H. B., 1990. A Constitutive Model for Frozen Sand, Trans. of ASME, Vol. 112, pp. 208-212.

3) Hashiguchi, K., Ueno, M., 1977. Elastoplastic constitutive laws of granular materials. In: Constitutive Equations of Soils (Proc. 9th ICFSME, Spec. Session 9), Tokyo, JSSMFE, Tokyo, 73–82.

4) Kitagawa, H. 1972. Thermodynamic constitutive theories of elastic-plastic material. *Journal of the Society of Materials Science* 21(230): 969-977 (in Japanese).

5) Lebon, G., Jou, D. and Casas-Vázquez, J. 2008. Understanding Non-equilibrium Thermodynamics, *Springer*.

6) Nakai, T. & Hinoko, M. 2004. A simple elastoplastic model for normally and overconsolidated soils with unified materials parameters. *Soils and Foundations* 44(2): 53-70.

7) Nishimura T. (2013): Experimental research and modeling of thermo-creep behavior of sedimentary soft rock and its application to BVP, Master thesis of Nagoya Institute of Technology.

8) Nishikami, H. and Horii, H. (1993): Plane strain compression test of cemented sand and measurement of strain localization, *Pro. 28th Annual Conf. of Japan Geotech. Soc.*, 548-548(in Japanese).

9) Oka, F. and Adachi, T., 1985. A constitutive equation of geologic materials with memory, Proc. of 5th Int. Conf. on Numerical Method in Geomechanics, No.1, 293-300.

10) Rojas, E. & Garnica, P. 2000. Thermomechanical anisotropic model for soils. *Soils and Foundations* 40(2): 61-75.

11) Sekine Y., Zhang F., Tasaka Y., Kurose H. and Ohmori T. (2009): Model tests and numerical analysis on the evaluation of long-term stability of existing tunnel, *Proc. 17th ICSMGE*, Vol.2, 1848-1854.

12) Zhang F., Yashima A., Nakai T., Ye G. L. and Aung H. (2005): An elasto-viscoplastic model for soft sedimentary rock based on tij concept and subloading yield surface, *Soils and Foundations*, Vol. 45, No. 1, 65-73.

13) Zhang S. and Zhang F. (2009): A thermo-elasto-viscoplastic model for soft sedimentary rock, *Soils and Foundations*, Vol. 49, No. 4, 583-595.

CHAPTER 3 THERMO-ELASTOPLASTIC CONSTITUTIVE MODEL FOR SATURATED/UNSATURATETD SOIL

3.1 General

As is well known, a soil is consisted of three phases: solid phase, water phase and air phase. Once the voids among the soil are occupied with both water and air, this soil can be regarded as unsaturated soil. As pointed out by Sheng (2011), an unsaturated soil is not a special type of soil, rather a state of the soil. All unsaturated soils can be fully saturated under appropriate hydraulic or stress paths. Therefore, a proper constitutive model for unsaturated soil should be able to describe the transition from unsaturated state to saturated state automatically.

Since the pioneering work by Alonso et al. (1990), in which Barcelona Basic Model (BBM) was proposed using the concept of loading-collapse (LC) yield surface and suction increase (SI) yield surface and regarded as one of the fundamental models for unsaturated soil, a number of elasto-plastic constitutive models have been developed for modeling the behavior of unsaturated soil. Some of these models are proposed in the space of net stress and suction such as Cui and Delage (1996), Chiu and Ng. (2003) and Sheng et al. (2008), whereas others are in the space of Bishop's effective stress and suction such as Kohgo et al.(1993), Loret and Khalili, (2002) and Sun et al. (2007a). More recently, some constitutive models used the effective stress and degree of saturation as independent state variables have been also established such as Ohno et al. (2007), Zhang and Ikariya (2011) and Zhou et al.(2012a, 2012b). As pointed out by Zhang and Ikariya (2011), using effective stress and degree of saturation in modelling unsaturated soil is much easier and smoother to describe the behavior of soil from unsaturated state to saturated state than using net stress or effective stress and suction as independent state variables.

The moisture characteristic curve (MCC), which is defined as the relationship between the degree of saturation, S_r and the matric suction, s, plays a very important role on the mechanical and hydraulic behaviors of an unsaturated soil. Such a curve is

obtained under constant stress. Extensive experimental research had been done and demonstrated that there is an explicit hysteretic behavior during drying-wetting cycle as shown in Fig.3.1. In other words, the change of degree of saturation is strongly dependent on the suction history. Indeed, the MCC is also influenced by the mechanical factor such as deformation or stress level, e.g., Sharma (1998). Honda (2000) demonstrated that the degree of saturation will change largely even if the suction is kept constant as shown in Fig.3.2. Fig.3.3 indicated from the work of Kawai et al. (2007) that the air entry value (AEV) and water entry value (WEV) increases when the initial void ratio decreases. Therefore, a coupled hydraulic-mechanical constitutive model for unsaturated soil should be conducted considering the influence of deformation on MCC. The issue of interaction between the mechanical and hydraulic behaviour was perhaps firstly raised by Wheeler (1996), and then by Dangla et al. (1997). The first complete model that deals with the coupled hydraulic-mechanical behavior of unsaturated soil was perhaps proposed by Vaunat et al. (2000). And then many other models followed, e.g., Gallipoli et al. (2003a, b), Wheeler et al. (2003), Sun et al. (2007a, 2007b), Sheng et al. (2008), Sheng and Zhou (2011).
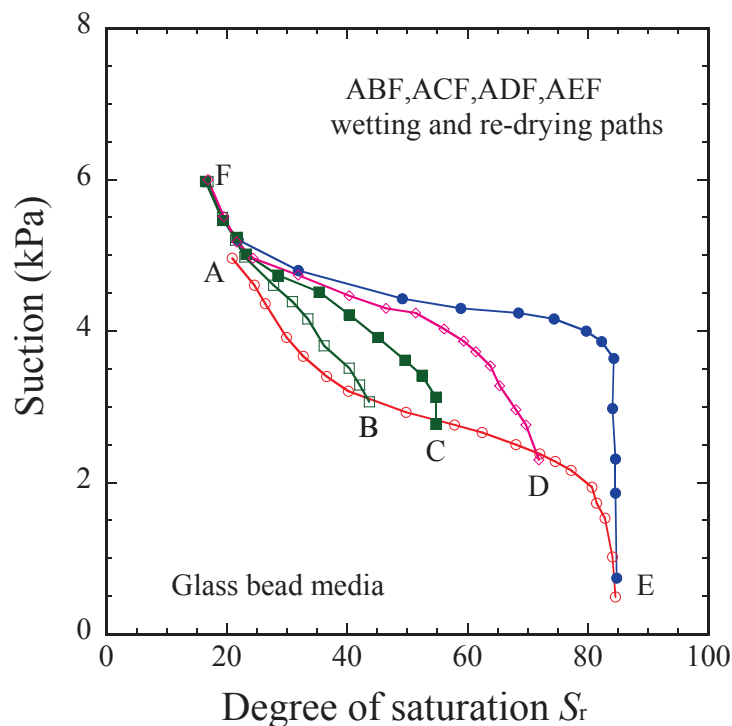

Fig.3.1 The hysteretic MCC (data from Topp and Miller, 1966)
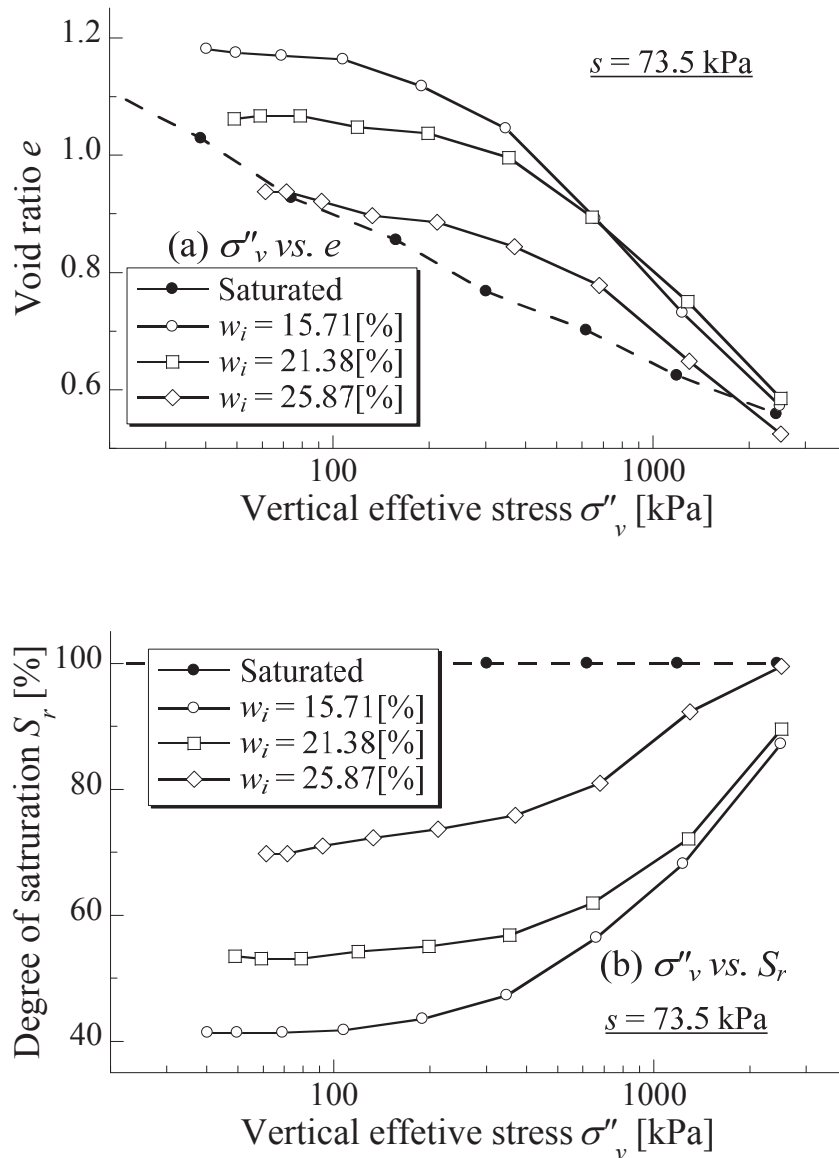
Fig.3.2 Behavior of unsaturated clay during isotropic loading at constant suction (data from Honda, 2000): (a) void ratio versus vertical effective stress (b) degree of saturation versus vertical effective stress
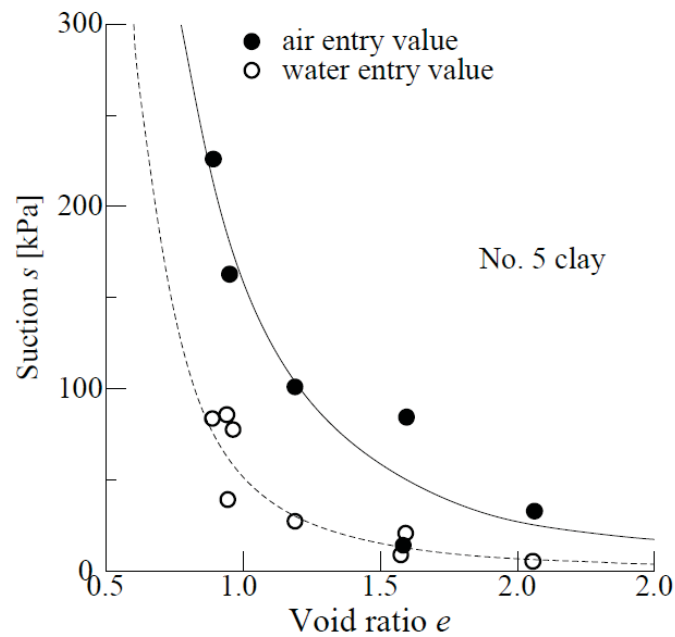
Fig.3.3 Influence of initial void ratio on air entry value and water entry value (data from Kawai et al. 2000)

On the other hand, research interest in the thermal effect on rock and soil has been growing as a result of the demand for performance assessment of geological nuclear waste repositories. Until now, a number of experimental studies have been done to investigate the thermal effect on mechanical behaviour of the saturated rock or soil. e.g., Campanella and Mitchell (1968), Baldi et al. (1988), Cekerevac and Laloui (2004), Okada (2005). At the same time, many theoretical constitutive models for saturated soil or rock considering the temperature influence have been also proposed, e.g., Cui et al. (2000), Laloui (2001), Zhang and Zhang (2009), Zhang et al. (2012). In comparison with saturated soil, research on thermal effects in unsaturated soils has been less studied because of the difficulty for independent measurement and control of pore air pressure, pore water pressure, mechanical loading and temperature at the same time. Uchaipichat and Khalili (2009) conducted a comprehensive program of non-isothermal testing on a compacted sample of silt in a triaxial cell. The influence of temperature on the mechanical behaviour of unsaturated soil can be summarized as follows:

(1) As shown in Fig.3.4, the slope of isotropic normal compression lines,λ, and the slope of unloading-reloading lines,κ, are independent on temperature in *e*-log

p', which is in accordance with the experimental results conducted by Tang et al. (2007).
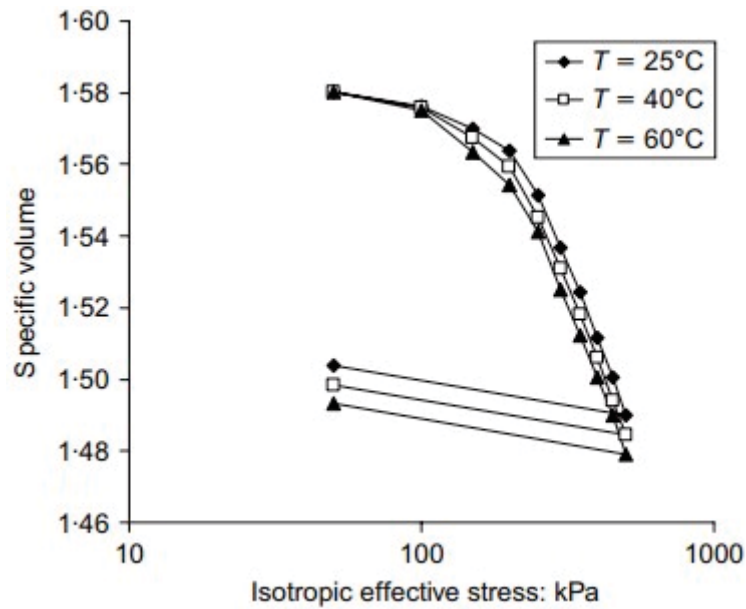
(a) *s*=0 kPa
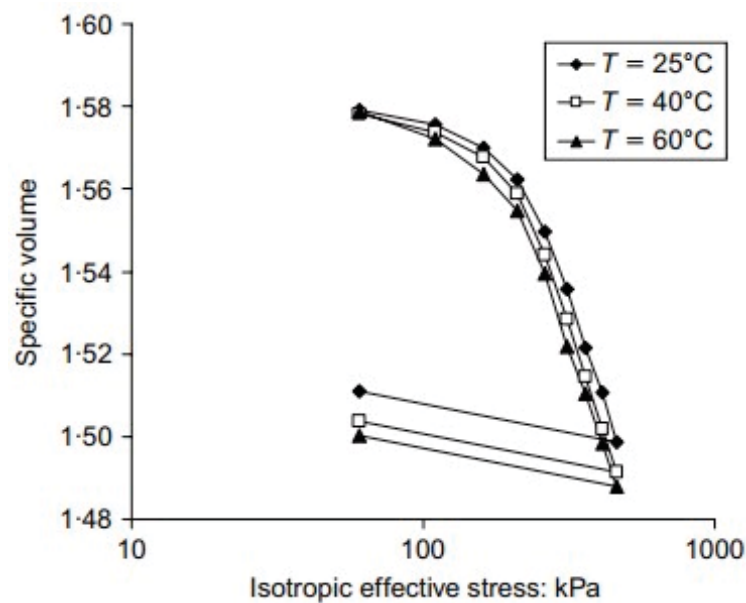
(b) *s*=10 kPa

Fig.3.4 Constant temperature isotropic loading tests at different suctions: (a) suction *s*=0 kPa; (b) suction *s*=10 kPa (data from Uchaipichat and Khalili, 2009)

(2) The effective pre-consolidation pressure shows a decrease with the increase of temperature as shown Fig 3.5, which is also confirmed in the work of Tang et al. (2007).
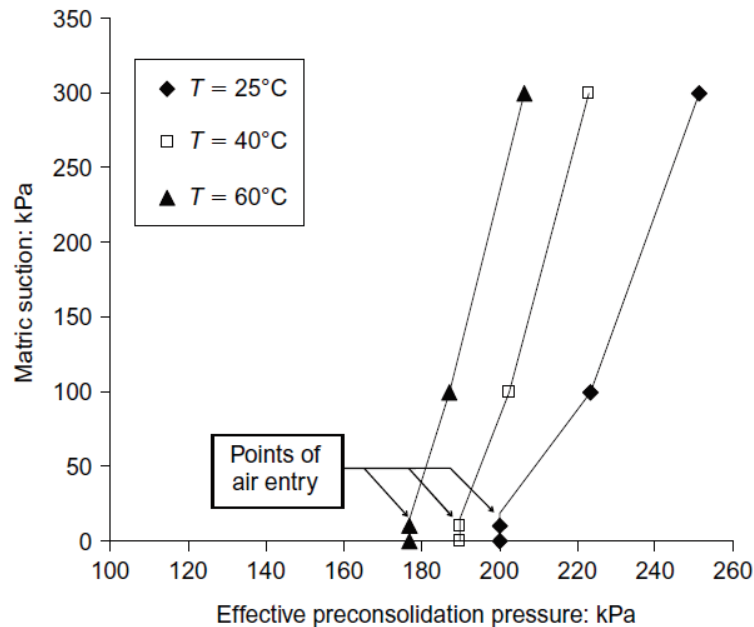
Fig.3.5 Loading collapse curve at different temperature (data from Uchaipichat and Khalili, 2009)

(3) With the increase of temperature, the peak stress reduces and occurs at a larger shear strain as shown in Fig.3.6.

(4) The stress-strain curves converge towards a single line with increasing strain at different temperature, in other word, the critical state is independent on temperature as shown in Fig.3.6.

(5) The yield surface contracts with the increase of temperature due to the thermal softening as shown in Fig3.7.
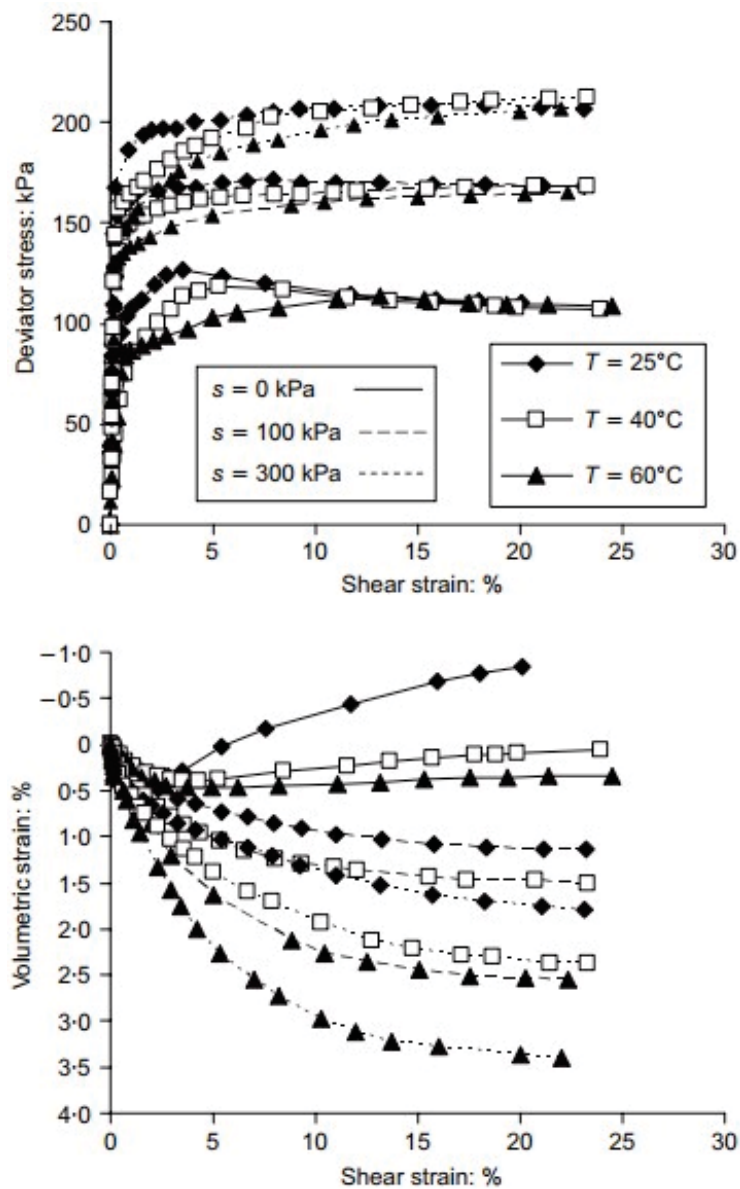
Fig.3.6 Suction and temperature controlled conventional compression shear tests at
initial mean net stress of 50 kPa (data from Uchaipichat and Khalili, 2009)
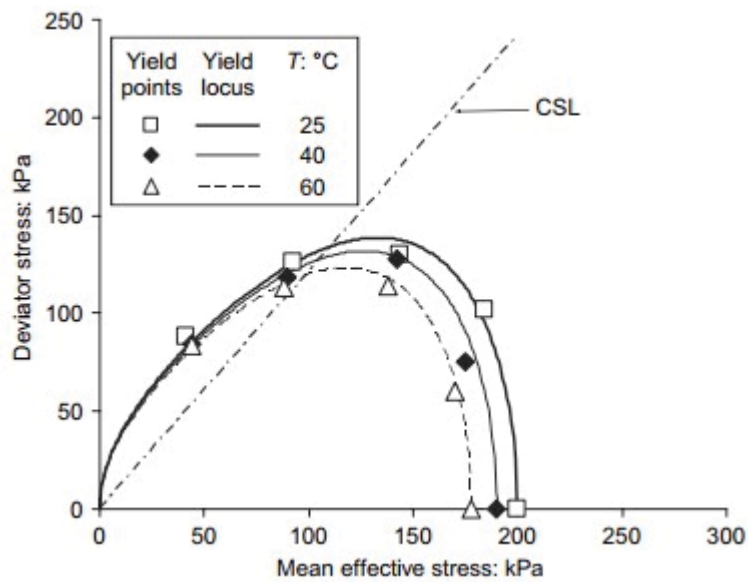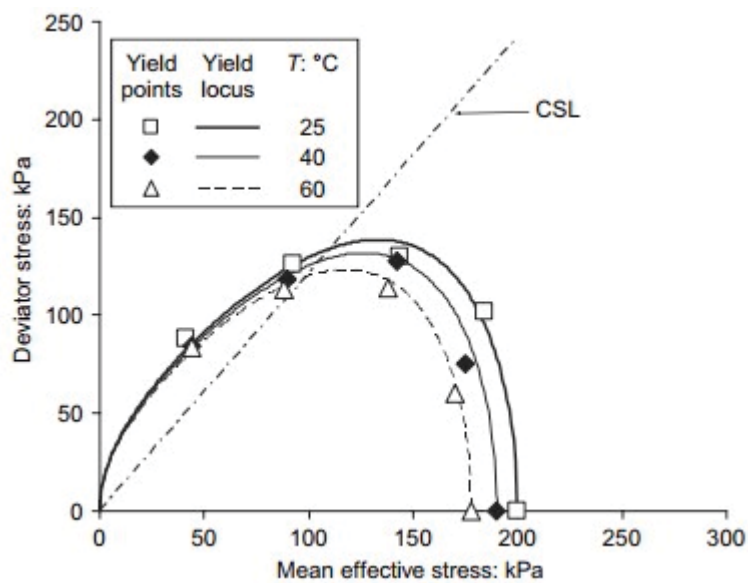
(a) *s=0* kPa

(b) *s=100* kPa

Fig.3.7 Evolution of yield locus with temperature at different suctions: (a) suction *s*=0 kPa; (b) suction *s*=100 kPa (data from Uchaipichat and Khalili, 2009)

The theoretical modelling of unsaturated soil under non-isothermal condition is also proposed last several years at the same time. Francois and Laloui (2008) proposed a unified thermo-mechanical modelling for unsaturated soils, in which the temperature and suction effects are studied within the framework of elasto-plastic theorem. Its

validation is confirmed by experimental results. Dumont et al. (2011) also conducted a thermo-hydro-mechanical model for unsaturated soils based on the extension of effective stress concept to unsaturated soils using a capillary stress. The capillary stress is based on a microstructural model and calculated from attraction forces due to water menisci.

As establishing a constitutive model for soils, it is necessary to use clear physical meaning parameters and easy to determine these parameters as much as possible. There are at least two parameters added in the two above constitutive models for unsaturated soil under non-isothermal condition in order to describe the behaviour of soils suffered from temperature change.

There is still a very important issue for constitutive model that whether it satisfies the thermodynamic theories or not. The work of Collins and Hilder (2002) outlines the structure of a general thermo-mechanical procedure for constructing elasto-plastic models for cohesionless materials relevant to triaxial tests and points out that not all the plastic work imposed during a deformation is dissipated, a fraction of his work is being stored. Sheng et al. (2004) conducted a constitutive model for unsaturated soils based on BBM, in which hydraulic hysteresis and the irreversible deformation during cyclic drying and wetting has been considered. The constitutive model is then cast into the thermodynamic theories and verified using the thermo-mechanical principles. It is shown that hydraulic hysteresis does not contribute to the plastic dissipation, though it contributes to the plastic work. All the plastic work associated with a plastic increment of the degree of saturation is stored and can be recovered in a reversed plastic increment of saturation.

Zhang and Ikariya (2011) proposed a simple elastoplastic constitutive model for unsaturated soil using a Bishop-type skeleton stress and the degree of saturation as the state variables. The constitutive model is able to describe not only the behavior of the unsaturated soil but also the saturated soil because the skeleton stress can smoothly shift to effective stress if the saturation changes from an unsaturated state to a saturated state. In the model, a simple MCC model considering wetting-drying moisture hysteresis of an unsaturated soil is also proposed. Meanwhile the overconsolidation of soil is also properly described based on the concept of subloading (Hashiguchi and Ueno, 1977). The main feature of the model is that the model can describe both the saturated and

unsaturated soils using one set of parameters.

In this chapter, the constitutive model and MCC model (Zhang and Ikariya, 2011) will be modified to deal with the fully coupling thermo-hydraulic-mechanical behaviour for unsaturated soil. The contents of this chapter are organized as follows. Firstly, in order to describe the influence of temperature on the mechanical behaviour of unsaturated soil, the equivalent stress concept proposed by Zhang and Zhang (2009) is incorporated into this constitutive model for unsaturated soil. Secondly, the influence of the deformation on MCC is discussed based on the intrinsic relationship between the void ratio, degree of saturation and gravimetric water content. Finally, the basic performance of the proposed model is illustrated through numerical study and validated against a variety of experimental data.

3.2 Derivation of Thermo-Elastoplastic Constitutive Model for Saturated /Unsaturated Soil

In discussing the mechanical behavior of an unsaturated soil, stress-strain relation is a key factor. The stress, here, might be total stress, net stress or effective stress defined by Bishop, according to the preference of researchers who deal with constitutive model of unsaturated soils. Throughout this paper, however, effective stress is defined by the concept of skeleton stress as shown in following relation,

$$\sigma_{ij}'' = \sigma_{ij}^t - U\delta_{ij} \tag{3.2.1}$$

$$U = S_r u_w + (1 - S_r) u_a \tag{3.2.2}$$

where U is mean pore pressure, σ_{ij}'' is skeleton stress tensor, S_r is degree of saturation, σ_{ij}^t is total stress tensor and u_a is air pressure. Eq.(3.2.1) means that the skeleton stress tensor is the difference of total stress tensor with mean pore pressure. Eq.(3.2.1) can also be rewritten as

$$\sigma_{ij}'' = \sigma_{ij}^t - u_a\delta_{ij} + S_r(u_a - u_w)\delta_{ij} = \sigma_{ij}^n + S_r s\delta_{ij} \tag{3.2.3}$$

where $\sigma_{ij}^n = \sigma_{ij}^t - u_a\delta_{ij}, \quad s = u_a - u_w$ \hfill (3.2.4)

σ_{ij}^n is net stress tensor and s is suction. Eq.(3.2.4) is just the definition of the effective

stress defined by Bishop if taking the value χ in Bishop's definition as S_r. The physical explanation for Eqs.(3.2.1) and (3.2.4), however, is different. For simplicity, throughout the context, the skeleton stress tensor $\sigma_{ij}^{''}$ will be abbreviated as σ_{ij} without specification in the following context.

Based on the experimental results such as Cui and Delage (1996), Honda (2000), a quantitative relation for void ratio-logarithmic mean skeleton stress *e-lnp* relation is established using the degree of saturation as a state variable. Here, it is assumed that normally consolidated line in unsaturated state (*N.C.L.S.*) is parallel to the normally consolidated line in saturated state (*N.C.L.*) but in a higher position than *N.C.L.*, as shown in Fig.3.8, which means that under the same mean skeleton stress, unsaturated soil can keep higher void ratio than those of saturated soil.

The *N.C.L.S.* and *C.S.L.S.* are given in the following relations as,

$$N.C.L.S. : \quad e = N(S_r) - \lambda \ln \frac{p}{p_r} \quad (\eta = \frac{q}{p} = 0) \tag{3.2.5}$$

$$C.S.L.S. : \quad e = \Gamma(S_r) - \lambda \ln \frac{p}{p_r} \quad (\eta = \frac{q}{p} = M) \tag{3.2.6}$$
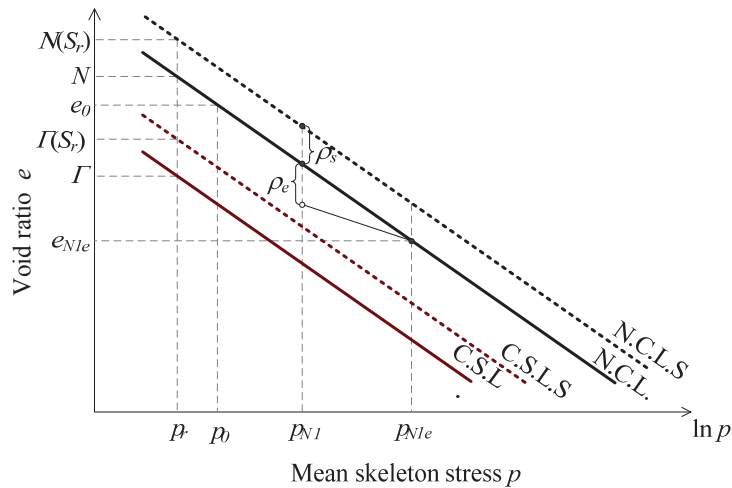
Fig.3.8 Illustration of e-lnp relation considering moving up of *N.C.L.* and *C.S.L.* due to instauration

where, $N(S_r)$ and $\Gamma(S_r)$ are the void ratios at *N.C.L.S.* and *C.S.L.S.* under a

reference mean skeleton stress p_r (Usually p_r =98kPa) and certain degree of saturation. $p = \sigma_{ii}/3$ and $q = \sqrt{3(\sigma_{ij} - p\delta_{ij})(\sigma_{ij} - p\delta_{ij})/2}$ are the mean skeleton stress and the second invariant of deviatory skeleton stress tensor. M is the stress ratio at critical state and has the same value for saturated and unsaturated states. Therefore, similar to the derivation of Cam-clay model for saturated soils, the void ratio e subjected to shearing is assumed to be,

$$e = \chi(\eta, S_r) - \lambda \ln \frac{p}{p_r} \tag{3.2.7}$$

where $\chi(\eta, S_r)$ is a function of shear stress ratio η and the degree of saturation S_r and can be expressed with simple functions as,

(i) For Cam-clay type (Roscoe et al., 1963):

$$e = N(S_r) - \frac{N(S_r) - \Gamma(S_r)}{M} \eta - \lambda \ln \frac{p}{p_r} \tag{3.2.8}$$

(ii) For Modified Cam-clay type (Schofield and Wroth, 1968):

$$e = N(S_r) - \frac{N(S_r) - \Gamma(S_r)}{\ln 2} \ln \frac{M^2 + \eta^2}{M^2} - \lambda \ln \frac{p}{p_r} \tag{3.2.9}$$

Under an saturated isotropic normally consolidated state, that is, s=0, p= p_0, η=0, S_r =1, $N = N(S_r = 1)$, e takes a value of e_0 and can be expressed as,

$$e_0 = N - \lambda \ln \frac{p_0}{p_r} \tag{3.2.10}$$

From Eqs.(3.2.9) and (3.2.10)

$$-\Delta e = e_0 - e = N - N(S_r) + \frac{N(S_r) - \Gamma(S_r)}{\ln 2} \ln \frac{M^2 + \eta^2}{M^2} + \lambda \ln \frac{p}{p_0} \tag{3.2.11}$$

where λ is compression index. Similar to the original Cam-Clay model, elastic change of void ratio of unsaturated soil can be calculated with swelling index κ as

$$-\Delta e^e = \kappa \ln \frac{p}{p_0} \tag{3.2.12}$$

From Eqs.(3.2.11) and (3.2.12), it is clear that unlike most constitutive models for unsaturated soils, both the compression index and swelling index are independet from suction or degree of saturation. Elastic volumetric strain can then be calculated as,

$$\varepsilon^e_v = \frac{-\Delta e^e}{1+e_0} = \frac{\kappa}{1+e_0} \ln \frac{p}{p_0} \tag{3.2.13}$$

By differentiating Equation (3.2.13), the following relation can be derived,

$$d\varepsilon^e_v = \frac{\kappa}{1+e_0} \frac{dp}{p} \tag{3.2.14}$$

Plastic part of the change of void ratio can be given as

$$-\Delta e^p = N - N(S_r) + \frac{N(S_r) - \Gamma(S_r)}{\ln 2} \ln \frac{M^2 + \eta^2}{M^2} + (\lambda - \kappa) \ln \frac{p}{p_0} \tag{3.2.15}$$

Therefore volumetric strain can also be divided into elastic and plastic parts and the plastic part can be expressed as,

$$\varepsilon^p_v = \frac{-\Delta e^p}{1+e_0} = \frac{N - N(S_r)}{1+e_0} + \frac{N(S_r) - \Gamma(S_r)}{(1+e_0)\ln 2} \ln \frac{M^2 + \eta^2}{M^2} + \frac{(\lambda - \kappa)}{1+e_0} \ln \frac{p}{p_0} \tag{3.2.16}$$
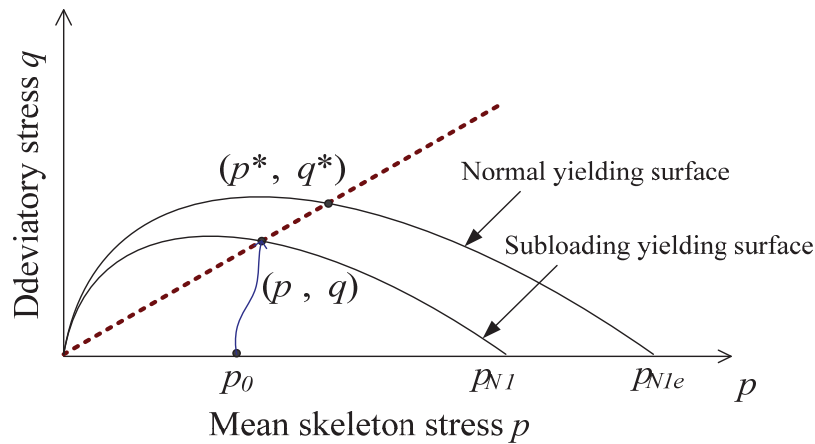
Fig.3.9 Extension of sub loading concept to unsaturated soil in skeleton stress space

Eq.(3.2.16) is only suitable for normally consolidated soil. For over consolidated soil, concept of sub loading surface proposed by Hashiguchi and Ueno (1977) can easily be applied to unsaturated soil as

$$\varepsilon_v^p = \frac{-\Delta e^p}{1+e_0} = \frac{N - N(S_r)}{1+e_0} + \frac{N(S_r) - \Gamma(S_r)}{(1+e_0)\ln 2} \ln \frac{M^2 + \eta^{*2}}{M^2} + \frac{(\lambda - \kappa)}{1+e_0} \ln \frac{p^*}{p_0} \quad (3.2.17)$$

where (p^*, q^*) represents a normally consolidated stress state through which a normal yielding surface passes, as shown in Fig.3.9.

According to the similarity between the normal yielding surface and sub-loading yielding surface, the following relations can easily be obtained.

$$\eta = \eta^* = \frac{q^*}{p^*} = \frac{q}{p}, \quad \frac{p^*}{p} = \frac{p_{N1e}}{p_{N1}} \quad (3.2.18)$$

$$\frac{p^*}{p_0} = \frac{p}{p_0} \frac{p^*}{p} = \frac{p}{p_0} \frac{p_{N1e}}{p_{N1}} \quad (3.2.19)$$

Substituting Eqs.(3.2.18) and (3.2.19) into Eq.(3.2.17), the following relation is obtained,

$$\begin{aligned}
\varepsilon_v^p &= \frac{N - N(S_r)}{1+e_0} + \frac{N(S_r) - \Gamma(S_r)}{(1+e_0)\ln 2} \ln \frac{M^2 + \eta^2}{M^2} + \frac{(\lambda - \kappa)}{1+e_0} \ln \frac{p}{p_0} \frac{p_{N1e}}{p_{N1}} \\
&= \frac{N - N(S_r)}{1+e_0} + \frac{N(S_r) - \Gamma(S_r)}{(1+e_0)\ln 2} \ln \frac{M^2 + \eta^2}{M^2} + C_p \ln \frac{p}{p_0} + \frac{\rho_e}{1+e_0}
\end{aligned} \quad (3.2.20)$$

where,

$$C_p = \frac{\lambda - \kappa}{1+e_0}, \quad \rho_e = (\lambda - \kappa) \ln \frac{p_{N1e}}{p_{N1}} \quad (3.2.21)$$

ρ_e represents a void ratio difference between normally consolidated state and over-consolidated state under the same mean skeleton stress.

As discussed in the previous section, the temperature has great effects on the mechanical behaviors of unsaturated soil. The equivalent stress proposed by Zhang and Zhang (2009) is used in order to consider the influence of temperature and is expressed in the following,

$$\tilde{p}_N = p_N + 3K^s \alpha_T^s (T - T_0) \quad (3.2.22)$$

where, p_N, is present mean stress, K^s is the bulk modulus of solid phase of soil. T is present temperature, T_0, a reference temperature, is an arbitrary value and is taken as the global average temperature, that is, 15°C. α_T^s is the linear thermal expansion coefficient of solid phase of soil whose value should be negative because compression is usually taken as positive in geomechanics.

It is known that the pre-consolidation stress decreases with the increase of the temperature from the experimental results discussed in the previous section, in other words, the OCR decreases with the increase of temperature. Therefore, the new void ratio difference $\tilde{\rho}_e$ considering the influence of temperature is given as,

$$\tilde{\rho}_e = (\lambda - \kappa) \ln[(\tilde{p}_{N1} \times \text{OCR}) / p_{N1}] \tag{3.2.23}$$

where, $\tilde{p}_{N1}$ is initial equivalent mean stress, p_{N1} is initial mean stress.

As shown in Fig.3.8, it is known that *N.C.L.S.* moves upward in parallel from *N.C.L.* when the degree of saturation decreases. Therefore, a new state variable ρ_s which represents a void ratio difference between *N.C.L.* and *N.C.L.S.* under the same mean skeleton stress, is expressed as,

$$\rho_s = N(S_r) - N \tag{3.2.24}$$

Eq.(3.2.20) then can be rewritten as,

$$\varepsilon_v^p = C_p \ln \frac{p}{p_0} + \frac{N(S_r) - \Gamma(S_r)}{(1 + e_0) \ln 2} \ln \frac{M^2 + \eta^2}{M^2} - \frac{\rho_s}{1 + e_0} + \frac{\tilde{\rho}_e}{1 + e_0} \tag{3.2.25}$$

Therefore, yielding function can be written as,

$$f = \ln \frac{p}{p_0} + \frac{N(S_r) - \Gamma(S_r)}{C_p(1 + e_0) \ln 2} \ln \frac{M^2 + \eta^2}{M^2} - \frac{\rho_s}{1 + e_0} \frac{1}{C_p} + \frac{\tilde{\rho}_e}{1 + e_0} \frac{1}{C_p} - \varepsilon_v^p \frac{1}{C_p} = 0 \tag{3.2.26}$$

By the definition of the critical state and some algebraic calculations, it is easy to obtain a useful relation as,

$$d\varepsilon_v^p = \Lambda \frac{\partial f}{\partial p}\bigg|_{\eta = M} = 0 \quad \Rightarrow \quad N(S_r) - \Gamma(S_r) = (\lambda - \kappa) \ln 2 \tag{3.2.27}$$

Substituting Eqs.(3.2.21) and (3.2.27) into Eq.(3.2.26), the following relation is obtained,

$$f = \ln \frac{p}{p_0} + \ln \frac{M^2 + \eta^2}{M^2} - \frac{\rho_s}{1+e_0} \frac{1}{C_p} + \frac{\tilde{\rho}_e}{1+e_0} \frac{1}{C_p} - \varepsilon_v^p \frac{1}{C_p} = 0$$

$$= f_\sigma + \frac{\tilde{\rho}_e - \rho_s}{1+e_0} \frac{1}{C_p} - \varepsilon_v^p \frac{1}{C_p} = 0 \tag{3.2.28}$$

where

$$f_\sigma = \ln \frac{p}{p_0} + \ln \frac{M^2 + \eta^2}{M^2} \tag{3.2.29}$$

From consistency equation *df*=0, it is known that

$$df = \frac{\partial f_\sigma}{\partial \sigma_{ij}} d\sigma_{ij} - d(\frac{\rho_s}{1+e_0}) \frac{1}{C_p} + d(\frac{\tilde{\rho}_e}{1+e_0}) \frac{1}{C_p} - d\varepsilon_v^p \frac{1}{C_p} = 0 \tag{3.2.30}$$

In Eq.(3.2.30), it is necessary to give evolution equations for the development of the state variables $\tilde{\rho}_e$ of overconsolidation and ρ_s of saturation, and the flow rule for plastic strain tensor in the following ways:

(i)   Associate flow rule: $d\varepsilon_{ij}^p = \Lambda \frac{\partial f}{\partial \sigma_{ij}}$ $\qquad\qquad$ (3.2.31)

(ii) $d(\frac{\tilde{\rho}_e}{1+e_0}) = -\Lambda \frac{\rho^\beta}{\tilde{p}}, \quad \rho = a\tilde{\rho}_e + b\rho_s$ $\qquad\qquad$ (3.2.32)

(iii) $\begin{cases} N(S_r) = N + \dfrac{N_r - N}{S_r^s - S_r^r}(S_r^s - S_r); \quad N_r = N(S_r^r) \\[2mm] \rho_s = N(S_r) - N = Q(S_r^s - S_r); \quad Q = \dfrac{N_r - N}{S_r^s - S_r^r} \\[2mm] d\rho_s = -QdS_r \end{cases}$ $\qquad$ (3.2.33)

where, $\tilde{p}$ is the equivalent stress, which is used to consider the influence of both stress and temperature. S_r^r and S_r^s are the degrees of saturation under residual and saturated condition. Eq.(3.2.33) means $N(S_r)$ changes linearly with the degree of saturation.

Parameters *a, b* and β control the development of the state variables $\tilde{\rho}_e$. N_r is the void ratios at *N.C.L.S.* under the reference mean skeleton stress p_r when the degrees of saturation is in residual state, that is, $N_r = N(S_r^r)$.

Volumetric strain increment can be divided into elastic and plastic parts as,

$$d\varepsilon_{ij} = d\varepsilon_{ij}^e + d\varepsilon_{ij}^p \tag{3.2.34}$$

Using Hooke's theory with elastic stiffness tensor E_{ijkl}, incremental stress tensor can be expressed as,

$$d\sigma_{ij} = E_{ijkl}(d\varepsilon_{kl} - d\varepsilon_{kl}^p - d\varepsilon_{kl}^T) = E_{ijkl}d\varepsilon_{kl} - E_{ijkl}\Lambda\frac{\partial f}{\partial\sigma_{kl}} - E_{ijkl}d\varepsilon_{kl}^T \tag{3.2.35}$$

Substituting this equation into Eq.(3.2.30), the following relation can be obtained,

$$\frac{\partial f}{\partial\sigma_{ij}}E_{ijkl}d\varepsilon_{kl} - \frac{\partial f}{\partial\sigma_{ij}}E_{ijkl}\Lambda\frac{\partial f}{\partial\sigma_{kl}} - \frac{\partial f}{\partial\sigma_{ij}}E_{ijkl}d\varepsilon_{kl}^T - \Lambda\frac{\rho^\beta}{\tilde{p}}\frac{1}{C_p} + \frac{Q}{1+e0}dS_r\frac{1}{C_p} - \Lambda\frac{1}{C_p}\frac{\partial f}{\partial\sigma_{mm}} = 0$$

$$\tag{3.2.36}$$

which resulting in,

$$\Lambda = \frac{\dfrac{\partial f}{\partial\sigma_{ij}}E_{ijkl}\,d\varepsilon_{kl} + \dfrac{1}{C_p}\dfrac{Q}{1+e_0}dS_r - \dfrac{\partial f}{\partial\sigma_{ij}}E_{ijkl}d\varepsilon_{kl}^T}{\dfrac{h_p}{C_p} + \dfrac{\partial f}{\partial\sigma_{ij}}E_{ijkl}\dfrac{\partial f}{\partial\sigma_{kl}}} \tag{3.2.37}$$

where, $\quad h_p = \dfrac{\partial f}{\partial\sigma_{mm}} + \dfrac{\rho^\beta}{\tilde{p}}$ $\tag{3.2.38}$

Therefore it is easy to define the loading criteria as,

$$\begin{cases} \Lambda > 0 & loading \\ \Lambda = 0 & neutral \\ \Lambda < 0 & unloading \end{cases} \tag{3.2.39}$$

Substituting Eq.(3.2.37) into Eq.(3.2.31),

$$d\varepsilon_{ij}^{p} = \frac{\dfrac{\partial f}{\partial \sigma_{mn}} E_{mnkl}\, d\varepsilon_{kl} + \dfrac{1}{C_p}\dfrac{Q}{1+e_0} dS_r - \dfrac{\partial f}{\partial \sigma_{mn}} E_{mnkl}\, d\varepsilon_{kl}^{T}}{\dfrac{h_p}{C_p} + \dfrac{\partial f}{\partial \sigma_{mn}} E_{mnkl} \dfrac{\partial f}{\partial \sigma_{kl}}} \frac{\partial f}{\partial \sigma_{ij}} \tag{3.2.40}$$

Meanwhile,

$$d\sigma_{ij} = E_{ijkl}(d\varepsilon_{kl} - d\varepsilon_{kl}^{p} - d\varepsilon_{kl}^{T}) = E_{ijkl} d\varepsilon_{kl} - E_{ijkl}\Lambda \frac{\partial f}{\partial \sigma_{kl}} - E_{ijkl} d\varepsilon_{kl}^{T}$$

$$= E_{ijkl}\, d\varepsilon_{kl} - E_{ijqr} E_{mnkl} \frac{\partial f}{\partial \sigma_{mn}} \frac{\partial f}{\partial \sigma_{qr}} \frac{1}{\tilde{D}} d\varepsilon_{kl} - \frac{1}{C_p}\frac{Q}{1+e_0} dS_r \frac{1}{\tilde{D}} E_{ijqr} \frac{\partial f}{\partial \sigma_{qr}}$$

$$+ \frac{1}{D} \frac{\partial f}{\partial \sigma_{mn}} \frac{\partial f}{\partial \sigma_{qr}} E_{ijqr} E_{mnkl}\, d\varepsilon_{kl}^{T} - E_{ijkl} d\varepsilon_{kl}^{T}$$

$$= (E_{ijkl} - E_{ijkl}^{p}) d\varepsilon_{kl} - E_{ij}^{ERS} dS_r - (E_{ijkl} - E_{ijkl}^{p}) d\varepsilon_{kl}^{T}$$

$$\tag{3.2.41}$$

where, $\quad E_{ij}^{ERS} = \dfrac{1}{C_p}\dfrac{Q}{1+e_0}\dfrac{1}{\tilde{D}} E_{ijkl} \dfrac{\partial f}{\partial \sigma_{kl}}$

$$\tilde{D} = \frac{h_p}{C_p} + \frac{\partial f}{\partial \sigma_{mn}} E_{mnkl} \frac{\partial f}{\partial \sigma_{kl}} \tag{3.2.42}$$

$$E_{ijkl}^{p} = \frac{E_{ijqr} E_{mnkl} \dfrac{\partial f}{\partial \sigma_{mn}} \dfrac{\partial f}{\partial \sigma_{qr}}}{\tilde{D}} \tag{3.2.43}$$

$$E_{ijkl}^{ep} = E_{ijkl} - E_{ijkl}^{p} \tag{3.2.44}$$

3.3 Moisture Characteristic Curve Considering the Hydraulic Hysteresis, the Influence of Void Ratio and Temperature

It is well known that the mechanical behaviors of unsaturated soil are greatly influenced by the hydraulic characteristic, which is expressed with the relationship between the degree of saturation and suction. A proper model of moisture characteristic curve (MCC), therefore, should be proposed in advance to describe the mechanical behavior of unsaturated soil, especially the transition from unsaturated state to saturated state. Until now, a lot of MCC models have been proposed, in which van Genuchten

model (1980) is often used in the unsaturated analysis. However, van Genuchten model cannot consider some features observed in the experiment: (1) the hydraulic hysteresis effect, which means that the MCC of unsaturated soil usually traces a different path during the drying process and wetting process; (2) the influence of void ratio/soil deformation.

Zhang and Ikariya (2011) also proposed a new MCC model in the infinitesimal scheme, which can consider the hydraulic hysteresis properly using the boundary surface concept. The three skeleton curves for the MCC is expressed with tangential and arc-tangential functions as follow:

(i)   Primary drying curve from slurry:

$$S_r = S_r^{s0} - \frac{2}{\pi}(S_r^{s0} - S_r^r)\tan^{-1}((e^{c_1 s} - 1)/e^{c_1 s_d})\tag{3.2.45}$$

or $$s = \frac{1}{c_1}\ln\left[1 + e^{c_1 s_d}\tan(\frac{\pi}{2}\frac{S_r^{s0} - S_r}{S_r^{s0} - S_r^r})\right]\tag{3.2.46}$$

(ii) Secondary drying curve experienced drying-wetting process:

$$S_r = S_r^s - \frac{2}{\pi}(S_r^s - S_r^r)\tan^{-1}((e^{c_1 s} - 1)/e^{c_1 s_d})\tag{3.2.47}$$

or $$s = \frac{1}{c_1}\ln\left[1 + e^{c_1 s_d}\tan(\frac{\pi}{2}\frac{S_r^s - S_r}{S_r^s - S_r^r})\right]\tag{3.2.48}$$

(iii) Wetting curve:

$$S_r = S_r^s - \frac{2}{\pi}(S_r^s - S_r^r)\tan^{-1}((e^{c_2 s} - 1)/e^{c_2 s_w})\tag{3.2.49}$$

or $$s = \frac{1}{c_2}\ln\left[1 + e^{c_2 s_w}\tan(\frac{\pi}{2}\frac{S_r^s - S_r}{S_r^s - S_r^r})\right]\tag{3.2.50}$$

where, S_d is a parameter corresponding to drying AEV and S_w is a parameter corresponding to wetting AEV, as shown in Fig3.10. c_1 and c_2 are scaling factors that controlling the shape of the curves. S_r^{s0} is the degree of saturation of a slurry under fully saturated condition and is equal to 1.0.

As to the scanning curve in the process of drying-wetting process between the skeleton curves, the incremental relation between suction and saturation is expressed as,

$$k_s^{-1} = k_{s0}^{-1} + k_{s1}^{-1}\tag{3.2.51}$$

k_{s0} is the gradient of suction-saturation relation under the condition that inner variable r

equals to 0. k_{s1} is expressed as:

$$k_{s1} = k_{s1}^s (1 + c_3 \frac{1-r}{r}) \tag{3.2.52}$$

where, c_3 is a scaling factor which controlling the curvature of the scanning curve. k_{s1}^s is the gradient of the corresponding skeleton curve on which the moisture state (S_r, s) is locating under the condition that r equals to 1, as shown in Fig.3.10. According the illustration in Fig.3.10, the inner variable r is defined as,

$$r = \begin{cases} \delta_2 / \delta & ds > 0 \\ \delta_1 / \delta & ds \leq 0 \end{cases} \tag{3.2.53}$$
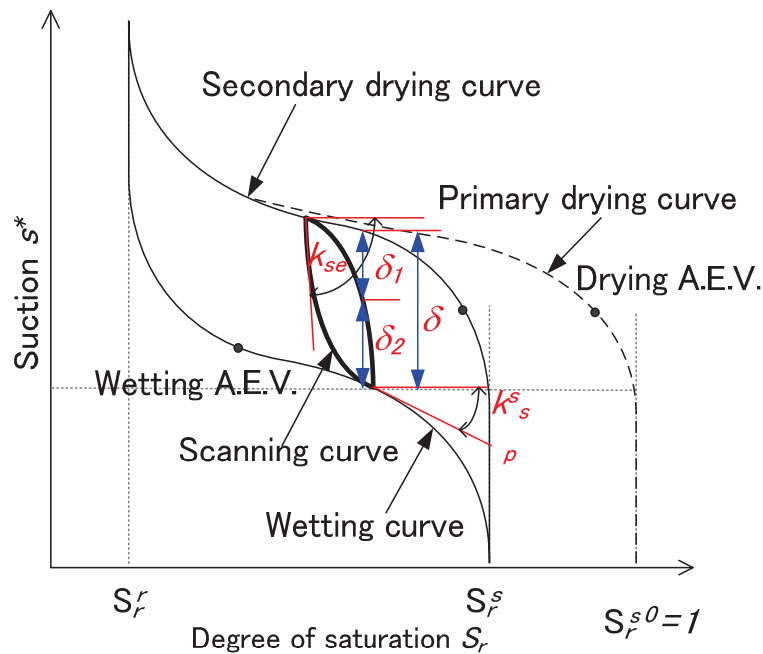
Fig.3.10 Image of moisture characteristic curve of unsaturated soil

Eq.(3.2.51) means that the stiffness of k_s consists of two parts, k_{s0} and k_{s1} in a way that its value looks like the value of a spring consisted from two series springs. It is easily understood from Eqs.(3.2.51) and (3.2.52) that if $r=0$, k_{s1} will be infinite and $k_s=k_{s0}$. While if $r=1$ and $k_{s0}>>k_{s1}^s$, k_s will equal to k_{s1}^s, which coincides with the gradient of the skeleton curve. This explanation can also be easily understood by means of the illustration shown in Fig.3.10.

And the incremental relation between suction and the degree of saturation is given

as

$$dS_r = k_s^{-1} ds \tag{3.2.54}$$

where, k_s is the tangential stiffness of suction-saturation relation.

Eight parameters are involved in the modified moisture characteristics curve, among which three parameters c_1, c_2 and c_3 are determined with curve fitting method while other seven parameters, k_{s0}, S_r^s, S_r^r, S_d, and S_w have definite physical meaning and can be determined by the test of moisture characteristics easily.

On the other hand, many isotropic loading tests (Sharma, 1998; Sun et al., 2007b and 2007c) have been shown that the degree of saturation will still increase even when the suction is kept constant. In other words, MCC is dependent on the deformation of unsaturated soil, which will play a great important role on the behavior of soil when deformation becomes large enough to reach the range of finite deformation.

When dealing with the above problem, there is the basic and intrinsic relationship between the state variables (void ratio e) and the hydraulic state variables (saturation S_r and gravimetric water content w), which must be satisfied,

$$w = \frac{S_r e}{G_s}, \quad G_s dw = e dS_r + S_r de \tag{3.2.55}$$

where G_s is the specific gravity and is usually treated as a constant for a soil. The above equation is always true as long as the solid particles of soil are assumed to be incompressible.

Many researchers regard this problem as the constitutive relation of unsaturated soil and correspondingly propose many new MCC models in order to take into consideration the influence of the deformation, such as Gallipoli et al. (2003a, b), Wheeler et al. (2003), Sun et al. (2007a, 2007b), Sheng et al. (2008), Nuth and Laloui (2008), in which it is assumed that either the air entry value depends on the void ratio or the suction is dependent on the void ratio. Sheng and Zhou (2011) also proposed an alternative method to consider the influence of the deformation based on the intrinsic relationship between the degree of saturation and the volumetric strain under undrained compression condition and its expression is given as

$$dS_r = \frac{\partial S_r}{\partial s} ds - \frac{S_r(1-S_r)^{\xi}}{e} de \qquad (3.2.56)$$

where $\partial S_r / \partial s$ is the relation between the degree of saturation and the suction in MCC model and is equal to k_s^{-1}, ξ is a parameter controlling the influence of void ratio on MCC and its value is between 0.0 and 1.0.

It is worth emphasizing here that the incremental saturation is not only dependent on the state variable e but also the state variable w from the Eq.(3.2.55). And furthermore any proposed constitutive models should be able to describe the mechanical-hydro behavior of unsaturated soil observed in the tests under drained and undrained condition using one set of parameter for the same soil, while the intrinsic relation of Eq.(3.2.55) is also satisfied. It is clearly known that this problem should be handled under drained and undrained condition separately when using the aforementioned models. In other words, two set of parameters should be given when we reproduce the experimental data, which gives rise to the infeasibility in applying to numerical simulation of boundary value problem. As author's viewpoint, the influence of the finite deformation on MCC can be considered automatically using Eq.(3.2.55) in the framework of finite deformation numerical simulation when the state variable w is decided in advance, which is related with the quantity of water flow. This work would be studied in the future.

In the chapter, a simple way to understand and explain the influence of the deformation on MCC will be introduced. From Eq.(3.2.55), the saturation is the function of the gravimetric water content and void ratio. According to the differential theory, the incremental saturation can be divided into:

$$dS_r = \frac{\partial S_r}{\partial w} dw \mid_{de=0} + \frac{\partial S_r}{\partial e} de \mid_{dw=0} \qquad (3.2.57)$$

The right first term of above equation is regarded as the condition that the finite deformation is not considered. While the right second term means that the water content is kept constant in the finite deformation scheme.

And finally the MCC considering the influence of the finite deformation is obtained according to Eq.(3.2.57):

$$dS_r = k_s^{-1} ds - \frac{S_r}{e} de \qquad (3.2.58)$$

It should be emphasized again that the above equation is just used to illustrate the effect of the finite deformation on MCC here, but is not useful in applying to boundary value problem.

3.4 Performance of the MCC Model

Fig.3.11 shows a theoretical prediction of moisture characteristics curve of a fictional unsaturated silt. It is very clear that hydraulic hysteresis of the moisture characteristics curve can be properly described. The values of the parameters are listed in Table 3.1.
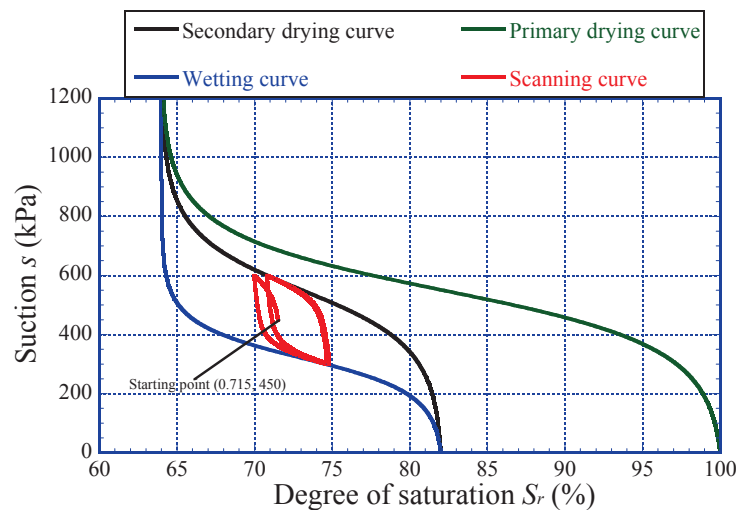
Fig.3.11 Simulated moisture characteristics curve of unsaturated fictional silt

Table 3.1 Parameters of moisture characteristics curve of unsaturated fictional silt

Saturated degrees of saturation S_r^s		0.82
Residual degrees of saturation S_r^r		0.64
Parameter corresponding to drying AEV (kPa)	S_d	550
Parameter corresponding to wetting AEV (kPa)	S_w	320
Initial stiffness of scanning curve (kPa) k_{sp}^e		200000
Parameter of shape function c_1		0.008
Parameter of shape function c_2		0.013
Parameter of shape function c_3		10.0

(a) Drying curve: A-B-C-D-A   (b) Wetting curve: A-B-C-D-A

Fig.3.12 Hysteretic MCC curves of White silica sand (data from Huang, 2005) and corresponding results of calculations

Table 3.2 Parameters of moisture characteristics curve (MCC) of white silica sand

Saturated degrees of saturation S_r^s		1.00
Residual degrees of saturation S_r^r		0.26
Parameter corresponding to drying AEV (kPa)	S_d	11.00
Parameter corresponding to wetting AEV (kPa)	S_w	2.00
Initial stiffness of scanning curve (kPa) k_{sp}^e		90.0
Parameter of shape function c_1		0.35
Parameter of shape function c_2		0.23
Parameter of shape function c_3		3.00

Fig.3.12 shows the comparison between experiment results, which are obtained from water retentive test with cyclic suction loading on white silica sand (Huang, 2005) at room temperature, and corresponding calculated results by proposed model. White silica sand, whose grain size is 0.074 - 0.297 mm, is sample, and the average void ratio of samples is produced by compaction is approximately 0.56. Parameters used in this simulation are summarized in Table 3.2. Diagrams (a) and (b) in Fig.3.12 show results of cyclic path "drying, wetting, drying and wetting" and "wetting, drying, wetting and drying path" respectively, and the main drying and wetting curves are shown in each figures simultaneously. It is indicated from this figure that the proposed model can accurately describe not only the main drying and wetting curve represented by ordinary van Genuchten model, but also hysteretic water retention characteristic under

complicated suction histories.

3.5 Performance of the Constitutive Model
3.5.1 One dimensional behavior of the model

(a) Case1: Drying→isotropic loading to fully saturation→suction reduction

As the first example, a numerical study under a drying-isotropic loading- suction reduction circle is carried out to illustrate the performance of the proposed hydro-mechanical model, in which the span of loading is enough larger. The parameters of MCC model and constitutive model are listed in Table 3.3 and 3.4 respectively.

Table 3.3Parameters of MCC of fictional silt

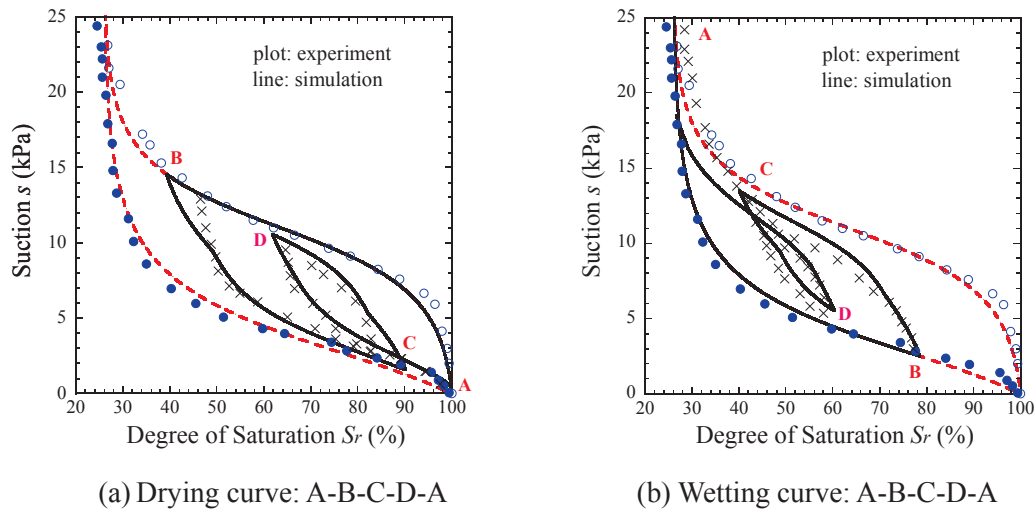|	
Saturated degrees of saturation S_r^s	1.00
Residual degrees of saturation S_r^r	0.35
Parameter corresponding to drying AEV (kPa) S_d	20.0
Parameter corresponding to wetting AEV (kPa) S_w	5.0
Initial stiffness of scanning curve k_{sp}^e	2500
Parameter of shape function c_1	0.009
Parameter of shape function c_2	0.023
Parameter of shape function c_3	30.0

Table 3.4 Material parameters of unsaturated fictional silt

Compression index λ	0.09
Swelling index κ	0.006
Critical state shear ratio **M**	2.15
Void ratio **N** (p'=98 kPa on *N.C.L.*)	0.638
Poisson's ratio **v**	0.30
Initial OCR	1.0
Parameter of overconsolidation **a**	200.0
Parameter of suction **b**	0.00
Parameter of overconsolidation **β**	1.00
Void ratio N_r (p'=98 kPa on *N.C.L.S.*)	0.728
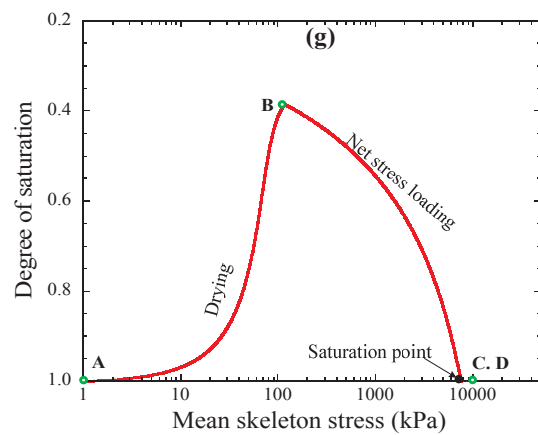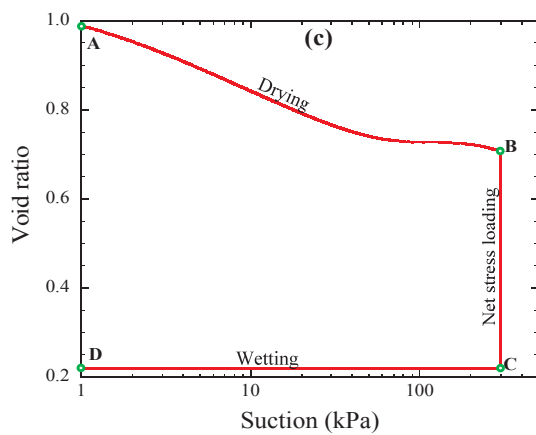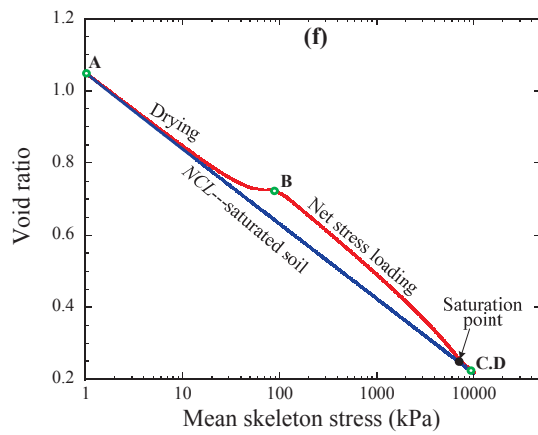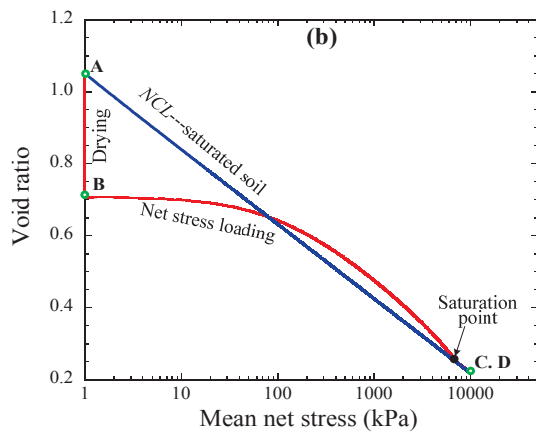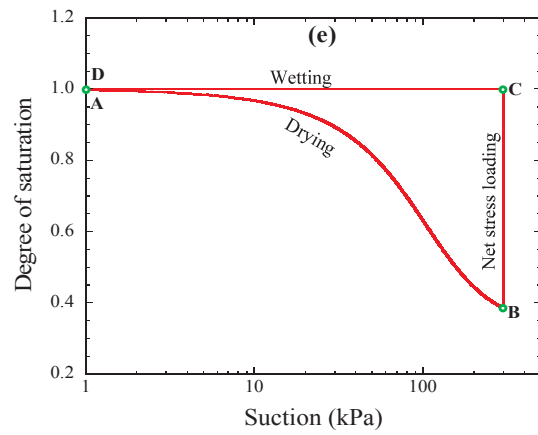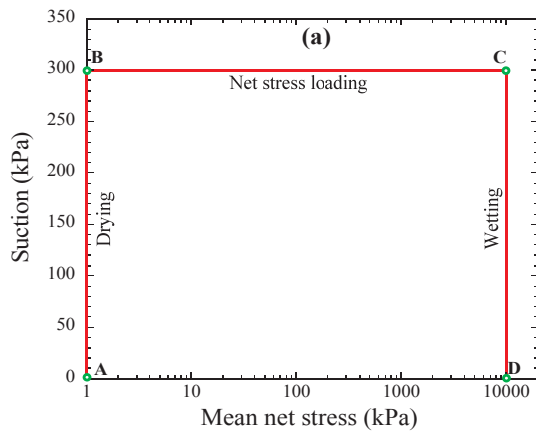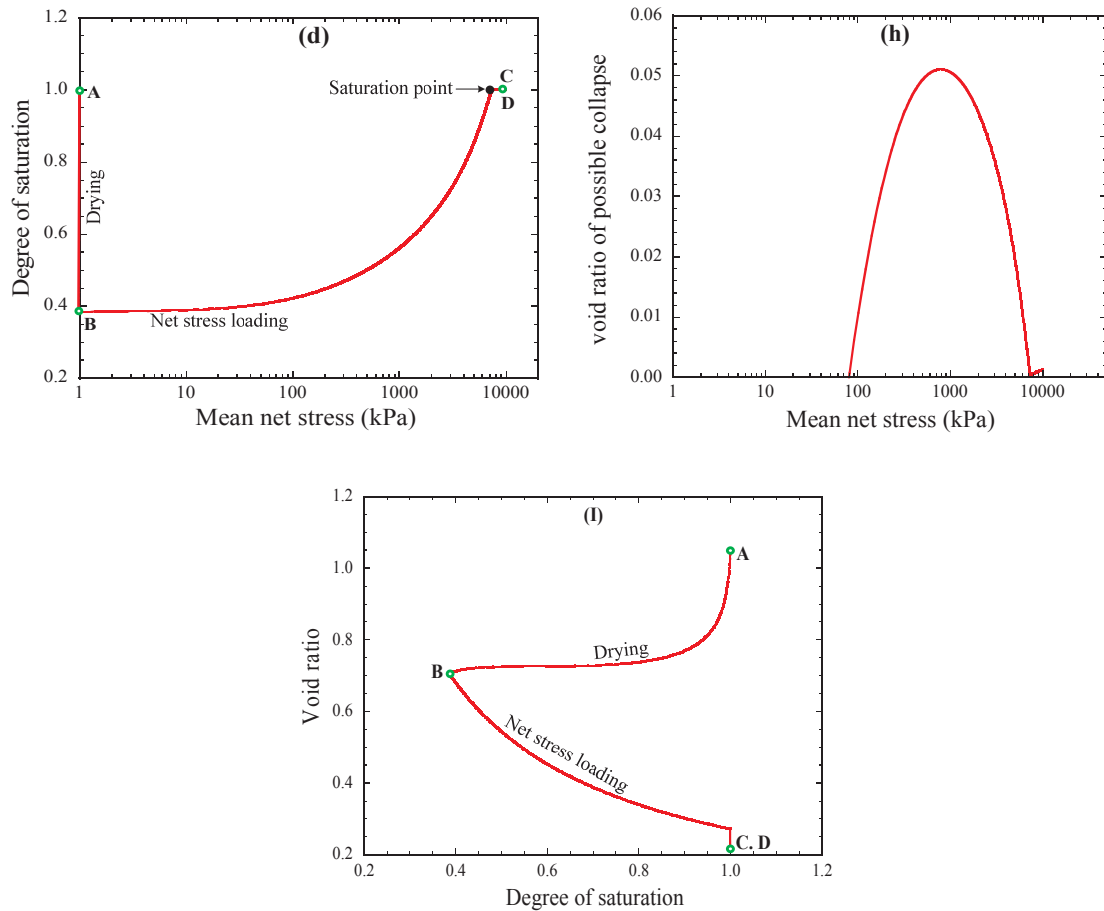
Fig.3.13 Calculated results in the drying-isotropic loading to full saturation-suction reduction: (a) *s* vs. *p*^net, (b) *e* vs. *p*^net, (c) *e* vs. *s*, (d) *S*r vs. *p*^net, (e) *S*r vs. *s*, (f) *e* vs. *p″*, (g) *S*r vs. *p″*, (h) Δ*e* vs. *p*^net

Fig.3.13(a) shows the relationship between the suction and the mean net stress (*s* vs. *p*^net), in which a suction of 300 kPa is firstly loaded under a constant mean net stress (1 kPa) for a fully saturated slurry soil sample, then mean net stress of 10 MPa is acted on the sample under the constant suction (300 kPa), finally the reduction of suction to 0 is done by holding the constant mean net stress (10 Mpa). Fig.3.13(b) shows the relationship between the void ratio and the mean net stress (*e* vs. *p*^net). The specimen is firstly compressed due to the suction loading (drying process), and then the line is close to the normal consolidated line (*NCL*) of saturated soil and at a time it coincides with the NCL when the mean net stress is loading. Fig.3.13(c) shows the relationship between the void ratio and the suction (*e* vs. *s*). Because the full saturation is reached at point C, the process of suction reduction is only given rise to a small value of elastic

expansive strain due to the decrease of the mean effective stress. Fig.3.13(d) shows the relationship between the degree of saturation and the mean net stress (S_r vs. p^{net}). At a time the specimen will be re-saturated by applying the net stress loading.

　　　Fig.3.13(e) is the relationship between the saturation and the suction (S_r vs. s). Path AB and CD is the main drying curve and main wetting curve, but under different mean net stress condition. The relationship between the void ratio and the mean skeleton stress (effective stress) is plotted in Fig.3.13(f) (e vs. p''). The specimen is started from the initial full saturated state, and then goes up the higher position due to the de-saturation, and finally is back to the NCL. Fig.3.13(g) shows the relationship between the saturation and the mean skeleton stress (S_r vs. p''). Fig.3.13(h) shows the change of void ratio due to the wetting collapse, which is consistent with the experimental results conducted by Sun et al. (2007c). Fig.3.13(I) shows the relation between the void ration and saturation. And it is known that the degree of saturation is increasing with the decrease of void ratio even when the suction is kept constant.

(b) Case2: Drying→isotropic loading→wetting collapse
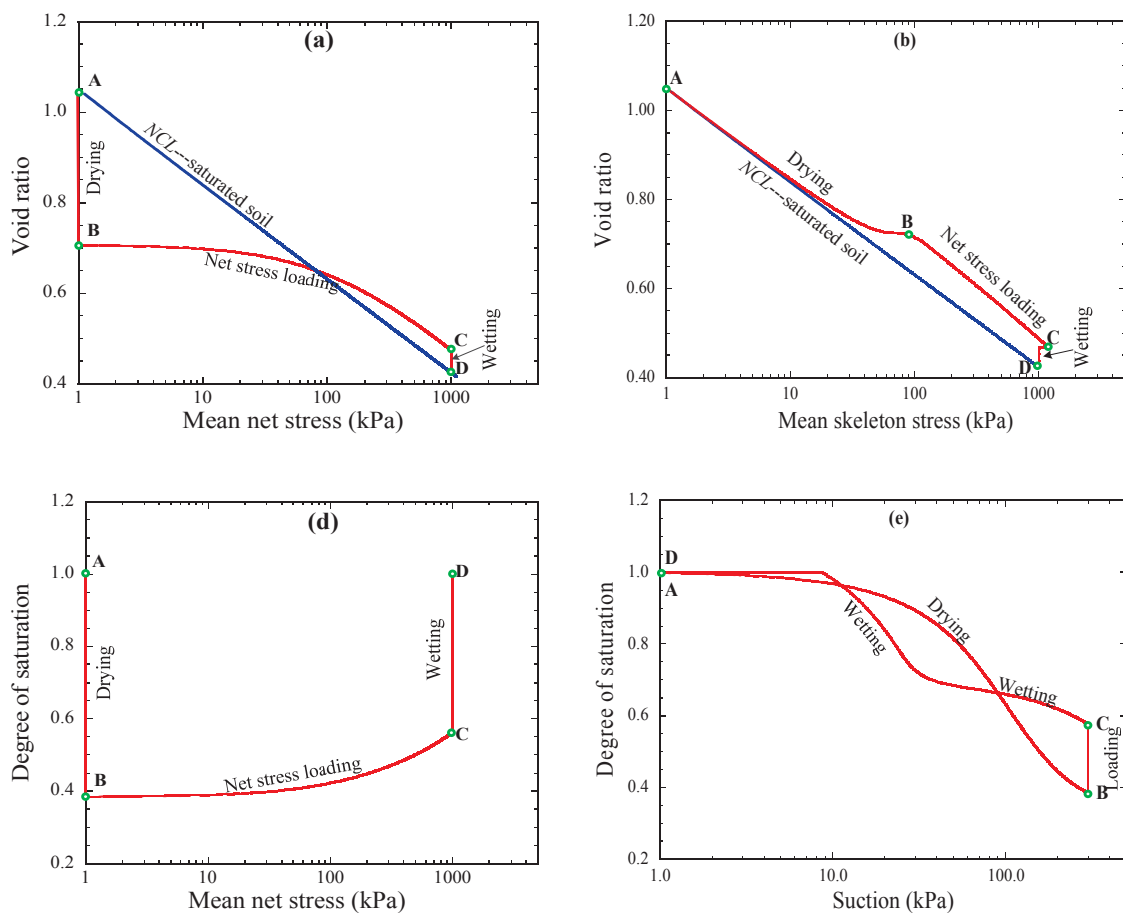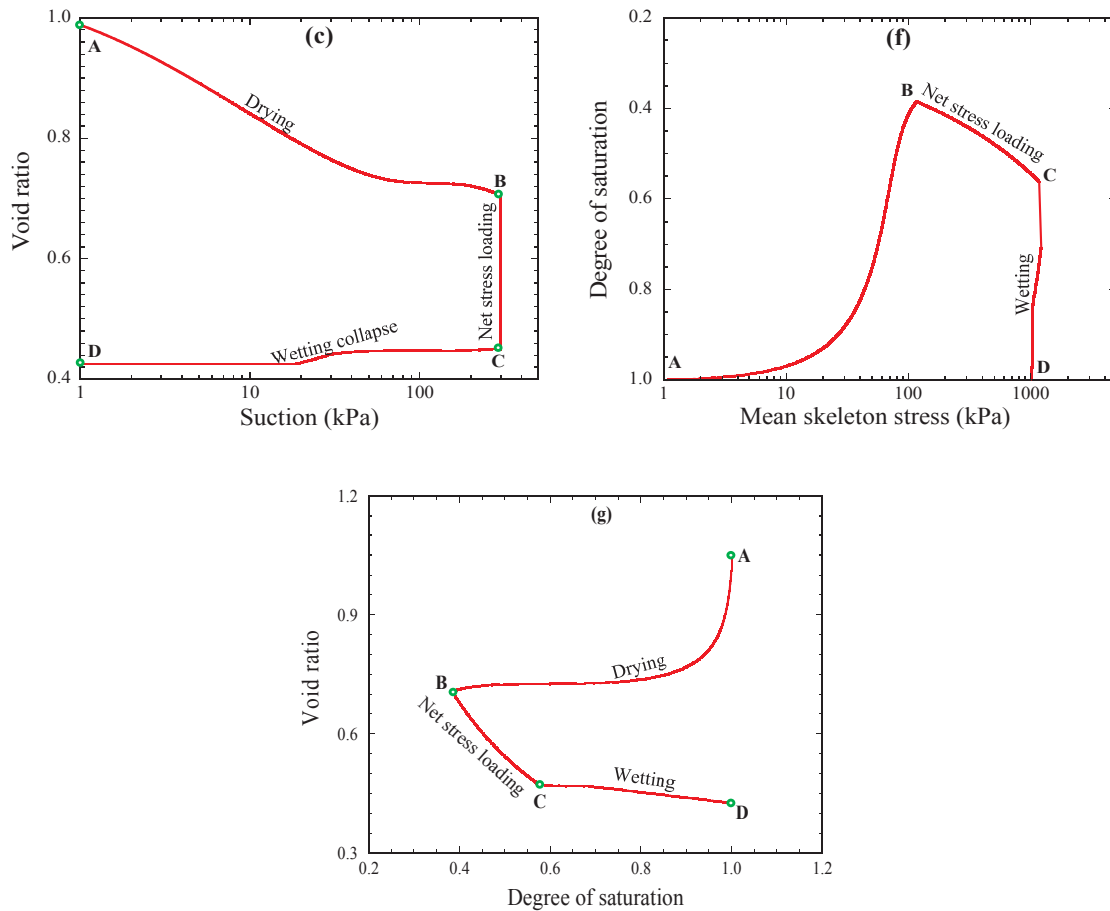
Fig.3.14 Calculated results in the drying-isotropic loading-wetting collapse: (a) e vs. p'', (b) e vs. p^{net}, (c) e vs. s, (d) S_r vs. p^{net}, (e) S_r vs. s, (f) S_r vs. p''

In this case, the same loading path is given but the value of net stress loading is smaller that Case 1. In other word, the net stress loading does not continue until the specimen reaches the saturated state. The performance of this case in the drying process is the same as the Case 1. Figs.3.14(a), (b) and (c) show the relationship between the void ratio and the mean net stress, the void ratio and the mean net stress, the void ratio and the suction respectively. The wetting is beginning, when the loading reaches point C. Subsequently a certain collapse volume is generated due to the wetting until the state goes back to the NCL. The relationship between the degree of saturation and the suction is plotted in the Fig.3.14(e). A nonlinear relation is found out in the wetting process. Fig.3.14(g) shows the relation between the void ration and saturation.

(c) Case3: Drying test at the different net stress

(a) $p^{net} \sim s$ (b) $S_r \sim s$
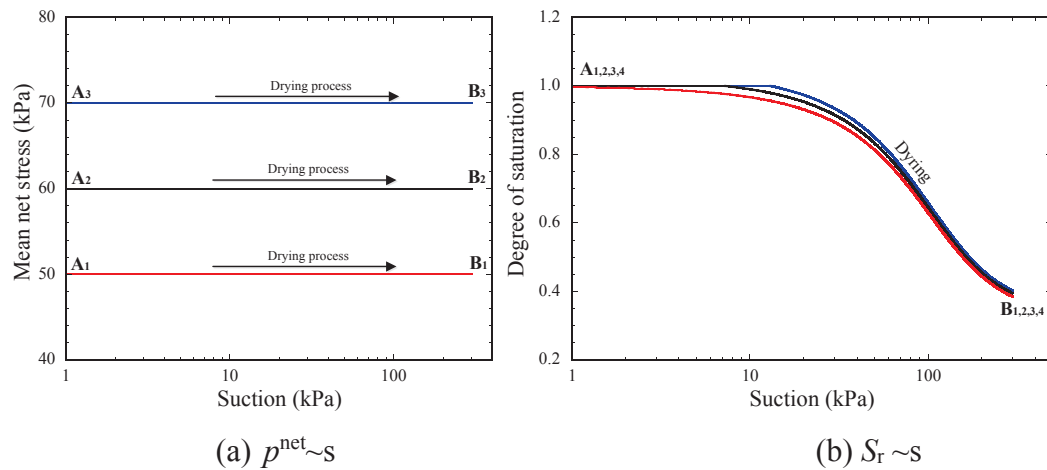
Fig.3.15 Simulation of drying tests under different net stress

The drying tests under different net stress is simulated in the section. The slurry specimens are first consolidated at the net stress of 50 kPa (point A_1 in Fig.3.15a), 60 kPa (point A_2), 70 kPa (point A_3) respectively, and then dried to a suction of 300 kPa (points B_1-B_4). The stress paths are shown in Fig.3.15a. The predicted drying curves under different net stress are shown in Fig.3.15b. It is shown that the drying curve is shifting with the different net stress. The used parameters are the same as those of Case 1 and Case 2.

(d) Case4: Drying-isotropic loading under different temperature condition

In order to investigate the influence of temperature on the strength and deformation of unsaturated soil, Uchaipichat and Khalili (2009) conducted an extensive experiment research on a compacted silt using a modified triaxial equipment that allowed independent control and measurement of pore water pressure, pore air pressure and temperature at same boundaries. In the test, the identical soil samples with 50mm in diameter and 20mm in height are prepared carefully, and all tested samples had an initial pre-consolidation pressure of 200 kPa and an overconsolidation ratio of 4. In other words, all soil specimens are under the confining stress of 50 kPa at the beginning. In this part, the consolidation test at different temperatures conducted by Uchaipichat and Khalili (2009) is firstly used to validate the availability of the proposed model.

The influence of temperature on the MCC is neglected in the simulation because the MCCs of compacted silt measured in the tests at different temperature have a little difference. Only MCC of compacted silt at room temperature 25°C is employed in the simulation and the calculated and experimental MCCs of compacted silt is shown in

Fig.3.16. The parameters of MCC are listed in Table 3.5. It is known that there is a good agreement between the test result and calculated result.
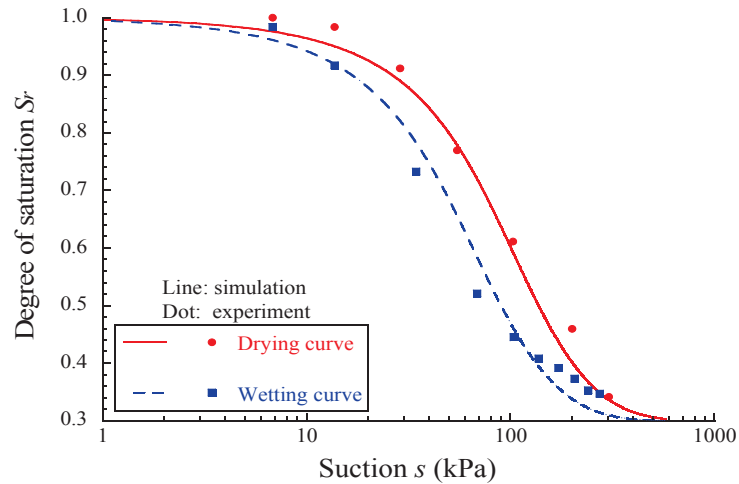
Fig.3.16 Calculated and experimental results of MCC of compacted silt (data after Uchaipichat and Khalili, 2009)
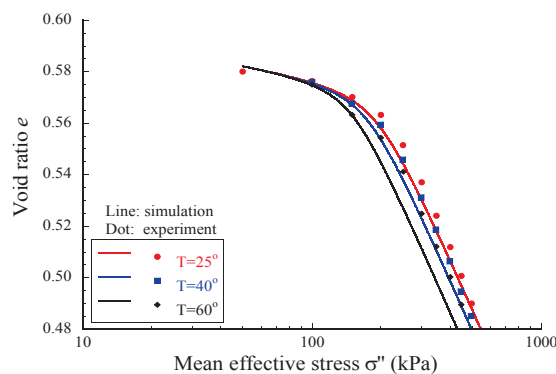
(a) *s*=0 kPa
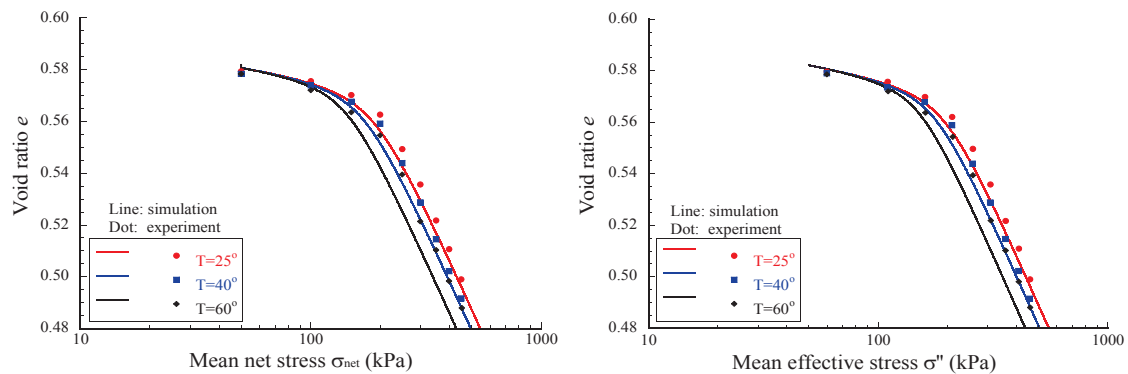
(b) *s*=10 kPa
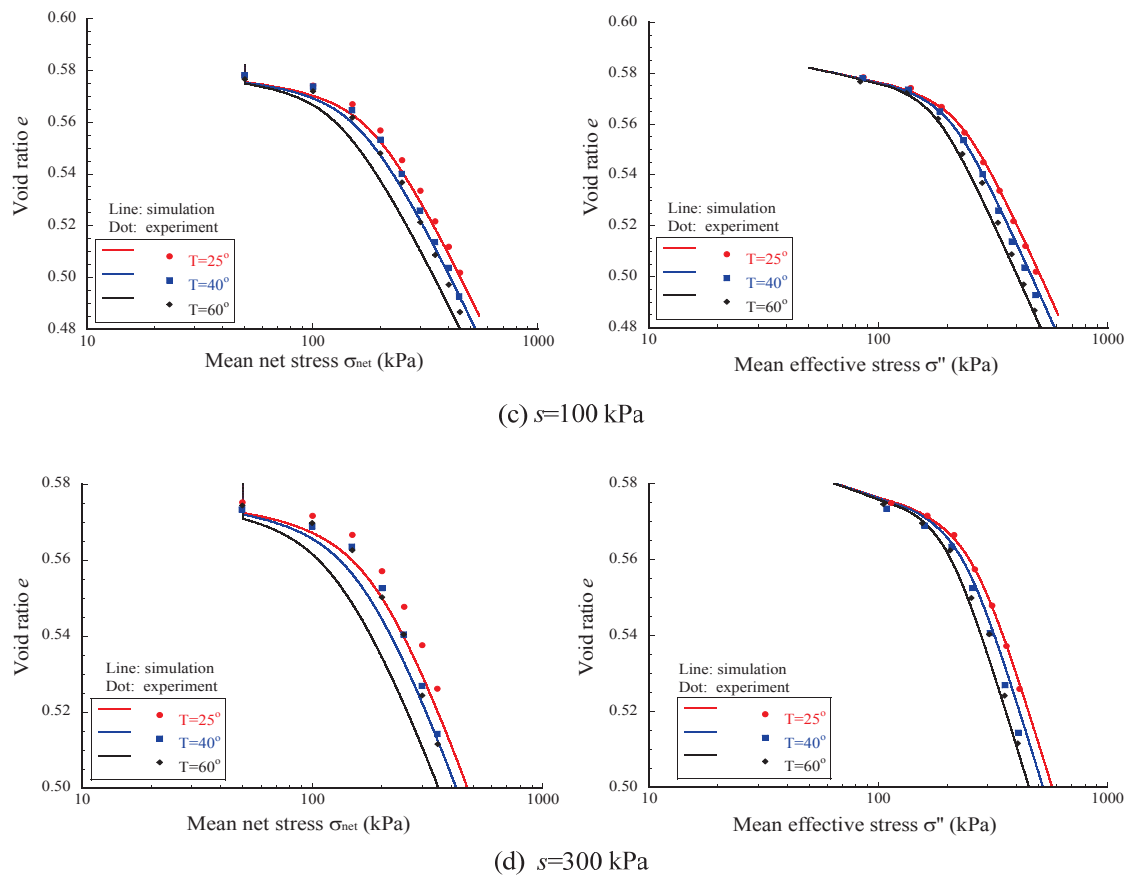
(c) *s*=100 kPa

(d) *s*=300 kPa

Fig.3.17 Isotropic loading tests (data after Uchaipichat and Khalili, 2009) under different constant suctions and different constant temperatures: (a) *s*=0 kPa; (b) *s*=10 kPa; (c) *s*=100 kPa; (d) *s*=300 kPa

Fig.3.17 shows the comparisons between isotropic loading tests and simulations at different constant suctions (*s*=0, 10, 100 and 300 kPa) and different constant temperatures (*T*=25 °C, 40 °C and 60 °C). In the figures, the left is the relation between mean net stress and void ratio, the right is the relation between mean effective stress and void ratio except for diagram (a) because the mean net stress is equal to mean effective stress for saturated soil (*s*=0 kPa). The higher the temperature is, the smaller the pre-consolidated stress is. It is indicated by comparing the calculated results with experimental results that the proposed model can well describe the shift of normal compression lines with different constant temperature observed in the tests not only for unsaturated sample but also for saturated sample. The used material parameters of compacted silt are listed in Table 3.6.

Table 3.5 Parameters of moisture characteristics curve of unsaturated compacted silt

Saturated degrees of saturation S_r^{ss}	1.00
Residual degrees of saturation S_r^{r}	0.30
Parameter corresponding to drying AEV (kPa) S_d	18.0
Parameter corresponding to wetting AEV (kPa) S_w	5.0
Initial stiffness of scanning curve (kPa) k_{sp}^{e}	90.0
Parameter controlling the influence of density ξ_e	0.00
Parameter controlling the influence of temperature ζ_T	0.00
Parameter of shape function c_1	0.009
Parameter of shape function c_2	0.013
Parameter of shape function c_3	3.0

Table 3.6 Material parameters of compacted silt

Compression index λ	0.09
Swelling index κ	0.006
Critical state parameter **M**	2.45
Void ratio N (p'=10 kPa on *N.C.L.*)	0.638
Poisson's ratio v	0.30
Parameter of overconsolidation a	60.00
Parameter of suction b	0.00
Parameter of overconsolidation β	2.00
Void ratio N_r (p'=10 kPa on *N.C.L.S.*)	0.665

3.5.2 Three dimensional behavior of the model

Uchaipichat and Khalili (2009) also conducted a series of compression shear tests under different constant suction and temperature condition in order to investigate the influence of suction and temperature on the deformation and shear strength of unsaturated silt.

Figs.3.18 and 3.19 show the comparisons between the test results and the calculated results under initial mean net stress 50 kPa and 100 kPa respectively. The larger the value of suction is, the larger the shear stress is. But the higher the temperature is, the smaller the shear stress is. Comparing with the test results, it is found that the calculated results agree well with the test results on the whole. The used parameters, of course, are the same as the parameters listed in Table 3.6 and 3.7.
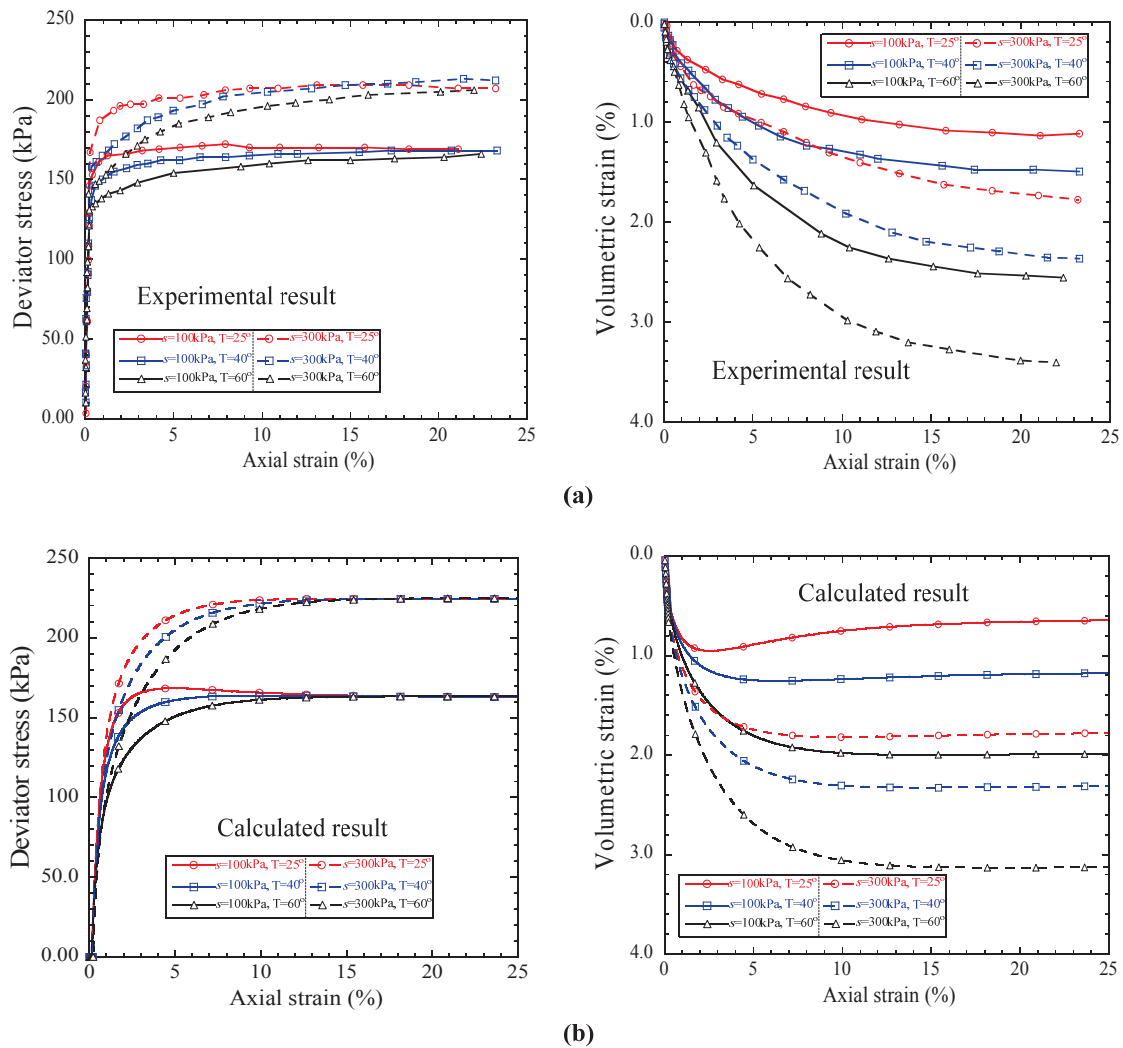
Fig.3.18 Conventional compression shear tests (data after Uchaipichat and Khalili, 2009) under different constant suction and temperature condition at initial mean net stress of 50 kPa: (a) experimental results (b) calculated results
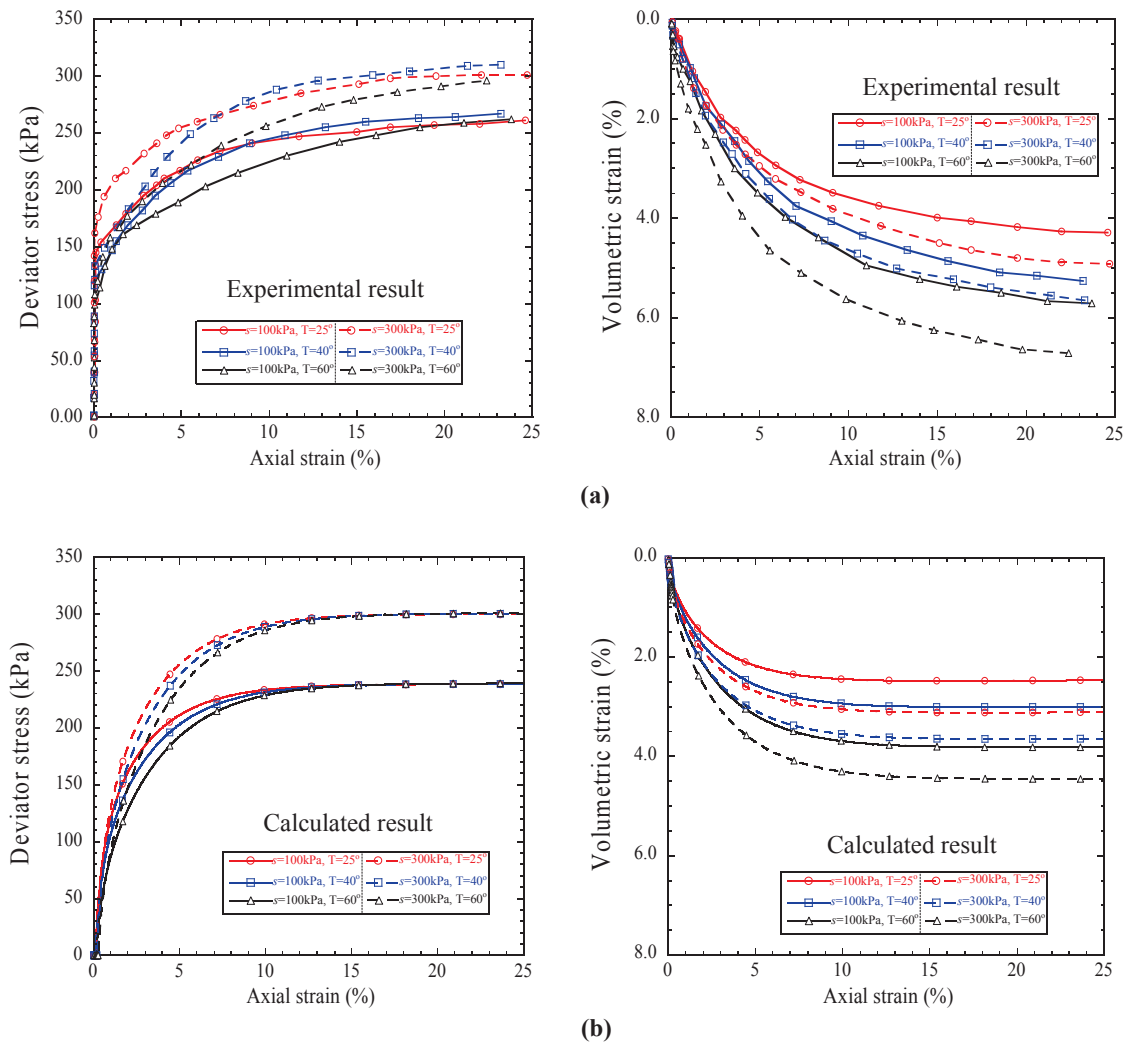
Fig.3.19 Conventional compression shear tests (data after Uchaipichat and Khalili, 2009) under different constant suction and temperature condition at initial mean net stress of 100 kPa: (a) experimental results (b) calculated results

3.6 Conclusions

In this chapter, a new thermo-elastoplastic constitutive model for unsaturated soil is proposed based on the model proposed by Zhang and Ikariya (2011), in which all the merits possessed in the model of Zhang and Ikariya (2011) are not only kept, but also some other features of unsaturated soil are also considered. The main conclusions are made in the following:

1. The proposed model is very simple and is derived from the base of modified Cam-clay mode. It also can describe not only the behavior of unsaturated soil but also saturated soil because the skeleton stress and smoothly shift to effective stress if saturation changes from unsaturated condition to saturated condition.

2. In order to consider the influence of void ratio/deformation on MCC, a new method proposed by Sheng and Zhou. (2011) is discussed. It is found out that this method is only valid and rational under undrained condition in term of the basic and intrinsic relationship. And this problem should be solved as BVP from author's viewpoint. Because the state variable (S_r) is dependent on the gravimetric water content (w) and the void ratio (e), while the gravimetric water content is dependent on the drained condition.

3. The effect of temperature on the deformation and strength of unsaturated soil in the proposed model can be reasonable to be considered. In the model, the equivalent stress proposed by Zhang et al. (2009, 2012) is adopted to the model proposed by Zhang and Ikariya (2011). It is known from the comparison between test results and calculated results that the proposed model can describe well the influence of temperature on the deformation and strength of unsaturated soil, not only the one-dimensional consolidation tests but also three-dimensional compression shear tests with one set of parameters.

4. The disadvantage of the model, as pointed out in the work by Sheng (2011), is that when using Bishop-type effective stress as the state valuable and assuming that e-log$p$'curves at different Sr parallel to each other, an overlooked restriction exists at zero mean effective stress, which may contradict to the aforementioned assumption under typical stress state, e.g., p'=1. Further revision on this model is needed in the near future.

References

1) Alonso, E. E., Gens, A., and Josa, A. (1990): A constitutive model for partially saturated soils. *Geotechnique*, 40(3): 405-430.

2) Baldi, G, Hueckel, T, Pellegrini, R. (1988): Thermal volume changes of mineral-water system in low porosity clay soils. *Canadian Geotechnical Journal*, 25, 807–825.

3) Campanella, R.G, Mitchell, J.K. (1968): Influence of temperature variations on soil behaviour. *ASCE Journal of Soils Mechanics and Foundation Division*, 94(SM3):709–734.

4) Cekerevac, C, Laloui, L. (2004): Experimental study of thermal effects on the mechanical behaviour of a clay. *International Journal for Numerical and Analytical Methods in Geomechanics*, 28, 209–228.

5) Chiu, C. F., and Ng, C. W. W. (2003). A state-dependent elasto-plastic model for saturated and unsaturated soils. *Geotechnique*, 53(9): 809-829.

6) Cui, Y. J. and Delage, P. (1996): Yielding and plastic behavior of an unsaturated compacted silt, *Geotechnique*, 46(2), 291-311.

7) Cui, Y. J., Sultan, N. and Delage, P. (2000): A thermomechanical model for saturated clays. *Canadian Geotechnical Journal*, 37, 607-620.

8) Collins, I. F. and Hilder, T. (2002): A theoretical framework for constructing elastic/plastic constitutive models of triaxial tests. *Int. J. Numer. Anal. Meth. Geomech.*, 26, 1313-1347.

9) Dangla, P., Malinsky, L. and Coussy, O. (1997): Plasticity and imbibition-drainage curves for unsaturated soils: a unified approach. *In Proceedings of 6th International Symposium on Numerical Models in Geomechanics-NUMOG*, 141-146.

10) Dumont, M., Taibi, S., Fleureau, J., Abou-Bekr, N. and Saouab, A. (2011): A thermo-hydro-mechanical model for unsaturated soils based on the effective stress

concept. *Int. J. Numer. Anal. Meth. Geomech.*, 35, 1299-1317.

11) Francois, B. and Laloui, L. (2008): ACMES-TS: A constitutive model for unsaturated soils under non-isothermal conditions. *Int. J. Numer. Anal. Meth. Geomech.*, 32, 1955–1988.

12) Gallipoli, D., Gens, A., Sharma, R. and Vaunat, J. (2003a): An elasto-plastic model for unsaturated soil incorporating the effects of suction and degree of saturation on mechanical behavior. *Geotechnique*, 53(1),41-54.

13) Gallipoli, D., Wheeler, S.J. and Karstunen, M. (2003b): Modelling of variation of degree of saturation in a deformable unsaturated soil, *Getechnique*, 53(1), 123-135.

14) Honda, M. (2000): Research on the prediction methods for the mechanical behaviors of unsaturated soils, *Doctoral Dissertation*, Kobe University.

15) Hashiguchi, K. and Ueno, M. (1977): Elastoplastic constitutive laws of granular material, Constitutive Equations of Soils, *Proc. 9th Int. Conf. Soil Mech. Found. Engrg.*, Spec. Ses. 9, eds. By Murayama, S. and Schofield, A. N., Tokyo, JSSMFE, 73-82.

16) Kawai, K., Karube, D., Ashida, W. and Kado Y. (2000): Modeling of water retention curves with effect of void ratio. *JSCE*, 666(III-53), 291-302.

17) Kohgo, Y., Nakano, M., and Miyazaki, T. (1993): Theoretical aspects of constitutive modelling for unsaturated soils. Soils and Foundations, 33(4): 49-63.

18) Laloui, L. (2001): Thermo-mechanical behaviour of soils. *Environmental Geomechanics*, 5, 809-843.

19) Loret, B., and Khalili, N. (2002): An effective stress elastic-plastic model for unsaturated porous media. *Mechanics of Materials*, 34(2): 97-116.

20) Nuth, M. and Laloui, L. (2008): Advances in modelling hysteretic water retention curve in deformable soils, *Computers and Geotechnics*, 32, 771-801

21) Okada T. (2005): Mechanical properties of sedimentary soft rock at high temperatures (Part 1)-Evaluation of temperature dependency based on triaxial

compression test. *Civil Engineering Research Laboratory Report*, No. N04026 (in Japanese).

22) Ohno, S., Kawai, K. and Tachibana, S. (2007): Elasto-plastic constitutive model for unsaturated soil applied effective degree of saturation as parameter expressing stiffness. *JSCE*, 63(4), 1132-1141. (in Japanese)

23) Sharma, R. (1998): Mechanical behavior of unsaturated highly expansive soil. PhD thesis. University of Oxford, UK.

24) Sheng, D., Sloan, S. W. and Gens, A. (2004): A constitutive model for unsaturated soils: thermomechanical and computational aspects. *Computational Mechanics*, 33, 453-465.

25) Sheng, D. (2011): Constitutive modelling of unsaturated soils: Discussion of fundamental principles. *Unsaturated Soils*, (E. E. Alonso and A. Gens, eds.), Barcelona, Spain, 1: pp. 91-112. CRC Press

26) Sheng, D., Fredlund, D. G., and Gens, A. (2008): A new modelling approach for unsaturated soils using independent stress variables. *Canadian Geotechnical Journal*, 45(4): 511-534.

27) Sheng, D. and Zhou, A. N. (2011): Coupling hydraulic with mechanical models for unsaturated soils. *Canadian Geotechnical Journal*, 48(5), 826-840.

28) Sun, D. A., Cui, H. B., Matsuoka, H., and Sheng, D. (2007a). A three-dimensional elastoplastic model for unsaturated compacted soils with hydraulic hysteresis. *Soils and Foundations*, 47(2): 253-264.

29) Sun, D. A., Sheng, D. and Sloan, S. W. (2007b): Elastoplastic modeling of hydraulic and stress-strain behavior of unsaturated soils. *Mechanics of Materials*, 39(3), 212-221.

30) Sun, D. A., Sheng, D. and Xu, Y.F. (2007c): Collapse behavior of unsaturated compacted soil with different initial densities, *Canadian Geotechnical Journal*, 44, 673-686.

31) Tang, A. M., Cui, Y. J. and Barnel, N. (2007): A new isotropic cell for studying the

thermo-mechanical behavior of unsaturated expansive clays. *Geotechnical Testing Journal*, 30(5), 341-348.

32) Tarantino, A. (2009): A water retention model for deformable soils. *Geotechnique*, 59(9):751-762.

33) Topp, G.C. and Miller, E.E. (1966): Hysteretic moisture characteristics and hydraulic conductivities for grass-bead media. *Soil Sci. Soc. Amer. Proc.* 30, 156-162.

34) Uchaipichat, A. and Khalili, N. (2009): Experimental investigation of thermo-hydro-mechanical behaviour of an unsaturated silt. *Geotechnique*, 59(4), 339-353.

35) Van Genuchten, M. T. (1980): A closed-form equation for predicting the hydraulic conductivity of unsaturated soils, *Soil Sci. Soc. Am, J.*, No.44, 892-898.

36) Vaunat, J., Romero, E. and Jommi, C. (2000): An elastoplastic hydro-mechanical model for unsaturated soils. *In Experimental evidence and theoretical approaches in unsaturated soils Proceedings of international workshop on unsaturated soil*, 121-138.

37) Villar, M.V. and Gómez-Espina, R. (2007): Retention curves of two bentonites at high temperature, *Experimental Unsat. Soil Mech.*, 267-274.

38) Wheeler, S. J. (1996): Inclusion of specific water volume within an elasto-plastic model for unsaturated soil. *Canadian Geotechnical Journal*, 33(1):42-57.

39) Wheeler, S. J., Sharma, R. S. and Buisson, M. S. R. (2003): Coupling of hydraulic hysteresis and stress-strain behaviour in unsaturated soils. *Geotechnique*, 53(1), 41-54.

40) Zhang, S. and Zhang, F. (2009): A thermo-elasto-viscoplastic model for soft sedimentary rock. *Soils and Foundations*, 49(4), 583-595.

41) Zhang, S., Leng, W.M., Zhang, F. and Xiong, Y. L. (2012): A simple thermo-elastoplastic model for geomaterials. *International Journal of Plasticity*, 34, 93-113

42) Zhang, F. and Ikariya, T. (2011): A new model for unsaturated soil using skeleton stress and degree of saturation as state variables. Soils and Foundations, 51(1), 67-81.

43) Zhou, A. N., Sheng, D. C., Sloan, S. W. and Gens, A. (2012a): Interpretation of unsaturated soil behaviour in the stress-saturation space, I: Volumetric change and water retention behaviour, *Computers and Geotechnics*, 43, 178-187.

44) Zhou, A. N., Sheng, D. C., Sloan, S. W. and Gens, A. (2012b): Interpretation of unsaturated soil behaviour in the stress-saturation space, II: Constitutive relationships and validations, *Computers and Geotechnics*, 43, 111-123.

CHAPTER 4 THERMO-HYDRAULIC-MECHANICAL-AIR COUPLING FIELD THEORY

4.1 General

As we know, soil is different from some other engineering materials, such as steel, that it consists of more than one phase. In general, soil is made of soil-grain, water, and air. When the voids are fully occupied with water, it is called as saturated soil, otherwise unsaturated soil.

Oka *et al.* (1991, 1994) proposed a soil-water coupled two-phase field theory with *u-p* formulation, in which the displacement of the solid, *u*, and the pore water pressure, *p*, are used as the unknown variables. Moreover, in the discretization of the governing equations in space, both FEM (Finite Element Method) and FDM (Finite Difference Method) are used. FEM is used for the discretization of the equation of motion for the mixture, and FDM is used for the discretization of the continuity equation for the pore fluid.

Oka's two-phase field theory has been proved to be effective in liquefaction analysis, but it still adopts the assumption of infinitesimal strain. However, liquefaction of soil is often accompanied by large flow deformation, so the assumption of infinitesimal strain seems not sufficient. Ye *et al.* (2006) and Ye (2007) established and re-derived the equations of two-phase field theory based on finite deformation algorithm.

As pointed out by Sheng (2011), an unsaturated soil is not a special type of soil, rather a state of the soil. Unsaturated soil is usually encountered in the geotechnical problems, especially in arid area. The two-phase field theory, therefore, is not sufficient to deal with the geotechnical problems relating with unsaturated ground. At the same time, the temperature effect on the geomaterials has also been investigated recently. In this chapter, the field theory of soil-water-air three-phase fully coupling finite element method under non-isothermal condition is derived in detailed based on the Oka's two-phase field theory.

4.2 Thermo-Hydraulic-Mechanical-Air Coupling Finite Deformation Algorithm of Field Equations

For simplicity, the following convention is used: the superscripts *s, w* and *a* refer to soil phase, water phase and air phase respectively.

The following assumptions are adopted in the derivation of the three-phase field theory:

(1) The distribution of porosity, *n*, in space and time are very small comparing to other variables.

(2) The distribution of degree of saturation, S_r, in space is very small comparing to other variables.

(3) The relative acceleration of the fluid (water and air) phase to the solid phase is much smaller than the acceleration of the solid phase.

(4) Soil grain is incompressible.

4.2.1 Equilibrium equation

For the convenience of deriving the field equations, we introduced the definition of appearance density. The appearance densities of the solid phase $\bar{\rho}^s$, the water phase $\bar{\rho}^w$ and the air phase $\bar{\rho}^a$ are defined as

$$\bar{\rho}^s = (1-n)\rho^s \tag{4.2.1}$$

$$\bar{\rho}^w = nS_r\rho^w \tag{4.2.2}$$

$$\bar{\rho}^a = n(1-S_r)\rho^a \tag{4.2.3}$$

With the use of appearance density, the density of mixture can be expressed as

$$\rho = \bar{\rho}^s + \bar{\rho}^w + \bar{\rho}^a = (1-n)\rho^s + n\left[S_r\rho^w + (1-S_r)\rho^a\right] \tag{4.2.4}$$

Considering the mean pore pressure p^F, the relationship between total stress tensor $\boldsymbol{T}$ and effective stress tensor $\boldsymbol{T}'$ are as follows

$$\boldsymbol{T} = \boldsymbol{T}' + p^F\boldsymbol{I}, \qquad \dot{\boldsymbol{T}} = \dot{\boldsymbol{T}}' + \dot{p}^F\boldsymbol{I}, \qquad p^F = S_r p^w + (1-S_r)p^a \tag{4.2.5}$$

The total stress tensor and stress tensors that act on each phase have the following form

$$\boldsymbol{T} = \boldsymbol{T}^s + \boldsymbol{T}^w + \boldsymbol{T}^a \tag{4.2.6}$$

$$T^s = T' + (1-n)p^F I \tag{4.2.7}$$

$$T^w = nS_r p^w I \tag{4.2.8}$$

$$T^a = n(1-S_r)p^a I \tag{4.2.9}$$

Some gradient tensors used in the derivation are defined as following

$$\mathbf{L} = \left(\frac{\partial v_i}{\partial x_j}\right)\mathbf{e_i} \otimes \mathbf{e}_j \tag{4.2.10}$$

$$\mathbf{D} = \frac{1}{2}\left(\frac{\partial v_i}{\partial x_j} + \frac{\partial v_j}{\partial x_i}\right)\mathbf{e_i} \otimes \mathbf{e}_j \tag{4.2.11}$$

$$\mathbf{W} = \frac{1}{2}\left(\frac{\partial v_i}{\partial x_j} - \frac{\partial v_j}{\partial x_i}\right)\mathbf{e_i} \otimes \mathbf{e}_j \tag{4.2.12}$$

where, L is the velocity gradient tensor; D is the strain rate tensor; W is the rotation rate tensor; v_i is the velocity vector. There is a relationship of $L=D+W$. The definitions of the above three tensors can be applied to both solid phase and fluid phase.

The constitutive equation of each phase can be defined as:

$$\overset{\triangledown}{T} = C : D^s \quad \text{or} \quad \overset{\circ}{T} = C : D^s \tag{4.2.13}$$

$$\dot{p}^w = K^w tr(D^w) \tag{4.2.14}$$

$$\dot{p}^a = K^a tr(D^a) \tag{4.2.15}$$

where $\overset{\triangledown}{T}$ is the Jaumann stress rate tensor or $\overset{\circ}{T}$ the Green-Naghdi stress rate tensor and their definitions will be given later. C is the stiffness tensor, which is a fourth-order tensor. K^w is volume elastic coefficient of water phase and K^a is volume elastic coefficient of air phase.

As to the relative velocity $\dot{w}^w$ and $\dot{w}^a$, Darcy's law is assumed to be still applicable to unsaturated soil problems.

$$\dot{w}^w = -k^w \frac{\partial h^w}{\partial x} = -k^w \frac{\partial\left(h_d^w + h_{ini}^w\right)}{\partial x} = -k^w \frac{\partial}{\partial x}(\frac{p_d^w}{\gamma^w} + h_{ini}^w) = -\frac{k^w}{\gamma^w} \cdot \frac{\partial p_d^w}{\partial x} \tag{4.2.16}$$

$$\dot{w}^a = -k^a \frac{\partial h^a}{\partial x} - k^a \frac{\partial \left(h_d^a + h_{ini}^a\right)}{\partial x} = -k^a \frac{\partial}{\partial x}\left(\frac{p_d^a}{\gamma^a} + h_{ini}^a\right) = -\frac{k^a}{\gamma^a} \cdot \frac{\partial p_d^a}{\partial x} \qquad (4.2.17)$$

where k^w and k^a are coefficient of permeability for water and air, h^w and h^a are total hydraulic head for water and air. h_d^w and h_d^a are hydraulic head for water and air caused by excessive pore water and pore air pressure. h_{ini}^w and h_{ini}^a are initial total hydraulic head for water and air. $p_d^w (= \gamma_w h_d^w)$ and $p_d^a (= \gamma_a h_d^a)$ are excessive pore water pressure and excessive pore air pressure. w^w is relative displacement vector of water phase to solid phase, w^a is relative displacement vector of air phase to solid phase, the definitions of them are given as

$$w^w = v^w - v^s \qquad (4.2.18)$$

$$w^a = v^a - v^s \qquad (4.2.19)$$

The mass conservation law for solid phase, water phase and air phase in the local form can be written as follows

$$\frac{\partial \bar{\rho}^s}{\partial t} + div(\bar{\rho}^s v^s) = 0 \qquad (4.2.20)$$

$$\frac{\partial \bar{\rho}^w}{\partial t} + div(\bar{\rho}^w v^w) = 0 \qquad (4.2.21)$$

$$\frac{\partial \bar{\rho}^a}{\partial t} + div(\bar{\rho}^a v^a) = 0 \qquad (4.2.22)$$

And the momentum conservation law for solid phase, water phase and air phase in the local form can be written as follows

$$div \, T^s + \bar{\rho}^s b + R + Q = 0 \qquad (4.2.23)$$

$$div \, T^w + \bar{\rho}^w b - R = 0 \qquad (4.2.24)$$

$$div \, T^a + \bar{\rho}^a b - Q = 0 \qquad (4.2.25)$$

Where, R is interaction force vector between water phase and solid phase, Q is interaction force vector between air phase and solid phase, b is the body force vector.

Adding Eqs.(4.2.23), (4.2.24) and (4.2.25) together, the equilibrium equation of soil-water-air three-phase filed theory can be given as

$$div\, \boldsymbol{T} + \rho \boldsymbol{b} = 0 \tag{4.2.26}$$

4.2.2 Continuum equation of water phase

Substituting Eqs.(4.2.1) and (4.2.2) into the mass conservation Eqs.(4.2.20) and (4.2.21) respectively, we have

$$(1-n)\frac{\partial \rho^s}{\partial t} + \rho^s \frac{\partial (1-n)}{\partial t} + \rho^s div\left\{(1-n)\boldsymbol{v}^s\right\} + (1-n)\boldsymbol{v}^s div\,(\rho^s \boldsymbol{I}) = 0 \tag{4.2.27}$$

$$nS_r \frac{\partial \rho^w}{\partial t} + \rho^w \frac{\partial (nS_r)}{\partial t} + \rho^w div\,(nS_r \boldsymbol{v}^w) + nS_r \boldsymbol{v}^w div\,(\rho^w \boldsymbol{I}) = 0 \tag{4.2.28}$$

Multiplying $S_r \rho^w / \rho^s$ to Eq.(4.2.27) and then adding it to Eq.(4.2.28), the following equation can be obtained

$$S_r \rho^w \left(\frac{\partial (1-n)}{\partial t} + \frac{\partial n}{\partial t}\right) + \rho^w div\left\{nS_r (\boldsymbol{v}^w - \boldsymbol{v}^s)\right\} + S_r \rho^w div\, \boldsymbol{v}^s +$$

$$nS_r \left(\frac{\partial \rho^w}{\partial t} + \boldsymbol{v}^w div\,(\rho^w \boldsymbol{I})\right) + n\rho^w \frac{\partial S_r}{\partial t} + S_r (1-n)\frac{\rho^w}{\rho^s}\left(\frac{\partial \rho^s}{\partial t} + \boldsymbol{v}^s div\,(\rho^s \boldsymbol{I})\right) = 0$$

$$\tag{4.2.29}$$

The first term in the Eq.(4.2.29) obviously equals to zero. Considering that the assumption (4), the last term equals to zero too. Substituting $div\boldsymbol{v} = tr\boldsymbol{D}$ and Eq.(4.2.18) into Eq.(4.2.29) and then dividing $nS_r \rho^w$, continuum equation of water phase can be obtained as the following form

$$div\dot{\boldsymbol{w}}^w + \frac{tr\boldsymbol{D}^s}{n} + \frac{1}{\rho^w}\dot{\rho}^w + \frac{1}{S_r}\dot{S}_r = 0 \tag{4.2.30}$$

Considering the influence of temperature, the change of water density can be given as

$$\dot{\rho}^w = -(\frac{1}{K^w}\dot{p}_d^w + 3\alpha_T^w \dot{T})\rho^w \tag{4.2.31}$$

where α_T^w is the linear thermal expansion coefficient of water phase.

Substituting Eqs.(4.2.31) and (4.2.16) into Eq.(4.2.30), continuum equation of

water phase can be written as

$$\frac{tr\boldsymbol{D}^s}{n} - \frac{k^w}{\gamma^w} div\{div(p_d^w \boldsymbol{I})\} - \frac{1}{K^w} \dot{p}_d^w - 3\alpha_T^w \dot{T} + \frac{1}{S_r} \dot{S}_r = 0 \tag{4.2.32}$$

4.2.3 Continuum equation of air phase

Substituting Eqs.(4.2.1) and (4.2.3) into the mass conservation Eq.(4.2.20) and Eq.(4.2.22) respectively, we have

$$(1-n)\frac{\partial \rho^s}{\partial t} + \rho^s \frac{\partial(1-n)}{\partial t} + \rho^s div\left\{(1-n)\boldsymbol{v}^s\right\} + (1-n)\boldsymbol{v}^s div\left(\rho^s \boldsymbol{I}\right) = 0 \tag{4.2.33}$$

$$n(1-S_r)\frac{\partial \rho^a}{\partial t} + \rho^a \frac{\partial n(1-S_r)}{\partial t} + \rho^a div\left\{n(1-S_r)\boldsymbol{v}^a\right\} + n(1-S_r)\boldsymbol{v}^a div\left(\rho^a \boldsymbol{I}\right) = 0 \tag{4.2.34}$$

Multiplying $(1-S_r)\rho^a/\rho^s$ to Eq. (4.2.33) and then adding it to Eq.(4.2.34), the following equation can be obtained

$$(1-S_r)\rho^a \left(\frac{\partial(1-n)}{\partial t} + \frac{\partial n}{\partial t}\right) + \rho^a div\left\{n(1-S_r)(\boldsymbol{v}^a - \boldsymbol{v}^s)\right\} + (1-S_r)\rho^a div\,\boldsymbol{v}^s +$$

$$n(1-S_r)\left(\frac{\partial \rho^a}{\partial t} + \boldsymbol{v}^a div\left(\rho^a \boldsymbol{I}\right)\right) + n\rho^a \frac{\partial(1-S_r)}{\partial t} + (1-S_r)(1-n)\frac{\rho^a}{\rho^s}\left(\frac{\partial \rho^s}{\partial t} + \boldsymbol{v}^s div\left(\rho^s \boldsymbol{I}\right)\right) = 0 \tag{4.2.35}$$

The first term in the Eq.(4.2.35) obviously equals to zero. Considering that the assumption (4), the last term equals to zero too. Substituting $div\boldsymbol{v} = tr\boldsymbol{D}$ and Eq. (4.2.19) into Eq.(4.2.35) and then dividing $n(1-S_r)\rho^a$, continuum equation of air phase can be obtained as the following form

$$div\dot{\boldsymbol{w}}^a + \frac{tr\boldsymbol{D}^s}{n} + \frac{1}{\rho^a}\dot{\rho}^a - \frac{1}{1-S_r}\dot{S}_r = 0 \tag{4.2.36}$$

Ignoring the influence of temperature, the change of air density can be given as

$$\dot{\rho}^a = -(\frac{1}{K^a}\dot{p}_d^a + 3\alpha_T^a \dot{T})\rho^a \tag{4.2.37}$$

where α_T^a is the linear thermal expansion coefficient of air phase.

Substituting Eqs.(4.2.17) and (4.2.37) into Eq.(4.2.36), continuum equation of air phase can be written as

$$\frac{tr\boldsymbol{D}^s}{n} - \frac{k^a}{\gamma^a} div\{div(p_d^a \boldsymbol{I})\} - \frac{1}{K^a} \dot{p}_d^a - 3\alpha_T^a \dot{T} - \frac{1}{1-S_r} \dot{S}_r = 0 \tag{4.2.38}$$

or $\{\dfrac{tr\boldsymbol{D}^s}{n} - \dfrac{k^a}{\gamma^a} div\{div(p_d^a \boldsymbol{I})\} - \dfrac{1}{1-S_r} \dot{S}_r\} K^a - 3\alpha_T^a \dot{T} - \dot{p}_d^a = 0$ (4.2.39)

The Eq.(4.2.26), (4.2.32) and (4.2.38) are the governing equations of soil-water-air coupled three phase field theory and are widely used in FEM analysis.

4.2.4 Equation of energy conservation

Based on the first law of thermodynamics, the following equation can be obtained in the time interval dt :

$$dU = d\Phi_{k_t} + d\Phi_h + E \tag{4.2.40}$$

where, dU denotes the increment of thermal energy, $d\Phi_{k_t}$ and $d\Phi_h$ indicate the net energy induced by conduction and convection respectively, E signifies the energy produced by itself such as heat source.

The increment of thermal energy in the region dv can be expressed in the following equation:

$$dU = (1-n)(c\rho)^s dv \frac{\partial T}{\partial t} dt + nS_r(c\rho)^w dv \frac{\partial T}{\partial t} dt + n(1-S_r)(c\rho)^a dv \frac{\partial T}{\partial t} dt$$
$$= (\overline{c}\,\overline{\rho}) \frac{\partial T}{\partial t} dv dt$$

$$\tag{4.2.41}$$

where, $(\overline{\rho c}) = (1-n)(c\rho)^s + nS_r(c\rho)^w + n(1-S_r)(c\rho)^a$, n is the porosity of the soil. S_r is the degree of saturation. c is the specific heat.

The net energy of $d\Phi_{k_t}$ can be expressed as:

$$d\Phi_{k_t} = (1-n)(-div\boldsymbol{q}^s)dv + nS_r(-div\boldsymbol{q}^w)dv + n(1-S_r)(-div\boldsymbol{q}^a)dv \tag{4.2.42}$$

where, $\boldsymbol{q}$ is heat flux.

According to Fourier's law, Eq.(4.2.42) can be rewritten as:

$$d\Phi_{k_t} = (1-n)k_t^s div(divT)dvdt + nS_r k_t^w div(divT)dvdt + n(1-S_r)k_t^a div(divT)dvdt$$
$$= \overline{k_t} div(divT)dvdt$$

(4.2.43)

where, $\overline{k_t} = (1-n)k_t^s + nS_r k_t^w + n(1-S_r)k_t^a$, and is the average heat conductivity of the three-phase soil material.

Similar to $d\Phi_{k_t}$, $d\Phi_h$ also can be expressed as:

$$d\Phi_h = -nS_r(\rho c)^w div(\boldsymbol{v}^w T)dvdt - n(1-S_r)(\rho c)^a div(\boldsymbol{v}^a T)dvdt$$
$$= -nS_r(\rho c)^w T div(\boldsymbol{v}^w)dvdt - nS_r(\rho c)^w \boldsymbol{v}^w div(T)dvdt$$
$$-n(1-S_r)(\rho c)^a T div(\boldsymbol{v}^a)dvdt - n(1-S_r)(\rho c)^a \boldsymbol{v}^a div(T)dvdt$$
$$= -nS_r(\rho c)^w \boldsymbol{v}^w div(T)dvdt - n(1-S_r)(\rho c)^a \boldsymbol{v}^a div(T)dvdt$$

(4.2.44)

where, the term $div(\boldsymbol{v})$ can be regarded as zero because the gradient of velocity is very small in soft rock. $\boldsymbol{v}$ represents the velocity which can be calculated by Darcy's law.

Substituting Eq.(4.2.41), (4.2.44) and (4.2.43) into Eq.(4.2.40), the equation of energy conservation can be obtained:

$$(\overline{\rho c})\frac{\partial T}{\partial t} + nS_r(\rho c)^w \boldsymbol{v}^w div(T) + n(1-S_r)(\rho c)^a \boldsymbol{v}^a div(T) = \overline{k_t} div\{div(T)\} + E$$

(4.2.45)

4.2.5 Discretization of equilibrium equation in space and time

We have obtained the equilibrium equations in last section

$$div\,\boldsymbol{T} + \rho\boldsymbol{b} = 0 \qquad\qquad (4.2.46)$$

here, Cauchy stress $\boldsymbol{T}$ is defined in the coordinate system of current time, i.e. the coordinate system in which the object has deformed. In FEM analysis of finite deformation, however, stress calculation is all based on the initial reference coordinate system so that it is necessary to use the nominal stress, such as the first Piola-Kirchhoff stress, instead of the Cauchy stress.

By using the first Piola-Kirchhoff stress and virtual work theorem, the weak form of the equilibrium equation in an arbitrary region V can be expressed as following

$$\int_V \left(div\boldsymbol{\Pi} + \rho\boldsymbol{b}\right)\delta\dot{\boldsymbol{u}}^s dV = 0 \tag{4.2.47}$$

where, $\delta\dot{\boldsymbol{u}}^s$ is the arbitrary virtual velocity vector of solid phase, and $\boldsymbol{\Pi}$ is the first Piola-Kirchhoff stress tensor. It is in relation with the Cauchy stress tensor by

$$\boldsymbol{\Pi} = J\boldsymbol{T}\boldsymbol{F}^{-T} \tag{4.2.48}$$

where, $J = \det\boldsymbol{F}$ is the volume change rate, and $\boldsymbol{F}$ is the deformation gradient tensor.

Integrating the first term of Eq. (4.2.47) by partial integrating method, we have

$$\int_S \boldsymbol{\Pi}\ \boldsymbol{n}\delta\dot{\boldsymbol{u}}^s dS + \int_V \rho\boldsymbol{b}\delta\dot{\boldsymbol{u}}^s dV = \int_V \boldsymbol{\Pi}\delta\boldsymbol{L}\, dV \tag{4.2.49}$$

here, $\delta\boldsymbol{L}$ is arbitrary virtual velocity gradient. S is the close surface of region v. $\boldsymbol{n}$ is the outward unit normal vector of surface S. Considering boundary condition, the surface force vector $\boldsymbol{q}$ can be calculated from the Cauchy equation.

$$\boldsymbol{q} = \boldsymbol{\Pi}\ \boldsymbol{n} \tag{4.2.50}$$

Substituting Eq.(4.2.50) into Eq.(4.2.49), the following equation can be obtained

$$\int_V \boldsymbol{\Pi}\delta\boldsymbol{L}dV = \int_V \rho\boldsymbol{b}\delta\dot{\boldsymbol{u}}^s dV + \int_S \boldsymbol{q}\delta\dot{\boldsymbol{u}}^s dS \tag{4.2.51}$$

The incremental form of the above equation in finite element scheme can be written as follow:

$$\int_V \Delta t\dot{\boldsymbol{\Pi}}_{|t+\Delta t}\delta\boldsymbol{L}dV = \int_V \rho\Delta\boldsymbol{b}\delta\dot{\boldsymbol{u}}^s dV + \int_S \Delta\boldsymbol{q}\delta\dot{\boldsymbol{u}}^s dS \tag{4.2.52}$$

here, the stress rate at the current time $t+\Delta t$ according to the work by Yatomi et al. (1989) :

$$\dot{\boldsymbol{\Pi}}_{|t+\Delta t} = (\boldsymbol{\Pi}_{|t+\Delta t} - \boldsymbol{\Pi}_{|t})/(\Delta t) = (\Delta\boldsymbol{\Pi}_{|t+\Delta t}/\Delta t) = \dot{\boldsymbol{T}} + (tr\boldsymbol{D})\boldsymbol{T} - \boldsymbol{T}\,\boldsymbol{L}^T \tag{4.2.53}$$

On the other hand, from the definition of Jaumann stress rate tensor and Green-Naghdi stress rate tensor and the effective stress theory

Jaumann stress rate tensor: $\overset{\triangledown}{\boldsymbol{T}} = \dot{\boldsymbol{T}}' - \boldsymbol{W}\,\boldsymbol{T}' + \boldsymbol{T}'\boldsymbol{W}$ $\tag{4.2.54}$

Green-Naghdi stress rate tensor: $\overset{\circ}{T} = \dot{T}' - \Omega T' + T' \Omega$ (4.2.55)

we can obtain

$$\dot{\Pi} = \overset{\triangledown}{T} + (trD)T - TL^{\mathrm{T}} + (WT' - T'W) + (S_r p^w)^\bullet I + [(1-S_r)p^a]^\bullet I$$ (4.2.56)

or

$$\dot{\Pi} = \overset{\circ}{T} + (trD)T - TL^{\mathrm{T}} + (\Omega T' - T'\Omega) + (S_r p^w)^\bullet I + [(1-S_r)p^a]^\bullet I$$ (4.2.57)

where, $W = \dfrac{1}{2}(L - L^T)$, is spin tensor, $\Omega = \dot{R}R^T$, is rigid body spin tensor. $[\ ]^\bullet$ means the material derivation.

The first item of Eq.(4.2.52) can be rewritten as

$$\int_V \Delta t \dot{\Pi} \delta L dV = \int_V \Delta t \left\{ \overset{\triangledown}{T} + (trD)T - TL^{\mathrm{T}} + (WT' - T'W) + (S_r p^w)^\bullet I + [(1-S_r)p^a]^\bullet I \right\} \delta L dV$$

$$= \Delta t \int_V \overset{\triangledown}{T} \delta D dV + \Delta t \int_V \left\{ (trD)T - TL^{\mathrm{T}} \right\} \delta L dV + \Delta t \int_V (WT' - T'W) \delta L dV$$

$$+ \Delta t \int_V [S_r \dot{p}^w I + (1-S_r)\dot{p}^a I] \delta L dV$$

(4.2.58)

or

$$\int_V \Delta t \dot{\Pi} \delta L dV = \Delta t \int_V \left\{ \overset{\circ}{T} + (trD)T - TL^{\mathrm{T}} + (\Omega T' - T'\Omega) + (S_r p^w)^\bullet I + [(1-S_r)p^a]^\bullet I \right\} \delta L dV$$

$$= \Delta t \int_V \overset{\circ}{T} \delta D dV + \Delta t \int_V \left\{ (trD)T - TL^{\mathrm{T}} \right\} \delta L dV + \Delta t \int_V (\Omega T' - T'\Omega) \delta L dV$$

$$+ \Delta t \int_V [S_r \dot{p}^w I + (1-S_r)\dot{p}^a I] \delta L dV$$

(4.2.59)

We use different shape function for displacement and pore pressure (water and air) in FEM discretization. The variables of displacement are given at the nodes and the variables of pore pressure are given at the gravitational center and denoted as p_{dE}^w and p_{dE}^a respectively.

$\vec{u}_N$ is the nodal displacement velocity vector of all nodes in one element. The displacement velocity vector (virtual displacement vector) of any arbitrary point within this element, $\vec{u}^s$ ($\delta \vec{u}^s$), can be expressed by the nodal displacement vector of $\vec{u}_N$

$$\vec{u}^s = [N]\vec{u}_N \quad , \quad \delta\vec{u}^s = [N]\delta\vec{u}_N \tag{4.2.60}$$

where, $[N] = \begin{bmatrix} N_1 & 0 & 0 & N_i & 0 & 0 & N_n & 0 & 0 \\ 0 & N_1 & 0 \dots 0 & N_i & 0 \dots 0 & N_n & 0 \\ 0 & 0 & N_1 & 0 & 0 & N_i & 0 & 0 & N_n \end{bmatrix}$, $[N_i]$ is shape function. n

is the number of nodes in one element. The strain rate vector of any arbitrary point within an element can be written as,

$$\vec{D} = [L]\vec{u}^s = [L][N]\vec{u}_N = [B]\vec{u}_N \tag{4.2.61}$$

$$tr\,\boldsymbol{D} = [M][L][N]\vec{u}_N = \vec{B}_v^T\vec{u}_N = \vec{u}_N^T\vec{B}_v \tag{4.2.62}$$

The velocity gradient vector of any arbitrary point within an element can be changed to vector form

$$\vec{L} = [B_{NL}]\vec{u}_N \tag{4.2.63}$$

where, $[M] = \begin{bmatrix} 1 & 0 & 0 & 0_{1\times3} \\ 0 & 1 & 0 & 0_{1\times3} \\ 0 & 0 & 1 & 0_{1\times3} \\ 0_{3\times1} & 0_{3\times1} & 0_{3\times1} & 0_{3\times3} \end{bmatrix}$, $[L] = \begin{bmatrix} \partial/\partial x & 0 & 0 \\ 0 & \partial/\partial y & 0 \\ 0 & 0 & \partial/\partial z \\ \partial/\partial y & \partial/\partial x & 0 \\ 0 & \partial/\partial z & \partial/\partial y \\ \partial/\partial z & & \partial/\partial x \end{bmatrix}$,

$[B_i] = \begin{bmatrix} \partial N_i/\partial x & 0 & 0 \\ 0 & \partial N_i/\partial y & 0 \\ 0 & 0 & \partial N_i/\partial z \\ \partial N_i/\partial y & \partial N_i/\partial x & 0 \\ 0 & \partial N_i/\partial z & \partial N_i/\partial y \\ \partial N_i/\partial z & 0 & \partial N_i/\partial x \end{bmatrix}$, $[B_{NL}] = \begin{bmatrix} \partial N_i/\partial x & 0 & 0 \\ 0 & \partial N_i/\partial y & 0 \\ 0 & 0 & \partial N_i/\partial z \\ \partial N_i/\partial y & 0 & 0 \\ 0 & \partial N_i/\partial x & 0 \\ 0 & \partial N_i/\partial z & 0 \\ 0 & 0 & \partial N_i/\partial y \\ 0 & 0 & \partial N_i/\partial x \\ \partial N_i/\partial z & 0 & 0 \end{bmatrix}$ and

$$[B] = [B_1 \cdots B_i \cdots B_n].$$

On the one hand, the constitutive model for unsaturated soil used with the vector form can be written as (here, take constitutive model for unsaturated soil for example, referred to Chapter 3)

$$\overset{\triangledown}{\boldsymbol{T}} = \left[D\right]^{ep}\left[B\right]\Delta\vec{u}_N - E^{RFS}\Delta\dot{S}_r - \alpha_T^s\left[D\right]^{ep}\left[M\right]\left[N\right]\Delta\vec{T}_N$$

or $$\overset{\circ}{\boldsymbol{T}} = \left[D\right]^{ep}\left[B\right]\Delta\vec{u}_N - E^{RFS}\Delta\dot{S}_r - \alpha_T^s\left[D\right]^{ep}\left[M\right]\left[N\right]\Delta\vec{T}_N \tag{4.2.64}$$

where, $E^{RFS} = \dfrac{1}{C_p}\dfrac{Q}{1+e_0}\dfrac{1}{\tilde{D}}\left[D\right]^e\dfrac{\partial f}{\partial\sigma}$, $\left[D\right]^e$ and $\left[D\right]^{ep}$ are the elastic matrix stiffness and elasto-plastic matrix stiffness respectively (Zhang and Ikariya, 2011). α_T^s is the linear thermal expansion of soil. $\left[M\right]^T = (1,1,1,0,0,0)$, $\Delta\vec{T}_N = \vec{T}_{N|t+\Delta t} - \vec{T}_{N|t}$ is the matrix of the nodal incremental temperature.

(a) *Jaumann stress rate tensor*

Expressing the items in Eq.(4.2.58) with vector form (detailed derivation can be referred to Appendix 1), we have

$$\int_V \Delta t \dot{\boldsymbol{\Pi}}\,\delta\boldsymbol{L}dV = \Delta t\int_V \overset{\triangledown}{\boldsymbol{T}}\,\delta\boldsymbol{D}dV + \Delta t\int_V \left\{(tr\boldsymbol{D})\boldsymbol{T} - \boldsymbol{T}\boldsymbol{L}^{\mathrm{T}} + \boldsymbol{W}\,\boldsymbol{T}' - \boldsymbol{T}'\boldsymbol{W}\right\}\delta\boldsymbol{L}dV$$

$$+\Delta t\int_V \left\{(S_r p^w)^{\bullet}\boldsymbol{I} + [(1-S_r)p^a]^{\bullet}\boldsymbol{I}\right\}\delta\boldsymbol{L}dV$$

$$= \Delta t\int_V \delta\vec{u}_N^{\ T}[B]^T[D^{ep}][B]\vec{u}_N dV - \Delta t\int_V \delta\vec{u}_N^{\ T}[B]^T\vec{E}^{RFS}dV\,\Delta\dot{S}_r + \Delta t\int_V \delta\vec{u}_N^{\ T}[B_{NL}]^T[T^*][B_{NL}]\vec{u}_N dV$$

$$-(\Delta t\alpha_T^s\int_V \delta\vec{u}_N^{\ T}[B]^T[D]^{ep}[M][N]dV)\Delta\vec{T}_N + \Delta t\int_V \delta\vec{u}_N^{\ T}\vec{B}_v\left\{(S_r p^w)^{\bullet} + [(1-S_r)p^a]^{\bullet}\right\}dV$$

$$\tag{4.2.65}$$

Moreover, the following items can be easily obtained

$$\int_V \rho\Delta\boldsymbol{b}\delta\dot{\boldsymbol{u}}^s dV = \int_V \delta\vec{u}_N[N]^T\rho\Delta\vec{b}dV \tag{4.2.66}$$

$$\int_S \Delta\boldsymbol{q}\delta\dot{\boldsymbol{u}}^s dS = \int_S \delta\vec{u}_N[N]^T\Delta\vec{q}\,dS \tag{4.2.67}$$

Substituting Eqs.(4.2.64) ~ (4.2.67) into Eq.(4.2.52), and because the virtual displacement velocity is arbitrary and pore pressure is taken as a constant value within one element in discretization, the following equation can be obtained with vector form

$$\Delta t \int_V [B]^T [D^{ep}][B]\vec{u}_N dV - \Delta t \int_V [B]^T \vec{E}^{RFS} dV \, \Delta \dot{S}_r + \Delta t \int_V [B_{NL}]^T [T^*][B_{NL}]\vec{u}_N dV$$

$$+ \Delta t \int_V \vec{B}_v dV \left\{ (S_r p_{dE}^w)^\bullet + [(1-S_r) p_{dE}^a]^\bullet \right\}$$

$$= \int_V \rho[N]^T \Delta \vec{b} dV + \int_S [N]^T \Delta \vec{q} dS + (\Delta t \alpha_T^s \int_V [B]^T [D]^{ep} [M][N] dV)\Delta \vec{T}_N \qquad (4.2.68)$$

In nonlinear FEM analysis, it is necessary to do incremental calculation so that the above equation is changed to incremental form

$$\int_V [B]^T [D^{ep}][B]\Delta \vec{u}_N dV - \int_V [B]^T \vec{E}^{RFS} dV \, \Delta S_r + \int_V [B_{NL}]^T [T^*][B_{NL}]\Delta \vec{u}_N dV$$

$$+ \int_V \vec{B}_v dV \left\{ \Delta(S_r p_{dE}^w) + \Delta\left[(1-S_r) p_{dE}^a \right] \right\} \qquad (4.2.69)$$

$$= \int_V \rho[N]^T \Delta \vec{b} dV + \int_S [N]^T \Delta \vec{q} dS + (\alpha_T^s \int_V [B]^T [D]^{ep} [M][N] dV)\Delta \vec{T}_N$$

By defining the following equations

$$\Delta \vec{F} = \int_V \rho[N]^T \Delta \vec{b} dV + \int_S [N]^T \Delta \vec{q} dS \qquad (4.2.70)$$

$$[K] = \int_V [B]^T [D]^{ep} [B] dV + \int_V B_{NL}]^T [T^*][B_{NL}] dV \qquad (4.2.71)$$

$$\vec{K}_{Sat} = \int_V [B]^T \vec{E}^{RFS} dV \qquad (4.2.72)$$

$$\vec{K}_v = \int_V \vec{B}_v dV \qquad (4.2.73)$$

$$\vec{F}_T = \alpha_T^s \int_V [B]^T [D]^{ep} [M][N] dV \qquad (4.2.74)$$

(b) *Green-Naghdi stress rate tensor*

Expressing the items in Equation (4.2.59) with vector form (detailed derivation can be referred to Appendix 1 and 2), we have

$$\int_V \Delta t \dot{\boldsymbol{\Pi}} \delta \boldsymbol{L} dV = \Delta t \int_V \overset{\circ}{\boldsymbol{T}} \delta \boldsymbol{D} dV + \Delta t \int_V [(tr\boldsymbol{D})\boldsymbol{T} - \boldsymbol{T}\boldsymbol{L}^{\mathrm{T}}] \delta \boldsymbol{L} dV + \Delta t \int_V (\boldsymbol{\Omega} \boldsymbol{T}' - \boldsymbol{T}'\boldsymbol{\Omega}) \delta \boldsymbol{D} dV$$

$$+ \Delta t \int_V \left\{ (S_r p^w)^\bullet \boldsymbol{I} + [(1 - S_r) p^a]^\bullet \boldsymbol{I} \right\} \delta \boldsymbol{L} dV$$

$$= \Delta t \int_V \delta \vec{u}_N^{\ T} [B]^T [D^{ep}] [B] \vec{u}_N dV - \Delta t \int_V \delta \vec{u}_N^{\ T} [B]^T \vec{E}^{RFS} dV \Delta \dot{S}_r + \Delta t \int_V \delta \vec{u}_N^{\ T} [B_{NL}]^T [T^{**}] [B_{NL}] \vec{u}_N dV$$

$$+ \Delta t \int_V \delta \vec{u}_N^{\ T} [B]^T [T_\Omega] dV + \Delta t \int_V \delta \vec{u}_N^{\ T} \vec{B}_v \left\{ (S_r p^w)^\bullet + [(1 - S_r) p^a]^\bullet \right\} dV$$

$$- (\Delta t \alpha_T^s \int_V \delta \vec{u}_N^{\ T} [B]^T [D]^{ep} [M] [N] dV) \Delta \vec{T}_N$$

$$(4.2.75)$$

Substituting Eqs.(4.2.64), (4.2.66) (4.2.67) into Eq.(4.2.52), the following equation with incremental form can be obtained:

$$\int_V [B]^T [D^{ep}] [B] \Delta \vec{u}_N dV - \int_V [B]^T \vec{E}^{RFS} dV \Delta S_r + \int_V [B_{NL}]^T [T^{**}] [B_{NL}] \Delta \vec{u}_N dV$$

$$+ \int_V \vec{B}_v dV \left\{ \Delta (S_r p_{dE}^w) + \Delta [(1 - S_r) p_{dE}^a] \right\} = \int_V \rho [N]^T \Delta \vec{b} dV + \int_S [N]^T \Delta \vec{q} dS \qquad (4.2.76)$$

$$- \Delta t \int_V [B]^T [T_\Omega'] dV + (\alpha_T^s \int_V [B]^T [D]^{ep} [M] [N] dV) \Delta \vec{T}_N$$

By defining the following equations

$$\Delta \vec{F} = \int_V \rho [N]^T \Delta \vec{b} dV + \int_S [N]^T \Delta \vec{q} dS - \Delta t \int_V [B]^T [T_\Omega'] dV$$

$$(4.2.77)$$

$$[K] = \int_V [B]^T [D]^{ep} [B] dV + \int_V [B_{NL}]^T [T^{**}] [B_{NL}] dV \qquad (4.2.78)$$

Eq. (4.2.69) or (4.2.76) can be rewritten as

$$[K] \Delta \vec{u}_N - \vec{K}_{Sat} \Delta S_r + \vec{K}_v \Delta (S_r p_{dE}^w) + \vec{K}_v \Delta [(1 - S_r) p_{dE}^a] = \Delta \vec{F} + \vec{F}_T \Delta \vec{T}_N \qquad (4.2.79)$$

The incremental forms of $\Delta(S_r p_{dE}^w)$ and $\Delta[(1 - S_r) p_{dE}^a]$ are approximated as

$$\Delta(S_r p_{dE}^w) = \Delta S_r p_{dE}^w + S_r \Delta p_{dE}^w = \Delta S_{r|t+\Delta t} p_{dE|t}^w + S_{r|t} \Delta p_{dE|t+\Delta t}^w \qquad (4.2.80)$$

$$\Delta[(1 - S_r) p_{dE}^a] = \Delta(1 - S_r) p_{dE}^a + (1 - S_r) \Delta p_{dE}^a = (1 - S_{r|t}) \Delta p_{dE|t+\Delta t}^a - \Delta S_{r|t+\Delta t} p_{dE|t}^a \qquad (4.2.81)$$

$$\Delta S_{r|t+\Delta t} = S_{r|t+\Delta t} - S_{r|t} \qquad (4.2.82)$$

where, $t + \Delta t$ is the current time.

On the other hand, in the work by Zhang and Ikariya (2011), a new moisture characteristics curve (MCC) is also proposed, where the relationship between the incremental suction and saturation is expressed as

$$\Delta S_{r|t+\Delta t} = k_s^{-1} \Delta s_{|t+\Delta t} \tag{4.2.83}$$

$$\begin{aligned}
\Delta s_{|t+\Delta t} &= (p_{dE|t+\Delta t}^a - p_{dE|t+\Delta t}^w) - (p_{dE|t}^a - p_{dE|t}^w) \\
&= (p_{dE|t+\Delta t}^a - p_{dE|t}^a) - (p_{dE|t+\Delta t}^w - p_{dE|t}^w) = \Delta p_{dE|t+\Delta t}^a - \Delta p_{dE|t+\Delta t}^w
\end{aligned} \tag{4.2.84}$$

where, k_s^{-1} is the stiffness of saturation-suction relation.

Substituting Eq. (4.2.80)~ (4.2.84) into Eq. (4.2.79), the equilibrium equation discretized in space and time can be obtained

$$\begin{aligned}
&[K]\Delta\vec{u}_{N|t+\Delta t} + \{\vec{K}_v S_{r|t} - (\vec{K}_v p_{dE|t}^w - \vec{K}_v p_{dE|t}^a - \vec{K}_{Sat})k_s^{-1}\} p_{dE|t+\Delta t}^w \\
&+ \{(1 - S_{r|t})\vec{K}_v + (\vec{K}_v p_{dE|t}^w - \vec{K}_v p_{dE|t}^a - \vec{K}_{Sat})k_s^{-1}\} p_{dE|t+\Delta t}^a \\
&= \Delta\vec{F}_{|t+\Delta t} + \vec{F}_T \Delta\vec{T}_{N|t+\Delta t} + \{\vec{K}_v S_{r|t} - (\vec{K}_v p_{dE|t}^w - \vec{K}_v p_{dE|t}^a - \vec{K}_{Sat})k_s^{-1}\} p_{dE|t}^w \\
&+ \{(1 - S_{r|t})\vec{K}_v + (\vec{K}_v p_{dE|t}^w - \vec{K}_v p_{dE|t}^a - \vec{K}_{Sat})k_s^{-1}\} p_{dE|t}^a
\end{aligned} \tag{4.2.85}$$

By defining the following equation

$$\vec{I}_{Sat}^w = \vec{K}_v S_{r|t} - (\vec{K}_v p_{dE|t}^w - \vec{K}_v p_{dE|t}^a - \vec{K}_{Sat})k_s^{-1} \tag{4.2.86}$$

$$\vec{I}_{Sat}^a = (1 - S_{r|t})\vec{K}_v + (\vec{K}_v p_{dE|t}^w - \vec{K}_v p_{dE|t}^a - \vec{K}_{Sat})k_s^{-1} \tag{4.2.87}$$

Finally Eq.(4.2.85) can be rewritten as

$$[K]\Delta\vec{u}_{N|t+\Delta t} + \vec{I}_{Sat}^w p_{dE|t+\Delta t}^w + \vec{I}_{Sat}^a p_{dE|t+\Delta t}^a = \Delta\vec{F}_{|t+\Delta t} + \vec{F}_T \Delta\vec{T}_{N|t+\Delta t} + \vec{I}_{Sat}^w p_{dE|t}^w + \vec{I}_{Sat}^a p_{dE|t}^a \tag{4.2.88}$$

4.2.6 Discretization of continuum equation of water phase in space and time

The discretization of continuum equation of water phase can be implemented by the same way used in last section.

From Eq.(4.2.62), it can be known that

$$tr\boldsymbol{D} = \vec{B}_v^T \cdot \vec{u}_N \tag{4.2.89}$$

By using Eq.(4.2.89), the integration of Eq.(4.2.32) in region v with the vector

form leads to the following equation

$$\int_V \frac{\gamma^w}{nk^w} \vec{B}_v^T \cdot \vec{u}_N dV - \int_V \frac{\partial^2 p_{dE}^w}{\partial x_i \partial x_i} dV - \int_V \frac{\gamma^w}{k^w K^w} \dot{p}_{dE}^w dV - \int_V \frac{3\gamma^w \alpha_T^w}{k^w}[N]dV\vec{\dot{T}}_N + \int_V \frac{\gamma^w}{k^w S_r} \dot{S}_r dV = 0$$

$$(4.2.90)$$

Because the excessive pore water pressure has been assumed be constant within an element, Eq.(4.2.90) can be rewritten as

$$\int_V \frac{\gamma^w}{nk^w} \vec{B}_v^T \cdot \vec{u}_N dV - \int_V \frac{\partial^2 p_{dE}^w}{\partial x_i \partial x_i} dV - A\dot{p}_{dE}^w - [K_{WT}]\vec{\dot{T}}_N + \int_V \frac{\gamma^w}{k^w S_r} \dot{S}_r dV = 0$$

$$(4.2.91)$$

where, $A = \int_V \frac{\gamma^w}{k^w K^w} dV = \frac{\gamma^w}{k^w K^w} \bar{V}, \quad [K_{WT}] = \int_V \frac{3\gamma^w \alpha_T^w}{k^w}[N]dV$ (4.2.92)

$\bar{V}$ is the volume of region v. The volume integration of the second term on left side of the above equation can be calculated as following

$$\int_V \frac{\partial^2 p_{dE}^w}{\partial x_i \partial x_i} dV = \alpha p_{dE}^w - \sum_{i=1}^m \alpha_i p_{i|dE}^w$$

$$(4.2.93)$$

where, $\alpha = \sum_{i=1}^m \frac{A_i}{S_i}, \quad \alpha_i = \frac{A_i}{S_i}$ (4.2.94)

m is the number of element sides (e.g. m=4 for four-node element of two dimension) or element faces (e.g. m=6 for hexahedron element of three dimension), S_i is center-to center distance of an arbitrary element to its ith neighboring element, b_i is drainage area of an arbitrary element in edge i.

Because of static problem, the change of soil displacement, pore water pressure and degree of saturation can be calculated by finite difference method

$$\vec{\dot{u}}_N = \frac{\Delta \vec{u}_{N|t+\Delta t}}{\Delta t} = \frac{\vec{u}_{N|t+\Delta t} - \vec{u}_{N|t}}{\Delta t}$$

$$(4.2.95)$$

$$\dot{p}_{dE}^w = \frac{\Delta p_{dE|t+\Delta t}^w}{\Delta t} = \frac{p_{dE|t+\Delta t}^w - p_{dE|t}^w}{\Delta t}$$

$$(4.2.96)$$

$$\dot{p}_{dE}^a = \frac{\Delta p_{dE|t+\Delta t}^a}{\Delta t} = \frac{p_{dE|t+\Delta t}^a - p_{dE|t}^a}{\Delta t}$$

$$(4.2.97)$$

$$\dot{S}_r = \frac{\Delta S_{r|t+\Delta t}}{\Delta t} = \frac{S_{r|t+\Delta t} - S_{r|t}}{\Delta t}$$

$$(4.2.98)$$

$$\vec{\dot{T}}_N = \frac{\Delta \vec{T}_{|t+\Delta t}}{\Delta t} = \frac{\vec{T}_{|t+\Delta t} - \vec{T}_{|t}}{\Delta t} \tag{4.2.99}$$

Substituting Eqs.(4.2.83), (4.2.84), (4.2.89), (4.2.92)~(4.2.93), (4.2.95) ~(4.2.99) into Eq.(4.2.91), the following equation can be obtained

$$S_{r|t} \vec{K}_v^T \cdot \Delta \vec{u}_{N|t+\Delta t} - \left[\frac{k^w \Delta t}{\gamma^w} nS_{r|t} \alpha + \frac{k^w}{\gamma^w} \left(nS_{r|t} A + \frac{\gamma^w}{k^w} n\overline{V} k_s^{-1} \right) \right] p_{dE|t+\Delta t}^w + n\overline{V} k_s^{-1} p_{dE|t+\Delta t}^a$$

$$+ \sum_{i=1}^{m} \frac{k^w \Delta t}{\gamma^w} n\alpha_i S_{r|t} p_{idE|t+\Delta t}^w = \frac{k^w}{\gamma^w} (AnS_{r|t} - \frac{\gamma^w}{k^w} n\overline{V} k_s^{-1}) p_{dE|t}^w + n\overline{V} k_s^{-1} p_{dE|t}^a + \left[K_{WT} \right] \Delta \vec{T}_{N|t+\Delta t}$$

$$\tag{4.2.100}$$

By defining the following equations

$$\overline{\alpha} = \frac{nS_{r|t} \Delta t k^w}{\gamma^w} \alpha \tag{4.2.101}$$

$$\overline{\alpha}_i = \frac{nS_{r|t} \Delta t k^w}{\gamma^w} \alpha_i \tag{4.2.102}$$

$$\overline{A} = \frac{nS_{r|t} k^w}{\gamma^w} A \tag{4.2.103}$$

$$F_{sr} = n\overline{V} k_s^{-1} \tag{4.2.104}$$

$$\left[\overline{K}_{WT} \right] = \frac{nk^w S_r}{\gamma^w} \left[K_{WT} \right] = \frac{nk^w S_r}{\gamma^w} \int_V \frac{3\gamma^w \alpha_T^w}{k^w} [N] dV = 3nS_r \alpha_T^w \int_V [N] dV \tag{4.2.105}$$

Substituting Eqs.(4.2.101)~(4.2.105) into Eq.(4.2.91), the discretization of continuum equation of water phase in space and time can be written as

$$S_{r|t} \vec{K}_v^T \cdot \Delta \vec{u}_{N|t+\Delta t} - \left[\overline{\alpha} + \overline{A} + F_{sr} \right] p_{dE|t+\Delta t}^w + F_{sr} p_{dE|t+\Delta t}^a + \sum_{i=1}^{m} \overline{\alpha}_i p_{idE|t+\Delta t}^w$$

$$= -[\overline{A} + F_{sr}] p_{dE|t}^w + F_{sr} p_{dE|t}^a + \left[\overline{K}_{WT} \right] \Delta \vec{T}_{N|t+\Delta t} \tag{4.2.106}$$

or

$$S_{r|t} \vec{K}_v^T \cdot \Delta \vec{u}_{N|t+\Delta t} - \left[\overline{\alpha} + \overline{A} + F_{sr} \right] \gamma^w h_{|t+\Delta}^w + F_{sr} p_{dE|t+\Delta t}^a + \sum_{i=1}^{m} \overline{\alpha}_i \gamma^w h_{i|t+\Delta t}^w$$

$$= -[\overline{A} + F_{sr}] \gamma^w h_{|t}^w + F_{sr} p_{dE|t}^a + \left[\overline{K}_{WT} \right] \Delta \vec{T}_{N|t+\Delta t} \tag{4.2.107}$$

4.2.7 Discretization of continuum equation of air phase in space and time

The discretization of continuum equation of air phase can be implemented by the same way as water phase.

Integration of Eq.(4.2.38) in region **V** with the vector form can be written as

$$\int_V \frac{\gamma^a}{nk^a} \vec{B}_v^T \cdot \vec{u}_N dV - \int_V \frac{\partial^2 p_{dE}^a}{\partial x_i \partial x_i} dV - \int_V \frac{\gamma^a}{k^a K^a} \dot{p}_{dE}^a dV - \int_V \frac{3\gamma^a \alpha_T^a}{k^a} [N] dV \vec{\dot{T}}_N - \int_V \frac{\gamma^a}{k^a(1-S_r)} \dot{S}_r dV = 0$$

(4.2.108)

Because the pore air pressure is also assumed to be constant within an element, Eq.(4.2.108) can be rewritten as

$$\int_V \frac{\gamma^a}{nk^a} \vec{B}_v^T \cdot \vec{u}_N dV - \int_V \frac{\partial^2 p_{dE}^a}{\partial x_i \partial x_i} dV - B\dot{p}_{dE}^a - [K_{AT}]\vec{\dot{T}}_N - \int_V \frac{\gamma^a}{k^a(1-S_r)} \dot{S}_r dV = 0 \qquad (4.2.109)$$

where, $\quad B = \int_V \frac{\gamma^a}{k^a K^a} dV = \frac{\gamma^a}{k^a K^a} \overline{V}, \quad [K_{AT}] = \int_V \frac{3\gamma^a \alpha_T^a}{k^a} [N] dV \qquad (4.2.110)$

The volume integration of the second term on left side of the above equation can also be calculated by the same way as water phase

$$\int_V \frac{\partial^2 p_{dE}^a}{\partial x_i \partial x_i} dV = \alpha p_{dE}^a - \sum_{i=1}^m \alpha_i p_{i|dE}^a \qquad (4.2.111)$$

Substituting Eqs.(4.2.83), (4.2.84), (4.2.89), (4.2.95)~ (4.2.99) and (4.2.110) ~(4.2.111) into Eq.(4.2.109), the following equation can be obtained

$$(1-S_{r|t})\vec{K}_v^T \cdot \Delta\vec{u}_{N|t+\Delta t} + n\overline{V}k_s^{-1} p_{dE|t+\Delta t}^w + \sum_{i=1}^m \frac{k^a \Delta t}{\gamma^a} n\alpha_i (1-S_{r|t}) p_{idE|t+\Delta t}^a$$

$$- \left[\frac{k^a \cdot \Delta t}{\gamma^a} n(1-S_{r|t})\alpha + \frac{k^a}{\gamma^a} [n(1-S_{r|t})B + \frac{\gamma^a}{k^a} n\overline{V}k_s^{-1}] \right] p_{dE|t+\Delta t}^a \qquad (4.2.112)$$

$$= -\frac{k^a}{\gamma^a}[n(1-S_{r|t})B + \frac{\gamma^a}{k^a} n\overline{V}k_s^{-1}]p_{dE|t}^a + n\overline{V}k_s^{-1} p_{dE|t}^w + \frac{nk^a}{\gamma^a}[K_{AT}]\Delta\vec{T}_{N|t+\Delta t}$$

By defining the following equations

$$\bar{\beta} = \frac{n(1-S_{r|t})\Delta t k^a}{\gamma^a}\alpha \tag{4.2.113}$$

$$\bar{\beta}_i = \frac{n(1-S_{r|t})\Delta t k^a}{\gamma^a}\alpha_i \tag{4.2.114}$$

$$\bar{B} = \frac{n(1-S_{r|t})k^a}{\gamma^a}B \tag{4.2.115}$$

$$\left[\bar{K}_{AT}\right] = \frac{nk^a}{\gamma^a}\left[K_{AT}\right] = \frac{nk^a}{\gamma^a}\int_V \frac{3\gamma^a\alpha_T^a}{k^a}\left[N\right]dV = 3n(1-S_r)\alpha_T^a\int_v\left[N\right]dv \tag{4.2.116}$$

Substituting Eqs.(4.2.113), (4.2.114), (4.2.115) and (4.2.116) into Eq.(4.2.112), the discretization of continuum equation of air phase in space and time can be written as

$$(1-S_{r|t})\vec{K}_v^T \cdot \Delta\vec{u}_{N|t+\Delta t} + F_{sr}p_{dE|t+\Delta t}^w - \left[\bar{\beta}+\bar{B}+F_{sr}\right]p_{dE|t+\Delta t}^a + \sum_{i=1}^m \bar{\beta}_i p_{idE|t+\Delta t}^a$$
$$= F_{sr}p_{dE|t}^w - [\bar{B}+F_{sr}]p_{dE|t}^a + \left[\bar{K}_{AT}\right]\Delta\vec{T}_{N|t+\Delta t} \tag{4.2.117}$$

or,

$$(1-S_{r|t})\vec{K}_v^T \cdot \Delta\vec{u}_{N|t+\Delta t} + F_{sr}\gamma^w h_{|t+\Delta t}^w - \left[\bar{\beta}+\bar{B}+F_{sr}\right]p_{dE|t+\Delta t}^a + \sum_{i=1}^m \bar{\beta}_i p_{idE|t+\Delta t}^a$$
$$= F_{sr}\gamma^w h_{|t}^w - [\bar{B}+F_{sr}]p_{dE|t}^a + \left[\bar{K}_{AT}\right]\Delta\vec{T}_{N|t+\Delta t} \tag{4.2.118}$$

4.2.8 Discretization of continuum equation of air phase in space and time

Basing on the Galerkin law, the energy conservation equation will be discretized in space for adopting into the FEM.

At any arbitrary time t, the temperature $T(x,y,z,t)$ of any arbitrary point within any arbitrary element can be expressed by the nodal temperatures of this element. So, the temperature can be written as:

$$T = [N]\vec{T}_N \tag{4.2.119}$$

where, $[N]$ is the shape function matrix, $\vec{T}_N$ is the matrix of nodal temperatures at a arbitrary time within an element. By using the Galerkin law, the energy conservation Eq.(4.2.45) in any arbitrary element can be expressed as:

$$\int_V [N]^T \left(\overline{k}_t \frac{\partial^2 T}{\partial x_i \partial x_i} + E - \overline{\rho c} \frac{\partial T}{\partial t} - nS_r(\rho c)^w v_i^w \frac{\partial T}{\partial x_i}) - n(1-S_r)(\rho c)^a v_i^a \frac{\partial T}{\partial x_i}) \right) dV = 0 \quad (4.2.120)$$

Basing on the Green-Gauss theorem:

$$\int_V \overline{k}_t [N]^T \frac{\partial^2 T}{\partial x_i \partial x_i} dV = -\int_V \overline{k}_t \frac{\partial [N]^T}{\partial x_i} \frac{\partial T}{\partial x_i} dV + \int_S \overline{k}_t [N]^T \frac{\partial T}{\partial n} dS \qquad (4.2.121)$$

where, V is region of the element; S is boundary surface of the element; $\frac{\partial}{\partial n}$ is the partial differentiation of the surface's outward normal direction.

Basing on Fourier's law and substituting Eq.(4.2.119) into the right side of Eq.(4.2.121), it can be rewritten as:

$$-\int_V \overline{k}_t \frac{\partial [N]^T}{\partial x_i} \frac{\partial T}{\partial x_i} dV + \int_S \overline{k}_t [N]^T \frac{\partial T}{\partial n} dS$$
$$= -\int_V \overline{k}_t \frac{\partial [N]^T}{\partial x_i} \frac{\partial [N]}{\partial x_i} dV \vec{T}_N - \int_S q[N]^T dS \qquad (4.2.122)$$

Then, by substituting Eqs.(4.2.119) and (4.2.122) into Eq.(4.2.120), it can be expressed as:

$$\int_V \overline{k}_t \frac{\partial [N]^T}{\partial x_i} \frac{\partial [N]}{\partial x_i} dV \vec{T}_N + \int_S q[N]^T dS - \int_V [N]^T E dV$$
$$+ \int_V \overline{\rho c} [N]^T [N] dV \dot{\vec{T}}_N + \int_V nS_r(\rho c)^w v_i^w [N]^T \frac{\partial [N]}{\partial x_i} \cdot dV T_N \qquad (4.2.123)$$
$$+ \int_V n(1-S_r)(\rho c)^a v_i^a [N]^T \frac{\partial [N]}{\partial x_i} \cdot dV \vec{T}_N = 0$$

By defining the equations as following:

$$[C^t] = \iiint \overline{\rho c} [N]^T [N] dV \qquad (4.2.124)$$

$$
\left[K^t\right] = \int_V \bar{k}_t \frac{\partial[N]^T}{\partial x_i} \frac{\partial[N]}{\partial x_i} dV + \int_V n S_r (\rho c)^w v_i^w [N]^T \frac{\partial[N]}{\partial x_i} dV
$$
$$
+ \int_V n(1 - S_r)(\rho c)^a v_i^a [N]^T \frac{\partial[N]}{\partial x_i} dV
$$

(4.2.125)

$$
[f^t] = \int_V [N]^T E dV - \int_S q [N]^T dS
$$

(4.2.126)

Therefore, Eq.(4.2.123) can be rewritten as:

$$
\left[C^t\right] \vec{\dot{T}}_N + \left[K^t\right] \vec{T}_N = \left[f^t\right]
$$

(4.2.127)

In this section, the Newmark method will be used for discretization of the energy conservation equation in time. The current time is denoted as $t+\varDelta t$ in derivation, Eq.(4.2.127) can be written as:

$$
\left[C^t\right] \vec{\dot{T}}_{N|t+\Delta t} + \left[K^t\right] \vec{T}_{N|t+\Delta t} = \left[f^t\right]
$$

(4.2.128)

According to the Newmark method and the intermediate value theorem, the temperature of current time can be expressed as:

$$
\vec{T}_{N|t+\Delta t} = \vec{T}_{N|t} + \Delta t \vec{\dot{T}}_{N|t} + \beta \Delta t \left(\vec{\dot{T}}_{N|t+\Delta t} - \vec{\dot{T}}_{N|t} \right)
$$

(4.2.129)

where, $\varDelta t$ is the time increment; β is a parameter with a value $0 \leq \beta \leq 1$. When the parameter β is equal to or greater than 0.5, iteration calculation will always be convergent.

By substituting Eq.(4.2.129) into Eq.(4.2.128), the energy conservation discretized in space and time can be obtained:

$$
\left(\left[C^t\right] + \beta \Delta t \left[K^t\right] \right) \vec{\dot{T}}_{N|t+\Delta t} = \left[f^t\right] - \left[K^t\right] \left(\vec{T}_{N|t} + (1 - \beta) \Delta t \vec{\dot{T}}_{N|t} \right)
$$

(4.2.130)

Combining Eqs.(4.2.85), (4.2.106), (4.2.117) and (4.2.130), the THMA FE-FD formulation for static analysis can be obtained

$$
\begin{bmatrix}
[K] & \vec{I}_{Sat}^{w} & \vec{I}_{Sat}^{a} \\
S_r \vec{K}_v^{T} & -\left[\bar{\alpha} + \bar{A} + F_{sr}\right] & F_{sr} \\
(1-S_r)\vec{K}_v^{T} & F_{sr} & -\left[\bar{\beta} + \bar{B} + F_{sr}\right]
\end{bmatrix}
\begin{Bmatrix}
\Delta\vec{u}_{N|t+\Delta t} \\
p_{dE|t+\Delta t}^{w} \\
p_{dE|t+\Delta t}^{a}
\end{Bmatrix}
+
\begin{Bmatrix}
0 \\
\sum_{i=1}^{m}\bar{\alpha}_i p_{idE|t+\Delta t}^{w} \\
\sum_{i=1}^{m}\bar{\beta}_i p_{idE|t+\Delta t}^{a}
\end{Bmatrix}
\quad (4.2.131)
$$

$$
=
\begin{bmatrix}
\Delta\vec{F}_{|t+\Delta t} + \vec{F}_T\Delta\vec{T}_{N|t+\Delta t} + \vec{I}_{Sat}^{w}p_{dE|t}^{w} + \vec{I}_{Sat}^{a}p_{dE|t}^{a} \\
-(\bar{A}+F_{sr})p_{dE|t}^{w} + F_{sr}p_{dE|t}^{a} + \left[\bar{K}_{WT}\right]\Delta\vec{T}_{N|t+\Delta t} \\
F_{sr}p_{dE|t}^{w} - (\bar{B}+F_{sr})p_{dE|t}^{a} + \left[\bar{K}_{AT}\right]\Delta\vec{T}_{N|t+\Delta t}
\end{bmatrix}
$$

$$
\left(\left[C^t\right] + \beta\Delta t\left[K^t\right]\right)\vec{T}_{N|t+\Delta t} = \left[f^t\right] - \left[K^t\right]\left(\vec{T}_{N|t} + (1-\beta)\Delta t\dot{\vec{T}}_{N|t}\right) \quad (4.2.130)
$$

Because the water head is conveniently used as the unknown in the FEM program, and the following relation holds:

$$
p_d^{w} = \gamma_w h_d^{w} \quad (h^{w} = h_d^{w} + h_{ini}^{w}, \ p^{w} = p_d^{w} + p_{ini}^{w}, \quad h_{ini}^{w} \text{ is the initial water head})
$$

Finally, thermo-hydraulic-mechanical-air coupling FEM equation can be rewritten as

$$
\begin{bmatrix}
[K] & \gamma^{w}\vec{H}_{Sat}^{w} & \vec{H}_{Sat}^{a} \\
S_r \vec{K}_v^{T} & -\gamma^{w}\left[\bar{\alpha} + \bar{A} + F_{sr}\right] & F_{sr} \\
(1-S_r)\vec{K}_v^{T} & \gamma^{w}F_{sr} & -\left[\bar{\beta} + \bar{B} + F_{sr}\right]
\end{bmatrix}
\begin{Bmatrix}
\Delta\vec{u}_{N|t+\Delta t} \\
h_{dE|t+\Delta t}^{w} \\
p_{dE|t+\Delta t}^{a}
\end{Bmatrix}
+
\begin{Bmatrix}
0 \\
\sum_{i=1}^{m}\bar{\alpha}_i \gamma^{w} h_{idE|t+\Delta t}^{w} \\
\sum_{i=1}^{m}\bar{\beta}_i p_{idE|t+\Delta t}^{a}
\end{Bmatrix}
$$

$$
=
\begin{bmatrix}
\Delta\vec{F}_{|t+\Delta t} + \vec{F}_T\Delta\vec{T}_{N|t+\Delta t} + \gamma^{w}\vec{H}_{Sat}^{w}h_{dE|t}^{w} + \vec{H}_{Sat}^{a}p_{dE|t}^{a} \\
-(\bar{A}+F_{sr})\gamma^{w}h_{dE|t}^{w} + F_{sr}p_{dE|t}^{a} + \left[\bar{K}_{WT}\right]\Delta\vec{T}_{N|t+\Delta t} \\
F_{sr}\gamma^{w}h_{dE|t}^{w} - (\bar{B}+F_{sr})p_{dE|t}^{a} + \left[\bar{K}_{AT}\right]\Delta\vec{T}_{N|t+\Delta t}
\end{bmatrix}
$$

$$
(4.2.132)
$$

$$
\left(\left[C^t\right] + \beta\Delta t\left[K^t\right]\right)\vec{T}_{N|t+\Delta t} = \left[f^t\right] - \left[K^t\right]\left(\vec{T}_{N|t} + (1-\beta)\Delta t\dot{\vec{T}}_{N|t}\right) \quad (4.2.130)
$$

where,

$$
\vec{H}_{Sat}^{w} = \vec{K}_v S_{r|t} - (\vec{K}_v\gamma^{w}h_{dE|t}^{w} - \vec{K}_v p_{dE|t}^{a} - \vec{K}_{Sat})k_s^{-1}
\quad (4.2.133)
$$

$$
\vec{H}_{Sat}^{a} = (1-S_{r|t})\vec{K}_v + (\vec{K}_v\gamma^{w}h_{dE|t}^{w} - \vec{K}_v p_{dE|t}^{a} - \vec{K}_{Sat})k_s^{-1}
\quad (4.2.134)
$$

4.3 Conclusions

In this chapter, the theory of a thermo-hydraulic-mechanical-air coupling finite element method is derived in detail. In the field equations, the excessive pore water pressure, the excessive pore air pressure, the displacement of solid phase and the temperature are used as unknown variables. In the THMA FE-FD scheme, FEM is used for spatial discretization of the equilibrium and the energy conservation equations, while the backward finite difference scheme proposed by Akai and Tamura (1978) is used for the spatial discretization of the continuity equation. It is worth noting that the energy conservation is not fully coupled with mechanical behavior in the scheme, because the energy dissipation due to the plastic deformation, described by the constitutive model (Chapter 3), is not included in the above conservation equation, though it might be very small and can be neglected in engineering sense if compared with the heat energy produced by nuclear waste.

References

1) Akai K. and Tamura T. (1978): Numerical analysis of multi-dimensional consolidation accompanied with elasto-plastic constitutive equation, *Journal of Japanese Civil Engineering Society*, No. 269, 95-104 (in Japanese).

2) Borja R. (2005): Conservation laws for three-phase partially saturated granular media, *Unsaturated soils: numerical and theoretical approaches*, Vol. 94, 3-14

3) Li C, Borja R. and Regueiro R. (2004): Dynamics of porous media at finite strain, *Computer methods in applied mechanics and engineering*, Vol. 193, 3837-3870.

4) Oka F, Yashima A, Shimata T et al. (1994): FEM-FDM coupled liquefaction analysis of a porous soil using an elasto-plastic model, *Applied Scientific Research*, Vol. 52, 209-245.

5) Yatomi, C., Yashima, A., Iizuka, A. and Sano, I. (1989): General theory of shear bands formation by a non-coaxial Cam-clay model, Soils and Foundations, Vol. 29, No. 3, 41-53.

6) Ye, B. (2007): doctor dissertation, Department of Civil Engineering, Gifu University, Japan.

7) Uzuoka, et al. (2007): Finite element analysis for dynamic finite deformation in unsaturated soil, *Proceedings of the conference on computational engineering and science*, Vol.12, No.2, 523-526 (In Japanese).

8) Uzuoka, et al. (2008): Finite element analysis of coupled of unsaturated soil and water using aerial elements, *Proceedings of the conference on computational engineering and science*, Vol.13, No.1, 219-222 (In Japanese).

9) Uzuoka, et al. (2009): Soil-water-air coupled dynamic analysis of unsaturated fill, *Proceedings of the conference on computational engineering and science*, Vol.14, No.1, 461-464 (In Japanese).

10) Uzuoka, R., Effective stress analysis (Finite deformation scheme), private

discussion, Feb. 2, 2010 (In Japanese).

11) Zhang, F. and Ikariya. T. (2011): A new model for unsaturated soil using skeleton and degree of saturation as state variables, *Soil and Foundations*, Vol. 51, No. 1, 67-81.

12) Oka, F., Yashima, A., Shibata, T., and Kato, M. (1991): A finite element analysis of liquefaction of seabed due to wave action, GEO-COAST, 91, 621-626.

13) Ye, B., Yokawa, H., Kondo, T., Yashima, A., Zhang, F. and Yamada, H. (2006): Investigation on stiffness recovery of liquefied sandy ground after liquefaction using shaking-table tests, *Proc. of International Conference GeoShanghai2006*, Shanghai, China.

14) Sheng, D. (2011): Constitutive modelling of unsaturated soils: Discussion of fundamental principles. *Unsaturated Soils*, (E. E. Alonso and A. Gens, eds.), Barcelona, Spain, 1: pp. 91-112. CRC Press.

CHAPTER 5 THERMO-HYDRAULIC-MECHANICAL-AIR ANALYSIS ON SLOPE FAILURE IN UNSATURATED GROUND

5.1 General

Slope failure is always one of the greatest interesting topics to geotechnical researchers and engineers, not only because it may lead to tremendous disaster to human being and civil facilities, but also the difficulties to predict when and where the slope failure will occur in most cases. Generally speaking, slope failure is thought to be related to the shearing deformation due to excavation, cyclic drying-wetting process, and the decrease of effective stress due to the elevation of the groundwater table or heavy rainfall.

In a slope, groundwater table is usually below the ground surface and the pore water pressure (PWP) in the soil above the groundwater table is negative, or in other words, suction exists. This suction will enhance the stability of the slope in the unsaturated ground. With the infiltration of water from rainfall or the elevation of the groundwater table, the water seepage may cause a gradual loss of the suction in the unsaturated soil of the slope. The loss of suction consequently causes a decrease in effective stress, which may then give rise to a decrease of shear strength of the soil and sometimes may even cause a slope failure, a typical surface failure of a slope.

In order to investigate the mechanism of slope failure, some model experiments on slope failure due to rainfall had been done in the laboratory such as the works by Yagi et al. (1983), Kitamura et al. (2007), Tohari et al. (2007) and Maeda et al. (2012). In the work by Kitamura et al. (2007), model tests on slope failure with unsaturated Shirasu ground in different infiltration patterns were conducted. In the tests, the PWP at some selected points of slope was carefully measured by tensiometer and PWP sensor.

Meanwhile, many numerical analyses on the slope failure were also conducted in the past decades. Zhang et al. (2003) conducted a soil-water coupled finite element analysis on the progressive failure of a cut slope in a model ground based on an

elastoplastic model with strain hardening and strain softening. In the work by Cai and Ugai (2004), the finite element method with shear strength reduction technique was used to evaluate the stability of slopes due to rainfall. Ye et al. (2005) conducted numerical analyses on progressive failure of slope due to heavy rain with 2D and 3D FEM. FEM simulation using 2D unsaturated-saturated seepage analysis and slope stability analysis was performed to clarify the slope failure mechanisms due to heavy rain in the work by Sako et al. (2006).

The above-mentioned simulations, however, are conducted in soil-water coupling formulation, the air pressure is assumed as constant, and its value is taken as zero for unsaturated soil. In general circumstances, however, the air pressure does not always keep constant, but varies, as pointed out in the work by Yamamura (1971) and Gens et al. (2009). In the work by Oka et al. (2010b), a multiphase deformation analysis of a river embankment was carried out using a soil-water-air fully coupling finite element method, in which a complex elasto-viscoplastic constitutive model for unsaturated soil proposed by Oka et al. (2008) was used. Iwai et al. (2013) also conducted a numerical simulation for the deformation of sea bed due to the pressure reduction of methane hydrate, which is called as depressurization method in the excavation process of the methane hydrate. In Iwai's calculation, a multi-phase-mixture theory, in which not only the soil-water-air coupling problem but also the energy conservation was considered, was employed in the finite deformation analysis for the deformation problem caused by the depressurization of the methane hydrate beneath sea bed.

Much research has been done on the mechanical behavior of unsaturated soils experimentally, empirically, and theoretically. Many constitutive models for unsaturated soils had been developed, e.g., Barcelona Basic Model (BBM) (Alonso et al., 1990), Kohgo et al. (1993a, b), Cui and Delage (1996) and Sun et al. (2000). In these models, taken the stress and the suction as independent state variables, the stress-suction-strain relations of unsaturated soil was considered explicitly while the degree of saturation is not considered directly. On the other hand, constitutive models considering the influence of the degree of saturation were also proposed, e.g., the works by Karube et al. (1997), Gallipoli et al. (2003), Sheng et al. (2004), Sun et al. (2007) and Sheng et al. (2008).

In this chapter, based on the model presented in Chapter 3, the proposed THMA

coupling FE-FD method is used to investigate the mechanism of the surface failure of slope. Firstly, the validity of the proposed numerical method is confirmed by element tests on unsaturated silty clay under undrained and unvented condition, conducted by Oka et al. (2010a). Then, the model tests on a slope failure in an unsaturated Shirasu ground, carried out by Kitamura et al. (2007), are also simulated by the proposed numerical method. The applicability of the proposed numerical method is verified in detail. It is worth noting that the temperature is kept constant in the simulation.

5.2 The Validation of the Proposed Numerical Method

In order to check the validity of the proposed numerical method, a triaxial test on unsaturated silty clay under undrained and unvented conditions, conducted by Oka et al. (2010a), is firstly simulated by the proposed numerical method. The size of the test specimen is 50mm in diameter and 100mm in height. In the test, the initial cell pressure was 450kPa, and initial air pressure was set as 250kPa. Four cases are carried out with different initial suctions, namely, 10kPa, 30kPa, 50kPa and 100kPa and the strain-controlled loading rate is 0.5%/min.
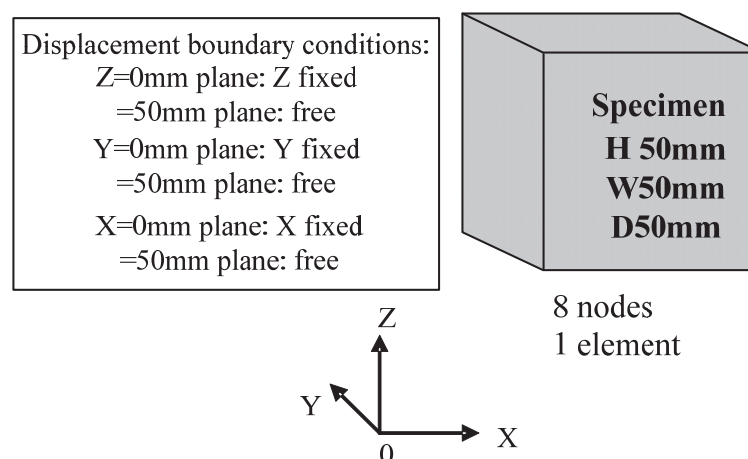

Fig.5.1. One-element 3D FEM mesh for analyzing triaxial tests under undrained and unvented conditions

Table 5.1 Parameters of moisture characteristics curve (MCC) of silty clay

Saturated degrees of saturation S_r^s		0.99
Residual degrees of saturation S_r^r		0.10
Parameter corresponding to drying AEV (kPa)	S_d	220.2
Parameter corresponding to wetting AEV (kPa)	S_w	5.10
Initial stiffness of scanning curve (kPa) k_{sp}^e		58500.
Parameter of shape function c_1		0.0108
Parameter of shape function c_2		0.010
Parameter of shape function c_3		24.0

Fig.5.1 shows the three dimensional (3D) finite element mesh with only one element and the boundary condition used in the simulation for the triaxial test under undrained and unvented conditions. Because the tests were conducted in constant-confining-pressure condition, two dimensional (2D) FE-FD analysis in plane-strain condition is not suitable. Therefore the elemental behavior of the triaxial tests should be simulated with 2D axisymmetric condition or 3D conditions. In this paper, 3D condition is considered. The half size of the specimen is considered because of the symmetric condition along vertical direction. In the simulation, all the boundary conditions are the same as those in the test. Fig.5.2 shows the MCC for the silty clay in the simulation. The values of the parameters involved in the MCC are listed in Table 5.1.

Fig.5.3 shows the comparisons between the test and simulated results of the silty clay under fully undrained and unvented conditions. Because the test was conducted under constant-strain-rate condition, therefore the time axis is proportional to the strain axis, in other words, the time evolution of the suction is totally the same as the strain evolution of the suction. The left figures are the test results and the rights are the simulation. The material parameters of the unsaturated silty clay are listed in Table 5.2. The way to calibrate the material parameters by triaxial tests can be referred to the works by Zhang and Ikariya (2011). From the test results, it is known that the higher the initial suction is, the deviator stress at the same axial strain will be larger, and that the PWP and the PAP decrease with the increase of the initial suction. It is known by the comparisons that the simulation can describe the element test results of the silty clay in a satisfactory accuracy on the whole.
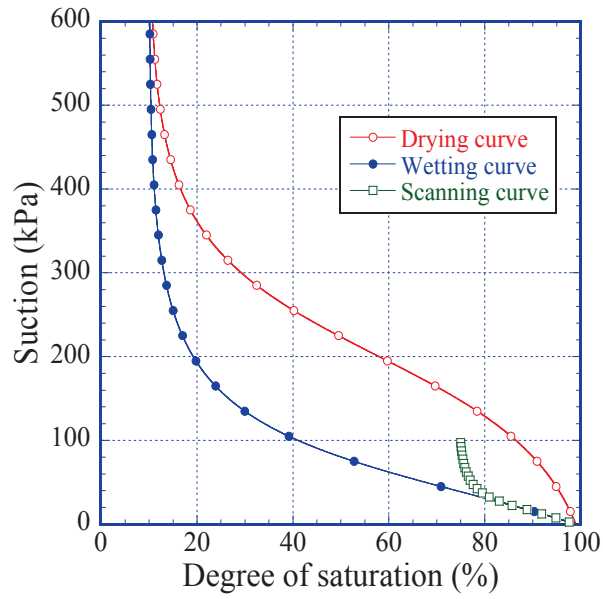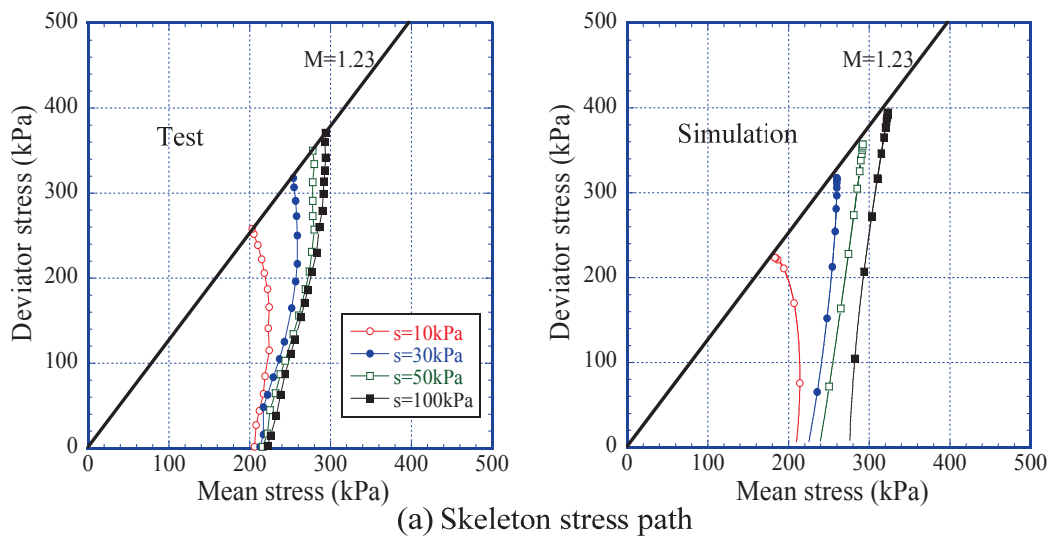
Fig.5.2. MCC used for silty clay in the simulation

(a) Skeleton stress path

(b) Stress-strain relationship
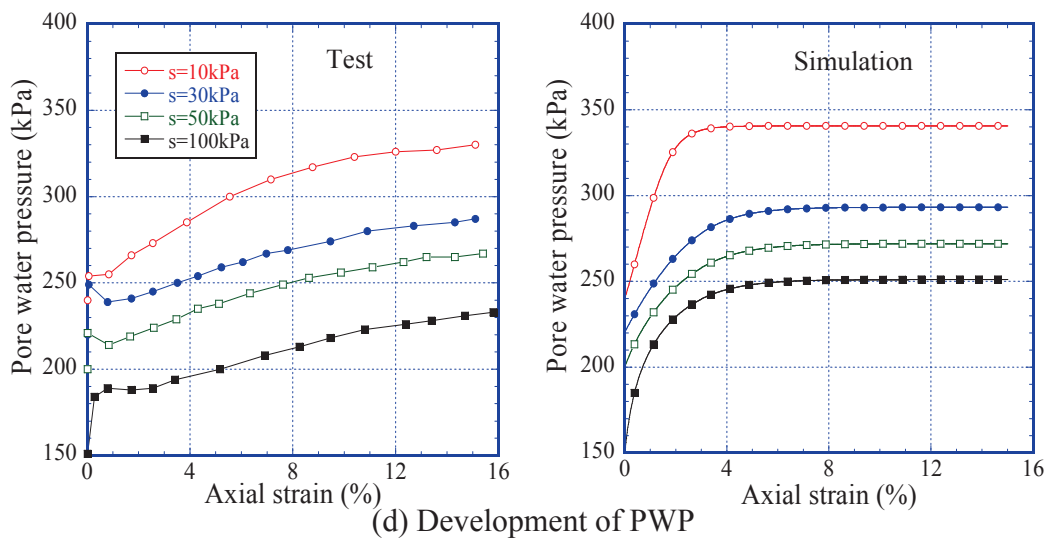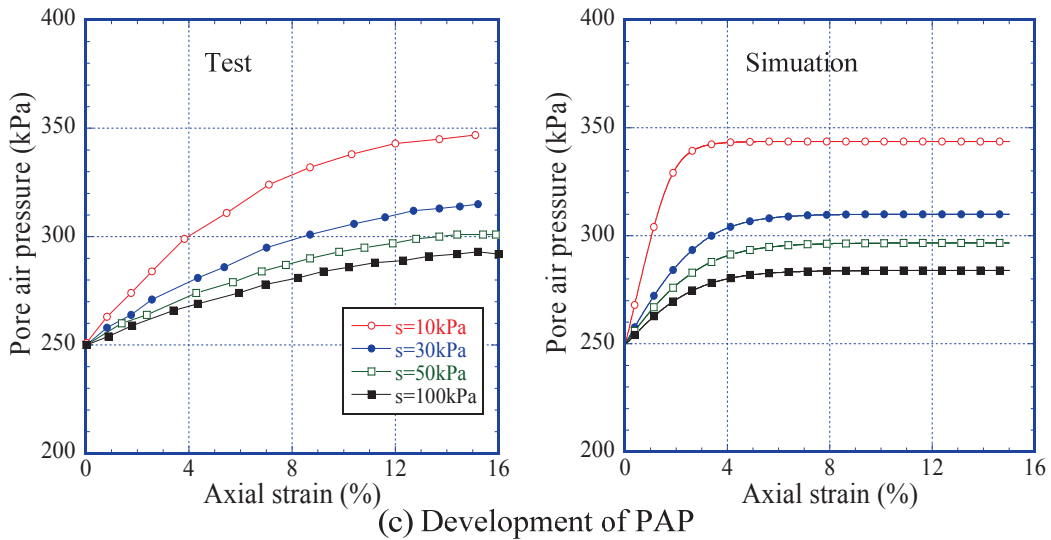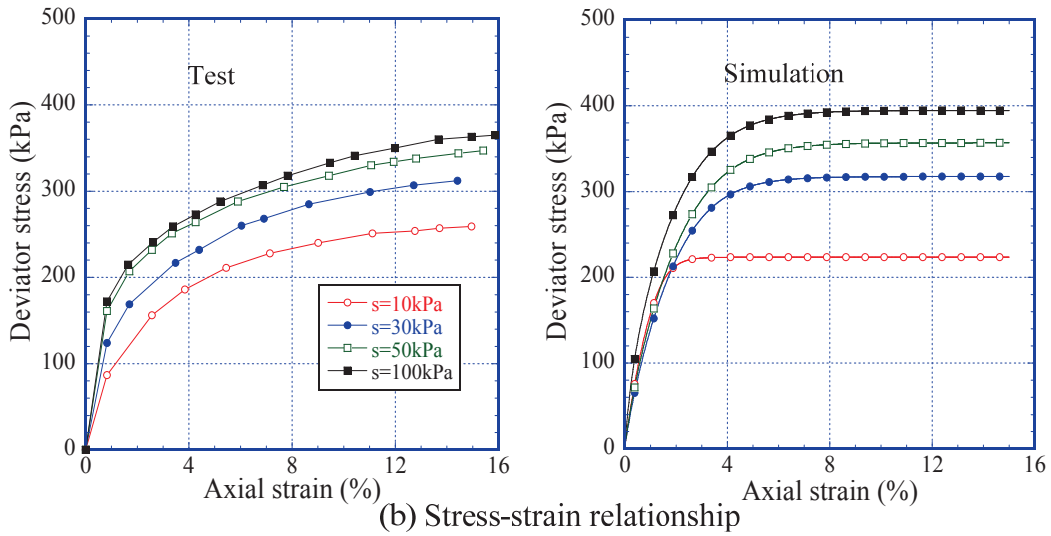

(c) Development of PAP

(d) Development of PWP

Fig.5.3. Comparisons between the test and simulated results of silty clay under
undrained and unvented conditions (Test results from the work by Oka et al, 2010a)

Table 5.2 Material parameters of silty clay

Compression index λ	0.123
Swelling index κ	0.012
Critical state parameter **M**	1.23
Void ratio **N** (p'=98 kPa on *N.C.L.*)	0.81
Poisson's ratio v	0.30
Parameter of overconsolidation a	5.00
Parameter of suction b	0.50
Parameter of overconsolidation β	1.00
Void ratio N_r (p'=98 kPa on *N.C.L.S.*)	1.12

5.3 Numerical Simulation of Model Tests on Slope Failure in Unsaturated Shirasu Ground

In the work by Kitamura et al. (2007), model tests with several different patterns were carried out to investigate the mechanism of slope failure in unsaturated Shirasu ground, among which three patterns are selected to simulate in 2D FE-FD analyses using the proposed numerical method.

Photo 5.1 shows the bird view of the test apparatus and the model ground (Kitamura et al., 2007). The ground of the model slope was made of a lightly compacted unsaturated Shirasu. The model slope was compacted carefully layer by layer and each soil layer was 5cm in depth. The density of the soils listed in Table 5.3 was obtained by controlling the compaction numbers (Kitamura et al., 2007). The slope angle is 45º with a height of 80cm. The permeable plates were used on the edges of the soil tank to control the drainage boundary condition.
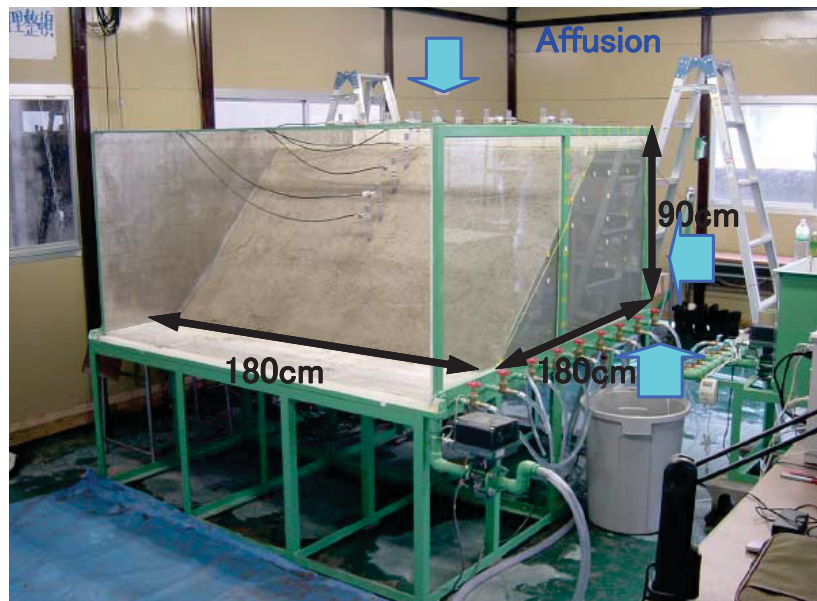
Photo 5.1. Bird view of test apparatus and model ground (Kitamura et al., 2007)

Table 5.3 Physical properties and initial value of state variable ρ_e of Shirasu

	Case 1	Case 2	Case 3
Water content in nature[**] (%)	25.6	23.3	23.1
Void ratio[**](p'=10 kPa)	1.57	1.47	1.57
Density of soil particle[**] (g/cm^3)	2.45	2.40	2.45
ρ_e (OCR)[*]	0.04 (1.5)	0.14 (4.0)	0.04 (1.5)

[*] $\rho_e = (\lambda - \kappa) \ln OCR$; [**] Date from the work by Kitamura et al (2007)

Fig.5.4 shows the arrangement of measuring devices and the positions of the water injection in the model tests. In Case 3, an artificial turf sheet with holes was placed on the top surface of the slope in order to prevent from washing away of the soils when water was showered from the ceiling with a manmade rainfall system. The measuring devices, indicated by No. 1, No. 2…etc., are composed of tensiometers that were used to record the development of the suction or the negative PWP within the model ground.
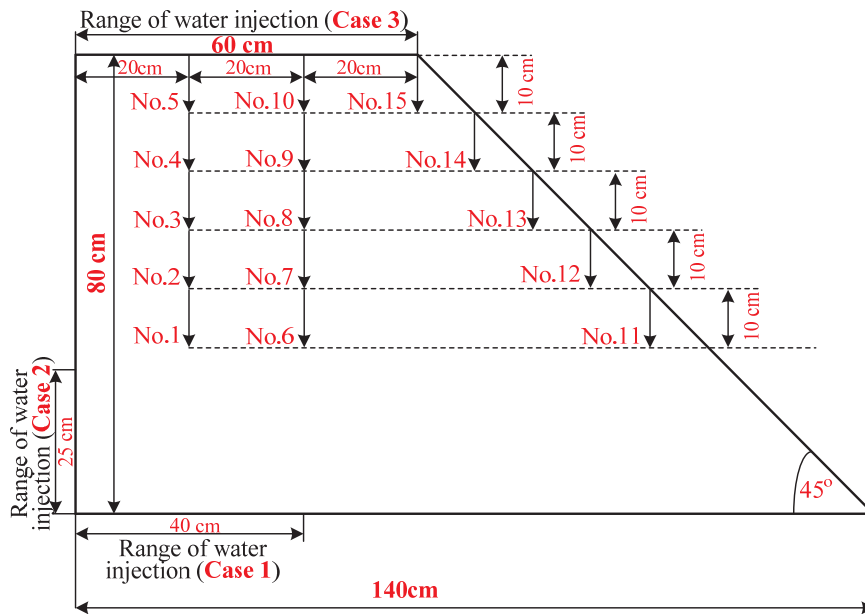
Fig.5.4. Arrangement of measuring devices and injection positions in different testing cases
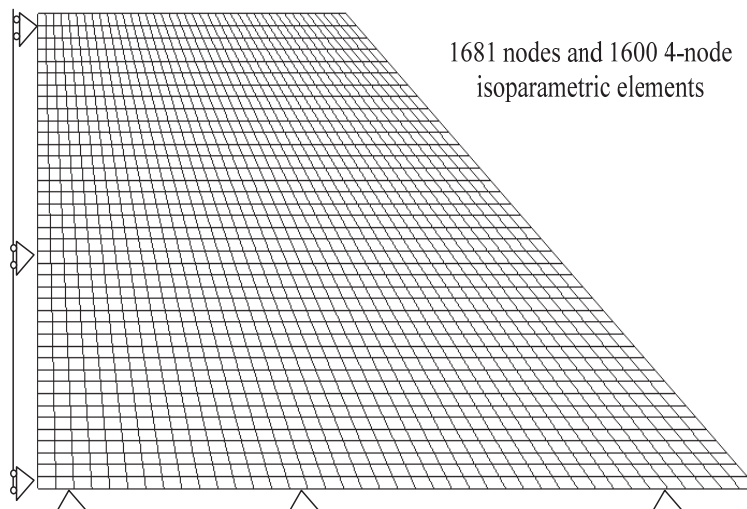
Fig.5.5. 2D FEM mesh and mechanical boundary condition of Shirasu model ground

Fig.5.5 shows the finite element mesh used in the simulation of the slope failure. The size of FEM mesh, composed of 1681 nodes and 1600 4-node isoparametric elements, is the same as that of the model tests under plane strain condition. The boundary condition is given as: (a) for the displacement condition, it is fixed at the bottom in both x, y directions and is fixed at the vertical displacement in x direction for

only left surface. The other surfaces are free at x, y directions; (b) for drainage and vented conditions, the top and slope surfaces are permeable for all the cases, while the bottom and left surfaces are impermeable except for the range of water injection as shown in Fig.5.6.
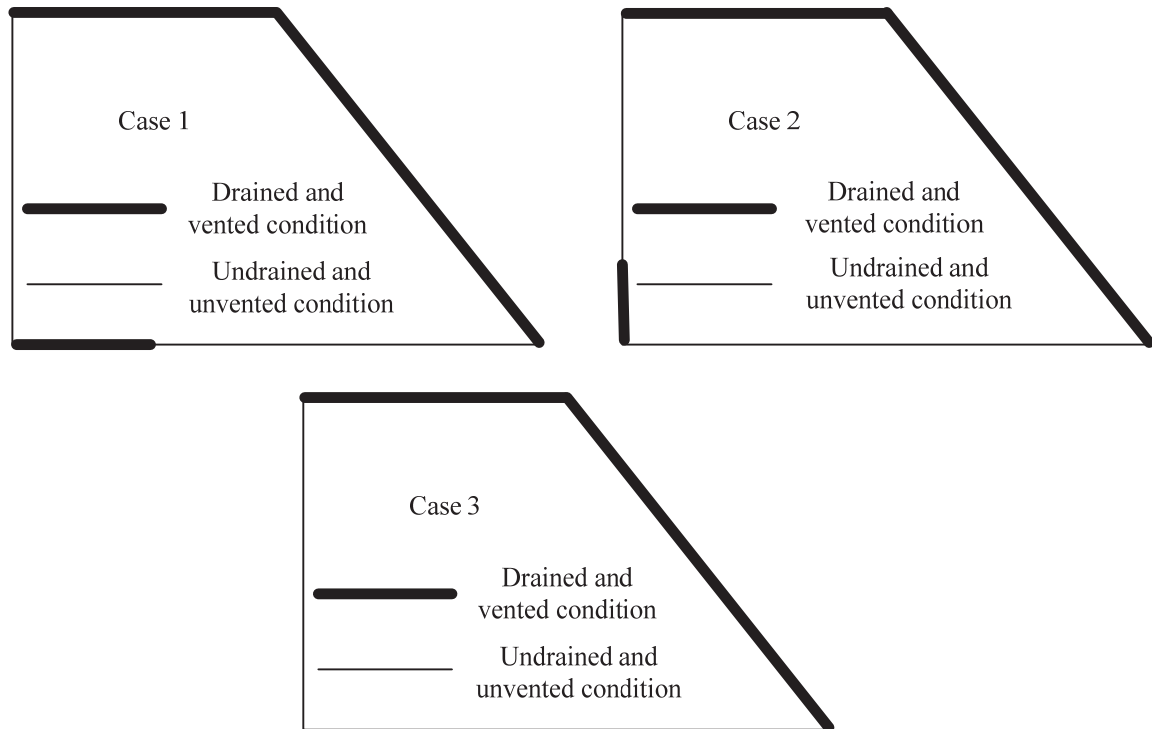
Fig.5.6. The drainage and vented conditions for different 3 cases

The grain size distribution of the Shirasu is shown in Fig.5.7. The density of the Shirasu is about 2.42g/cm^3, which is smaller than those of normal sandy soil. The physical properties of the Shirasu are listed in Table 5.3. In the test, since the model ground was prepared by light compaction (Kitagawa et al., 2007), the ground was under slightly overconsolidated condition at the initial state. The initial value of the state variable ρ_e (=$(\lambda-\kappa)$ ln OCR), based on the physical properties of the Shirasu, can be determine in the way as illustrated in Fig.5.8 and its value is listed in Table 5.3.
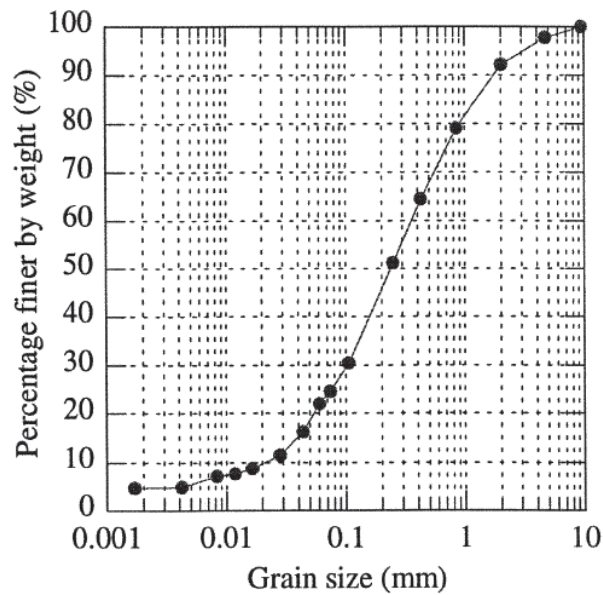
Fig.5.7. Grain size distribution of Shirasu (Kitamura et al., 2007)
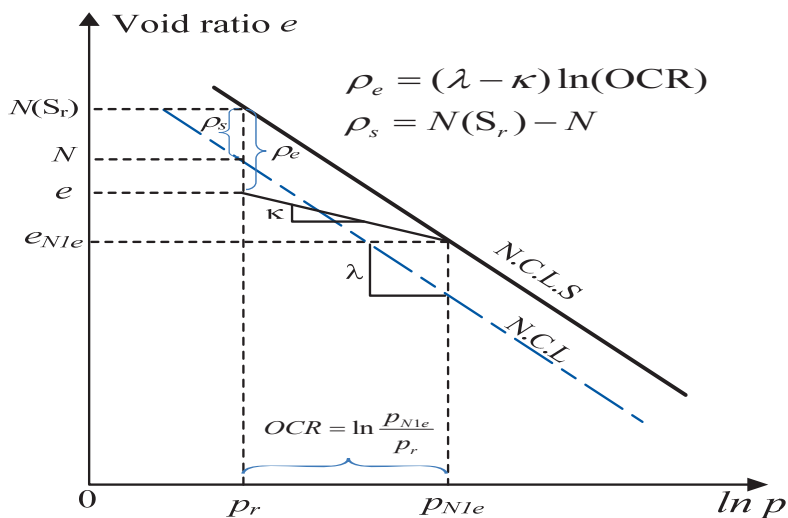
Fig.5.8. Way of calculating the initial state variable of ρ_e

The material parameters of the Shirasu used in the simulation are estimated based on the work by Kitamura et al. (1984) in which the mechanical properties of the Shirasu under the confining stress of 0.2~3.0 MPa were carefully investigated. These parameters are basically determined with triaxial compression tests and the way of calibration for these parameters can be referred to the work by Zhang and Ikariya (2011). In present

case, however, the model ground is under very low confining stress (around 10kPa) and there is no element test result available. Therefore the parameters listed in Table 5.4 are estimated based on the test results (Kitamura et al., 1984) and the assumption that the extrapolation of the $e{\sim}\ln p$ relation to the region of $p=$ 10 kPa$\sim$0.2 MPa is still valid.

Table 5.4 Material parameters of Shirasu

Compression index λ		0.105
Swelling index κ		0.007
Critical state parameter **M**		0.47
Void ratio N (p'=10 kPa on *N.C.L.*)		1.59
Poisson's ratio v		0.30
Parameter of overconsolidation a		5.00
Parameter of suction b		0.50
Parameter of overconsolidation β		1.00
Void ratio N_r (p'=10 kPa on *N.C.L.S.*)		1.61
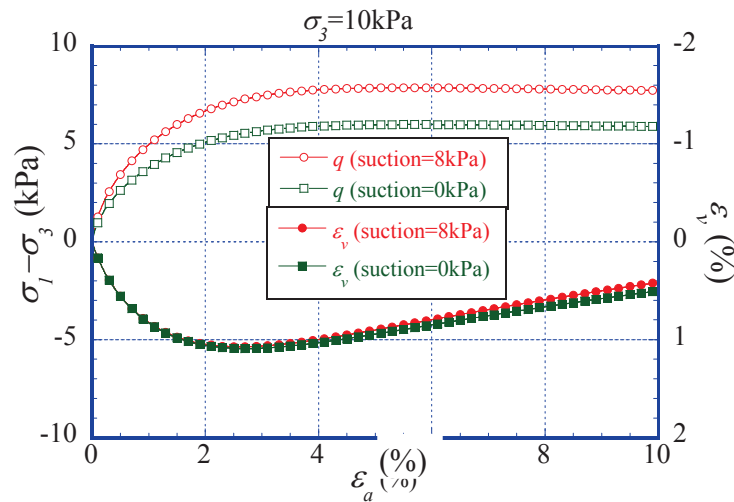
Fig.5.9. Theoretical stress-strain-dilatancy relations under different constant suctions for Shirasu

Fig.5.9 shows the theoretical stress-strain-dilatancy relations at constant confining stress but different constant suctions, under drained and vented condition. It should be emphasized again here that due to the absence of the element test result for the Shirasu at a confining stress of 10 kPa, the simulation for the BVP of the slope failure due to rainfall in the model ground test, can only be expected to be able to give an overall description of the test, but not precisely because the element behavior of the ground at

low confining stress is only an estimated one and cannot be confirmed yet.

It is known that a suitable initial stress field should be given in advance in any numerical calculation with FEM. The initial stress field, caused by gravitational force and other external forces, represents the equilibrium state of the ground at initial state. In this calculation, the gravitational loading method is adopted. Since the initial effective stress near the top surface is very small, an extra mean effective stress 5 kPa is added to the whole area to consider the compaction effect in preparing the model slope. Fig.5.10 shows the initial vertical effective stress in the calculation.
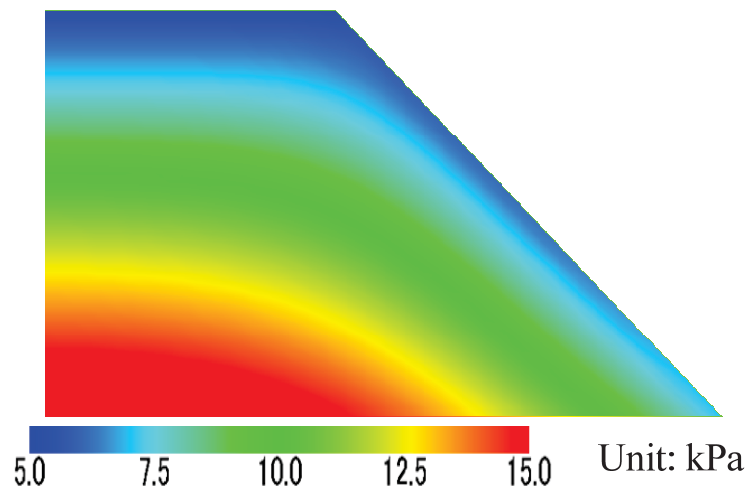
Fig.5.10. Initial vertical effective stress field of model ground

The initial negative PWP measured in the tests (Kitamura et al., 2007) is about -6~-9kPa in all three cases. For simplicity, the initial negative PWP in the simulation is assumed to be -8kPa in the whole area for the three cases. While the initial degree of saturation is 38%, the same value as measured in the tests. Fig.5.11 shows the simulated MCC of the Shirasu for the three cases based on the test results carried out by Kitamura et al. (2007). The parameters of the MCC are listed in Table 5.5.

Table 5.5 Parameters of MCC of Shirasu

		Case 1	Case 2	Case 3
Saturated degrees of saturation S_r^s		0.87	0.89	0.95
Residual degrees of saturation S_r^r		0.20	0.25	0.20
Parameter corresponding to drying AEV (kPa)	S_d	12.0	15.0	12.0
Parameter corresponding to wetting AEV (kPa)	S_w	0.07	0.10	0.17
Initial stiffness of scanning curve (kPa) k_{sp}^e		90.0	20.0	50.0
Parameter of shape function c_1		0.30	0.30	0.33
Parameter of shape function c_2		0.60	0.40	0.18
Parameter of shape function c_3		30.0	50.0	5.0

It is known that the permeability of water and the permeability of air for unsaturated soil change with the degree of saturation. Many methods have been proposed in literature related to the change of the permeability of water/air phase under unsaturated condition. In the work by Kamiya et al. (2006), a test method for measuring the permeability of air was proposed, in which the degree of saturation for an unsaturated sample can be controlled by adjusting the suction individually. It is found that the permeability of air is dependent on the degree of saturation, that is, it decreases with the increase of the degree of saturation. Because the permeability of water/air is not directly measured with saturation in the model test, the interpolation method employing some values of the permeability at some specified saturation, reported in the work by Takeshita and Morii (2006), Kamiya et al. (2006), is used to fit the results of model tests. The relation between the permeability and the degree of saturation used in the analysis is shown in Fig.5.12. It should be pointed out that because the water permeated very quickly in Case 3, the permeability of water in Case 3 is larger than those in Case 1 and Case 2, as shown in Fig.5.12.
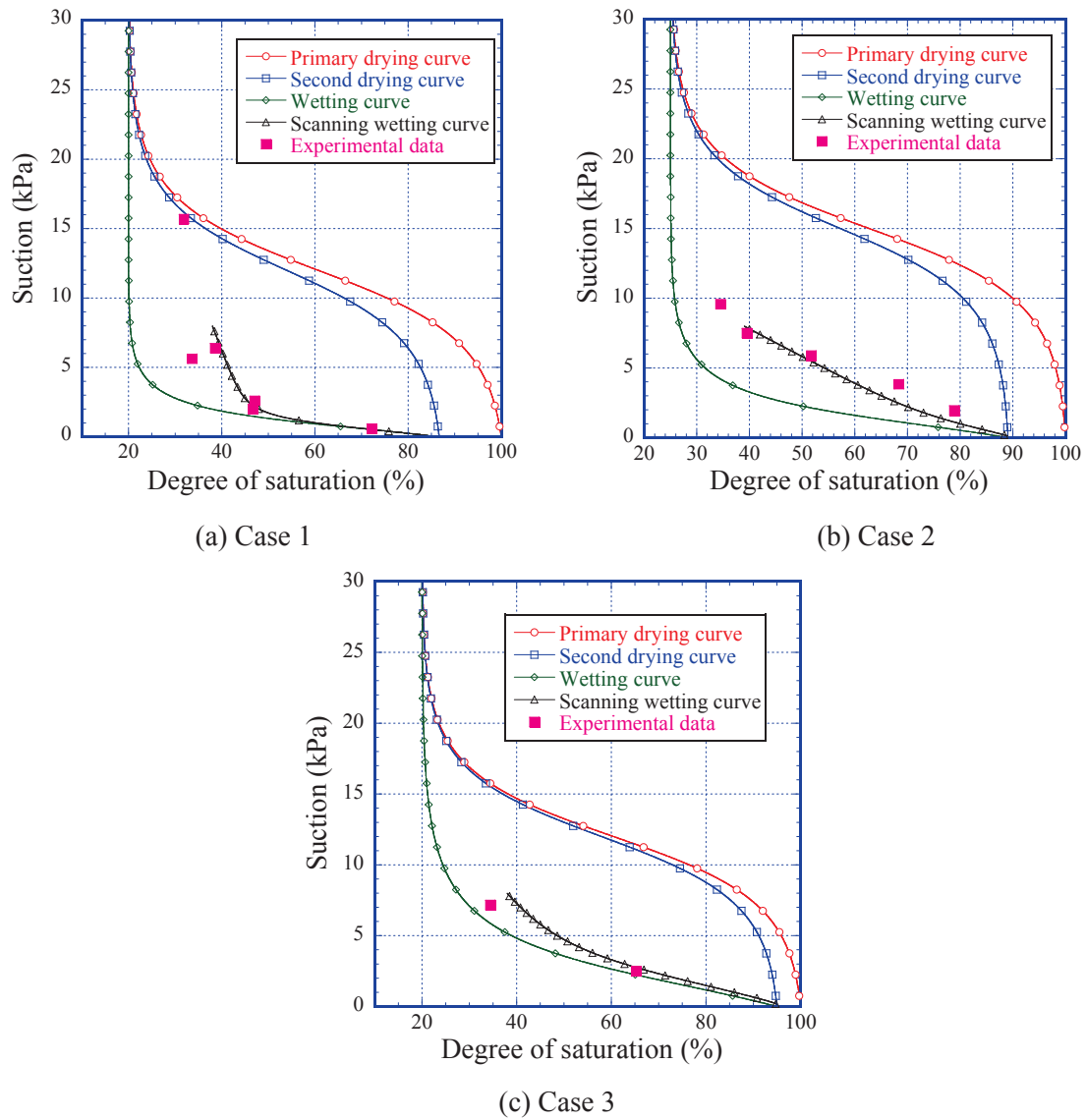
(a) Case 1

(b) Case 2

(c) Case 3

Fig.5.11. MCC of Shirasu (Test results from the work by Kitamura et al., 2007)

(a) Case 1 and Case 2   (b) Case 3
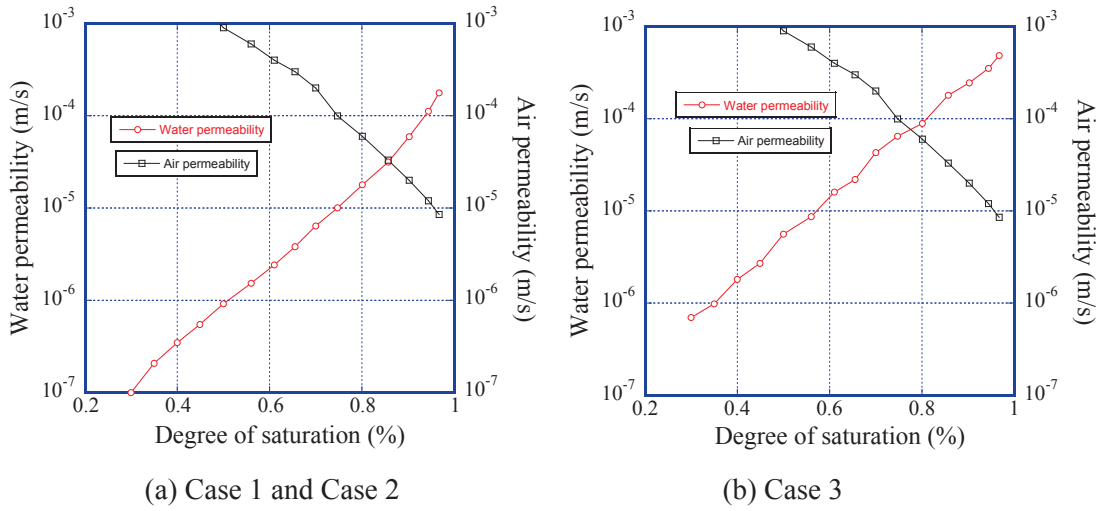
Fig.5.12. Relationship between permeability of water and air with degree of saturation
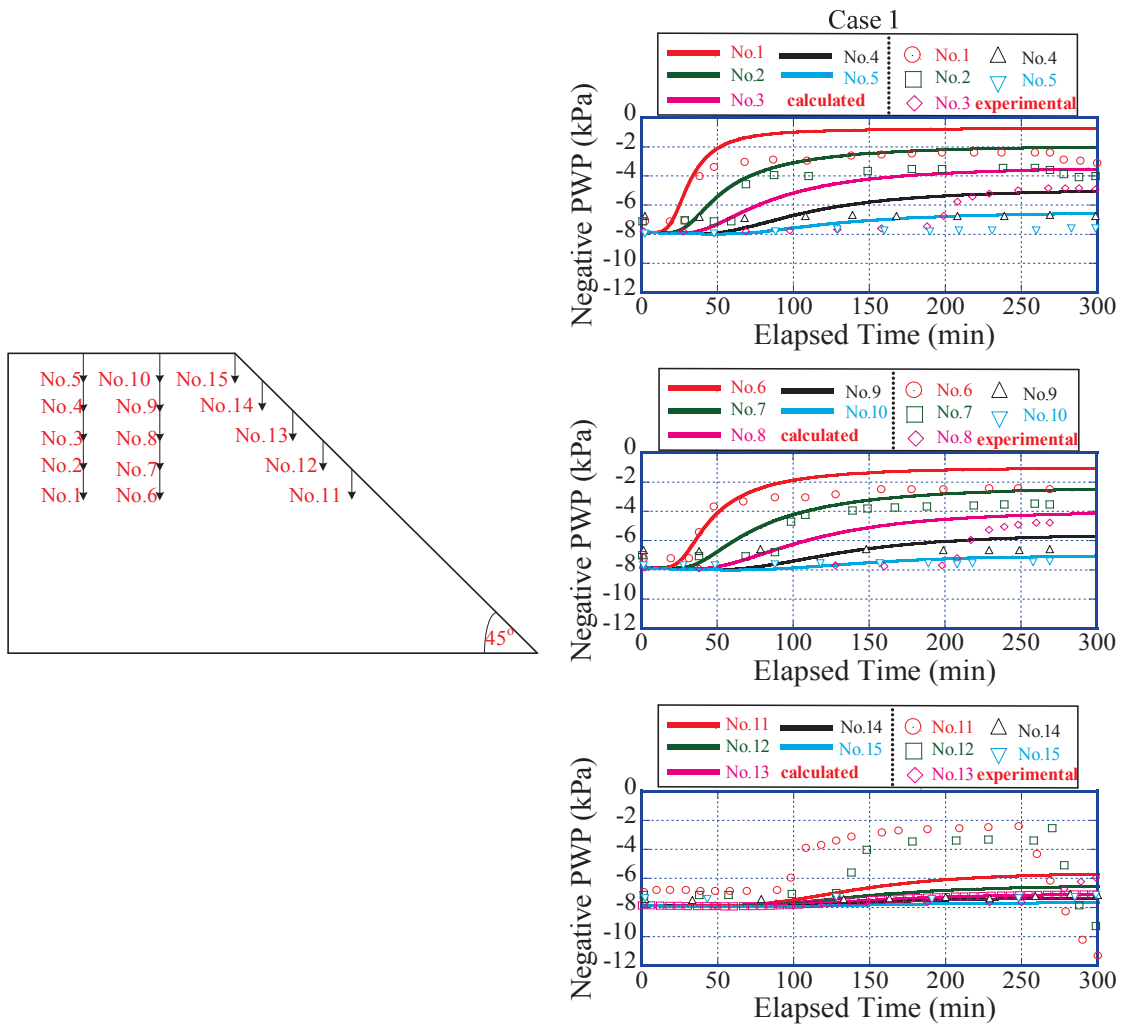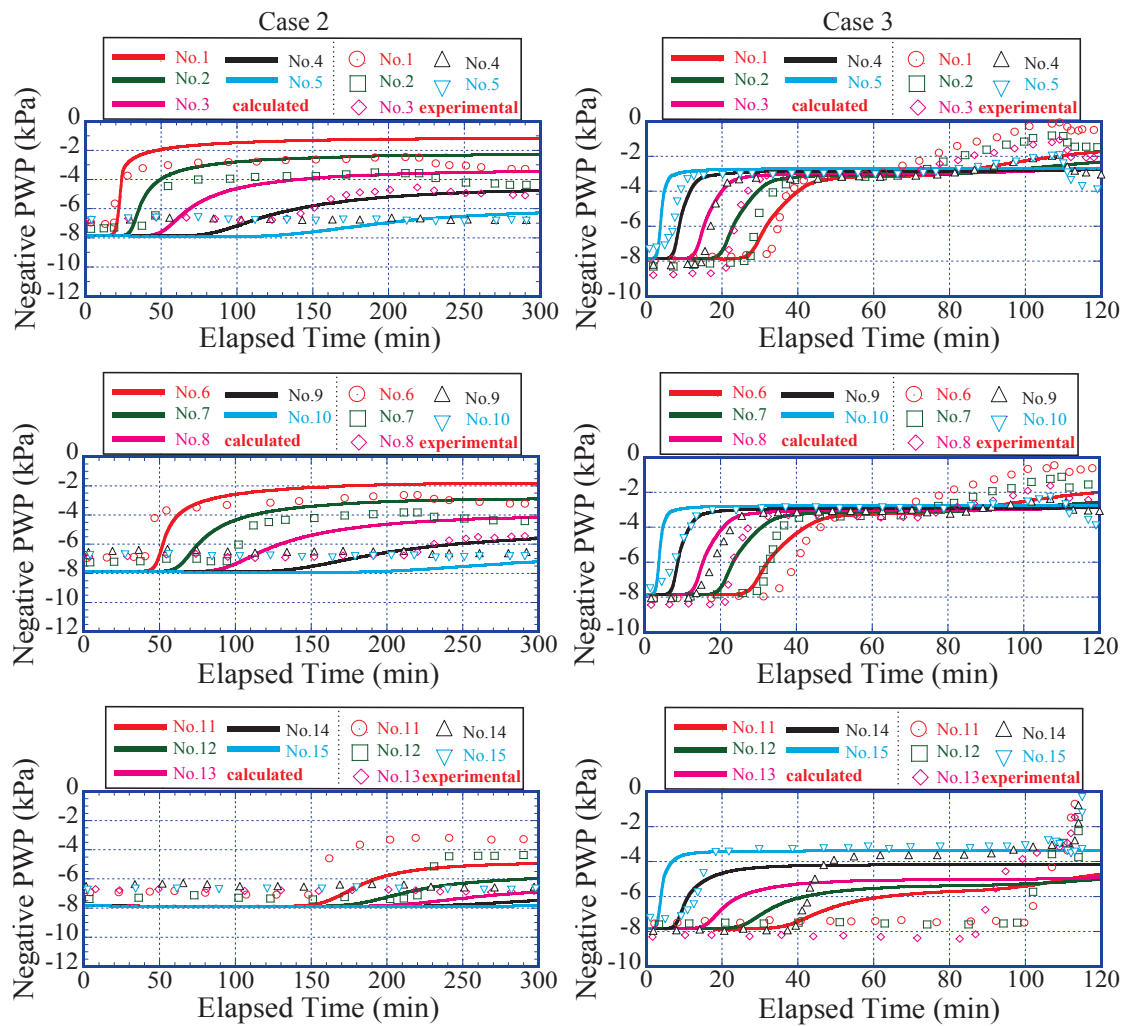
Fig.5.13. Comparisons between test and calculated results of negative PWP at some measured positions (Test results from the work by Kitamura et al., 2007)

In the calculations, the first stage is to calculate the initial stress field; then a prescribed increment of water head is applied in the second stage. The increment of water head is the same as that of the test. 1,000 steps of calculation with a time interval of 20 sec/step are conducted to simulate the infiltration of water and the seepage of the negative PWP in Case 1 and Case 2. While in Case 3, 1000 steps of calculation with a time interval of 8 sec/step are conducted.

Fig.5.13 shows the comparisons of the negative PWP between the test and the calculated results at some measured positions for 3 cases respectively. From these figures, it is found out that the simulation can generally describe the development of PWP well on the whole in the points far away from the slope surface. In the points

along the slope surface, however, a rather big difference between the calculation and the test existed. This might be caused by the assumption that the coefficients of permeability are the same in vertical and horizontal direction, and that the initial suction and the degree of saturation are the same in the whole model ground.

Fig.5.14 shows the comparison of the change in the distribution of the saturation at different times for 3 cases respectively. In Case 1 and Case 2, it is known that the water is infiltrated gradually toward the slope surface from the initial position. In Case 1 the seepage of water is more intensive than that in Case 2. Therefore, 300 min after the start of the water infiltration, the soil at the toe of the slope is saturated earlier in Case 1 than in Case 2. In Case 3, the water is infiltrated from the top of the slope surface toward the bottom. It is known from the calculation that about 50min after the seepage, the infiltrated water reached the bottom surface, and then the water began to accumulate at the left corner of the slope due to the impermeability of the bottom surface. An interesting phenomenon can be seen in Fig.5.14 (c) that until about 50min, the degree of saturation at the top area is larger than that at the left bottom corner. After then, however, the situation became conversed, that is, the degree of saturation at the left bottom corner is larger than that at the top area, showing clearly the migration process of the infiltrated water due to gravitational force. This phenomenon is also confirmed with the change of the PWP at the measured points, where the PWP increased gradually at the time 60min after the infiltrated, as shown in Fig.5.13.

Case 1

Case 2

Case 3
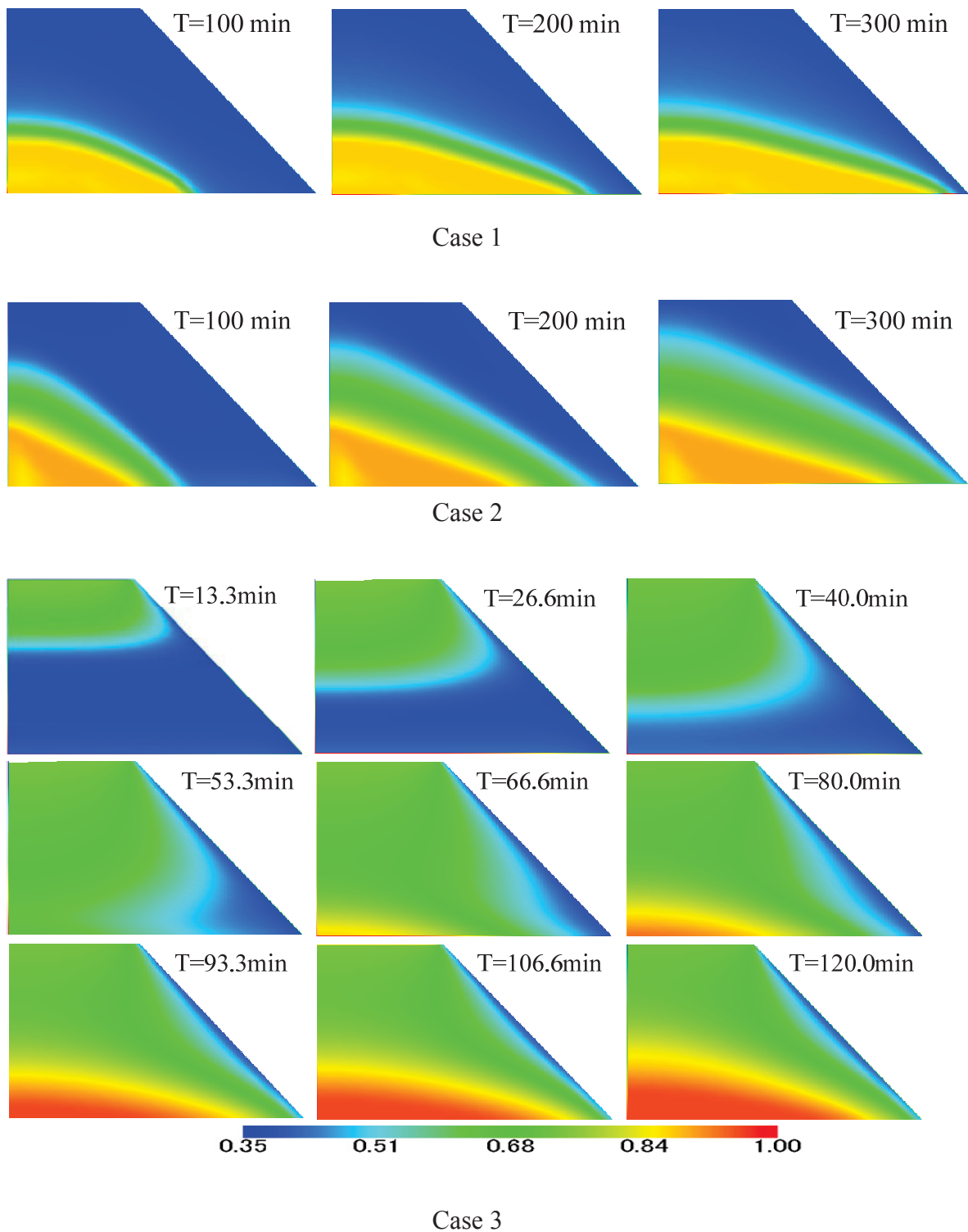
Fig.5.14. Comparison of the change in the distribution of the saturation at different times

Case 1   Case 2   Case 3

T=200min   T=200min   T=80 min

T=300 min   T=300 min   T=120 min

0.00   0.04   0.07   0.11   0.15
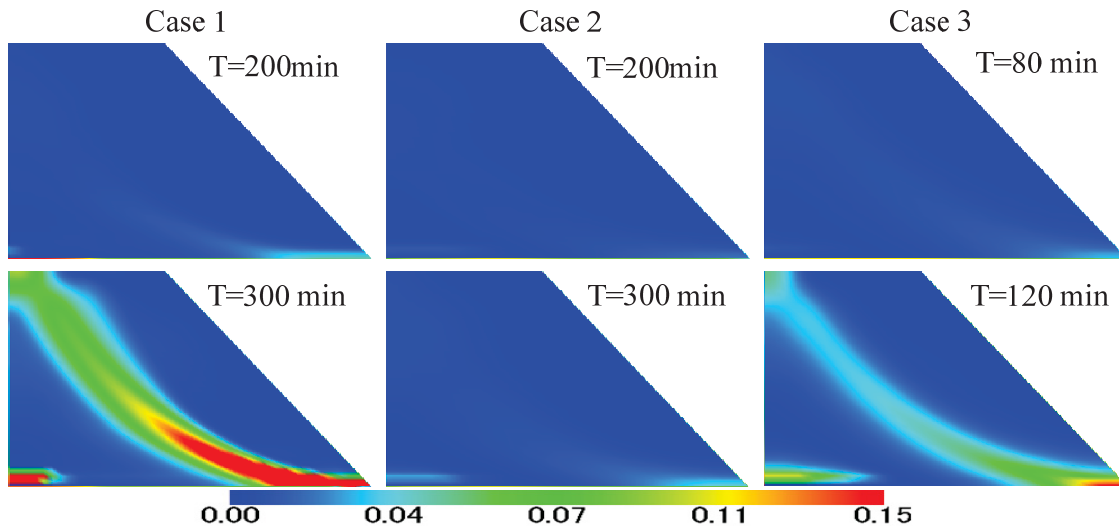
Fig.5.15. Calculated distribution of plastic shear strain ($\sqrt{2I_2^p}$) at different times

Fig.5.15 shows the change in the distribution of the plastic shear strain $\sqrt{2I_2^p}$ with time for all the three cases, where I_2^p is the second invariant of deviatoric plastic strain tensor. It is found that the shear strain firstly occurred at the toe of slope in all cases, and then propagated backward toward the top surface. At the end of tests (also calculations), a shear band developed clearly in Case 1 and Case 3 but did not show up clearly in Case 2.

Fig.5.16 shows comparison of the stress paths at three selected elements for three cases in terms of mean effective stress p and shear stress $\sqrt{2J_2}$, where J_2 is the second invariant of deviatoric stress tensor. It is found that the stress moves toward the critical state in all three cases during the whole seepage process. In Case 1 and Case 3, however, the stress state reaches the critical state much earlier than in Case 2. In other words, the slope fails much earlier in Case 1, 3 than in Case 2.
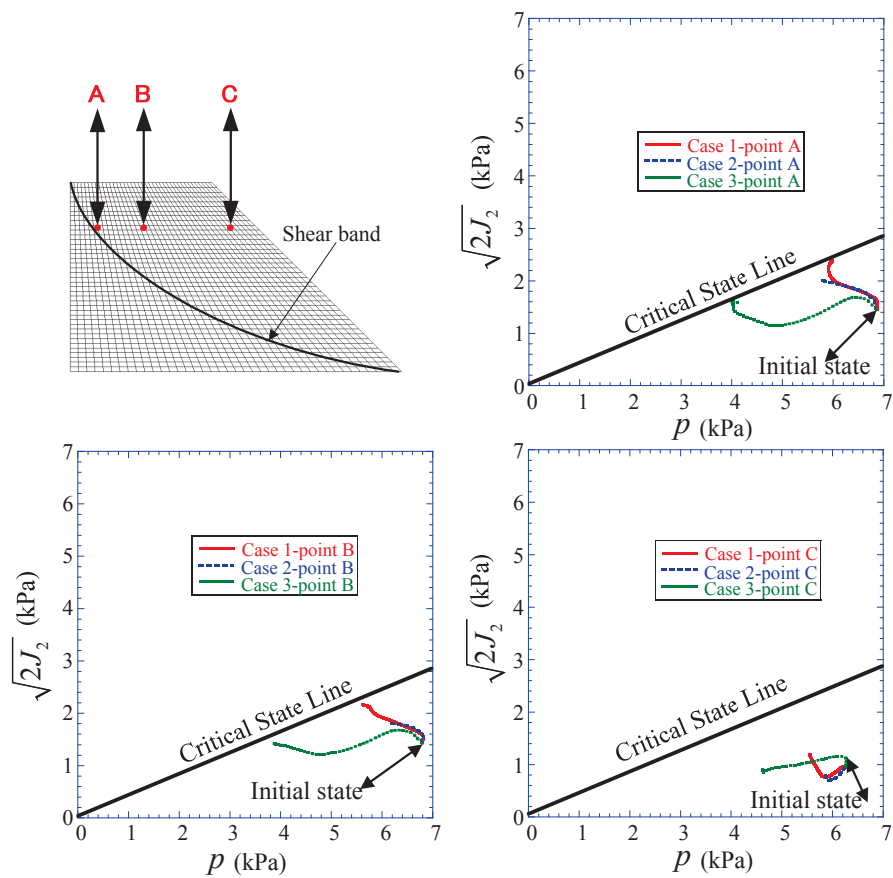
Fig.5.16. Stress paths at selected elements during water infiltrated process

Fig.5.17 shows the calculated displacement vectors at the end of tests (also calculations) in all cases. It is known from the figure that a lager displacement along the shear band toward the slope toe developed in Case 1 and Case 3. Compared with the shear band formed in the slope shown in Fig.5.15, the stress paths shown in Fig.5.16, it is reasonable to judge that the slope is more dangerous in Case1 and Case 3 than in Case 2, which is consistent with the observed results in the tests that an entire slope failure

had occurred in Case 1 and Case 3 (Kitamura et al. 2007). In Case 2, however, failure only happened in the vicinity area near the toe of the slope, where the maximum shear strain reached about 10%, as shown in Fig.5.15.

| Case 1 | Case 2 | Case 3 |
| T=300 min | T=300 min | T=120 min |
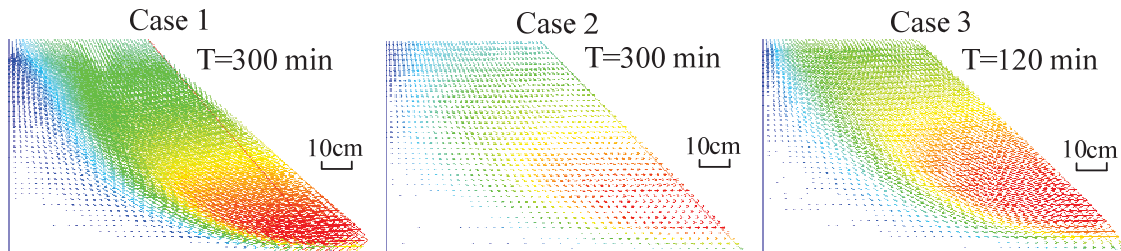
Fig.5.17. Calculated displacement vectors at the end of tests (Calculation) in all cases

Because the permeability of air for the Shirasu is very lager, the influence of the air pressure is very little and can be neglected due to the vented condition in Case 1 and Case 2, where the air can be ventilated from the ground very easily due to the water injection from the bottom area. In Case 3, however, the permeability of air decreased greatly due to the infiltrated water at the top surface. As the result, the air pressure increased at the corner of the slope along with the seepage of the water from the top surface to the bottom surface, as shown in Fig.5.18. When the infiltrated water reached the bottom surface, the air pressure reached its maximum value and then turned to decrease gradually due to the escape of the air from the vented boundaries at the top and slope surface. Though the value of PAP is very small compared with the PWP, the changing pattern with time, is quite natural, which is also confirmed in the model test and field observation (Maeda et al., 2010). It is reported in the works by Maeda et al. (2010) that due to the water infiltration on the top of a river dike from rainfall, the vented boundary of the top surface was enclosed and the air within the area enclosed with the unvented boundaries was compressed and finally blasted, which enhanced the failure of the slope. In the model tests, because the height of the model ground is only 80cm and the vented boundary is not fully enclosed in the test, the compressed air pressure cannot reach a large value. This is the reason why in the present model ground the air pressure is negligible. In field observation, however, the air pressure may become large enough when the vented boundary at the top of a dike is enclosed due to

heavy rainfall, and may affect the stability of a slope, as pointed out by Maeda et al. (2010).
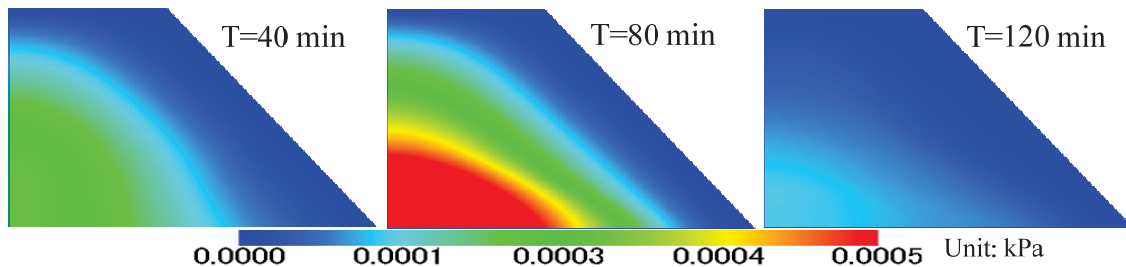
Fig.5.18. Calculated distribution of air pressure at different times in Case 3

5.4 Conclusions

In this chapter, the proposed numerical analysis is based on a simple unsaturated constitutive model and a MCC model described in Chapter 3, and its validity is confirmed by the triaxial tests on unsaturated silty clay (Oka et al., 2010a) and the model tests on slope failure in a compacted unsaturated Shirasu (Kitamura et al, 2007). The following conclusions can be made:

1. The triaxial compression tests under undrained and unvented conditions were simulated by the proposed numerical method in order to verify the validity of the proposed numerical method. In the simulation, the elementary behavior of the triaxial tests is calculated with 3D FE-FD analysis using one-element mesh. From the comparisons between the test and simulation, it is found that the proposed numerical method can well describe the test behaviors such as the skeleton stress path, the stress-strain relation, and the developments of PWP and PAP under different suctions.

2. The model tests on slope failure due to water injection or rainfall have also been simulated by the same proposed numerical method. Because the method is based on the soil-water-air fully coupling scheme, not only the seepage of water due to rainfall or water injection, the change of the degree of saturation, the migration of the air pressure, but also the mechanical behaviors of the unsaturated soil such as

the deformation of the ground, the change of pore water pressure, the formation of the shear band occurred in the slope failure, can be simulated on the whole in an unified way, judging from the comparisons between the measured and calculated results. It is particularly worth mentioning that due to the incorporation of a proper constitutive model for unsaturated soil, the calculation can well simulate the different failure behavior of the model Shirasu ground observed in the tests that, in Case 1 and Case 3, the slope collapses entirely while in Case 2, only the toe of the slope failed. In the analyses, all the material parameters of the Shirasu in different test cases are the same, which makes the sense for the application of the proposed numerical method

3. In the simulation of slope failure due to rainfall, though the air pressure is very small, its development is well simulated qualitatively if compared with field observation available in literature. In the future study, verification with real scale field observation should be done. Another important issue related to the future research is the application to the deep geologic disposal of high-level nuclear waste in the unsaturated clay or soft rock, where the air pressure is expected to change largely due to hydraulic and thermal factors. Meanwhile, the water retention curve used in this formulation does not consider the influence of the change in void ratio and stress based on the infinitesimal strain condition. This can be done by taking into consideration a finite deformation scheme in the water retention curve or adopting the way proposed by Sheng and Zhou (2011). Further work should be done in near future.

References

1) Alonso, E. E., Gens, A. and Josa, A. (1990): A constitutive model for partially saturated soils, *Geotechnique*, Vol.40, No.3, 405-430.

2) Cai, F. and Ugai, K. (2004): Numerical analysis of rainfall effects on slope stability, *International journal of geomechanics,* Vol. 4, No. 2, 69-78.

3) Cui, Y. J. and Delage, P., (1996): Yielding and plastic behaviour of an unsaturated compacted silt, *Geotechnique*, 46(2), 291-311.

4) Gallipoli. D., Gens, A., Sharma, R., and Vaunat, J. (2003): An elastoplastic model for unsaturated soil incorporating the effects of suction and degree of saturation on mechanical behaviour. *Geotechnique*, 53(1): 123-135.

5) Gens, A., Sanchez, M., Guimaraes, L. D., lonso, E. E., Lloret, A., Olivella, S., Villar, M. V. and Huertas, F. (2009): A full-scale in situ heating test for high-level nuclear waste disposal: observations, analysis and interpretation, *Geotechnique*, Vol. 59, No. 4, 377-399.

6) Kamiya, K., Bakrie, R. and Honjo Y. (2006): The measurement of air permeability coefficient of unsaturated soil with controlling water retentivity, *proceedings of JSCE*, Vol.62, No. 3, 679-688 (in Japanese).

7) Kato, R., Oka, F., Kimoto, S., Kodaka, T. and Sunami S. (2009): A method of seepage-deformation coupled analysis of unsaturated ground and its application to river embankment, *proceedings of JSCE*, Vol.65, No. 1, 226-240 (in Japanese).

8) Kitamura, R., Haruyama, M. and Misumi, K. (1984): Mechanical properties of Shirasu under intermediate and low pressures, *Japanese Geotechnical Journal*, Vol. 32, No.2, 17-21 (in Japanese).

9) Kitamura, R., Sako, K., Kato, S., Mizushima, T. and Imanishi, H. (2007): Soil tank test on seepage and failure behaviors of Shirasu slope during rainfall, *Japanese Geotechnical Journal*, Vol. 2, No. 3, 149-168 (in Japanese).

10) Kohgo, Y., Nakano, M. and Miyazaki, T. (1993a): Theoretical Aspects of

constitutive model for unsaturated soils, *Soils and Foundations*, Vol.33, No.4, 49-63.

11) Kohgo, Y., Nakano, M. and Miyazaki, T. (1993b): Verification of the generalized elastoplastic model for unsaturated soils, *Soils and Foundations*, Vol.33, No.4, 64-73.

12) Karube, D., Honda, M., Kato, S. and Tsurugasaki, K. (1997): The relationship between shearing characteristics and the composition of pore-water in unsaturated soil, *JSCE*, No.575/III-40, 49-58 (in Japanese).

13) Maeda, K., Shibata, S., Baba, K., Masuo, T. & Imase, T. (2010): Laying effect of breathable - water proof sheet on river dike considering heavy rain and air bubble, , Geosynthetics Journal, Japan Chapter of International Geosynthetics Society (JCIGS), Vol.25: 107-112 (in Japanese).

14) Maeda K., Shibata S., Baba K., Kobayashi T., Masuo T. and Obata I. (2012): Air blow Phenomenon in unsaturated river dike model and numerical simulation, Vol.18, 305-310 (in Japanese).

15) Oka, F., Yashima, A., Shimata, T., Kato, M. and Uzuoka, R. (1994): FEM-FDM coupled liquefaction analysis of a porous soil using an elasto-plastic model, *Applied Scientific Research*, Vol. 52, 209-245.

16) Oka, F., Feng, H. and Kimoto, S. (2008): A numerical simulation of triaxial tests of unsaturated soil at constant water and constant air content by using an elasto-viscoplastic model, *Proceeding of 1st European conference on unsaturated soils*, 735-741

17) Oka, F., Kodaka, T., Suzuki, H., Kim, Y., Nishimatsu, N. and Kimoto, S. (2010a): Experimental study on the behavior of unsaturated compacted silt under triaxial compression, *Soil and Foundations*, Vol. 50, No. 1, 27-44.

18) Oka, F., Kimoto, S., Takada, N., Gotoh, H. and Higo, Y. (2010b): A seepage-deformation coupled analysis of an unsaturated river embankment using a multiphase elasto-viscoplastic theory, *Soil and Foundations*, Vol. 50, No. 4, 483-494.

19) Iwai, H., Oka, F., Kimoto, S., Kitano, T. and Akai, T. (2013): A numerical simulation of decomposition behavior and ground deformation of methane hydrate bearing sediments induced by depressurization method, *Proc. of 13th Japan Symposium on Rock Mechanics & 6th Japan-Korea Joint Symposium on Rock Engineering*, 401-405.

20) Sako, K., Kitamura, R. and Fukugawa, R. (2006): Study of slope failure due to rainfall: a comparison between experiment and simulation, *Proc. of the fourth international conference on unsaturated soil*, Vol.2, 2324-2335.

21) Sheng, D., Sloan, S., Gens. A. (2004): A constitutive model for unsaturated soils: thermo mechanical and computational aspects, *Computational Mechanics*, Vol. 33, 453-465.

22) Sheng, D., Fredlund, D. G. and Gens. A. (2008): A new modelling approach for unsaturated soils using independent stress variables, *Canadian Geotechnique*, No.45, 511-534.

23) Sheng, D., and Zhou, A. N. (2011): Coupling hydraulic with mechanical models for unsaturated soils, Canadian Geotechnical Journal, Vol.48 (5), 826-840.

24) Sheng, D. (2011): Review of fundamental principles in modelling unsaturated soil behaviour, Computers and Geotechnics, Vol.38, Issue 6, 757–776.

25) Sun, D. A., Matsuoka, H., Yao, Y. P. and Ichihara, W. (2000): An elasto-plastic model for unsaturated soil in three-dimensional stresses, *Soils and Foundations*, Vol.40, No.3, 17-28.

26) Sun, D. A., Sheng, D., and Sloan, S. W. (2007): Elastoplastic modelling of hydraulic and stress-strain behaviour of unsaturated soil. *Mechanics of Materials*, 39(3): 212-221.

27) Takeshita, Y. and Morii, T. (2006): Field measurement of field saturated and unsaturated hydraulic conductivity using soil moisture profile, *JSCE*, Vol.62 No.4, 831-839(In Japanese).

28) Tohari, A., Nishigaki, M. and Komutsu, M. (2007): Laboratory rainfall-induced

slope failure with moisture content measurement, *Journal of Geotechnical and Geoenvironmental engineering*, Vol.133, No. 5, 575-587.

29) Yagi, N., Yatabe, R. and Yamamoto, K. (1983): Slope failure due to seepage of rainwater, *proceedings of JSCE*, No.330, 107-114.

30) Yamamura, K. (1971): Soil engineering research of river embankment, *Ph.D. dissertation of Kyoto University* (in Japanese).

31) Ye, G. L., Zhang, F., Yashima, A., Sumi, T. and Ikemura, T. (2005): Numerical analysis on progressive failure of slope due to heavy rain with 2D and 3D FEM, *Soil and Foundations*, Vol. 45, No. 2, 1-15.

32) Zhang, F., Yashima, A., Osaki, H., Adachi, T. and Oka, F. (2003): Numerical simulation of progressive failure in cut slope of soft rock using a soil-water coupled finite element analysis, *Soil and Foundations*, Vol. 43, No. 5, 119-131.

33) Zhang, F. and Ikariya, T. (2011): A new model for unsaturated soil using skeleton and degree of saturation as state variables, *Soil and Foundations*, Vol. 51, No. 1, 67-81.

CHAPTER 6 THERMO-HYDRAULIC-MECHANICAL-AIR ANALYSIS ON HEATING TESTS IN SATURATED GROUND

6.1 General

In considering the problem of the deep geologic disposal for the high level radioactive waste, not only artificial barrier that has been investigated intensively during the past decades, but also the thermo-hydro-mechanical (THM) behavior of the natural barrier, most of which is sedimentary rock or granite, is also a very important factor to be studied. The high level radioactive materials might permeate with underground water through the barrier systems to biosphere. The temperature effect on soft sedimentary rock due to the heat emitting of the nuclear waste canisters also needs to be investigated. The water absorption may induce a swelling of geomaterials that might lead to a damage of the nuclear waste containers. All these THM behaviors of the natural barrier need to be well understood in order to guarantee the safety and the efficiency of the waste sealing construction in long time.

Generally speaking, field experiment is one of the most effective and persuasive ways to make clear the above-mentioned THM behaviors of the natural barrier. A lot of field heating experiments have been reported in the last decades, such as the works by Gens et al. (2007, 2009), Gens (2010), Jia et al. (2007), Sawada et al. (2009) and Akesson et al. (2009). In reality, however, the heating period caused by the high-level nuclear waste will last for tens of thousands years or even longer for some radioactive substances. Therefore, sometime it is impossible to reproduce the whole process in the field tests. Numerical simulation will be another effective method to describe and predict the above-mentioned THM behaviors on the condition that the numerical method is able to fit the results of field experiments, at least in a limited period. For this reason, the laboratory tests on THM behavior of geomaterials at element level will play an important role in improving the accuracy of the numerical analyses. Many laboratory element tests of geomaterials have been done in order to investigate the basic thermo-mechanical behavior such as the work by Salager et al. (2008) and Cui et al.

(2011). It is overwhelmingly reported that the strength of geomaterial will decrease when its temperature increases, e.g., the works by Okada (2005 and 2006). Volumetric change of geomaterials induced by heating was also conducted by Towhata et al. (1993), Laloui and Cekerevac (2003), Cekerevac and Laloui (2004). For instance, an interesting phenomenon was reported in the work by Cekerevac and Laloui (2004) that, the volumetric change of geomaterials due to heating under constant isotropic stress condition depends on the initial overconsolidation ratio (OCR), that is, the thermal volumetric strain will change from contraction to expansive when OCR increases from 1 to 12.

In the following chapter, an isotropic element heating test and a field heating experiment reported by Gens et al. (2007) have been simulated by the proposed program called as SOFT in order to verify the applicability of the proposed numerical method presented in Chapter 4. The used constitutive model is the thermo-elasto-viscoplastic model for soft rock described in Chapter 2.

6.2 THM Analysis of Isotropic Element Heating Test

Thermodynamic behavior of geomaterials has been investigated extensively for years and many results can be found in literature. Isotropic element heating test under drained condition is an effective way to investigate the volumetric change of the test specimen due to heating, in which the specimen is firstly consolidated to a prescribed stress and then unloaded to form a specified OCR state. After then the specimen is heated to a prescribed temperature under constant confining stress in a very slow rate in order to prevent the generation of EPWP. In laboratory test at room temperature, the volumetric change of a specimen is usually measured by the water discharge of the specimen. In the heating test, however, it is no longer possible because the thermal dilation of the specimen comes from both the soil particles and the pore water. Campanella and Mitchell (1968) suggested a simple formula to estimate the volumetric change of the specimen under the isotropic element heating test as:

$$\varepsilon_v^T = \frac{\Delta V_{drain} - (\alpha_T^f V_f + \alpha_T^s V_s)\Delta T}{V} \tag{6.2.1}$$

where, $\Delta V_{drain}, V_f, V_s$ and V are the volumes of the measured drained water, the pore

water, the soil particles and the total volume of sample.
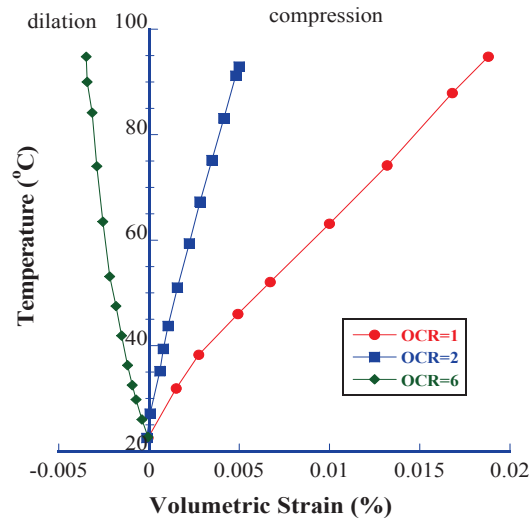
Fig.6.1 Thermal volumetric strain of soft rock measured by drained water in laboratory test under different OCR (Baldi G. et al., 1991)

Fig.6.1 shows a very interesting result (Baldi et al., 1991), in which the heat-induced volumetric strain, measured by the quantity of the drained water and calculated by Eq.(6.2.1), was dependent on OCR. That is, the specimen will change from shrinking to expansion as OCR increases. Afterwards, some other researchers also reported the same test results, e.g., the works by Cekerevac and Laloui (2004) and Cui et al. (2009).

Fig.6.2 FEM mesh (one element) for analyzing heating test

It is worth noting that Eq.(6.2.1) does consider the expansive volume contributed both from the soil particles and the pore water due to heating, the influence of soil-water interaction 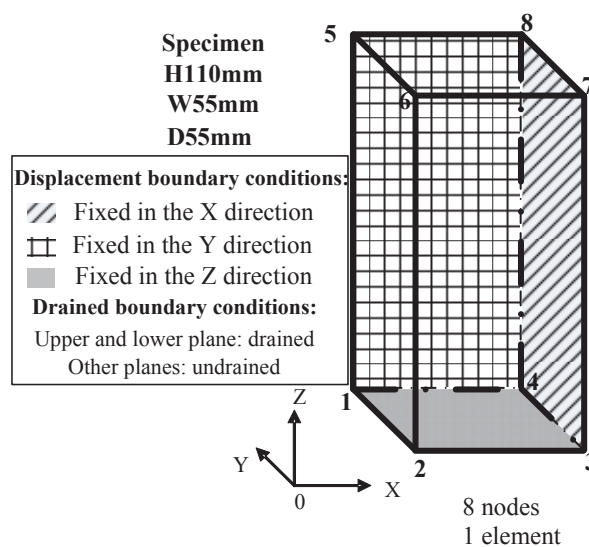during the heating process, however, is not considered. In the present paper, the heating test on a clay (Baldi et al., 1991) is simulated by the proposed THM-FEM scheme as a BVP. In the work by Zhang et al. (2005), one important assumption is that the soft rock can be considered as a heavily overconsolidated soil, and the model for soft rock is based on the concept of critical state adopted firstly in Cam-clay model. Therefore, the proposed model is also applicable to clay by using the parameters for soil.

The finite element mesh and boundary condition (one element) used in the THM analysis using the program SOFT is shown in Fig.6.2. Because only three planes are fixed in one direction, that is, only one node, Node 4, is fixed in all three directions, the sample can change its volume freely due to thermal expansion, the same condition as in the test. The initial temperature is set to be 22°C and the specimen is heated gradually up to 90°C with a rate of 4°C /h.
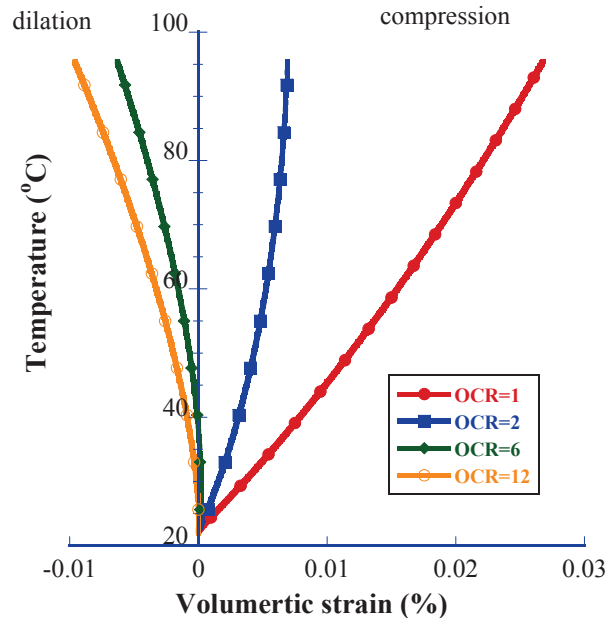

Fig.6.3 Thermal volumetric strain under different OCR calculated by drained water in THM analysis for the heating test

Table 6.1 Physical properties and material parameters of clay

	parameters		Physical properties	
	Young's modulus E (MPa)	300.	Pre-consolidation pressure σ_c (MPa)	0.60
	Poisson's ratio ν	0.35	**Thermal expansion** rock α^s_T (1/K)	8.0×10^{-6}
	Stress ratio at critical $R_{CS}(=\sigma_1/\sigma_3)$	10.9	**coefficient** water α^f_T (1/K)	2.1×10^{-4}
	Plastic stiffness E_p	0.020	Permeability k (m/min)	3.0×10^{-9}
	Potential shape parameter β	1.5	Thermal conductivity K^s_t (kJ m^{-1} K^{-1}Min^{-1})	0.18
	Time dependent parameter $\tilde{\alpha}$	0.42	Specific heat C^s (kJ Mg^{-1} K^{-1})	840.
	Time dependent parameter C_n	0.025	Heat transfer coefficient of air boundary	
	Overconsolidation parameter $\mathbf{a}$	2000.	α_c ((kJ m^{-2} K^{-1} Min^{-1})	230.
	Reference void ratio e_0 (at σ_{m0}=98kPa)	0.85	Specific heat of water C^w (kJ Mg^{-1} K^{-1})	4184.

The material parameters and the initial stress condition for the specimen of the clay are listed in Table 6.1. In calibrating the material parameters, due to the lack of element shear loading test, it is impossible to calibrate the value of the stress ratio at critical $R_{CS}(=\sigma_1/\sigma_3)$. For simplicity, the value was assumed to be the same value as those of soft sedimentary rocks at low confining stress (σ_3=98kPa). This assumption is thought to be acceptable because only isotropic loading was involved in the heating test.

The heat-induced volumetric strain is calculated by the amount of drained water indirectly, and its relation with the temperature for different OCR is depicted in Fig.6.3. It is known from the figure that the thermal volumetric strain changes from shrinking to expansion as the OCR increases, which coincides well with the experimental results depicted in Fig.6.1. In Fig.6.4, however, it is found that the calculated volumetric strain of soil particle is always dilatant with the increase of temperature, no matter what OCR may be! This phenomenon just indicates that during heating, both the pore water and the soil particles expand but with different degree because the thermal expansion coefficient of water is much larger than those of soil particle, resulting in an apparent phenomenon of water discharge, which was explained as 'shrinking or compression'. In high value of OCR, the expansion of the soil particles becomes much larger than those of water, resulting in water absorption, which was explained as expansion. In conclusion, the observed phenomenon in the laboratory heating test is just a BVP of soil-water-heat interaction, rather than an inherent property of the soil itself. Under the free condition in which the isotropic confining stress is kept constant, the soil particles will always expand with the increase of temperature, no matter what OCR may be.
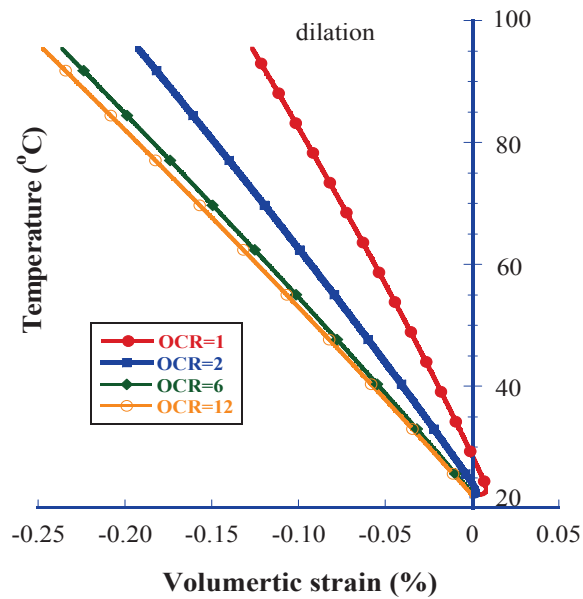
Fig.6.4 Calculated change of volumetric strain of soil particles under different OCR due to thermal effect

6.3 THM Analysis of Real-Scale Field Heating Test

In this section, a field experiment of heating process (HE-D), carried out within a soft rock called as Opalinus clay by Mont Terri underground laboratory, is simulated by the THM analysis using the program SOFT. The schematic layout of field test is shown in Fig.6.5. Two heaters were installed in a niche excavated from the main laboratory tunnel. The heaters are 2m in length and 30cm in diameter. A confining pressure of 1MPa was applied to the surrounding ground so that it can ensure a good contact between the heaters and the surrounding ground. The separating distance between the two heaters is 0.8m. Three phases of heating process had been implemented, as showed in Table 6.2. The soft rock is initially saturated by water. The detailed information about the experimental condition can be referred to the works by Jia et al. (2007) and Gens et al. (2007).
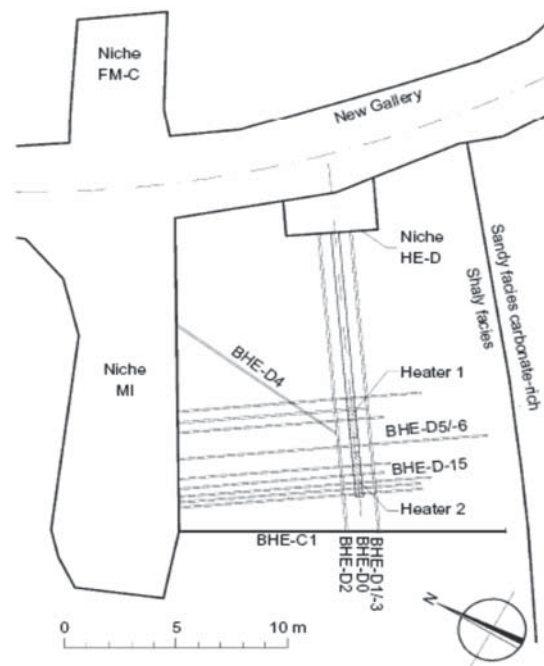
(a) Overview plane view of the field heating test
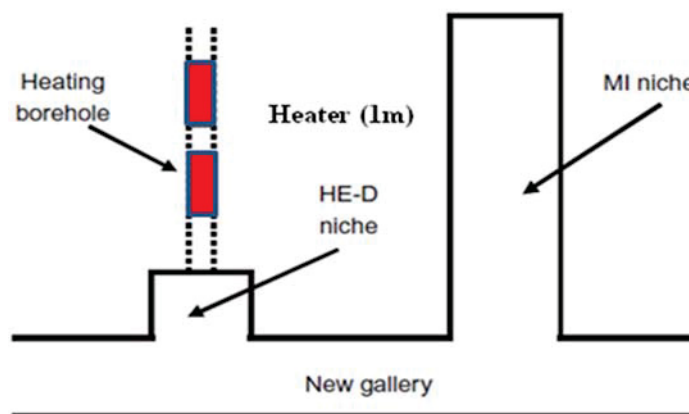
(b) Enlarged plane view of the field heating test

Fig.6.5 Layout of the field heating test (Jia et al., 2007)

For simplicity, the mechanically isotropic condition of the soft rock is assumed in the present calculation, which may partly negate the benefits of the proposed model, that is, the ability to take into consideration the influence of intermediate principal stress. Therefore, compared to the simulation by Gens et al. (2007), only 1/8 area is considered. The 3D mesh consists of 4275 cubic 8-node isoparametric elements with the size of

8m×10.4m×8m, as shown in Fig.6.6. The upper, the back and the right surfaces are under undrained and insulated condition, while the other three surfaces are under drained condition and the initial temperature at these surfaces is fixed at 15°C. The initial water pressure is given 1MPa and the initial principal stresses are given 3MPa, 5MPa and 7MPa respectively, which are the same as those in the test (Gens et al., 2007).

Table 6.2 Stages of the heating test and corresponding analyses

Stage	Start: day	End: day	Duration: day	Activity
1	0	90	90	First heating phase (19.5kJ/min/heater)
2	91	339	248	Second heating phase (58.5kJ/min/heater)
3	340	518	180	Cooling phase
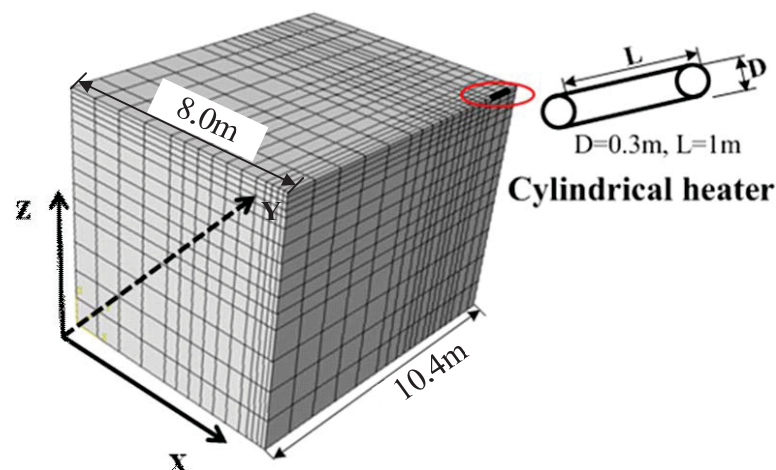
Fig.6.6 Bird view of 3D FEM mesh

In order to investigate the mechanical behavior of the rock near HE-D experiment site, conventional drained triaxial compression tests (Jia et al., 2007) were conducted on two geomaterials at Mont Terri site under different confining pressures at room temperature. The test results are simulated with the proposed modified model, by which it is possible to calibrate the material parameters of the geomaterial where the HE-D experiment was conducted.

Fig.6.7 shows the simulations of the triaxial compression tests (Jia et al., 2007) under different constant comfining stress for Opalinus mudstone (silty facies). The material parameters of Opalinus mudstone used in the simulation are listed in Table 6.3.

It is known from the comparisons that under small confining pressure, the rock behaves more brittle, that is, a sharp drop of strength after peak strength occurred, which is still difficult to be described accurately by the modified model. This limitation of the model should be improved in the future study.

Table 6.3 Physical properties and parameters of Opalinus mudstone (silty facies)

E (MPa)	E_p	a	$\tilde{\alpha}$	β	C_n	v	R_{CS}		e_0
5000.	0.0116	900.	1.5	1.5	0.0050	0.020	19.4(σ_3=0.1MPa)	2.83(σ_3=1.0MPa)	0.157

σ_c =500 MPa
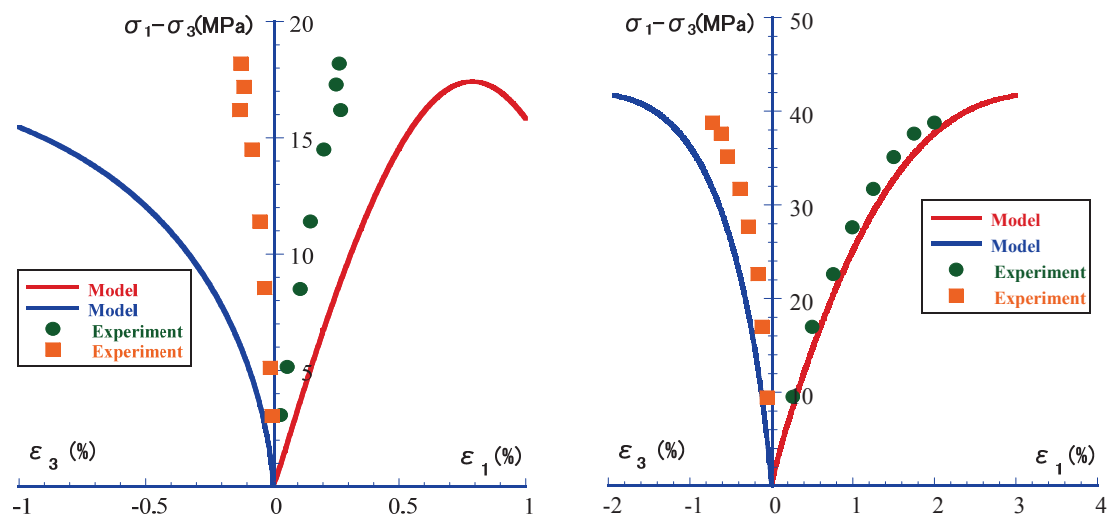
(a) Constant comfining stress (σ_3=0.1MPa)   (b) Constant comfining stress (σ_3=10MPa)

Fig.6.7 Simulations of triaxial compression tests (Jia et al., 2007) under different conditions for Opalinus mudstone (silty facies)

Fig.6.8 Simulations of triaxial compression tests (Jia et al., 2007) under confining

pressure σ₃=8.0 MPa for Opalinus clay (sand facies)

Fig.6.8 shows the simulations of triaxial compression tests (Jia et al., 2007) under confining pressure σ_3=8.0 MPa for Opalinus clay 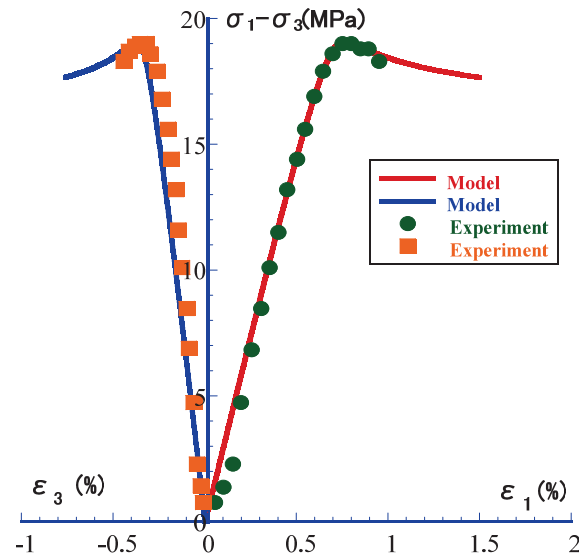(sand facies). It is seen from the figures that the proposed model can well describe the basic mechanical behavior of Mont Terri geomaterials, such as the confining pressure dependency, the strain-hardening and the strain-softening. Based on this calibration, the parameters of the Opalinus clay are determined and their values are listed in Table 6.4.

Table 6.4 Physical properties and material parameters of Opalinus clay (sand facies)

parameters			Physical properties		
	Young's modulus E (MPa)	9800.		Pre-consolidation pressure σ_c (MPa)	900.
	Poisson's ratio ν	0.295		**Thermal expansion** rock α^s_T (1/K)	8.0×10^{-7}
	Stress ratio at critical $R_{CS}(=\sigma_1/\sigma_3)$	3.0		**coefficient** water α^f_T (1/K)	2.1×10^{-4}
	Plastic stiffness E_p	0.0020		Initial permeability k (m/s)	3.0×10^{-13}
	Potential shape parameter β	1.5		Thermal conductivity K^s_t (kJ m^{-1} K^{-1}Min^{-1})	0.18
	Time dependent parameter $\tilde{\alpha}$	1.5		Specific heat C^s (kJ Mg^{-1} K^{-1})	840.
	Time dependent parameter C_n	0.0050		Heat transfer coefficient of air boundary	
	Overconsolidation parameter $\mathbf{a}$	8000.		α_c((kJ m^{-2} K^{-1} Min^{-1})	230.
	Reference void ratio e_0 (at σ_{m0}=98kPa)	0.159		Specific heat of water C^w(kJ Mg^{-1} K^{-1})	4184.

It is pointed out by Yashima et al. (1998), Gens et al. (2007, 2009) and Jia et al. (2007) that the value of permeability will increase with the increase of temperature. Two factors may be considered as the reasons for this phenomenon. One is that the rock

subjected to high temperature may result in a collapse of the integrity and occurring of micro cracks. Another is that the viscosity of the liquid will decrease with the increase of temperature. Because the permeability of water is not directly measured with temperature in the field test, Jia et al. (2005) or Gens et al. (2007) just gives a function to express the relationship between the permeability and temperature in order to fit the test results such as EPWP.   In the THM analysis for simulating the results of the HE-D experiment in this paper, the interpolation method employing some values of the permeability at some specified temperatures is used to describe the change of the permeability with temperature. The relation between the permeability and the temperature used in the analysis is shown in Fig.6.9.
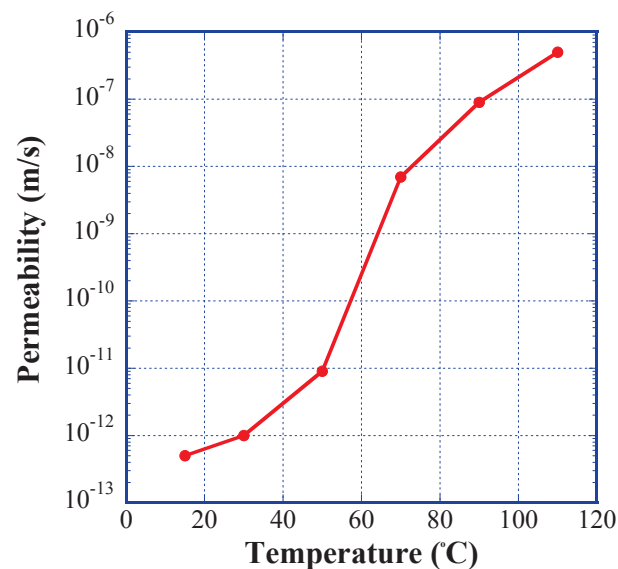
Fig.6.9 Relation between permeability and temperature used in THM analysis

Fig.6.10 shows the change of the temperature at the center of the heater with time. It is found that the temperature reaches about 40° at first heating phase, and then increases very sharply at the second heating phase up to the highest temperature of about 100°. When the power of heater is switched off, the temperature soon decreased sharply. From the results of the test and the calculation, it is known that the calculation can well describe the experimental data.

Fig.6.10 Change of temperature at the center of heater with time (test by Jia et al., 2007)

Fig.6.11 Change of temperature with time at different positions (test by Jia et al., 2007)

Fig.6.12 Calculated temperature distributions at different time on cross section

Fig.6.11 shows the evolutions of temperatures at different positions away from the heater. It is known that the THM analysis can also describe well the change of temperatures measured in the HE-D experiment on the whole, such as the sharp increase and the sharp decrease of the temperature for all selected positions.

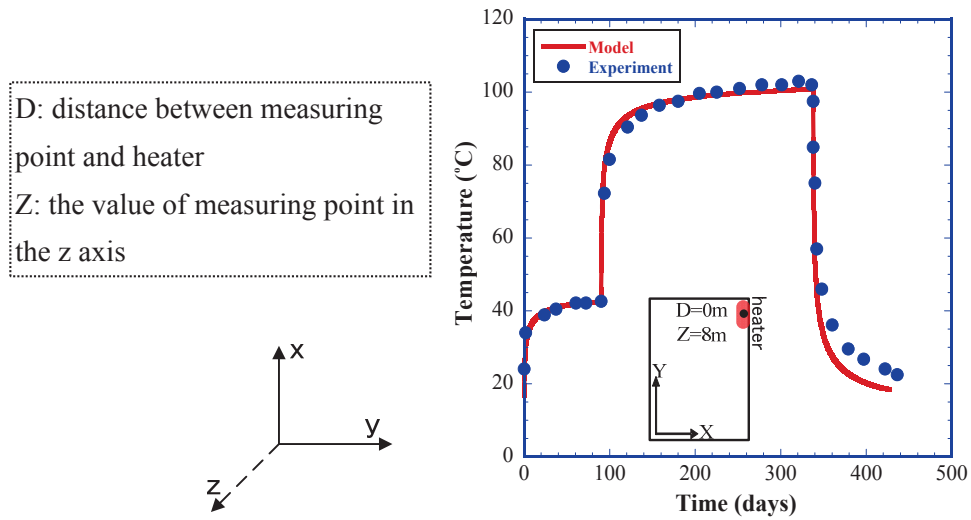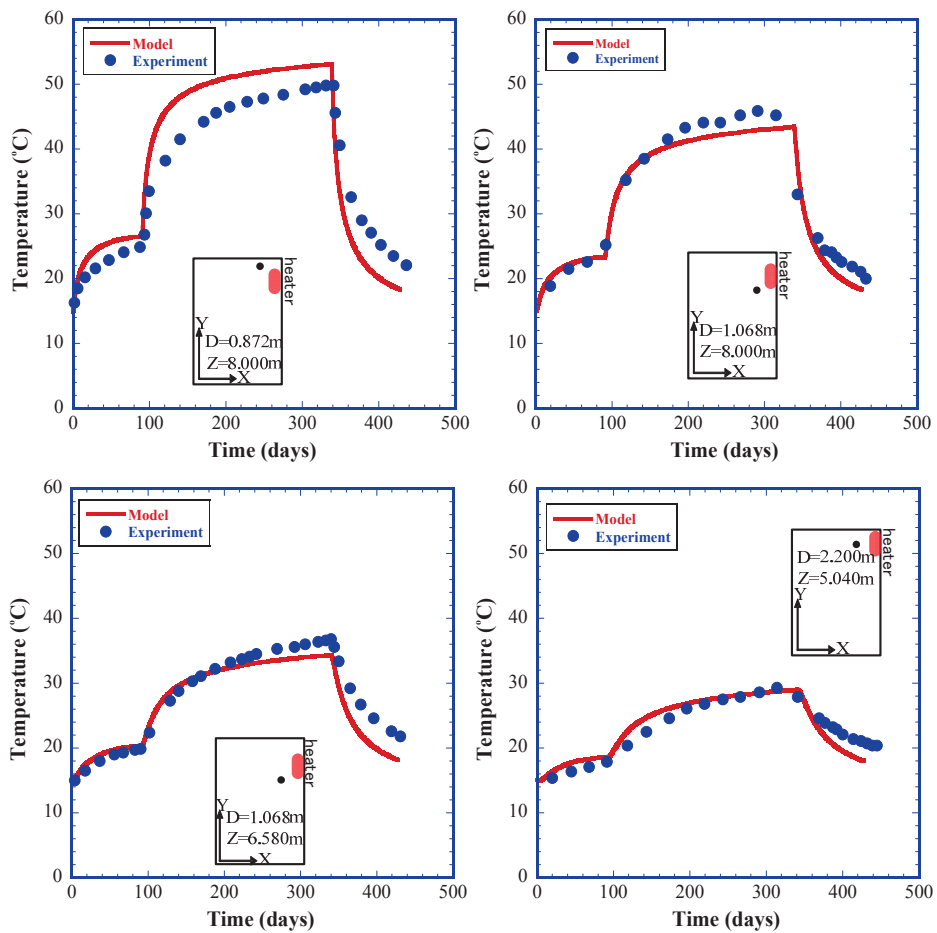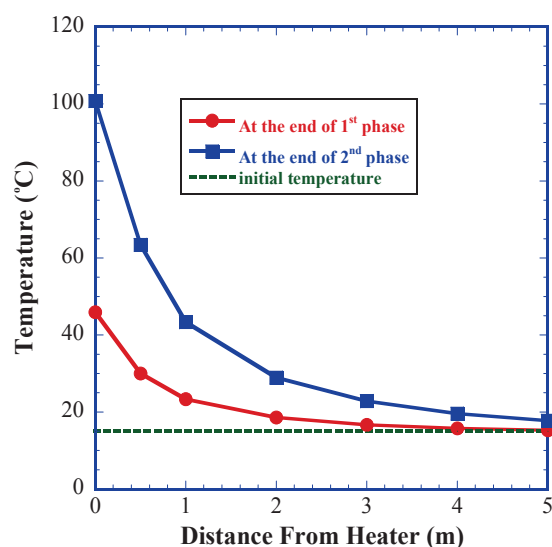Fig.6.12 shows the computed temperature distributions at various times on a cross section. It is known from the figure that the nearer the distance from the heater is, the higher the temperature will be. There is no prominent increase of temperature at the distance 5m away from the heater due to the low thermal conductivity of the rock.

The evolution of EPWP with time is depicted in Fig.6.13 at different positions away from the heater. It is found that EPWP increases sharply when the temperature rises up suddenly, and then it will decreases with time even though the temperature is increasing. The highest value of EPWP is up to about 3MPa. The increase of EPWP is mainly due to the fact that thermal expansion coefficient of water is much higher than that of the soft rock. Owing to the low permeability of rock, the drainage is slow and therefore the expansion of the pore water is impeded, resulting in the increase of the pore pressure at the initial time of heating. Later, as the migration of pore water from the heat source is gradually accelerated due to the increase of the permeability, EPWP is allowed to dissipate and consequentially decrease. On the whole, the evolution of EPWP is well reproduced except for the site at D=1.35m /Z=8.0m. The reason may be that the isotropic condition is assumed in the simulation. In fact, the Opalinus mudstone

exhibits significant anisotropy in its mechanical and thermal behaviour as reported in Gens et al. (2007).
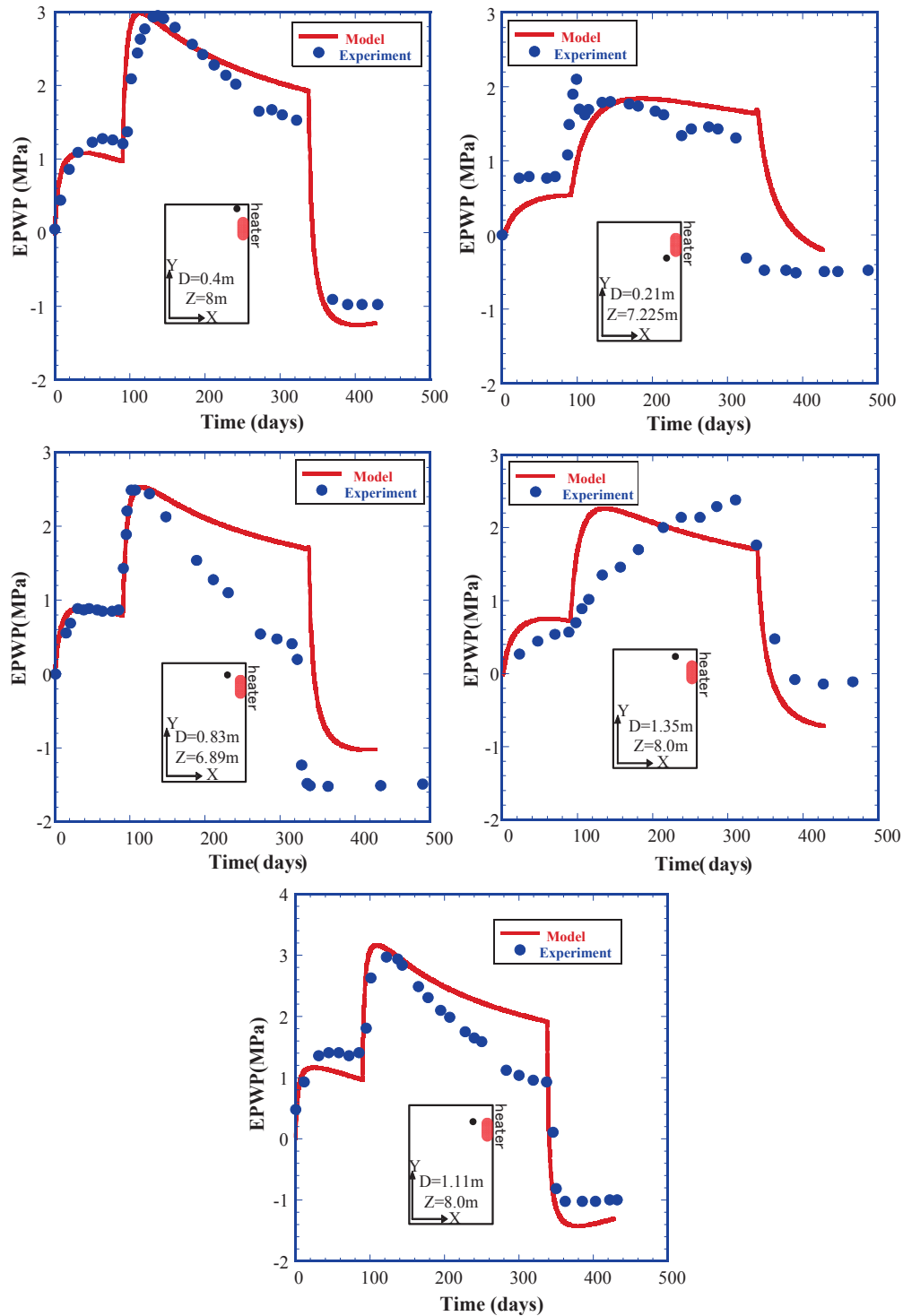
Fig.6.13 Variation of EPWP with time at different positions (test by Jia et al., 2007)

The heat-induced strains are also investigated. Fig.6.14 shows the calculated and test results of horizontal strain ε_y at different positions. It is found that the calculation can describe the change of the strain qualitatively if compared with the test data. The strain of the rock near the heater is expansive; while the strain of the rock far away from the heater is compressive. It is understandable that the rock may behave expansive due to the significant increase of temperature. Nevertheless, the change of temperature at the places far away from the heater is rather small. Therefore, the expansion of the soft rock far away from the heater is very small compared with those near the heater. As the results, swelling force caused by the expansion of the rock near the heater will cause a compression of the rock far away from the heater.
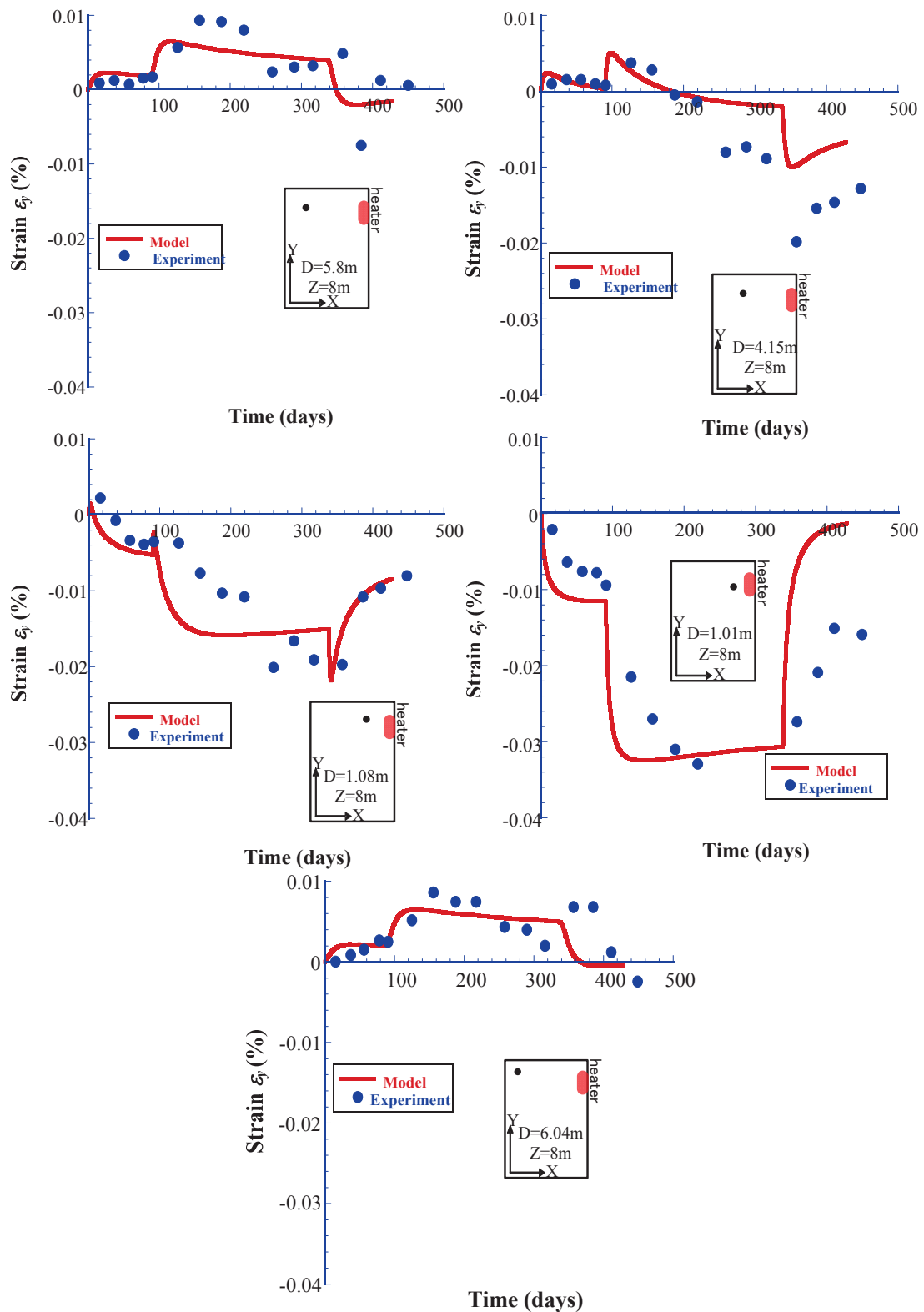
Fig.6.14 Variation of strain ε_y with time at different positions (test by Jia et al., 2007)

6.4 Conclusions

In this chapter, based on the modified model written in chapter 2, the proposed numerical analysis is used to simulate the thermo-hydraulic-mechanical behavior of geological materials. Simulations for an isotropic element heating test and a real-scale field heating test have been conducted to verify the applicability of the program. The following concluding remarks can be given as:

1. An isotropic element heating test is simulated by the proposed THM analysis based on the modified thermo-elasto-viscoplastic model. The calculation can explain well the phenomenon observed in the test that the heat-induced volumetric strain measured by the water discharge changes from shrinking to expansion as OCR increases during the isotropic heating process. From the THM analysis, it is found that soil skeleton always expands with the increase of temperature regardless of what kind of OCR may be. The discharge of the water is just caused by different thermal expansion properties of the soil particles and the pore water. In a word, this phenomenon is merely a boundary value problem with soil-water interaction, not an inherent property of the rock itself that was regarded by some researchers.

2. A field test of heating process Gens et al. (2007) is also simulated with the proposed THM analysis based on the modified thermo-elasto-viscoplastic model. It is found that the proposed numerical method can well describe the THM behavior observed in the test, such as the changes of temperature, the EPWP and the heat-induced strain.

REFERENCES

1) Akesson M., Jacinto A. C., Gatabin C., Sanchez M. and Ledesma A. (2009): Bentonite THM behavior at high temperatures: experimental and numerical analysis, *Getechnique*, Vol. 59, No. 4, 307-318.

2) Baldi G, Hueckel T, Peano A, Pellegrini R. (1991): Developments in modeling of thermo-hydro-geomechanical behavior of Boom clay and clay-based buffer materials, *Report EUR 13365, Commission of the European Communities, Nuclear science and technology*.

3) Campanella R. G. and Mitchell J. K. (1968): Influence of temperature variations on soil behavior, *Journal of Soil Mechanics & Foundations Division*, Vol. 94, No. 3, 709-734.

4) Cekerevac C. and Laloui L. (2004): Experimental study of thermal effects on the mechanical behavior of a clay, *International journal for numerical and analytical methods in geomechanics*, Vol. 28, 209-228.

5) Cui, Y.J., Tang, A.-M., Qian, L.X., Ye, W.M., Chen, B. (2011): Thermal-mechanical behavior of compacted GMZ bentonite, *Soils and Foundations*, Vol.51, No. 6, 1065-1074.

6) Cui Y. J., Le T. T., Tang A. M., Delage P. and Li X. L. (2009): Investigating the time-dependent behavior of Boom clay under thermomechanical loading, *Getechnique*, Vol. 59, No. 4, 319-329.

7) Gens A., Vaunat J., Garitte B. and Wileveau Y. (2007): In situ behavior of a stiff layered clay subject to thermal loading: observations and interpretation, *Geotechnique*, Vol.57, No. 2, 207-228.

8) Gens A., Sanchez M., Do L., Guimaraes N., Alonso E. E., Lloret A., Olivella S., Villar M. V., and Huertas F. (2009): A full-scale in situ heating test for high-level nuclear waste disposal: observations, analysis and interpretation, *Geotechnique*, Vol. 59, No. 4, 377-399.

9) Gens A. (2010): Soil-environment interactions in geotechnical engineering, *Geotechnique*, Vol. 60, No. 1, 3-74.

10) Jia Y., Wileveau Y., Su K., Duveau G. and Shao J. F. (2007): Thermo-hydro-mechanical modeling of a situ heating experiment, *Geotechnique*, Vol. 57, No. 10, 845-855.

11) Laloui L. and Cekerevac C. (2003): Thermo-plasticity of clays: an isotropic yield mechanism, *Computers and Geotechnics*, Vol. 38, No. 8, 649-660.

12) Oka F., Yashima A., Shimata T., Shibata T., Kato M. and Uzuoka R. (1994): FEM-FDM coupled liquefaction analysis of a porous soils using an elasto-plastic model, *Applied Scientific Research*, Vol. 52, 209-245.

13) Okada T. (2005): Mechanical properties of sedimentary soft rock at high temperatures (Part 1)-Evaluation of temperature dependency based on triaxial compression test, *Civil Engineering Research Laboratory Report*, No. N04026 (in Japanese).

14) Okada T. (2006): Mechanical properties of sedimentary soft rock at high temperatures (Part 2)-Evaluation of temperature dependency of creep behavior based on unconfined compression test, *Civil Engineering Research Laboratory Report*, No. N05057 (in Japanese).

15) Salager, S., Francois, B., Youssoufi, M.S.E., Laloui, L., Saix, C. (2008): Experimental investigations of temperature and suction effects on compressibility and pre-consolidation pressure of a sandy silt, *Soils and Foundations*, Vol. 48, No. 4, 453-466.

16) Sawada M., Okada T., Tani K., Takakura N. and Ikenoya T. (2009): In-situ heating test in the sedimentary soft rock (part 2)-Application of thermo-hydro-mechanical coupled analysis to the sedimentary soft rock, *Civil Engineering Research Laboratory Report*, No. N08055 (in Japanese).

17) Towhata I., Kuntiwattanaku P., Seko I. and Ohishi K. (1993): Volume change of clays induced by heating as observed in consolidation tests, *Soils and Foundations*, Vol. 33, No. 4, 170-183.

18) Yashima A., Leroueil S., Oka F. and Guntoro I. (1998): Modeling temperature and strain rate dependent behavior of clays: one dimensional consolidation, *Soils and Foundations*, Vol. 38, No. 2, 63-73.

19) Zhang F., Yashima A., Nakai T., Ye G. L. and Aung H. (2005): An elasto-viscoplastic model for soft sedimentary rock based on tij concept and subloading yield surface, *Soils and Foundations*, Vol. 45, No. 1, 65-73.

CHAPTER 7 THERMO-HYDRAULIC-MECHANICAL-AIR ANALYSIS ON HEATING TEST IN SATURATED/UNSATURATED GROUND

7.1 General

As the consequence of using radioactive materials in industrial, medical, military, a great challenge has been faced for the disposal of radioactive waste, especially for high-level radioactive waste (HLW). Until now, deep geologic disposal is considered as a valid and feasible way based on the concept of isolation from the biosphere, in which a nuclear waste repository is usually excavated below 300m within a stable geologic environment. It usually consists of three barriers: natural barrier, engineered barrier and technological barrier as shown in Fig.7.1. The technological barrier is a temporary canister including vitrified HLW during the transportation and storage. Engineered barrier is usually consisted of buffer material. Unsaturated bentonite is foreseen in many countries as the best candidate for buffer material because of its low hydraulic permeability, micro-porous structure, good sorption properties and swelling capacity. Natural barrier is usually soft rock or clay with low permeability.
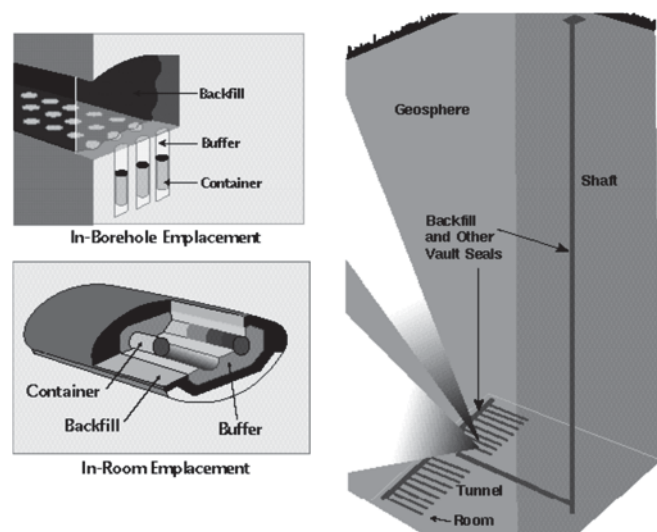

Fig.7.1 Multiple barrier concepts in deep geologic disposal

The engineered barrier and natural barrier will be subjected to high temperature released from the HLW, which will give rise to the coupled THMA problem. In addition, the bentonite is usually unsaturated during initial period, and will therefore be subjected to hydration from the surrounding rock, triggering further complex coupled THM phenomena. In order to have a good understanding of the processes that occurs in the near field, many larger-scale heating experiments in underground laboratories had been done around the world, e.g., the works by Gens et al. (2007, 2009), Munoz (2006). In reality, however, the heating period caused by the high-level nuclear waste disposal will last for tens of thousands years or even longer for some radioactive substances. Therefore, sometimes it is impossible to reproduce the whole process in the field tests. Numerical simulation will be another effective method to describe and predict the above-mentioned THMA behaviors on the condition that the numerical method is able to fit the results of field experiments, at least in a limited period.

The purpose of this Chapter is to understand and explain unsaturated water flow, temperature and mechanical behavior of the geomaterials during the hydration, heating and cooling phase. Two-dimensional (2D) finite element analysis of a field heating experiment (Munoz, 2006) is conducted using a program named as SOFT. In this research, thermo-mechanical behaviors of the ground are described by the unsaturated model introduced in Chapter 3. By comparing the numerical results with the test results, the applicability of the proposed numerical method is verified. In the THMA analysis, the air pressure is assigned as constant throughout the simulation.

7.2 Numerical Simulation of Heating Experiment

7.2.1 Brief description of heating test

The heating experiment is a large-scale heating test carried out in the Mont Terri Underground Rock Laboratory (Munoz, 2006). The objectives of the heating experiment were to acquire knowledge about the coupled THMA processes in the host rock and bentonite buffer.
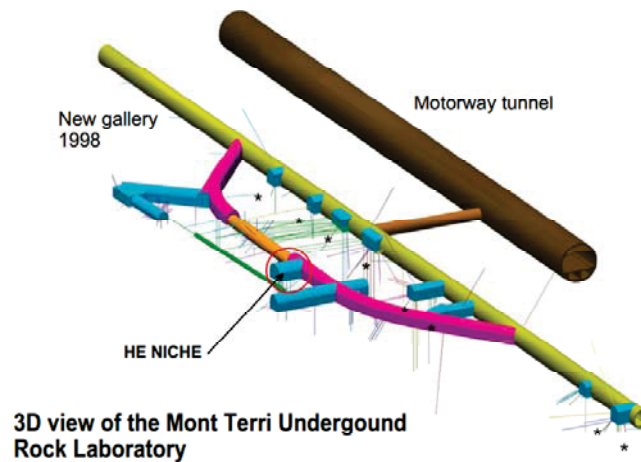
Fig.7.2. 3D view of the Mont Terri Underground Rock Laboratory and the location of the HE niche (Munoz, 2006)
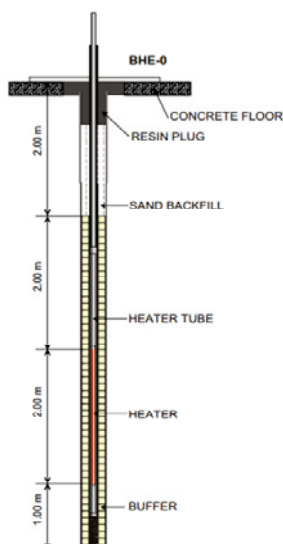
Fig.7.3. Vertical section of borehole BHE-0 (Munoz, 2006)

Fig.7.4. Setup of the test (Munoz, 2006)

The site of the heating experiment was located on the so-called "HE niche" on the west wall of the New Gallery of the underground rock laboratory, in the shaly faices of the Opalinus clay formations. Fig.7.2 shows the 3D view of the Mont Terri Underground Rock Laboratory and the location of the HE niche.

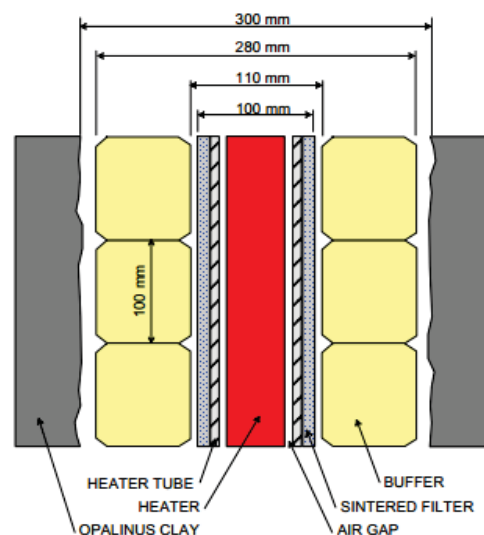A vertical borehole 300mm in diameter and 7.0m in depth, identified as BHE-0,

was drilled in the niche floor as shown in Fig.7.3. A heating tube with an external diameter of 100mm was placed in the axis of the borehole BHE-0. A heater of 75mm in diameter and 2.0m in length was placed into the heating tube. Details of the setup of the test are shown in Fig.7.4.

The heating experiment was conducted in 3 different phases. The first phase consists of the hydration of the bentonite buffer, which lasted 982 days. The hydration of the bentonite buffer was performed at four different depths at piezometric head of 2.0 m over the niche floor and the surrounding natural rock. The second phase is heating phase once the bentonite buffer was fully saturated. Firstly, heat power was applied in steps of 140W, 150W, 285W and 580W, until the heat-buffer contact reached a temperature of 100 ℃. Then, a constant temperature of 100 ℃ was maintained at the heater-bentonite contact, with a heating period of 540 days. Finally the heat power was switched off and the cooling phase began. In the experiment, the pore water pressure and the temperatures at some selected points are measured.

7.2.2 Numerical simulation and results

Due to the symmetry condition, only half of the area is considered. Fig.7.5 shows the 2D FEM mesh and mechanical boundary condition. In the analysis, the calculated results of THMA variables at some positions, marked with orange line in Fig.7.5, are selected to compare with the test results. For simplicity, the materials are assumed to be homogeneous and isotropic, focusing on THMA coupling process in the rock-buffer system. An isotropic stress state with a magnitude of 5MPa is assumed in the simulation, the same as the assumption in the wok by Munoz (2006). A total water head of 40m is given for the host rock, and initial temperature is 15 ℃. The atmospheric air pressure is kept constant. Material parameters of the bentonite and the rock used in the simulation are listed in Table 7.1.

Fig.7.6 shows the MCC of the bentonite and the host rock used in the simulation. It is found that the calculated MCC of the bentonite and the host rock can well describe the test results. The parameters of the MCC of the bentonite and the host rock are listed in Table 7.2. In the simulation, the initial degree of saturation of the bentonite buffer is 70%, which corresponds to a suction of s=136 MPa, measured at the field test.
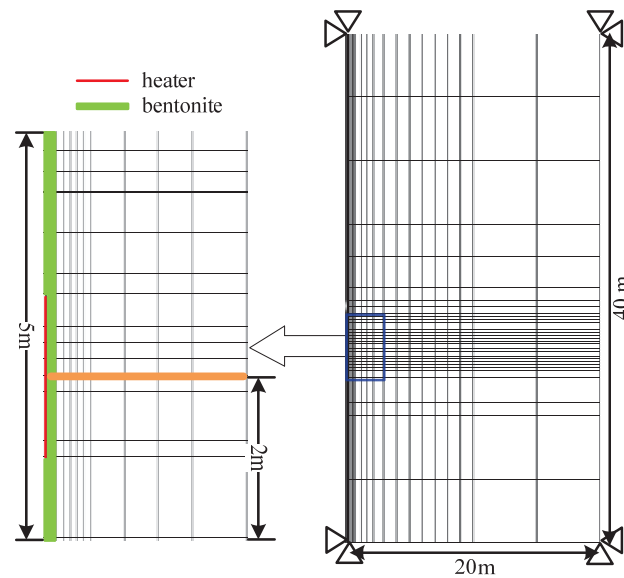
Fig.7.5. 2D FEM mesh and mechanical boundary condition

Table 7.1 Material parameters of　bentonite and rock

	Bentonite	Rock
Compression index	0.050	0.002
Swelling index	0.010	0.0001
Critical state parameter	1.80	1.90
Void ratio (*p'*=98 kPa on *N.C.L.*))	1.04	0.62
Poisson's ratio	0.30	0.3
Parameter of overconsolidation	5.00	5.0
Parameter of suction	0.00	0.00
Parameter of overconsolidation	1.00	1.0
Void ratio (*p'*=98 kPa on *N.C.L.S.*)	1.06	0.65
Thermal expansion coefficient (1/K)	1.0×10^{-5}	3.0×10^{-6}
Thermal expansion coefficient of water (1/K)	2.1×10^{-4}	
Thermal conductivity (kJ m^{-1} K^{-1}Min^{-1})	0.006	0.12
Specific heat (kJ Mg-1 K-1)	723	874
Specific heat of water	4184	

It is well known that the permeability of water is dependent on the degree of saturation, that is, the permeability increases along with the increase of the saturation. The permeability of water, however, was not measured in the test. In the THMA analysis on the heating test, as an alternative, an interpolation method employing some values of the permeability at some specified saturation is used to simulate the change of the permeability with saturation. The relation between the permeability of water and the degree of saturation used in the analysis is shown in Fig.7.7 in order to fit the results of

heating experiment.
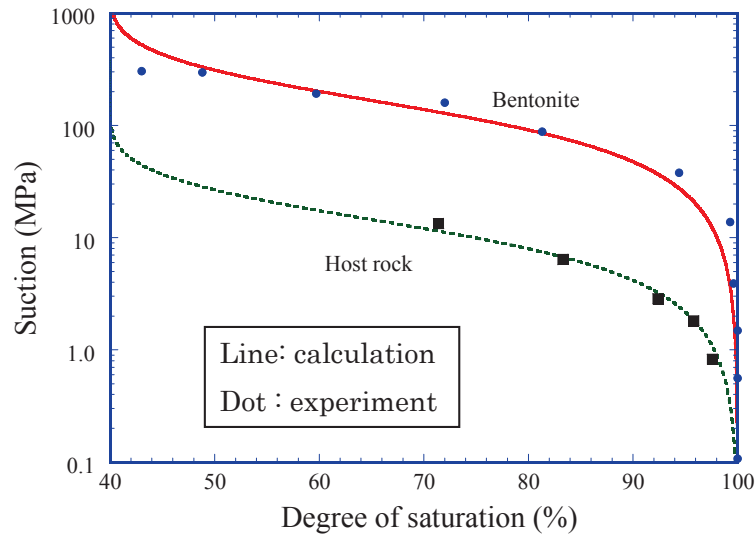
Fig.7.6. Moisture characteristic curve of bentonite and host rock
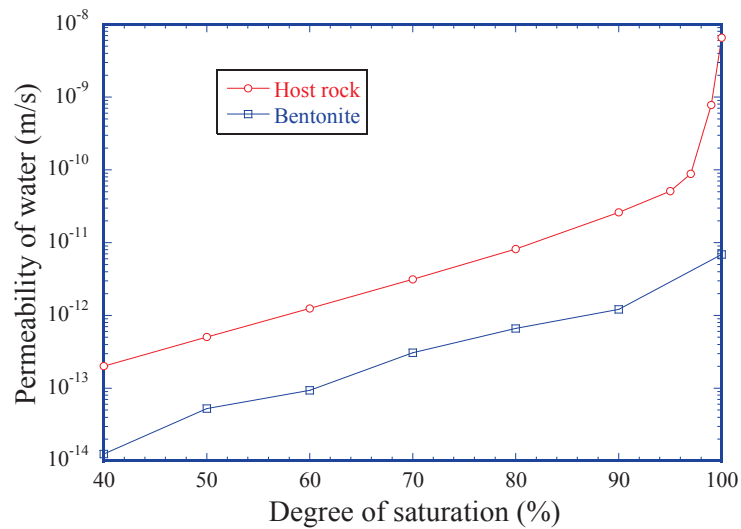
Fig.7.7. Estimated relationship between permeability of water and degree of saturation

Table 7.2 Material parameters of bentonite and rock

		Bentonite	**Rock**
Saturated degrees of saturation S_r^s		1.00	1.00
Residual degrees of saturation S_r^r		0.40	0.40
Parameter corresponding to drying AEV (kPa)	S_d	11000	21000
Parameter corresponding to wetting AEV (kPa)	S_w	800	1000
Initial stiffness of scanning curve (kPa) k_{sp}^e		25000	90000
Parameter of shape function c_1		0.000001	0.00003
Parameter of shape function c_2		0. 000005	0.00006
Parameter of shape function c_3		30.0	50.0
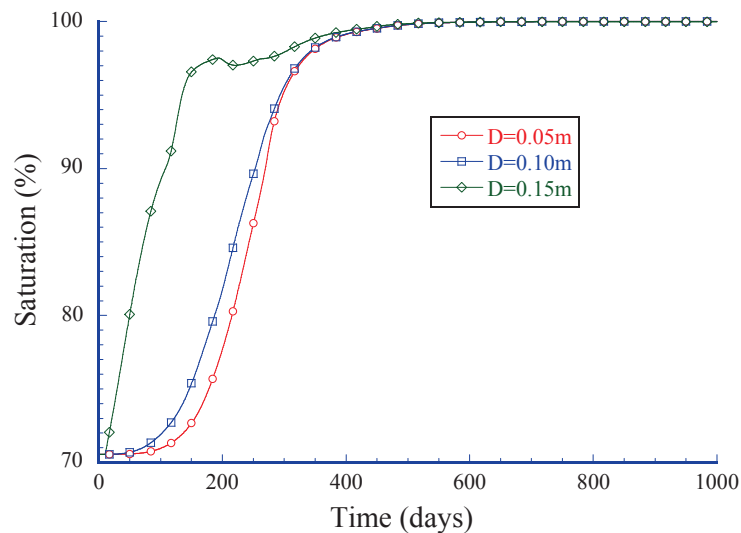
Fig.7.8. Change of degree of saturation for bentonite during hydration phase

Fig.7.8 shows the time evolution of the degree of saturation at different positions with time. It is known from the figure that the required time to fully saturate the bentonite is 400 days approximately. In the figure, D is the distance away from the heater

Fig.7.9 shows the transitory process of the degree of saturation in the surrounding rock at different positions with time, in which de-saturation and re-saturation process were clearly observed. It is found from the figure that the rock reaches the full saturation again after approximately 600 days of the hydration.
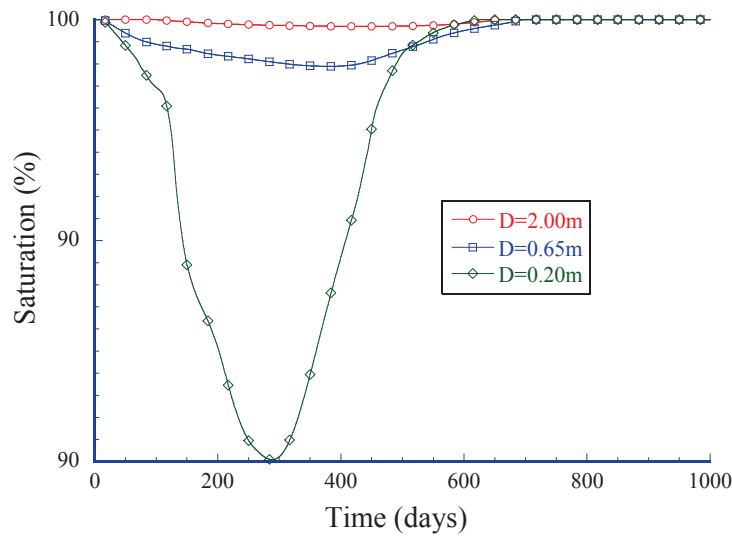
Fig.7.9. Change of degree of saturation for rock during hydration phase
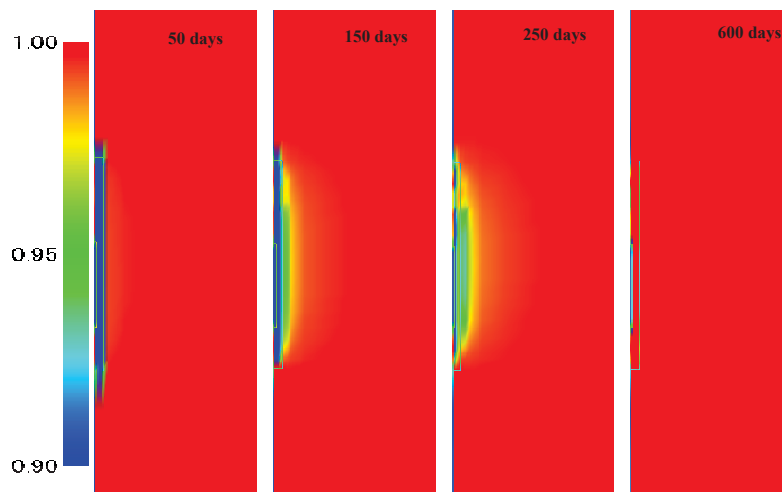
Fig.7.10. Distribution of the degree of saturation at some specified times during hydration phase

Fig.7.10 shows the distribution of the degree of saturation at specified time during the hydration phase. It is found that the rock near the bentonite firstly changes from saturated state to unsaturated state, this is because the water cannot transport in time due to the low permeability of rock. Later the rock was re-saturated with the migration of pore water.
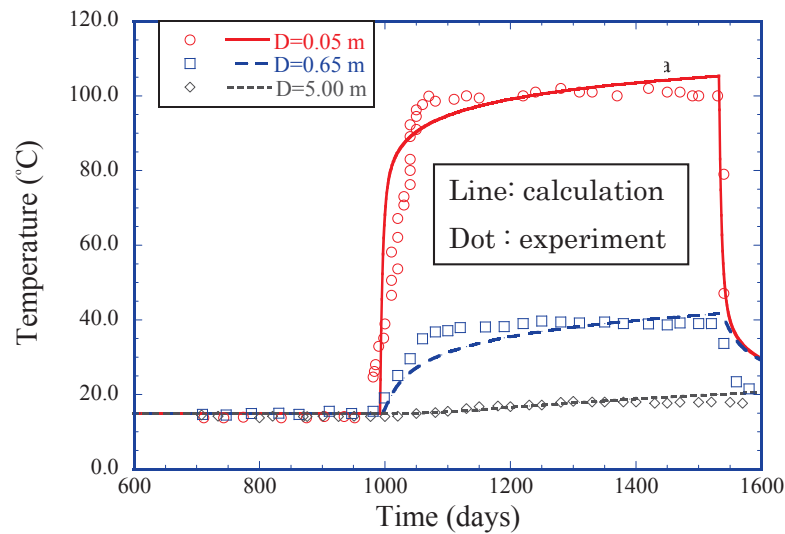
Fig.7.11. Change of temperature with time at different positions in heating phase

Fig.7.11 shows the evolutions of temperatures at different positions away from the heater. It is known that the THMA analysis can also well describe the change of temperatures measured in the HE-D experiment on the whole, such as the sharp increase and the sharp decrease of the temperature for all selected positions.
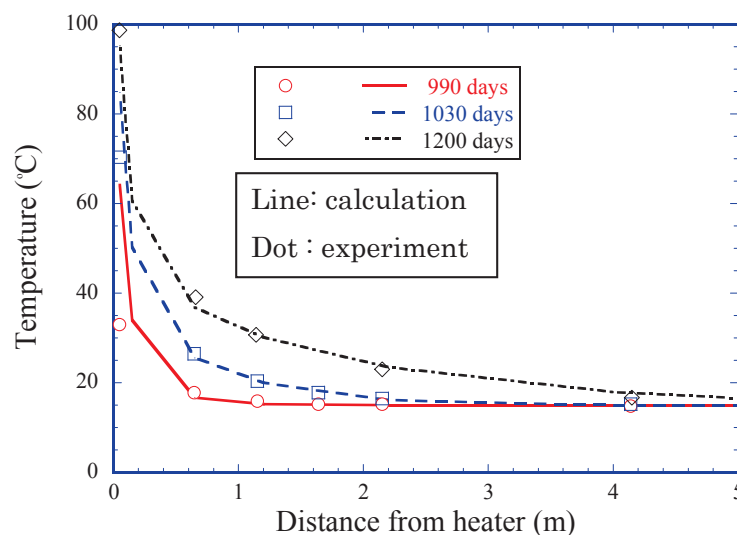
Fig.7.12. Temperature distributions at different time during heating phase
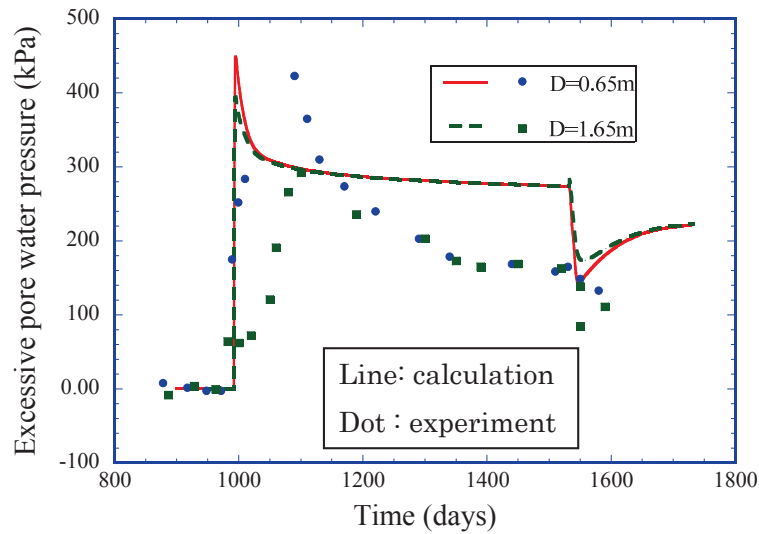
Fig.7.13. Change of excessive pore water pressure with time at different positions during heating and cooling phases

Fig.7.12 shows the comparison between the calculated and measured temperature distributions at different times along a cross section. It is known from the figure that the nearer the distance from the heater is, the higher the temperature will be. There is no prominent increase of temperature at the distance 5m away from the heater due to the low thermal conductivity of the rock.

Fig.7.13 shows the change of excessive pore water pressure with time at different positions during heating and cooling phases. It is known from the figure that the increase of temperature generates a significant increase of positive excessive water pressure, and the decrease of temperature will give rise to a decrease of the excessive water pressure. The change of the excessive pore water pressure is mainly due to the fact that thermal expansion coefficient of water is much higher than that of the rock. Owing to the low permeability of rock, the drainage is slow and therefore the expansion of the pore water is impeded, resulting in an increase of the pore pressure at the initial time of heating. Later, as the migration of the pore water, the excessive pore water pressure is allowed to dissipate and consequentially turns to decrease. The simulation can well describe the observed behavior on the whole.

7.3 Conclusions

In this chapter, a heating experiment (Munoz, 2006) is simulated, using a program of finite element method (FEM) named as SOFT, in order to investigate the THMA behavior of bentonite-host rock composite structure under unsaturated condition. The program is based on a FE-FD scheme in fully coupled soil-water-air three-phase field theory under non-isothermal condition. In the simulation, a rational constitutive model using the Bishop-type skeleton stress and the degree of saturation as the state variables is adopted, which can describe the behavior of saturated and unsaturated soil in unified way. Based on the simulated results, it is known that the present simulation can properly describe the THMA behaviors observed in the heating experiment such as the hydration of water, the evolution of temperature, the evolution of excessive pore water pressure to some extent. It is, therefore, possible to apply this numerical method to investigate the real field problem in the geologic disposal of high-level radioactive waste (HLW).

References

1) Gens A., Vaunat J., Garitte B. and Wileveau Y. (2007): In situ behavior of a stiff layered clay subject to thermal loading: observations and interpretation, *Geotechnique*, Vol.57, No. 2, 207-228.

2) Gens A., Sanchez M., Do L., Guimaraes N., Alonso E. E., Lloret A., Olivella S., Villar M. V., and Huertas F. (2009): A full-scale in situ heating test for high-level nuclear waste disposal: observations, analysis and interpretation, *Geotechnique*, Vol. 59, No. 4, 377-399.

3) Hashiguchi, K. and Ueno, M. (1977): Elastoplastic constitutive laws of granular material, Constitutive Equations of Soils, *Proc. 9th Int. Conf. Soil Mech. Found. Engrg.*, Spec. Ses. 9, eds. By Murayama, S. and Schofield, A. N., Tokyo, JSSMFE, 73-82.

4) Munoz, J. (2006): Thermo-hydro-mechanical analysis of soft rock, application to a large scale heating test and large scale ventilation test, *PhD thesis*.

5) Zhang, F. and Ikariya, T. (2011): A new model for unsaturated soil using skeleton and degree of saturation as state variables, *Soil and Foundations*, Vol. 51, No. 1, 67-81.

6) Zhang S. and Zhang F. (2009): A thermo-elasto-viscoplastic model for soft sedimentary rock, *Soils and Foundations*, Vol. 49, No. 4, 583-595.

CHAPTER 8 CONCLUDING REMARKS

8.1 Conclusions

The main objective of this study is to propose a unified THMA coupling finite element analysis to try to explain and investigate the geotechnical disasters related to multi-phase problem. This research can be divided into two parts:

The first part is the theoretic explanation of the proposed THMA numerical method. First of all, two rational constitutive models for soft sedimentary rock and unsaturated soils are introduced respectively. Then the theory of thermo-hydraulic-mechanical-air coupling finite element analysis is established in detail. The second part is the application of the proposed THMA numerical analysis into the BVP and its verifications. The following conclusions can be obtained in the present study:

(1) A thermo-elasto-viscoplastic model in normal stress space (Zhang and Zhang, 2009) is modified using the t_{ij} concept, which can not only describe the influence of temperature on the deformation and the strength of geomaterials but also can take into account the influence of intermediate principal stress. It needs to be emphasized here that compared with the model proposed by Zhang et al. (2005), only one physical property, the thermal expansion coefficient, is added to the modified model in the framework of the critical state soil mechanics. Then the performance of the modified model is confirmed with drained triaxial compression tests, plane-strain controlled compression tests and creep tests under different temperatures.

(2) In order to describe the influence of temperature on the mechanical behaviour of saturated/unsaturated soil, the equivalent stress concept proposed by Zhang and Zhang (2009) is incorporated into the constitutive model for unsaturated soil proposed by Zhang and Ikariya (2011). At the same time, the problem about the influence of void ratio on MCC is discussed according to the basic and intrinsic relationship of soil, and is considered as a BVP. The basic performance of the

proposed model is then illustrated through numerical study. Finally, the unified model will be validated against a variety of experimental data.

(3) The theory of a thermo-hydraulic-mechanical-air fully coupling finite element method is derived in detail. In the field equations, the excessive pore water pressure, the excessive pore air pressure, the displacement of solid phase and the temperature are used as unknown variables. In the THMA FE-FD scheme, FEM is used for spatial discretization of the equilibrium and the energy conservation equations, while the backward finite difference scheme proposed by Akai and Tamura (1978) is used for the spatial discretization of the continuity equation of water and air phase. It is worth noting that the energy conservation is not fully coupled with mechanical behavior in the scheme, because the energy dissipation due to the plastic deformation, described by the constitutive model (Chapter 3), is not included in the above conservation equation, though it might be very small and can be neglected in engineering sense if compared with the heat energy produced by nuclear waste.

(4) The triaxial compression tests under undrained and unvented conditions are firstly simulated by the proposed THMA numerical method in order to verify the validity of the proposed numerical method. In the simulation, the elementary behavior of the triaxial tests is calculated with 3D FE-FD analysis using one-element mesh. From the comparisons between the test and simulation, it is found that the proposed numerical method can well describe the test behaviors such as the skeleton stress path, the stress-strain relation, and the developments of PWP and PAP at different suctions under isothermal condition.

(5) The model tests on slope failure due to water injection or rainfall have also been simulated by the same proposed THMA numerical method under isothermal condition. Because the method is based on the soil-water-air fully coupling scheme, not only the seepage of water due to rainfall or water injection, the change of the degree of saturation, the migration of the air pressure, but also the mechanical behaviors of the unsaturated soil such as the deformation of the ground, the change of pore water pressure, the formation of the shear band occurred in the slope failure, can be simulated on the whole in an unified way, judging from the comparisons

between the measured and calculated results. It is particularly worth mentioning that due to the incorporation of a proper constitutive model for unsaturated soil, the calculation can well simulate the different failure behavior of the model Shirasu ground observed in the tests that, in Case 1 and Case 3, the slope collapses entirely while in Case 2, only the toe of the slope failed. In the analyses, all the material parameters of the Shirasu in different test cases are the same, which makes the sense for the application of the proposed numerical method. In the simulation of slope failure due to rainfall, though the air pressure is very small, its development is well simulated qualitatively if compared with field observation available in literature.

(6) An isotropic element heating test for saturated soil/soft rock is also simulated by the same proposed THMA analysis based on the modified thermo-elasto-viscoplastic model. The calculation can explain well the phenomenon observed in the test that the heat-induced volumetric strain measured by the water discharge changes from shrinking to expansion as OCR increases during the isotropic heating process. From the THMA analysis, it is found that soil skeleton always expands with the increase of temperature regardless of what kind of OCR may be. The discharge of the water is just caused by different thermal expansion properties of the soil particles and the pore water. In a word, this phenomenon is merely a boundary value problem with soil-water interaction, not an inherent property of the rock itself that was regarded by some researchers.

(7) A field test of heating process Gens et al. (2007) in saturated soft rock is also simulated with the proposed THMA analysis based on the same model. It is found that the proposed numerical method can well describe the THM behavior observed in the test, such as the changes of temperature, the EPWP and the heat-induced strain.

(8) Finally, a heating experiment (Munoz, 2006) is simulated in order to investigate the THMA behavior of unsaturated bentonite-saturated host rock composite structure using the same THMA analysis. In the simulation, a rational constitutive model introduced in Chapter 3 is adopted, which can describe the thermo-hydro-mechanical coupling behavior of saturated and unsaturated soil in unified way.

Based on the simulated results, it is known that the present simulation can properly describe the THMA behaviors observed in the heating experiment such as the hydration of water, the evolution of temperature, the evolution of excessive pore water pressure to some extent. It is, therefore, reasonable to say that the proposed numerical method can be applied to investigate the real field problem in the geologic disposal of high-level radioactive waste (HLW).

8.2 Future Work

Though a unified THMA numerical method has been proposed in this dissertation, many works should be done in the future work:

1. In the proposed THMA numerical method of this study, the problem, which water and air suffered from high temperature will cause a phase change to a certain extent, is not considered. In the future, this problem should be taken into consideration.

2. When the water/ air permeability is enough large (e.g. sand ground), the effect of the heat convection is much greater than that of the heat conduction in the process of heat transfer. Therefore, the heat convection should be considered in the proposed numerical program.

3. A unified constitutive model for geomaterials should be discussed and investigated more carefully in the future, because the hydro-mechanical behaviors of geomaterials are very sophisticated.

4. Much more numerical simulations should be done in the future to validate the performance of the numerical method against the experiment tests.

5. In this study, the proposed THMA numerical method can only deal with the static geotechnical problems, therefore, it should extend this method to dynamical condition in the future work.

References

1) Akai, K. and Tamura, T. (1978): Numerical analysis of multi-dimensional consolidation accompanied with elasto-plastic constitutive equation, *Proc. of JSCE*, No. 269, 95-104 (in Japanese).

2) Gens A., Vaunat J., Garitte B.   and Wileveau Y. (2007): In situ behavior of a stiff layered clay subject to thermal loading: observations and interpretation, *Geotechnique*, Vol.57, No. 2, 207-228.

3) Kitamura, R., Sako, K., Kato, S., Mizushima, T. and Imanishi, H. (2007): Soil tank test on seepage and failure behaviors of Shirasu slope during rainfall, *Japanese Geotechnical Journal*, Vol. 2, No. 3, 149-168 (in Japanese).

4) Munoz, J. (2006): Thermo-hydro-mechanical analysis of soft rock, application to a large scale heating test and large scale ventilation test, *PhD thesis*.

5) Sheng, D. and Zhou, A. N. (2011): Coupling hydraulic with mechanical models for unsaturated soils. *Canadian Geotechnical Journal*, 48(5), 826-840.

6) Zhang F., Yashima A., Nakai T., Ye G. L. and Aung H. (2005): An elasto-viscoplastic model for soft sedimentary rock based on tij concept and subloading yield surface, *Soils and Foundations*, Vol. 45, No. 1, 65-73.

7) Zhang S. and Zhang F. (2009): A thermo-elasto-viscoplastic model for soft sedimentary rock, *Soils and Foundations*, Vol. 49, No. 4, 583-595.

8) Zhang, F. and Ikariya, T. (2011): A new model for unsaturated soil using skeleton stress and degree of saturation as state variables. Soils and Foundations, 51(1), 67-81.

Appendix 1 (Jaumann stress rate tensor)

Some matrixes used for derivation

For simplicity, the superscript shows the node number (i=1,2,3···n-1,n), the subscript shows the *x,y,z* axis (j=1,2,3).

$$\vec{u} = [N]\vec{u}_N$$

$$\vec{L} = [B_{NL}]\vec{u}_N$$

$$\vec{D} = [B]\vec{u}_N$$

$$tr\vec{D} = \{B_v\}^T \vec{u}_N$$

$$\dot{\vec{u}} = \{\dot{u}_1 \quad \dot{u}_2 \quad \dot{u}_3\}^T$$

$$\vec{u}_N = \{\dot{u}_1^1 \quad \dot{u}_2^1 \quad \dot{u}_3^1 \quad \cdots \quad \dot{u}_1^n \quad \dot{u}_2^n \quad \dot{u}_3^n\}^T$$

$$\vec{L} = \{L_{11} \quad L_{22} \quad L_{33} \quad L_{12} \quad L_{21} \quad L_{23} \quad L_{32} \quad L_{31} \quad L_{13}\}^T$$

$$\vec{W} = \frac{1}{2}(\vec{L} - \vec{L}^T)$$

$$\{\Pi\} = \{\Pi_{11} \quad \Pi_{22} \quad \Pi_{33} \quad \Pi_{12} \quad \Pi_{21} \quad \Pi_{23} \quad \Pi_{32} \quad \Pi_{31} \quad \Pi_{13}\}^T$$

$$[B] = \begin{bmatrix} N_{,1}^1 & 0 & 0 & \cdots & N_{,1}^n & 0 & 0 \\ 0 & N_{,2}^1 & 0 & \cdots & 0 & N_{,2}^n & 0 \\ 0 & 0 & N_{,3}^1 & \cdots & 0 & 0 & N_{,3}^n \\ N_{,2}^1 & N_{,1}^1 & 0 & \cdots & N_{,2}^n & N_{,1}^n & 0 \\ 0 & N_{,3}^1 & N_{,2}^1 & \cdots & 0 & N_{,3}^n & N_{,2}^n \\ N_{,3}^1 & 0 & N_{,1}^1 & \cdots & N_{,3}^n & 0 & N_{,1}^n \end{bmatrix}$$

$$[B_{NL}] = \begin{bmatrix} N_{,1}^1 & 0 & 0 & \cdots & N_{,1}^n & 0 & 0 \\ 0 & N_{,2}^1 & 0 & \cdots & 0 & N_{,2}^n & 0 \\ 0 & 0 & N_{,3}^1 & \cdots & 0 & 0 & N_{,3}^n \\ N_{,2}^1 & 0 & 0 & \cdots & N_{,2}^n & 0 & 0 \\ 0 & N_{,1}^1 & 0 & \cdots & 0 & N_{,1}^n & 0 \\ 0 & N_{,3}^1 & 0 & \cdots & 0 & N_{,3}^n & 0 \\ 0 & 0 & N_{,2}^1 & \cdots & 0 & 0 & N_{,2}^n \\ 0 & 0 & N_{,1}^1 & \cdots & 0 & 0 & N_{,1}^n \\ N_{,3}^1 & 0 & 0 & \cdots & N_{,3}^n & 0 & 0 \end{bmatrix}$$

$$\{B_v\}^T = \left\{ N_{,1}^1 \quad N_{,2}^1 \quad N_{,3}^1 \quad \cdots \quad N_{,1}^n \quad N_{,2}^n \quad N_{,3}^n \right\}$$

$$\mathbf{W} = \begin{bmatrix} 0 & w_{12} & w_{13} \\ w_{21} & 0 & w_{23} \\ w_{31} & w_{32} & 0 \end{bmatrix}$$

$$\overset{\nabla}{\mathbf{T}'} \cdot \delta \mathbf{D} = \delta \vec{u}_N^{\ T} [B]^T [D^{ep}][B] \vec{u}_N$$

$$\left\{(tr\mathbf{D})\mathbf{T} - \mathbf{TL^T}\right\} \cdot \{\delta\mathbf{L}\} = (D_{11} + D_{22} + D_{33}) \begin{bmatrix} T_{11} & T_{12} & T_{13} \\ T_{21} & T_{22} & T_{23} \\ T_{31} & T_{32} & T_{33} \end{bmatrix} \cdot \{\delta\mathbf{L}\}$$

$$-\begin{bmatrix} T_{11} & T_{12} & T_{13} \\ T_{21} & T_{22} & T_{23} \\ T_{31} & T_{32} & T_{33} \end{bmatrix} \begin{bmatrix} L_{11} & L_{21} & L_{31} \\ L_{12} & L_{22} & L_{32} \\ L_{13} & L_{23} & L_{33} \end{bmatrix} \cdot \{\delta\mathbf{L}\}$$

$$= \{\delta\mathbf{L}\}^T \begin{bmatrix} T_{11} & T_{11} & T_{11} & 0 & 0 & 0 & 0 & 0 & 0 \\ T_{22} & T_{22} & T_{22} & 0 & 0 & 0 & 0 & 0 & 0 \\ T_{33} & T_{33} & T_{33} & 0 & 0 & 0 & 0 & 0 & 0 \\ T_{12} & T_{12} & T_{12} & 0 & 0 & 0 & 0 & 0 & 0 \\ T_{21} & T_{21} & T_{21} & 0 & 0 & 0 & 0 & 0 & 0 \\ T_{23} & T_{23} & T_{23} & 0 & 0 & 0 & 0 & 0 & 0 \\ T_{32} & T_{32} & T_{32} & 0 & 0 & 0 & 0 & 0 & 0 \\ T_{31} & T_{31} & T_{31} & 0 & 0 & 0 & 0 & 0 & 0 \\ T_{13} & T_{13} & T_{13} & 0 & 0 & 0 & 0 & 0 & 0 \end{bmatrix} \{\mathbf{L}\}$$

$$-\{\delta\mathbf{L}\}^T \begin{bmatrix} T_{11} & 0 & 0 & T_{12} & 0 & 0 & 0 & 0 & T_{13} \\ 0 & T_{22} & 0 & 0 & T_{21} & T_{23} & 0 & 0 & 0 \\ 0 & 0 & T_{33} & 0 & 0 & 0 & T_{32} & T_{31} & 0 \\ 0 & T_{12} & 0 & T_{11} & T_{13} & 0 & 0 & 0 & 0 \\ T_{21} & 0 & 0 & T_{22} & 0 & 0 & 0 & 0 & T_{23} \\ 0 & 0 & T_{23} & 0 & 0 & 0 & T_{22} & T_{21} & 0 \\ 0 & T_{32} & 0 & 0 & T_{31} & T_{33} & 0 & 0 & 0 \\ T_{31} & 0 & 0 & T_{32} & 0 & 0 & 0 & 0 & T_{33} \\ 0 & 0 & T_{13} & 0 & 0 & 0 & T_{12} & T_{11} & 0 \end{bmatrix} \{\mathbf{L}\}$$

$$= \{\delta\mathbf{L}\}^T \begin{bmatrix} 0 & T_{11} & T_{11} & -T_{12} & 0 & 0 & 0 & 0 & -T_{13} \\ T_{22} & 0 & T_{22} & 0 & -T_{12} & -T_{23} & 0 & 0 & 0 \\ T_{33} & T_{33} & 0 & 0 & 0 & 0 & -T_{23} & -T_{31} & 0 \\ T_{12} & 0 & T_{12} & 0 & -T_{11} & -T_{13} & 0 & 0 & 0 \\ 0 & T_{21} & T_{21} & -T_{22} & 0 & 0 & 0 & 0 & -T_{23} \\ T_{23} & T_{23} & 0 & 0 & 0 & 0 & -T_{22} & -T_{12} & 0 \\ T_{32} & 0 & T_{32} & 0 & -T_{31} & -T_{33} & 0 & 0 & 0 \\ 0 & T_{31} & T_{31} & -T_{32} & 0 & 0 & 0 & 0 & -T_{33} \\ T_{13} & T_{13} & 0 & 0 & 0 & 0 & -T_{12} & -T_{11} & 0 \end{bmatrix} \{\mathbf{L}\}$$

$$= \delta\vec{u}_N^{\ T} [B_{NL}]^T [T^{**}][B_{NL}]\vec{u}_N$$

$$(\boldsymbol{W}\cdot\boldsymbol{T}'-\boldsymbol{T}'\cdot\boldsymbol{W})\cdot\delta\boldsymbol{L}=\left\{\frac{1}{2}(\boldsymbol{L}-\boldsymbol{L}^{T})\cdot\boldsymbol{T}'-\boldsymbol{T}'\cdot\frac{1}{2}(\boldsymbol{L}-\boldsymbol{L}^{T})\right\}\cdot\delta\boldsymbol{L}$$

$$=\frac{1}{2}\begin{bmatrix}0 & L_{12}-L_{21} & L_{13}-L_{31}\\ L_{21}-L_{12} & 0 & L_{23}-L_{32}\\ L_{31}-L_{13} & L_{32}-L_{23} & 0\end{bmatrix}\begin{bmatrix}T'_{11} & T'_{12} & T'_{13}\\ T'_{21} & T'_{22} & T'_{23}\\ T'_{31} & T'_{32} & T'_{33}\end{bmatrix}\cdot\delta\boldsymbol{L}-\frac{1}{2}\begin{bmatrix}T'_{11} & T'_{12} & T'_{13}\\ T'_{21} & T'_{22} & T'_{23}\\ T'_{31} & T'_{32} & T'_{33}\end{bmatrix}\begin{bmatrix}0 & L_{12}-L_{21} & L_{13}-L_{31}\\ L_{21}-L_{12} & 0 & L_{23}-L_{32}\\ L_{31}-L_{13} & L_{32}-L_{23} & 0\end{bmatrix}\cdot\delta\boldsymbol{L}$$

$$=\{\delta\boldsymbol{L}\}^{T}\frac{1}{2}\begin{Bmatrix}T'_{21}(L_{12}-L_{21})+T'_{31}(L_{13}-L_{31})\\ T'_{12}(L_{21}-L_{12})+T'_{32}(L_{23}-L_{32})\\ T'_{13}(L_{31}-L_{13})+T'_{23}(L_{32}-L_{23})\\ T'_{22}(L_{12}-L_{21})+T'_{32}(L_{13}-L_{31})\\ T'_{11}(L_{21}-L_{12})+T'_{31}(L_{23}-L_{32})\\ T'_{13}(L_{21}-L_{12})+T'_{33}(L_{23}-L_{32})\\ T'_{12}(L_{31}-L_{13})+T'_{22}(L_{32}-L_{23})\\ T'_{11}(L_{31}-L_{13})+T'_{21}(L_{32}-L_{23})\\ T'_{23}(L_{12}-L_{21})+T'_{33}(L_{13}-L_{31})\end{Bmatrix}-\{\delta\boldsymbol{L}\}^{T}\frac{1}{2}\begin{Bmatrix}T'_{12}(L_{21}-L_{12})+T'_{13}(L_{31}-L_{13})\\ T'_{21}(L_{12}-L_{21})+T'_{23}(L_{32}-L_{23})\\ T'_{31}(L_{13}-L_{31})+T'_{32}(L_{23}-L_{32})\\ T'_{11}(L_{12}-L_{21})+T'_{13}(L_{32}-L_{23})\\ T'_{22}(L_{21}-L_{12})+T'_{23}(L_{31}-L_{13})\\ T'_{21}(L_{13}-L_{31})+T'_{22}(L_{23}-L_{32})\\ T'_{31}(L_{12}-L_{21})+T'_{33}(L_{32}-L_{23})\\ T'_{32}(L_{21}-L_{12})+T'_{33}(L_{31}-L_{13})\\ T'_{11}(L_{13}-L_{31})+T'_{12}(L_{23}-L_{32})\end{Bmatrix}$$

$$=\{\delta\boldsymbol{L}\}^{T}\frac{1}{2}\begin{bmatrix}0 & 0 & 0 & T'_{21} & -T'_{21} & 0 & 0 & -T'_{31} & T'_{31}\\ 0 & 0 & 0 & -T'_{12} & T'_{12} & T'_{32} & -T'_{32} & 0 & 0\\ 0 & 0 & 0 & 0 & 0 & -T'_{23} & T'_{23} & T'_{13} & -T'_{13}\\ 0 & 0 & 0 & T'_{22} & -T'_{22} & 0 & 0 & -T'_{32} & T'_{32}\\ 0 & 0 & 0 & -T'_{11} & T'_{11} & T'_{31} & -T'_{31} & 0 & 0\\ 0 & 0 & 0 & -T'_{13} & T'_{13} & -T'_{33} & T'_{33} & 0 & 0\\ 0 & 0 & 0 & 0 & 0 & -T'_{22} & T'_{22} & T'_{12} & -T'_{12}\\ 0 & 0 & 0 & 0 & 0 & -T'_{21} & T'_{21} & T'_{11} & -T'_{11}\\ 0 & 0 & 0 & T'_{23} & -T'_{23} & 0 & 0 & -T'_{33} & T'_{33}\end{bmatrix}\{\boldsymbol{L}\}-\{\delta\boldsymbol{L}\}^{T}\frac{1}{2}\begin{bmatrix}0 & 0 & 0 & -T'_{12} & T'_{12} & 0 & 0 & T'_{13} & -T'_{12}\\ 0 & 0 & 0 & T'_{21} & -T'_{21} & -T'_{23} & T'_{23} & 0 & 0\\ 0 & 0 & 0 & 0 & 0 & T'_{32} & -T'_{32} & -T'_{31} & T'_{31}\\ 0 & 0 & 0 & T'_{11} & -T'_{11} & -T'_{13} & T'_{13} & 0 & 0\\ 0 & 0 & 0 & -T'_{22} & T'_{22} & 0 & 0 & T'_{23} & -T'_{23}\\ 0 & 0 & 0 & 0 & 0 & T'_{22} & -T'_{22} & -T'_{21} & T'_{21}\\ 0 & 0 & 0 & T'_{31} & -T'_{31} & -T'_{33} & T'_{33} & 0 & 0\\ 0 & 0 & 0 & -T'_{32} & T'_{32} & 0 & 0 & T'_{33} & -T'_{33}\\ 0 & 0 & 0 & 0 & 0 & T'_{12} & -T'_{12} & -T'_{11} & T'_{11}\end{bmatrix}\{\boldsymbol{L}\}$$

$$=\{\delta\boldsymbol{L}\}^{T}\begin{bmatrix}0 & 0 & 0 & T'_{12} & -T'_{12} & 0 & 0 & -T'_{31} & T'_{31}\\ 0 & 0 & 0 & -T'_{12} & T'_{12} & T'_{23} & -T'_{23} & 0 & 0\\ 0 & 0 & 0 & 0 & 0 & -T'_{23} & T'_{23} & T'_{31} & -T'_{31}\\ 0 & 0 & 0 & -\frac{1}{2}(T'_{11}-T'_{22}) & \frac{1}{2}(T'_{11}-T'_{22}) & \frac{1}{2}T'_{31} & -\frac{1}{2}T'_{31} & -\frac{1}{2}T'_{23} & \frac{1}{2}T'_{23}\\ 0 & 0 & 0 & -\frac{1}{2}(T'_{11}-T'_{22}) & \frac{1}{2}(T'_{11}-T'_{22}) & \frac{1}{2}T'_{31} & -\frac{1}{2}T'_{31} & -\frac{1}{2}T'_{23} & \frac{1}{2}T'_{23}\\ 0 & 0 & 0 & -\frac{1}{2}T'_{31} & \frac{1}{2}T'_{31} & -\frac{1}{2}(T'_{22}-T'_{33}) & \frac{1}{2}(T'_{22}-T'_{33}) & \frac{1}{2}T'_{12} & -\frac{1}{2}T'_{12}\\ 0 & 0 & 0 & -\frac{1}{2}T'_{31} & \frac{1}{2}T'_{31} & -\frac{1}{2}(T'_{22}-T'_{33}) & \frac{1}{2}(T'_{22}-T'_{33}) & \frac{1}{2}T'_{12} & -\frac{1}{2}T'_{12}\\ 0 & 0 & 0 & \frac{1}{2}T'_{23} & -\frac{1}{2}T'_{23} & -\frac{1}{2}T'_{12} & \frac{1}{2}T'_{12} & \frac{1}{2}(T'_{11}-T'_{33}) & -\frac{1}{2}(T'_{11}-T'_{33})\\ 0 & 0 & 0 & \frac{1}{2}T'_{23} & -\frac{1}{2}T'_{23} & -\frac{1}{2}T'_{12} & \frac{1}{2}T'_{12} & \frac{1}{2}(T'_{11}-T'_{33}) & -\frac{1}{2}(T'_{11}-T'_{33})\end{bmatrix}\{\boldsymbol{L}\}$$

$$\left\{ (tr\boldsymbol{D})\boldsymbol{T} - \boldsymbol{T}\boldsymbol{L}^T + (\boldsymbol{W}\cdot\boldsymbol{T}' - \boldsymbol{T}'\cdot\boldsymbol{W}) \right\} \cdot \delta\boldsymbol{L} =$$

$$= \{\delta\boldsymbol{L}\}^T
\begin{bmatrix}
0 & T_{11} & T_{11} & 0 & -T_{12}' & 0 & 0 & -T_{31}' & 0 \\
T_{22} & 0 & T_{22} & -T_{12}' & 0 & 0 & -T_{23}' & 0 & 0 \\
T_{33} & T_{33} & 0 & 0 & 0 & -T_{23}' & 0 & 0 & -T_{31}' \\
T_{12} & 0 & T_{12} & -\frac{1}{2}(T_{11}'-T_{22}') & -\frac{1}{2}(T_{11}'+T_{22}')-p & -\frac{1}{2}T_{31}' & -\frac{1}{2}T_{31}' & -\frac{1}{2}T_{23}' & \frac{1}{2}T_{23}' \\
0 & T_{12} & T_{12} & -\frac{1}{2}(T_{11}'+T_{22}')-p & \frac{1}{2}(T_{11}'-T_{22}') & \frac{1}{2}T_{31}' & -\frac{1}{2}T_{31}' & -\frac{1}{2}T_{23}' & -\frac{1}{2}T_{23}' \\
T_{23} & T_{23} & 0 & -\frac{1}{2}T_{31}' & \frac{1}{2}T_{31}' & -\frac{1}{2}(T_{22}'-T_{33}') & -\frac{1}{2}(T_{22}'+T_{33}')-p & -\frac{1}{2}T_{12}' & \frac{1}{2}T_{12}' \\
T_{23} & 0 & T_{23} & -\frac{1}{2}T_{31}' & -\frac{1}{2}T_{31}' & -\frac{1}{2}(T_{22}'+T_{33}')-p & \frac{1}{2}(T_{22}'-T_{33}') & \frac{1}{2}T_{12}' & -\frac{1}{2}T_{12}' \\
0 & T_{31} & T_{31} & -\frac{1}{2}T_{23}' & -\frac{1}{2}T_{23}' & -\frac{1}{2}T_{12}' & \frac{1}{2}T_{12}' & -\frac{1}{2}(T_{33}'-T_{11}') & -\frac{1}{2}(T_{33}'+T_{11}')-p \\
T_{31} & T_{31} & 0 & \frac{1}{2}T_{23}' & -\frac{1}{2}T_{23}' & -\frac{1}{2}T_{12}' & -\frac{1}{2}T_{12}' & -\frac{1}{2}(T_{33}'+T_{11}')-p & \frac{1}{2}(T_{33}'-T_{11}')
\end{bmatrix}
\{\boldsymbol{L}\}$$

$$= \{\delta\dot{u}_N\}^T [B_{NL}]^T [T^*][B_{NL}]\{\dot{u}_N\}$$

$$\left\{ (tr\mathbf{D})\mathbf{T} - \mathbf{T}\mathbf{L}^{\mathbf{T}} + (\mathbf{W}\cdot\mathbf{T}' - \mathbf{T}'\cdot\mathbf{W}) \right\} \cdot \{\delta\mathbf{L}\} = \delta\vec{u}_N{}^T [B_{NL}]^T [T^*][B_{NL}]\vec{\dot{u}}_N$$

$$\left\{ S_r \dot{p}_d^w \boldsymbol{I} + (1-S_r)\dot{p}_d^a \boldsymbol{I} \right\}\{\delta\mathbf{L}\} = \delta\ddot{u}_N{}^T \{B_v\}\left\{ S_r \dot{p}_d^w \boldsymbol{I} + (1-S_r)\dot{p}_d^a \boldsymbol{I} \right\}$$

$$\dot{\mathbf{T}}' = \overset{\nabla}{\mathbf{T}} + \mathbf{W} \cdot \mathbf{T}' - \mathbf{T}' \cdot \mathbf{W}$$

$$= \begin{bmatrix} \overset{\nabla}{T}_{11} & \overset{\nabla}{T}_{12} & \overset{\nabla}{T}_{13} \\ \overset{\nabla}{T}_{21} & \overset{\nabla}{T}_{22} & \overset{\nabla}{T}_{23} \\ \overset{\nabla}{T}_{31} & \overset{\nabla}{T}_{32} & \overset{\nabla}{T}_{33} \end{bmatrix} + \begin{bmatrix} w_{11} & w_{12} & w_{13} \\ w_{21} & w_{22} & w_{23} \\ w_{31} & w_{32} & w_{33} \end{bmatrix}\begin{bmatrix} T_{11}' & T_{12}' & T_{13}' \\ T_{21}' & T_{22}' & T_{23}' \\ T_{31}' & T_{32}' & T_{33}' \end{bmatrix} - \begin{bmatrix} T_{11}' & T_{12}' & T_{13}' \\ T_{21}' & T_{22}' & T_{23}' \\ T_{31}' & T_{32}' & T_{33}' \end{bmatrix}\begin{bmatrix} w_{11} & w_{12} & w_{13} \\ w_{21} & w_{22} & w_{23} \\ w_{31} & w_{32} & w_{33} \end{bmatrix}$$

$$= \begin{bmatrix} \overset{\nabla}{T}_{11} & \overset{\nabla}{T}_{12} & \overset{\nabla}{T}_{13} \\ \overset{\nabla}{T}_{21} & \overset{\nabla}{T}_{22} & \overset{\nabla}{T}_{23} \\ \overset{\nabla}{T}_{31} & \overset{\nabla}{T}_{32} & \overset{\nabla}{T}_{33} \end{bmatrix} + \begin{bmatrix} w_{12}T_{21}' + w_{13}T_{31}' & w_{12}T_{22}' + w_{13}T_{32}' & w_{12}T_{23}' + w_{13}T_{33}' \\ w_{21}T_{11}' + w_{23}T_{31}' & w_{21}T_{12}' + w_{23}T_{32}' & w_{21}T_{13}' + w_{23}T_{33}' \\ w_{31}T_{111}' + w_{32}T_{21}' & w_{31}T_{12}' + w_{32}T_{22}' & w_{31}T_{13}' + w_{32}T_{23}' \end{bmatrix}$$

$$- \begin{bmatrix} T_{12}'w_{21} + T_{13}'w_{31} & T_{11}'w_{12} + T_{13}'w_{32} & T_{11}'w_{13} + T_{12}'w_{23} \\ T_{22}'w_{21} + T_{23}'w_{31} & T_{21}'w_{12} + T_{23}'w_{32} & T_{21}'w_{13} + T_{22}'w_{23} \\ T_{32}'w_{21} + T_{33}'w_{31} & T_{31}'w_{12} + T_{33}'w_{32} & T_{31}'w_{13} + T_{32}'w_{23} \end{bmatrix}$$

$$= \begin{bmatrix} \overset{\nabla}{T}_{11} + (w_{12}T_{21}' + w_{13}T_{31}') & \overset{\nabla}{T}_{12} + (w_{12}T_{22}' + w_{13}T_{32}') & \overset{\nabla}{T}_{13} + (w_{12}T_{23}' + w_{13}T_{33}') \\ \quad - (T_{12}'w_{21} + T_{13}'w_{31}) & \quad - (T_{11}'w_{12} + T_{13}'w_{32}) & \quad - (T_{11}'w_{13} + T_{12}'w_{23}) \\ \overset{\nabla}{T}_{21} + (w_{21}T_{11}' + w_{23}T_{31}') & \overset{\nabla}{T}_{22} + (w_{21}T_{12}' + w_{23}T_{32}') & \overset{\nabla}{T}_{23} + (w_{21}T_{13}' + w_{23}T_{33}') \\ \quad - (T_{22}'w_{21} + T_{23}'w_{31}) & \quad - (T_{21}'w_{12} + T_{23}'w_{32}) & \quad - (T_{21}'w_{13} + T_{22}'w_{23}) \\ \overset{\nabla}{T}_{31} + (w_{31}T_{111}' + w_{32}T_{21}') & \overset{\nabla}{T}_{32} + (w_{31}T_{12}' + w_{32}T_{22}') & \overset{\nabla}{T}_{33} + (w_{31}T_{13}' + w_{32}T_{23}') \\ \quad - (T_{32}'w_{21} + T_{33}'w_{31}) & \quad - (T_{31}'w_{12} + T_{33}'w_{32}) & \quad - (T_{31}'w_{13} + T_{32}'w_{23}) \end{bmatrix}$$

$$= \begin{bmatrix} \overset{\nabla}{T}_{11} - 2(w_{31}T_{31}' - w_{12}T_{12}') & \overset{\nabla}{T}_{12} + w_{12}(T_{22}' - T_{11}') & \overset{\nabla}{T}_{13} + w_{31}(T_{11}' - T_{33}') \\ & \quad + w_{23}T_{31}' - w_{31}T_{23}' & \quad + w_{12}T_{23}' - w_{23}T_{12}' \\ & \overset{\nabla}{T}_{22} - 2(w_{12}T_{12}' - w_{23}T_{23}') & \overset{\nabla}{T}_{23} + w_{23}(T_{33}' - T_{22}') \\ & & \quad + w_{31}T_{12}' - w_{12}T_{31}' \\ SYM & & \overset{\nabla}{T}_{33} - 2(w_{23}T_{23}' - w_{31}T_{31}') \end{bmatrix}$$

Calculation for two-dimension problem

$$\vec{u} = \{\dot{u}_1 \quad \dot{u}_2\}^T$$

$$\vec{u}_N = \{\dot{u}_1^1 \quad \dot{u}_2^1 \quad \cdots \quad \dot{u}_1^n \quad \dot{u}_2^n\}^T$$

$$\vec{L} = \{L_{11} \quad L_{22} \quad L_{12} \quad L_{21}\}^T$$

$$\{\Pi\} = \{\Pi_{11} \quad \Pi_{22} \quad \Pi_{12} \quad \Pi_{21}\}^T$$

$$[B] = \begin{bmatrix} N_{,1}^1 & 0 & \cdots & N_{,1}^n & 0 \\ 0 & N_{,2}^1 & \cdots & 0 & N_{,2}^n \\ N_{,2}^1 & N_{,1}^1 & \cdots & N_{,2}^n & N_{,1}^n \end{bmatrix}$$

$$[B_{NL}] = \begin{bmatrix} N_{,1}^1 & 0 & \cdots & N_{,1}^n & 0 \\ 0 & N_{,2}^1 & \cdots & 0 & N_{,2}^n \\ N_{,2}^1 & 0 & \cdots & N_{,2}^n & 0 \\ 0 & N_{,1}^1 & \cdots & 0 & N_{,1}^n \end{bmatrix}$$

$$\{B_v\}^T = \{N_{,1}^1 \quad N_{,2}^1 \quad \cdots \quad N_{,1}^n \quad N_{,2}^n\}$$

$$\mathbf{W} = \begin{bmatrix} 0 & w_{12} \\ w_{21} & 0 \end{bmatrix}$$

$$\{(tr\mathbf{D})\mathbf{T} - \mathbf{TL}^{\mathbf{T}}\} \cdot \{\delta\mathbf{L}\} =$$

$$= \{\delta\mathbf{L}\}^T \begin{bmatrix} T_{11} & T_{11} & 0 & 0 \\ T_{22} & T_{22} & 0 & 0 \\ T_{12} & T_{12} & 0 & 0 \\ T_{21} & T_{21} & 0 & 0 \end{bmatrix} \{\mathbf{L}\} - \{\delta\mathbf{L}\}^T \begin{bmatrix} T_{11} & 0 & T_{12} & 0 \\ 0 & T_{22} & 0 & T_{12} \\ 0 & T_{12} & 0 & T_{11} \\ T_{12} & 0 & T_{22} & 0 \end{bmatrix} \{\mathbf{L}\}$$

$$= \{\delta\mathbf{L}\}^T \begin{bmatrix} 0 & T_{11} & -T_{12} & 0 \\ T_{22} & 0 & 0 & -T_{12} \\ T_{12} & 0 & 0 & -T_{11} \\ 0 & T_{12} & -T_{22} & 0 \end{bmatrix}$$

$$= \delta\vec{u}_N^{\;T} [B_{NL}]^T [T^{**}][B_{NL}]\vec{u}_N$$

$$\left\{ (tr\mathbf{D})\mathbf{T} - \mathbf{T}\mathbf{L}^{\mathbf{T}} + (\mathbf{W} \cdot \mathbf{T}^{'} - \mathbf{T}^{'} \cdot \mathbf{W}) \right\} \cdot \{\delta\mathbf{L}\} =$$

$$= \{\delta\mathbf{L}\}^{T} \begin{bmatrix} 0 & T_{11} & 0 & -T_{12}^{'} \\ T_{22} & 0 & -T_{12}^{'} & 0 \\ T_{12} & 0 & -\dfrac{1}{2}(T_{11}^{'} - T_{22}^{'}) & -\dfrac{1}{2}(T_{11}^{'} + T_{22}^{'}) - p^{F} \\ 0 & T_{12} & -\dfrac{1}{2}(T_{11}^{'} + T_{22}^{'}) - p^{F} & \dfrac{1}{2}(T_{11}^{'} - T_{22}^{'}) \end{bmatrix} \{\mathbf{L}\}$$

$$= \delta\vec{u}_{N}^{\ T}[B_{NL}]^{T}[T^{*}][B_{NL}]\vec{u}_{N}$$

$$\dot{\mathbf{T}}^{'} = \overset{\triangledown}{\mathbf{T}} + \mathbf{W} \cdot \mathbf{T}^{'} - \mathbf{T}^{'} \cdot \mathbf{W}$$

$$= \begin{bmatrix} \overset{\triangledown}{T}_{11} & \overset{\triangledown}{T}_{12} \\ \overset{\triangledown}{T}_{21} & \overset{\triangledown}{T}_{22} \end{bmatrix} + \begin{bmatrix} w_{11} & w_{12} \\ w_{21} & w_{22} \end{bmatrix} \begin{bmatrix} T_{11}^{'} & T_{12}^{'} \\ T_{21}^{'} & T_{22}^{'} \end{bmatrix} - \begin{bmatrix} T_{11}^{'} & T_{12}^{'} \\ T_{21}^{'} & T_{22}^{'} \end{bmatrix} \begin{bmatrix} w_{11} & w_{12} \\ w_{21} & w_{22} \end{bmatrix}$$

$$= \begin{bmatrix} \overset{\triangledown}{T}_{11} & \overset{\triangledown}{T}_{12} \\ \overset{\triangledown}{T}_{21} & \overset{\triangledown}{T}_{22} \end{bmatrix} + \begin{bmatrix} w_{12}T_{21}^{'} & w_{12}T_{22}^{'} \\ w_{21}T_{11}^{'} & w_{21}T_{12}^{'} \end{bmatrix} - \begin{bmatrix} T_{12}^{'}w_{21} & T_{11}^{'}w_{12} \\ T_{22}^{'}w_{21} & T_{21}^{'}w_{12} \end{bmatrix}$$

$$= \begin{bmatrix} \overset{\triangledown}{T}_{11} + w_{12}T_{21}^{'} - T_{12}^{'}w_{21} & \overset{\triangledown}{T}_{12} + w_{12}T_{22}^{'} - T_{11}^{'}w_{12} \\ \overset{\triangledown}{T}_{21} + w_{21}T_{11}^{'} - T_{22}^{'}w_{21} & \overset{\triangledown}{T}_{22} + w_{21}T_{12}^{'} - T_{21}^{'}w_{12} \end{bmatrix}$$

$$= \begin{bmatrix} \overset{\triangledown}{T}_{11} + 2w_{12}T_{12}^{'} & \overset{\triangledown}{T}_{12} + w_{12}(T_{22}^{'} - T_{11}^{'}) \\ SYM & \overset{\triangledown}{T}_{22} - 2w_{12}T_{12}^{'} \end{bmatrix}$$

Appendix 2 (Green-Naghdi stress rate tensor)

Because $\boldsymbol{\Omega} = \dot{\boldsymbol{R}}\boldsymbol{R}^T$ is anti-symmetric matrix, for example:

$$\boldsymbol{\Omega} = \begin{bmatrix} 0 & \Omega_3 & \Omega_2 \\ -\Omega_3 & 0 & \Omega_1 \\ -\Omega_2 & -\Omega_1 & 0 \end{bmatrix}$$

$$(\boldsymbol{\Omega}\cdot\mathbf{T}' - \mathbf{T}'\cdot\boldsymbol{\Omega})\cdot\{\delta\boldsymbol{D}\}$$

$$= \left\{ \begin{bmatrix} 0 & \Omega_3 & \Omega_2 \\ -\Omega_3 & 0 & \Omega_1 \\ -\Omega_2 & -\Omega_1 & 0 \end{bmatrix} \cdot \begin{bmatrix} T'_{11} & T'_{12} & T'_{13} \\ T'_{21} & T'_{22} & T'_{23} \\ T'_{31} & T'_{32} & T'_{33} \end{bmatrix} - \begin{bmatrix} T'_{11} & T'_{12} & T'_{13} \\ T'_{21} & T'_{22} & T'_{23} \\ T'_{31} & T'_{32} & T'_{33} \end{bmatrix} \begin{bmatrix} 0 & \Omega_3 & \Omega_2 \\ -\Omega_3 & 0 & \Omega_1 \\ -\Omega_2 & -\Omega_1 & 0 \end{bmatrix} \right\} \{\delta\boldsymbol{D}\}$$

$$= \left\{ \begin{bmatrix} \Omega_3 T'_{21} + \Omega_2 T'_{31} & \Omega_3 T'_{22} + \Omega_2 T'_{32} & \Omega_3 T'_{23} + \Omega_2 T'_{33} \\ -\Omega_3 T'_{11} + \Omega_1 T'_{31} & -\Omega_3 T'_{12} + \Omega_1 T'_{32} & -\Omega_3 T'_{13} + \Omega_1 T'_{33} \\ -\Omega_2 T'_{11} - \Omega_1 T'_{21} & -\Omega_2 T'_{12} - \Omega_1 T'_{22} & -\Omega_2 T'_{13} - \Omega_1 T'_{23} \end{bmatrix} \right.$$
$$\left. - \begin{bmatrix} -\Omega_3 T'_{12} - \Omega_2 T'_{13} & \Omega_3 T'_{11} - \Omega_1 T'_{13} & \Omega_2 T'_{11} + \Omega_1 T'_{12} \\ -\Omega_3 T'_{22} - \Omega_2 T'_{23} & \Omega_3 T'_{21} - \Omega_1 T'_{23} & \Omega_2 T'_{21} + \Omega_1 T'_{22} \\ -\Omega_3 T'_{32} - \Omega_2 T'_{33} & \Omega_3 T'_{31} - \Omega_1 T'_{33} & \Omega_2 T'_{31} + \Omega_1 T'_{32} \end{bmatrix} \right\} \{\delta\boldsymbol{D}\}$$

$$= \left\{ \begin{bmatrix} 2(\Omega_3 T'_{12} + \Omega_2 T'_{13}) & \Omega_3(T'_{22} - T'_{11}) + \Omega_2 T'_{32} + \Omega_1 T'_{13} & \Omega_3 T'_{23} + \Omega_2(T'_{33} - T'_{11}) - \Omega_1 T'_{12} \\ \Omega_3(T'_{22} - T'_{11}) + \Omega_1 T'_{31} + \Omega_2 T'_{23} & -2\Omega_3 T'_{12} + 2\Omega_1 T'_{32} & -\Omega_3 T'_{13} - \Omega_2 T'_{21} + \Omega_1(T'_{33} - T'_{22}) \\ \Omega_2(T'_{33} - T'_{11}) - \Omega_1 T'_{21} + \Omega_3 T'_{32} & \Omega_1(T'_{33} - T'_{22}) - \Omega_2 T'_{12} - \Omega_3 T'_{31} & -2\Omega_2 T'_{13} - 2\Omega_1 T'_{23} \end{bmatrix} \right\} \{\delta\boldsymbol{D}\}$$

$$= \{\delta\boldsymbol{D}\}^T \begin{bmatrix} 2(\Omega_3 T'_{12} + \Omega_2 T'_{13}) \\ -2\Omega_3 T'_{12} + 2\Omega_1 T'_{32} \\ -2\Omega_2 T'_{13} - 2\Omega_1 T'_{23} \\ \Omega_3(T'_{22} - T'_{11}) + \Omega_2 T'_{32} + \Omega_1 T'_{13} \\ \Omega_3 T'_{23} + \Omega_2(T'_{33} - T'_{11}) - \Omega_1 T'_{12} \\ -\Omega_3 T'_{13} - \Omega_2 T'_{21} + \Omega_1(T'_{33} - T'_{22}) \end{bmatrix} = \vec{u}_N^T [B]^T \begin{bmatrix} 2(\Omega_3 T'_{12} + \Omega_2 T'_{13}) \\ -2\Omega_3 T'_{12} + 2\Omega_1 T'_{32} \\ -2\Omega_2 T'_{13} - 2\Omega_1 T'_{23} \\ \Omega_3(T'_{22} - T'_{11}) + \Omega_2 T'_{32} + \Omega_1 T'_{13} \\ -\Omega_3 T'_{13} - \Omega_2 T'_{21} + \Omega_1(T'_{33} - T'_{22}) \\ \Omega_3 T'_{23} + \Omega_2(T'_{33} - T'_{11}) - \Omega_1 T'_{12} \end{bmatrix}$$

$$= \delta\vec{u}_N^T [B]^T [T'_\Omega]$$

Calculation for two-dimension problem

$$\Omega = \begin{bmatrix} 0 & \Omega_3 \\ -\Omega_3 & 0 \end{bmatrix}$$

$$(\Omega \cdot \mathbf{T}' - \mathbf{T}' \cdot \Omega) \cdot \{\delta \mathbf{D}\}$$

$$= \left\{ \begin{bmatrix} 0 & \Omega_3 \\ -\Omega_3 & 0 \end{bmatrix} \begin{bmatrix} T'_{11} & T'_{12} \\ T'_{21} & T'_{22} \end{bmatrix} - \begin{bmatrix} T'_{11} & T'_{12} \\ T'_{21} & T'_{22} \end{bmatrix} \begin{bmatrix} 0 & \Omega_3 \\ -\Omega_3 & 0 \end{bmatrix} \right\} \{\delta \mathbf{D}\}$$

$$= \{\delta \mathbf{D}\}^T \begin{bmatrix} 2T'_{12}\Omega_3 \\ -2T'_{12}\Omega_3 \\ (T'_{22} - T'_{11})\Omega_3 \end{bmatrix} = \delta \vec{u}_N^T [B]^T [T'_{\Omega}]$$